Impacts of the oxidizable scaffold of catalase-peroxidase (KatG): Modulation of a heme peroxidase for catalytic versatility

by

Jessica Rose Krewall

A dissertation submitted to the Graduate Faculty of
Auburn University
in partial fulfillment of the
requirements for the Degree of
Doctor of Philosophy

Auburn, Alabama
December 11, 2021

[Keywords: catalase-peroxidase, peroxidase, hole-hopping, heme, catalase]

Copyright 2021 by Jessica Rose Krewall

Approved by

Douglas C. Goodwin, Chair, Professor and Dept. Chair, Chemistry and Biochemistry
Holly Ellis, Professor, Biochemistry and Molecular Biology, East Carolina University
Christopher Easley, C. Harry Knowles Professor, Chemistry and Biochemistry
Steven Mansoorabadi, J. Milton Harris Associate Professor, Chemistry and Biochemistry

Abstract

Catalase-peroxidase (KatG) is an antioxidant protein that plays a key role in the degradation of H_2O_2 for pathogenic and non-pathogenic bacteria and lower eukaryotes. Despite having the general structure of a heme peroxidase, KatG displays functionality distinct from a typical heme peroxidase. Two prominent examples are robust catalase activity and activation of antitubercular pro-drug isoniazid. Alongside other variations from the typical heme peroxidase scaffold, the astounding abundance of oxidizable residues within the protein structure of KatG, especially within the active-site containing N-terminal domain, seem to play a central role in the conversion of a heme peroxidase to a multifunctional enzyme. The plethora of redox-active residues within its protein structure has at least facilitated a mechanism by which KatG has converted protein oxidation from a detrimental phenomenon to a net catalytic benefit. In particular, oxidation of three active-site residues results in the formation of a KatG-unique post-translational modification (i.e., MYW adduct) near the heme center. Redox cycling of this MYW adduct between its fully-covalent and free-radical states supports robust catalase activity from an otherwise poorly catalase-active, heme-peroxidase active site. Simultaneously, the oxidation of the many Tyr, Trp, and Met positioned throughout the KatG scaffold provide hole-hopping pathways supports a unique peroxidase mechanism that functions to preserve the active site for catalase activity. The work presented here aims to better understand the heme intermediates involved in peroxidase and catalase mechanisms of KatG (Chapters 2 and 3) in addition to investigating other functionalities of the enzyme including the biosynthesis of the MYW

adduct of KatG and isoniazid activation (Chapters 4 and 5). Understanding the relationship between structure and function of KatG is likely to inform the processes and mechanisms by which enzymes, particularly oxidoreductases, gain novel catalytic function.

This work was supported by a grant from the National Science Foundation (MCB 1616059).

Acknowledgements

I cannot express how deeply grateful I am for the many people that encouraged, equipped, and challenged me to arrive to where I am today. I don't have enough space to give them each the recognition deserved, but I have written a brief thank you below.

To Ms. Carol March and Doc Saulmon, your fantastic teaching and guidance fueled my passion for chemistry and enabled me to have the confidence to pursue chemistry as my career – thank you. To the amazing professors at WBU, Dr. Gary Gray, Dr. Robert Moore, Dr. Emilia Moore, Dr. William Hahn, Dr. Adam Reinhart, Dr. Andy Kasner, Dr. Chris Thornhill, and Dr. Elise Adamson, I am here because of your investment in me, and words cannot express my gratitude. Each of you pushed me to achieve greatness, strived to provide me every opportunity to succeed, and encouraged me to keep moving forward.

A special thank you to, Dr. Doug Goodwin, my graduate research advisor and mentor. Doc, I am so grateful patient and understanding mentorship. I have learned so much from you, not only about conducting research, data analysis, and troubleshooting, but also about being an intentional, caring, and bold leader. I have greatly enjoyed being a part of your lab for the last six years. Thank you for investing in me.

I also want to thank my academic committee members, Dr. Holly Ellis, Dr. Chris Easley, Dr. Steve Mansoorabadi, and Dr. Robert Judd, my university reader, for their assistance and commitment to help me throughout graduate school, especially in the development of this document. To past and current members of the Goodwin group who I've been privileged to work with, Dr. Olive Njuma, Dr. Rene Fuanta, Dr. Hui Xu, Tarfi

Aziz, Rejaul Islam, Callie Barton, Jahangir Alam, Chidozie Ugochukwu, Savannah Petris, Patrick Sahrmann, Kirklin McWhorter, Aishah Lee, Laura Minton, and Madeleine Forbes – thank you for your help and delightful companionship. I will miss group meetings, birthday celebrations, and especially bocce ball days with you all.

Thank you to my dear friends and fellow graduate students: Dr. Kara Johnson, Dr. Julie Niklas, Dr. Ethan Hiti, Dr. Alex Bredar, Dr. Carly Engel, Dr. Ferdous Finklea, Dr. Nathan Roberts, Amanda Kurian, Niharika Dalpati, Shadi Yavari, Bryan Cronin, Kari Gasaway, and Shruti Somai. Your sweet friendship has made grad school so much better. Thank you also to my church family from West Auburn Baptist Church whose support and encouragement (and board-gaming days) kept me sane throughout graduate school. I am so grateful for the sweet memories and continued friendships with each of you.

A whole-hearted thank you to my life-long mentors and support system, my parents Rolland and Rhonda Kenneson and my grandparents Larry and Irene Kauffman. I couldn't be here without your love, support, and sacrifice! Thank you for encouraging me to follow my calling, helping me to keep perspective, and always cheering me on. I love you forever!

Thank you also to my husband, Joshua Krewall, and my dog Scout for not only journeying with me through graduate school, but also making me smile along the way. Josh, I love you and thank you for dealing with frequent late-night visits to check on bacteria and trudging through jargon to be my preliminary editor on many occasions.

Finally, and most of all, thank you to Him who has redeemed me and reclaimed me for a purpose, my Lord and Savior. It is only by His direction and strength that I have been able to accomplish anything, let alone the work presented in this document.

Table of Contents

Abstract ii

Acknowledgments iv

List of Figures xii

List of Tables xviii

List of Abbreviations xix

Chapter 1: Literature Review: Setting the Stage for Catalase-peroxidase (KatG) 1

- The trouble with oxygen 2
  - Activation of O_2 2
  - Role of cofactors in O_2 activation 4
  - Reactive oxygen species 6
- Weaponizing H_2O_2 12
  - Generation of HOX species from H_2O_2 13
  - Generation of RNS from H_2O_2 15
- Antioxidant proteins 17
  - Catalases 17
  - Peroxidases 18
  - Catalase-peroxidases 18
- Pathogens and ROS-eliminating enzymes 20
  - Pathogenicity and antioxidant proteins 20
  - KatG as a virulence factor 21

Drug resistant tuberculosis and KatG 24

Techniques for investigation of heme proteins 25

Utilization of heme *b* cofactor 25

UV-visible spectroscopy of heme proteins 29

Stopped-flow spectroscopy 32

Electron paramagnetic resonance spectroscopy 34

Mössbauer spectroscopy 42

Oxygen production by Clark electrode 49

Kinetics 49

Other methods utilized for mechanistic determination 52

Chapter 2: Understanding the Unique Peroxidase Activity of KatG 54

Introduction 54

Materials and Methods 61

Site-directed mutagenesis 61

Protein expression 62

Protein purification 62

Stopped-flow spectroscopy 63

Rapid freeze-quench electron paramagnetic resonance spectroscopy 64

Extent of O_2 production experiments 65

Identification of catalase inactive states of KatG 65

Kinetic studies of W321F KatG 65

Heme and protein-based radical states associated with proximal Trp 69

Reaction with PAA and *m*CPBA 76

Understanding enzyme rescue by PxEDs 88

Inactivation of KatG and preservation of catalysis by PxEDs....................88

Exploring range of effective exogenous electron donors 94

Conclusions....................98

Chapter 3: Toward Identification of Iron States in the Unique Catalase Mechanism of KatG: Protocols for Labeling Enzyme with ^{57}Fe 100

Introduction....................100

KatG's unique catalase activity 100

Proposed catalase mechanism of KatG....................104

Ambiguity of optical spectra of heme proteins....................106

Mössbauer spectroscopy and heme proteins....................110

Mössbauer sample preparation for KatG 113

Materials and Methods....................114

Synthesis of heme 114

Separation of heme from protoporphyrin IX 116

Characterization of synthesized heme 117

Acid-butanone removal of heme cofactor....................117

Reconstitution of apo KatG with synthesized heme 118

Heme synthesis by ferrochelatase....................118

Expression of KatG with δ-ALA and enriched iron salt....................119

Purification of KatG....................119

Preparation of ^{57}Fe ammonium sulfate 121

Rapid freeze-quench sample preparation....................121

Results and Discussion 122
Comparison of heme synthetic protocols..122
Comparison of synthesized heme and commercial heme.......................124
Reconstitution of aKatG with synthesized heme...................................124
Heme synthesis by ferrochelatase..129
Purified KatG from expression with δ-ALA and enriched Fe salt 134
Conclusions...136
Chapter 4: Toward Mechanistic Determination of the Autocatalytic Biosynthesis of the MYW Cofactor in *Mycobacterium tuberculosis* KatG..138
Introduction...138
Materials and Methods...144
Site-directed mutagenesis for R418N KatG variant 144
Expression of apo KatG..145
Purification of apo KatG...145
Reconstitution of apo KatG or preparation of rKatG..............................146
Purification of reconstituted KatG..147
Tryptic digestion and LC-MA detection...147
Predictions of absorption and fluorescence emissions............................148
Stopped-flow spectroscopy on rKatG proteins.......................................149
Results and Discussion 149
Reconstitution of aKatG 149
Prediction of optical features of YW and MYW adducts.......................154
Mass spectrometric detection of MYW cofactor...................................156

Heme state of rKatG involved in the formation of the MYW cofactor...166

Reactivity of rKatG variants at high concentrations of H_2O_2.................176

Oxidation of ABTS by reconstituted proteins 178

Conclusions...180

Chapter 5: Isoniazid Activation by Catalase-peroxidase (KatG) 181

Relationship between KatG and tuberculosis 181

MDR-TB and mutations of the *katG* gene...181

Isoniazid activation (by KatG) and mechanism of action........................182

Drug development efforts and INH derivatives......................................185

Methods for determining activation by KatG 188

Nitro blue tetrazolium (NBT) assays 188

Spectrophotometric determination of IN-NAD formation 188

Detection of IN-NAD formation by mass spectrometry..........................190

Synthesis of INH derivatives 191

Results 191

NBT assays 191

Spectrophotometric monitoring of IN-NAD formation...........................198

Attempts for IN-NAD formation by LC-MS analysis 202

Conclusions...202

Chapter 6: KatG Within the Context of the Peroxidase-Catalase Superfamily 204

The peroxidase-catalase superfamily of heme peroxidases 204

Family I 205

Family II 207

Family III 208

Hybrid A peroxidases (APx-C*c*P hybrids)..209

Hybrid B peroxidases...209

Roles of redox activity of residues within oxidoreductases...............................210

Redox sensing 211

Enzyme preservation...213

Catalytic mechanism intermediate 214

Intraprotein covalent structure 215

Roles of redox activity of residues within PC superfamily 218

Redox-active residue content across PC superfamily 219

Conservation of redox-active residues within peroxidase scaffold 222

Summary 229

Implications of the distinctions of KatG 232

Structure-function relationships of oxidoreductases..............................232

Exploring KatG as an inspiration for bioengineering 233

Methodology 236

Amino acid alignments 236

Visualization of structural similarities 237

References 238

List of Figures

Figure 1.1. Molecular orbital diagram of triplet and $^1\Delta_g$ singlet oxygen............................3

Figure 1.2. Typical mechanisms of O_2 reduction within biological systems......................7

Figure 1.3. Regeneration of Fe^{II} by ascorbate facilitates O_2 reduction.............................10

Figure 1.4. Reactive oxygen species and cellular damage...11

Figure 1.5. Weaponizing H_2O_2 to generate stronger ROS within neutrophils..................16

Figure 1.6. Examples of common peroxidatic electron donors of heme peroxidases 19

Figure 1.7. Structure and common intermediates of heme in catalases and peroxidases ..26

Figure 1.8. Peroxidatic mechanism of a typical heme peroxidase....................................28

Figure 1.9. Catalatic mechanism of a typcial heme catalase 28

Figure 1.10. Effect of ligands on *d*-electrons of iron...30

Figure 1.11. Electronic transitions responsible for heme absorption................................33

Figure 1.12. Diagram of stopped-flow spectrometer...35

Figure 1.13. Diagram of electron paramagnetic resonance spectrometer..........................37

Figure 1.14. Schematic representation of Zeeman effect in EPR spectroscopy 38

Figure 1.15. Diagram of hyperfine splitting of EPR signal from nucleus with I=1/2 39

Figure 1.16. Effect of ligand field on g-tensors and resulting EPR spectra.......................41

Figure 1.17. Schematic representation of rapid freeze-quench EPR sample preparation..44

Figure 1.18. Diagram of instrumental setup for Mössbauer spectroscopy 46

Figure 1.19. Schematic representation of Mössbauer spectrum 46

Figure 1.20. Electron configurations of common heme-Fe oxidation and spin states......48

Figure 1.21. Diagram of Clark electrode 50

Figure 1.22. Electrochemical diagram of Clark electrode 50

Figure 2.1. Typical heme peroxidase mechanism..........55

Figure 2.2. Heme peroxidase active site of KatG 57

Figure 2.3. Hole-hopping pathways through KatG enable PxED oxidation..........59

Figure 2.4. Possible mechanism of KatG peroxidase activity 60

Figure 2.5. Comparison between *wt* and W321F reactivity..........66

Figure 2.6. Effect of PxED on O_2 production by *wt* and W321F KatG..........68

Figure 2.7. Heme intermediates observed during *wt* KatG reaction with H_2O_2 71

Figure 2.8 Heme intermediates observed during *wt* KatG catalase turnover in the presence of PxED..........73

Figure 2.9. Protein-based radical intermediates identified for *wt* KatG 74

Figure 2.10. Protein-based radical intermediates of *wt* KatG in presence of PxED..........75

Figure 2.11. Absence of signal broadening upon inclusion of ABTS and ascorbate 77

Figure 2.12. Power saturation of 40 ms RFQ-EPR sample of *wt* KatG with 667 eq. H_2O_2 at pH 5..........78

Figure 2.13. Heme spectral features of *wt* and W321F KatG when reacted with PAA..........80

Figure 2.14. Comparison of protein-based radicals present when reacting *wt* KatG with H_2O_2 and PAA 81

Figure 2.15. Power saturation of EPR signal observed upon *wt* KatG reaction with PAA at 8 s..........82

Figure 2.16. Observed heme state of *wt* and W321F KatG reacted with *m*CPBA 84

Figure 2.17. Comparison of protein-based radicals present when reacting *wt* KatG with H_2O_2 and *m*CPBA 85

Figure 2.18. Power saturation of EPR signal observed upon *wt* KatG reaction with *m*CPBA at 10 ms..86

Figure 2.19. Power saturation of EPR signal observed upon *wt* KatG reaction with *m*CPBA at 24 s..87

Figure 2.20. Time-dependent rescue of *wt* and W321F by ABTS...................................89

Figure 2.21. Remaining catalase activity compared to O_2 production..............................90

Figure 2.22. Time-dependent rescue of *wt* and W321F by TMPD..................................91

Figure 2.23. Extent of O_2 production with various PxEDs..93

Figure 2.24. Aminoglycoside antibiotics and disaccharides...95

Figure 2.25. Antibiotics as electron donors with *wt* KatG..96

Figure 2.26. Sugars as electron donors for *wt* KatG..97

Figure 2.27. Synergistic scheme of the KatG bifunctional mechanism............................99

Figure 3.1. Comparison between a typical catalase and peroxidase with KatG.............101

Figure 3.2. KatG-unique structural features that enable unexpected robust catalase activity in a peroxidase active site 102

Figure 3.3. Mechanism of typical heme catalase..103

Figure 3.4. Proposed mechanisms for the KatG catalase mechanism 105

Figure 3.5. Comparison of KatG with ferric superoxol intermediate of HRP................107

Figure 3.6. Ferryl-oxo intermediates across two proteins and various substrates 109

Figure 3.7. Spectral comparison of products from various heme syntheses...................123

Figure 3.8. Comparison between commercial heme and synthesized heme...................125

Figure 3.9. Comparison of commercial heme, PpIX, and synthesized heme by FTIR ...126

Figure 3.10. Mass spectrometry analysis of commercial heme and ^{57}Fe-enriched heme 127

Figure 3.11. Contrast of KatG reconstitution with commercial heme and synthesized heme 128

Figure 3.12 Reconstitution from heme recovered from Erdman synthesis 130

Figure 3.13. Heme synthesis by ferrochelatase F110A with β-mercaptoethanol 131

Figure 3.14. Heme synthesis by ferrochelatase *wt* with 75 μM Fe and PpIX.................132

Figure 3.15. Heme synthesis by ferrochelatase *wt* with 450 μM Fe and PpIX...............133

Figure 3.16. KatG purified from expression with δ-ALA and Fe salt additives.............135

Figure 4.1. Interaction between MYW cofactor and Arg switch within KatG active site 139

Figure 4.2. Proposed mechanism for autocatalytic MYW cofactor formation...............141

Figure 4.3. Schematic representation of KatG preparation..143

Figure 4.4. Comparison of heme incorporation methods 150

Figure 4.5. EPR comparison of heme incorporation methods..152

Figure 4.6. Changes in heme spectral features of rKatG upon reaction with H_2O_2.........153

Figure 4.7. Structures of YW and MYW adducts investigated for prediction of spectral features....................155

Figure 4.8. LC chromatogram of KatG MYW and heme cofactors at 330 nm 157

Figure 4.9. Tryptic peptides detected by LC-MS and LC-MS/MS................................158

Figure 4.10. Confirmation of MYW adduct in mKatG by LC-MS and tandem MS.......159

Figure 4.11. Comparison of MS spectra across KatG preparation 161

Figure 4.12. Treating mKatG *wt* with PAA results in loss of MYW-related MS ions....163

Figure 4.13. Treatment with H_2O_2 increasing prominence of MYW-associated MS ions 164

Figure 4.14. LC-MS analysis of R418N KatG variant 165

Figure 4.15. Comparison at 429 nm of R418N and *wt* KatG across mature and reconstituted proteins 167

Figure 4.16. Heme transitions of rKatG *wt* reacted with 4 eq. H_2O_2 at pH 7 169

Figure 4.17. Heme transitions of rR418N KatG reacted with 4 eq. H_2O_2 at pH 7 171

Figure 4.18. Contrast between activity of heme transitions and MYW formation for rR418N and *wt* rKatG 173

Figure 4.19. Simulated spectra and concentration profiles from global fitting of *wt* rKatG and rR418N 174

Figure 4.20. Estimated rate constants of reconstituted proteins 175

Figure 4.21. Reaction of reconstituted KatGs with 2 mM H_2O_2 (667 eq.) at pH 7 177

Figure 4.22. Oxidation of ABTS by KatG *wt* and R418N proteins at pH 5 179

Figure 5.1. Effect of S315T mutation to the active-site channel of KatG 183

Figure 5.2. Formation of IN-NAD adduct from INH and NAD^+ 184

Figure 5.3. Conceptual representation of INH derivatives to be evaluated 186

Figure 5.4. Structures of INH derivatives for this study 187

Figure 5.5. Schematic representation of detection by NBT assays 189

Figure 5.6. NBT assay results of INH and acyl INH derivatives 194

Figure 5.7. NBT assay results of alkyl INH derivatives 195

Figure 5.8. NBT assay results of imine INH derivatives 196

Figure 5.9. NBT assay results of N33 and N34 compounds 197

Figure 5.10. IN-NAD formation by INH and KatG..199

Figure 5.11. IN-NAD formation by imine derivatives 200

Figure 5.12. IN-NAD formation by alkyl derivatives..201

Figure 5.13. INH and NAD MS ions detected from reactions of KatG with INH separated by HPLC 203

Figure 6.1. Active-site channel and *in vivo* expression comparison of PC superfamily .206

Figure 6.2. Common oxidation and oxygenation products of redox-active residues 212

Figure 6.3. Structures of covalent adducts common among oxidoreductases 217

Figure 6.4. Conservation of position and identity of redox-active residues across PC superfamily 224

Figure 6.5. Conservation of position and identity of redox-active residues across Fmaily I enzymes...225

Figure 6.6. Conservation of position and identity of redox-active residues across Fmaily II enzymes...226

Figure 6.7. Conservation of position and identity of redox-active residues across Fmaily III enzymes...227

Figure 6.8. Structural representation of conservation of redox-active residues within *Mt*KatG 228

Figure 6.9. Location and preference of redox-active residues unique to Family II enzymes 230

Figure 6.10. Location and preference of redox-active residues unique to Family III enzymes...231

Figure 6.11. Proposed mutation for YW formation within C*c*P 235

List of Tables

Table 2.1. Number of turnovers before inactivation by *wt* and W321F KatG..................70

Table 2.2. Effects of electron donors on initial rate and extent of O_2 production 93

Table 3.1 Mössbauer parameters of various heme proteins..111

Table 4.1 Comparison of KatG proteins...150

Table 4.2 Predicted YW and MYW absorption and emission values.............................155

Table 4.3 Tryptic peptides detected by mass spectrometry 158

Table 5.1 Rate of nitro blue formazan formation by INH derivatives............................192

Table 6.1 Abundance of redox-active residues across the PC superfamily....................220

Table 6.2 Relative abundance of redox-active residues across the PC superfamily........221

List of Abbreviations

Å	Angstrom
AADH	Aromatic amine dehydrogenase
ABTS	2,2’-azino-bis(3-ethylbenzthiazoline-6-sulfonic acid)
APx	Ascorbate peroxidase
Arg, R	Arginine
BPAN	*Tert*-butyl(10-phenyl-9-anthryl)nitroxide
C*c*O	Cytochrome *c* oxidase
C*c*P	Cytochrome *c* peroxidase
CDO	Cysteine dioxygenase
CPZ	Chlorpromazine
CTQ	Cysteine tryptophylquinone
Cys, C	Cysteine
δ-ALA	δ-aminolaevulinic acid
DMF	Dimethylformamide
EMB	Ethambutol
EPR	Electron paramagnetic resonance spectroscopy
EtOAc	Ethylacetate
Fe	Iron
Gly	Glycine
GO	Galactose oxidase

H_2O_2	Hydrogen peroxide
HemQ	Coproheme decarboxylase
His, H	Histidine
HPLC	High-performance liquid chromatograph
HRP	Horseradish peroxidase
HS	High-spin
$IN^\bullet$	Isonicotinoyl radical
IN-NAD	Isonicotinoyl-nicotinamide adenine dinucleotide adduct
INH	Isoniazid, isonicotinic acid hydrazide
InhA	Enoyl acyl-carrier protein reductase
JRP	Japanese radish peroxidase
KatG	Catalase-peroxidase
LiP	Lignin peroxidase
LC	Liquid chromatography
MADH	Methylamine dehydrogenase
MauG	Methylamine utilization protein
*m*CPBA	*m*-Chloroperoxybenzoic acid
MDR	Multi-drug resistant
Met, M	Methionine
MM	Molecular modeling
Mn	Manganese
MnP	Manganese peroxidase
MS	Mass spectrometry

MYW	Methionine-Tyrosine-Tryptophan adduct/cofactor
NAD	Nicotinamide adenine dinucleotide
nm	Nanometers
O_2	Molecular oxygen
PAA	Peracetic acid
PC	Peroxidase-catalase (superfamily)
PCET	Proton-coupled electron transfer
PGHS	Prostaglandin H synthase
Phe, F	Phenylalanine
PMSF	Phenylmethylsulfonyl fluoride
PNP	Peanut peroxidase
por	Porphyrin
PpIX	Protoporphyrin IX
Pro, P	Proline
PxED	Peroxidatic electron donor
PZA	Pyrazinamide
QHNDH	Quinohemoprotein amine dehydrogenase
QM	Quantum mechanics
RFQ	Rapid freeze-quench
RIF	Rifampin
RNR	Ribonucleotide reductase
RNS	Reactive nitrogen species
ROS	Reactive oxygen species

SbPx	Soybean peroxidase
TB	Tuberculosis
TMB	3,3’,5,5’-tetramehylbenzidine
TMPD	N,N,N’,N’-tetramethyl-*p*-phenylenediamine
Trp, W	Tryptophan
TTQ	Tryptophan tryptophylquinone
Tyr, Y	Tyrosine
VP	Versatile peroxidase
wt	Wild-type
YW	Tyrosine-Tryptophan adduct

Chapter One

Literature Review: Setting the Stage for Catalase-peroxidase (KatG)

Portions of this chapter are derived from the ACS symposium series chapter:
Krewall, J.R., Minton, L.E., Goodwin, D.C. (2020) *ACS Books Symposium Series: American Chemical Society,* Vol. 1357, pp 83-120.

Utilization of O_2 provides great metabolic benefit to aerobic organisms. The reduction of O_2, however, presents risks to biological systems from not only the reactive oxygen intermediates but also powerful reductants that catalyze the reduction of O_2. Enzymes, particularly those with redox-active transition metal cofactors, circumvent the inherent difficulties of direct reactions with molecular oxygen by generating highly oxidized metal complexes. Reactions between these highly oxidized metal complexes can result in generation of reactive oxygen species (ROS) and reactive nitrogen species (RNS) and therefore requires regulation in order to prevent cellular damage. The same mechanisms that are used across biology for the safe disposal of harmful reactive oxygen species ROS and RNS are the same mechanisms that harmful pathogens use to defend against the immune response of their host. This chapter will provide insight to the underlying chemistry between living systems and O_2, the consequences of O_2 activation, and the corresponding antioxidant proteins nature has developed to circumvent harmful damage. A prominent example of such an enzyme is catalase-peroxidase (KatG). The role of KatG within the context of cellular biology will be briefly addressed in Chapter 1 with greater detail of the various activities of KatG provided in Chapters 3 through 6.

1.1. The trouble with oxygen

Activation of O_2

The four-electron reduction of O_2 to H_2O comes with a very positive standard reduction potential (E°' = 0.815 V) (1). Consequently, the metabolic benefit, specifically ATP yield, from the full oxidation of carbon-based nutrients at the expense of O_2 is substantial. A direct comparison of ΔG values corresponding to the conversion of glucose to CO_2 by aerobic respiration and fermentation perfectly exemplifies the advantage of O_2 activation for metabolic benefit. Fermentation of glucose to either lactate or ethanol and CO_2 occurs according to a ΔG°' of about -200 kJ/mol while the conversion of glucose to CO_2 by O_2 occurs according to a ΔG°' of about -2870 kJ/mol. Furthermore, fermentative processing yields 2 ATP/mol glucose, but oxidative phosphorylation resulting from the complete conversion of glucose to CO_2 yields 30 or more mol ATP/mol glucose. In spite of the large thermodynamic driving force for O_2 reduction and utilization by the vast majority of biological molecules, kinetically, direct reactions with O_2 are notoriously sluggish. This is mostly due to the electronic configuration of molecular oxygen as a diradical and triplet molecule. In its ground state, ($^3\Sigma_g^-$), O_2 has two unpaired electrons of parallel spin which are distributed one each across two 2p π* orbitals (Fig. 1.1). As a result, direct reaction of $^3\Sigma_g^-$ O_2 with the singlet molecules that comprise the vast majority of those in biology comes with very high activation barrier at ambient temperature—just less than 100 kJ/mol. This is about the energy required to spin pair the two unpaired electrons of ground-state O_2 (i.e., to form singlet $^1\Delta_g$ O_2), and enable rapid reaction with singlet biomolecules. Ultimately, this arrangement is serendipitous, as without this activation

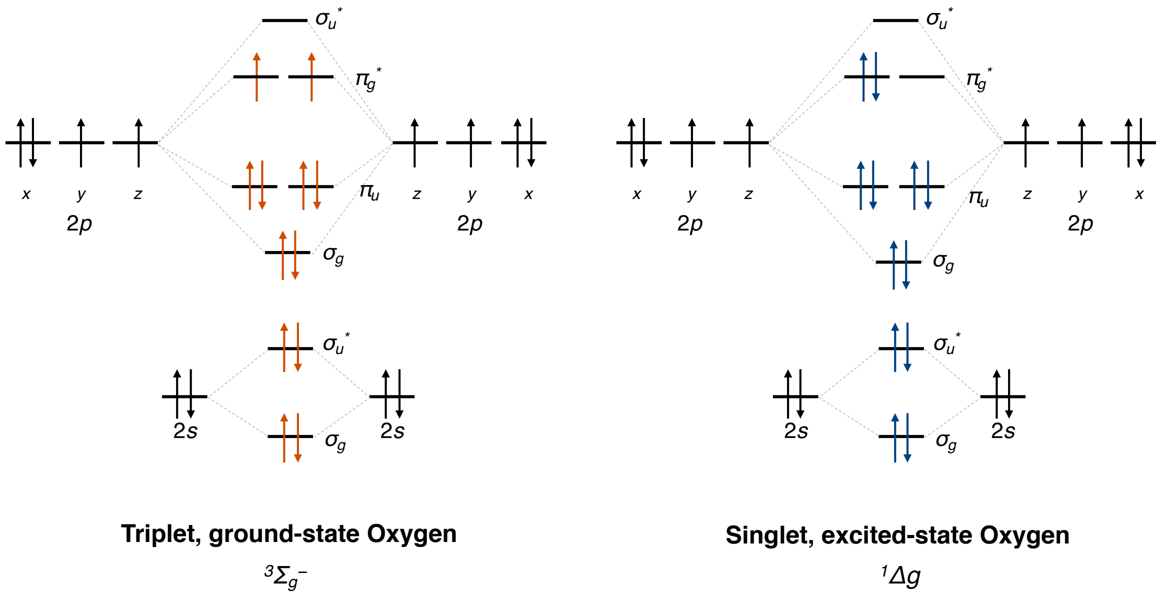
σu*
πg*
πu
σg
σu*
σg
x
y
z
2p
z
y
x
2p
2s
2s
σu*
πg*
πu
σg
σu*
σg
x
y
z
2p
z
y
x
2p
2s
2s

Triplet, ground-state Oxygen

$^3\Sigma_g^-$

Singlet, excited-state Oxygen

$^1\Delta g$

Figure 1.1. Molecular orbital diagram of triplet and $^1\Delta_g$ singlet oxygen.

barrier, life would not be possible in the presence of O_2 because anything resembling a biological molecule would be rapidly incinerated. The trick to the effective and safe use of $^3\Sigma_g^- O_2$ is strictly the time and place of its activation.

Role of cofactors in O_2 activation

To circumvent the need for photoactivation of $^3O_2$ to $^1O_2$, nature has evolved three main methods to profit from the chemical and energetic benefits of O_2 activation despite the spin restriction that prevents direct reaction with biomolecules. First, the isoalloxazine moieties of flavin cofactors (such as flavin adenine dinucleotide or flavin mononucleotide) are responsible for the transfer of an electron to molecular oxygen that results in a caged radical pair between the cofactor and the $O_2^{\bullet-}$ formed (2). Secondly, transition metals are commonly used by biological systems for the activation of O_2 because of range of spin and oxidation states available to the metal ions. Lastly, nature can circumvent the barrier to reaction with $^3O_2$ by oxidizing a target biological molecule to a radical (i.e., doublet) state. These types of reactions are often dependent on redox-active transition metals.

While redox-active transition metal cofactors are quite beneficial in the utilization/activation of O_2 for biological processes, the chemistries and reaction intermediates involved can be quite damaging. Specifically, the cytochrome P450 enzymes provide a prominent example of the double-edged nature of O_2 utilization. The oxygenase activity of cytochromes P450 is dependent not only on the heme cofactor for oxygenase activity, but also flavin-dependent reductases to regenerate the P450. The percent of decoupling between NADPH consumption to substrate oxidation varies from 50% – 90%, depending on the identity of the cytochrome P450 (3). The decoupling results in the generation of ROS by either the one-electron decay of the Fe^{II}-O_2 P450 intermediate or by protonation of the Fe^{III}-$O_2^{\bullet-}$ intermediate (i.e., the reversal of the hydrogen peroxide shunt), which result in the generation of superoxide and hydrogen peroxide, respectively (3). This decoupling by cytochromes P450 and their respective NADPH-reductases, located within the endoplasmic reticulum of animal tissues, can generate ROS concentrations comparable to that of mitochondria (3). Lipid peroxidation can serve as an example of such dysregulation of redox-active transition metals that leads to the generation of metal- and/or oxygen radical-based oxidants that initiate oxidation of lipids. Specifically, H-atom abstraction from the bis-allylic carbon of a polyunsaturated fatty acyl chain results in rapid rearrangement to form a conjugated dienyl radical which reacts at near diffusion-limited rates with O_2, forming the corresponding peroxyl radical which is itself a potent H- atom abstraction agent. Respectively, these reactions are integral to the initiation and propagation of a process called lipid peroxidation. Polyunsaturated fatty acyl chains are particularly vulnerable to reactions with intracellular ROS. Given the very broad roles these molecules play (e.g., membrane phospholipids, hormones, lipid transport particles, etc.) and the products that can be generated (e.g., peroxyl and alkoxyl radicals, reactive aldehydes and epoxides, etc.), the consequences of unregulated lipid peroxidation can be dire (e.g., DNA lesions and cancers, aging, cell necrosis, etc.) (4).

When electron transfers are properly controlled and regulated, there is tremendous benefit from the chemistry performed by cytochrome P450 enzymes. These enzymes play a prominent physiological role within living systems as they are responsible for the metabolism of xenobiotic compounds, especially those which are toxic, including drugs. Cytochromes P450 alter these compounds enabling them to be more water soluble and therefore easier to excrete by performing heteroatom oxidation, aliphatic or aromatic hydroxylation, or alkene epoxidation (5). These chemical reactions are particularly difficult given the high energy requirement for activation of C-C bonds. The same highly oxidizing heme intermediates that result in generation of molecules such as $O_2^{\bullet-}$ and H_2O_2 also catalyze the oxidation of compounds that would otherwise lead to the build-up of highly toxic compounds within organs such as the liver and kidneys.

Reactive oxygen species

Once mechanisms are in place to activate and use O_2 for aerobic metabolism (e.g., respiration), an inevitable consequence is the production of what are collectively known as ROS which are formed by partial reduction of O_2. Superoxide ($O_2^{\bullet-}$), hydrogen peroxide (H_2O_2), and hydroxyl radical ($OH^{\bullet}$) are all common ROS formed intracellularly (Fig 1.2). Due to the high permeability of membranes to O_2, in environments where O_2 is available, the one- electron and two-electron reduction of O_2 to generate $O_2^{\bullet-}$ and H_2O_2, respectively, is constantly occurring. It should be noted that H_2O_2 can be generated without the release of $O_2^{\bullet-}$ as an intermediate. Numerous flavin-dependent oxidases (e.g., glucose oxidase, choline oxidase, etc.) and some transition-metal-dependent oxidases (e.g., oxalate oxidase) generate H_2O_2 as an intentional product of substrate oxidation by O_2 (6, 7). The inadvertent leakage of electrons to O_2, forming primarily $O_2^{\bullet-}$ as an initial product, is also a major contributor to ROS production, and respiratory electron transport (RET) complexes are among the most prominent sites where this occurs. Specifically, the most prevalent offenders of inadvertent $O_2^{\bullet-}$ generation are RET complexes where reduced flavins are generated and/or complexes where quinone reduction occurs. Interestingly, cytochrome *c*

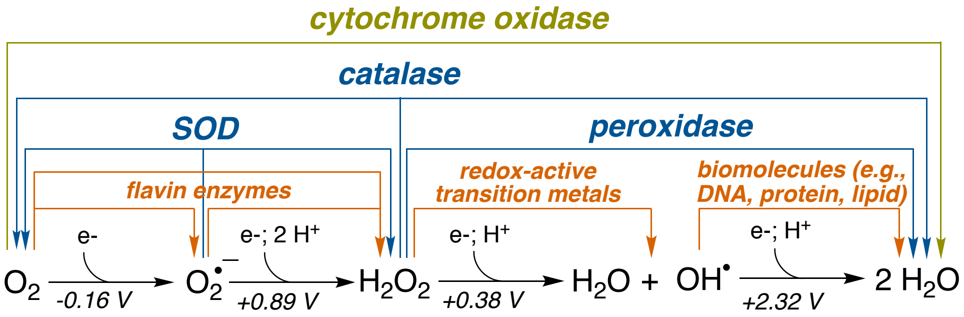
cytochrome oxidase
catalase
SOD
peroxidase
flavin enzymes
redox-active transition metals
biomolecules (e.g., DNA, protein, lipid)
e-
e-; 2 H+
e-; H+
e-; H+
O2
O2•−
H2O2
H2O + OH•
2 H2O
-0.16 V
+0.89 V
+0.38 V
+2.32 V

Figure 1.2. Typical mechanisms of O_2 reduction within biological systems. The four-electron reduction by cytochrome oxidase is presented in yellow. Common sources of one- and two-electron reductions are presented in orange. The reactions driven by ROS detoxifying enzyme are shown in blue. The standard reduction potentials ($E^{\circ'}$) for each step are provided between their respective reaction intermediates.

oxidase, the RET complex designated for O_2 binding and its complete four-electron reduction to H_2O very rarely fails to complete that process (8–10). Accordingly, all of the electron transport complexes except cytochrome *c* oxidase (i.e., complex IV) have some capacity to contribute to $O_2^{\bullet-}$ production; complexes I and III are regarded as the most prolific in this respect (9–11). Notably, the dihydrolipoamide dehydrogenase (E3) subunits of the α-ketoacid dehydrogenase complexes (e.g., α-ketoglutarate dehydrogenase) are also proposed to contribute to spurious $O_2^{\bullet-}$ production (11, 12). H_2O_2 is an inevitable byproduct of $O_2^{\bullet-}$ formation, resulting from a second one-electron reduction of $O_2^{\bullet-}$. Most commonly, H_2O_2 is generated from $O_2^{\bullet-}$ disproportionation where a second equivalent of $O_2^{\bullet-}$ is oxidized back to O_2. This can occur at high rates (~ 3 x 10^7 $M^{-1}s^{-1}$) non- enzymatically, particularly when the pH is near the $O_2^{\bullet-}/O_2H\bullet$ pK_a of 4.8 (13). As will be addressed below, this transformation is more extensively addressed enzymatically by superoxide disumtases (SODs). These are particularly efficient, catalyzing $O_2^{\bullet-}$ disproportionation close to the diffusion limit (~1 x 10^9 $M^{-1}s^{-1}$).

The single-electron reduction of H_2O_2 produces $OH^{\bullet}$, a reaction for which reduced transition metal complexes, particularly Fe^{II} and Cu^+, are well known. The notorious Fenton reaction (i.e., $Fe^{II} + H_2O_2$) generates $OH^{\bullet}$ [Eq. 1.1] or a ferryl (i.e., $[Fe^{IV}{=}O]^{2+}$) intermediate [Eq. 1.2], either of which is a potent oxidizing agent. Computational studies have suggested that the identity of the Fenton reaction product depends on, among other factors, pH and the ligand environment of the metal center (14, 15).

$$Fe^{II} + H_2O_2 + H^+ \longrightarrow Fe^{III} + OH^{\bullet} + H_2O \qquad \text{[Eq. 1.1]}$$

$$Fe^{II} + H_2O_2 \longrightarrow [FeO]^{2+} + H_2O \qquad \text{[Eq. 1.2]}$$

Indeed, with only O_2 and a suitable reductant like ascorbate, low molecular weight iron and copper complexes are able to generate the entire series of ROS, culminating in the formation of $OH^\bullet$ [Eqs. 2 – 6]. The reduction of O_2 by Fe facilitated by the addition of ascorbate (Asc) is shown in Figure 1.3.

$$Asc^{2-} + Fe^{III} \longrightarrow Asc^{\bullet-} + Fe^{II} \qquad \text{[Eq. 1.3]}$$

$$Fe^{II} + O_2 \longrightarrow Fe^{III} + O_2{}^{\bullet-} \qquad \text{[Eq. 1.4]}$$

$$2O_2{}^{\bullet-} + 2H^+ \longrightarrow H_2O_2 + O_2 \qquad \text{[Eq. 1.5]}$$

$$Fe^{II} + H_2O_2 \longrightarrow Fe^{III} + OH^\bullet + OH^- \qquad \text{[Eq. 1.6]}$$

Each ROS carries with it the capacity to participate in damaging reactions with biological molecules; however, a broadly observed pattern is that agents that are mildly destructive in their own right (e.g., $O_2{}^{\bullet-}$ and H_2O_2) end up generating far more destructive species in subsequent reactions. For example, $O_2{}^{\bullet-}$ is not particularly reactive as either a reductant or an oxidant, but it is well known to oxidize the labile 4Fe-4S clusters of aconitase and other dehydratases like those utilized in branched-chain amino acid biosynthesis. One of the particularly destructive results of this interaction is the release of a labile iron from the cluster (Fig. 1.4), generating an inactive 3Fe-4S cluster and contributing to a pool of unregulated Fe able to catalyze the generation of additional ROS (16, 17). In a similar manner, H_2O_2 itself is not an especially reactive or destructive molecule, however, if it is not removed it can be used to generate far more destructive species for which there are few defenses. Though the reaction is somewhat different, H_2O_2

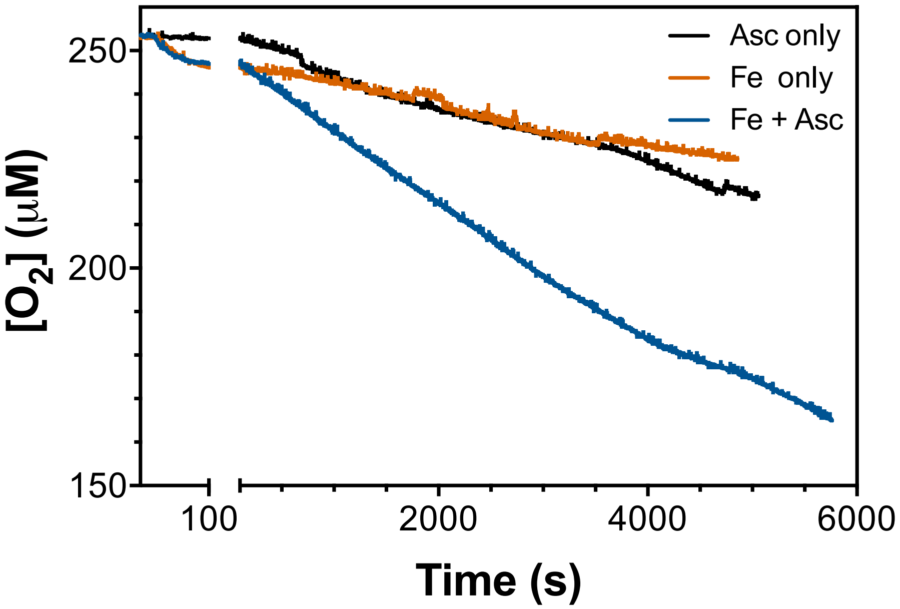

Figure 1.3. Regeneration of Fe^{II} by ascorbate facilitates O_2 reduction. O_2 reduction was monitored by Clark-type electrode in 100 mM phosphate, pH 7. Reactions contained, when present, 20 μM ferrous ammonium sulfate and 60 μM ascorbate.

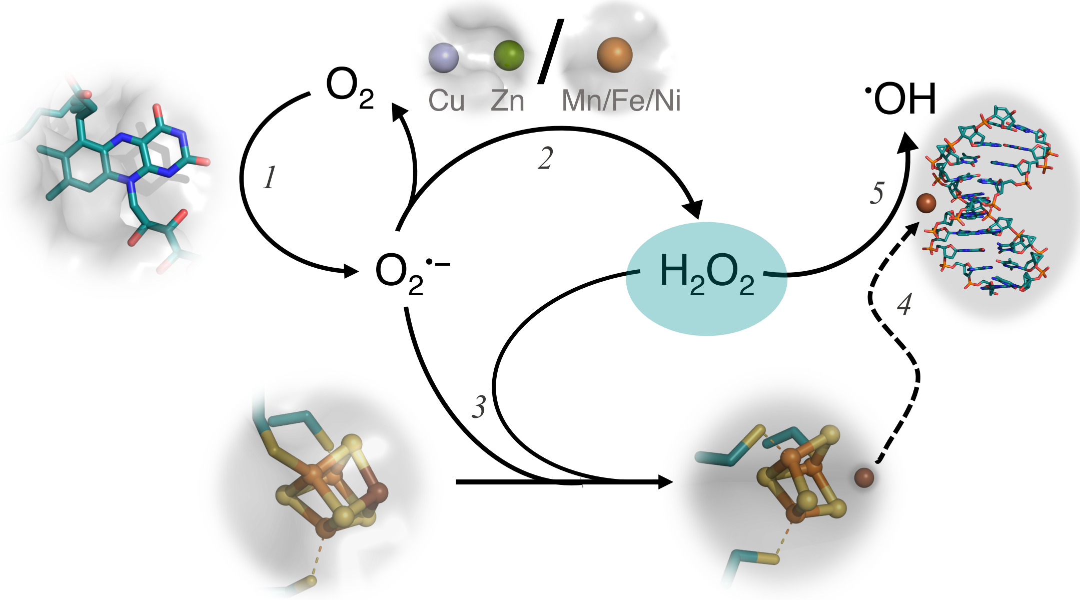

Figure 1.4. Reactive oxygen species and cellular damage. The reduced flavins and other cofactors of respiratory electron transport complexes, α-keto acid dehydrogenase complexes, etc., leak electrons to O_2, generating $O_2^{\bullet -}$ [step 1]. Superoxide disproportionation, either catalyzed by SOD (Cu-Zn-, Mn-, Fe-, and/or Ni-SOD) or uncatalyzed generates O_2 and H_2O_2 [step 2]. Either $O_2^{\bullet -}$ or H_2O_2 can react with the 4Fe4S clusters of dehydratases (e.g., aconitase), causing the release of the cluster's labile Fe ion [step 3]. Once freed from the cofactor, the Fe can adventitiously associate with critical biomolecular structures (e.g., DNA, RNA, membranes, etc.) [step 4]. Such Fe is capable of catalyzing on-site $OH^{\bullet}$ generation: Cellular reductants convert Fe^{III} to Fe^{II}; reaction of Fe^{II} with H_2O_2 produces $OH^{\bullet}$ and regenerates Fe^{III} for another reaction cycle; an indefinite supply of cellular reductants enables multiple turns of this destructive cycle. The very close proximity of the iron-associated biomolecule makes it a prime target for $OH^{\bullet}$-based oxidation/modification [step 5].

can also interact with the cubane Fe-S clusters of dehydratase enzymes, producing the release of the labile iron from the cluster (Fig. 1.4) (18). The distribution of unregulated iron into the cellular environment, combined with a ready supply of reductant and additional H_2O_2 is all that is necessary for the sustained production of OH• and similarly reactive species. The hydroxyl radical ($OH^{\bullet}$) is perhaps the most notorious of all ROS. It carries a standard reduction potential $E°'$ (pH 7) of 2.32 V (*1*), sufficient to oxidize just about any biological molecule, and it reacts at diffusion-controlled rates. Indeed, given its reactivity in thermodynamic and kinetic terms, the sites of $OH^{\bullet}$-based biological damage are dictated by the sites of adventitious binding of the metal ions that catalyze the $OH^{\bullet}$-generating reaction sequence (i.e., Fe, Cu, and other appropriately reactive redox-active transition metals). Accordingly, the failure to properly sequester these reactive metal ions in the requisite transport and storage proteins and/or deliver them safely to the proteins/enzymes that will use them as cofactors, results in substantial molecular damage at the sites their adventitious association (e.g., DNA, membranes, off-target proteins, etc.) (Fig. 1.4).

1.2. Weaponizing H_2O_2

Overall, H_2O_2 is not a strong oxidant and therefore *itself* not very threatening to pathogens. H_2O_2, however, can be and is leveraged to generate more damaging, highly oxidizing ROS and RNS. Such H_2O_2-weaponizing schemes are associated with immune response and antimicrobial efforts. Provided here will be key examples of heme peroxidases (not those from the peroxidase-catalase superfamily) and NADPH oxidases of enzymes known for weaponizing of H_2O_2.

Generation of HOX species from H_2O_2

Many enzymes from the peroxidase-cyclooxygenase superfamily catalyze oxidation of halides and/or pseudohalides. Thyroid peroxidase oxidizes $I^–$ and catalyzes iodothyronine coupling as essential steps in the synthesis of thyroxine and triiodothyronine hormones (19), but more commonly these enzymes serve a role in mammalian innate immune function where they peroxygenate halides or pseudohalides at the expense of H_2O_2 to generate the corresponding (pseudo)hypohalous acids. Although they are all capable of catalyzing these reactions, their abilities in terms of substrate range and preference vary, creating a type of specialization profile in (pseudo)halide peroxygenation. Lactoperoxidase (LPO) very efficiently performs O-atom transfer to $SCN^–$ and $I^–$; rates close to the diffusion limit ($\sim 10^8$ $M^{-1}s^{-1}$) are observed, but LPO is 4 orders of magnitude slower with $Br^–$ and does not oxidize $Cl^–$ at all (20). Eosinophil peroxidase (EPO) is similar to LPO in its reactivity with $SCN^–$ and $I^–$; however, EPO is also capable of O-atom transfer to $Br^–$ at 10^7 $M^{-1}s^{-1}$, and EPO does react with $Cl^–$ but very poorly so (21). Finally, myeloperoxidase (MPO) shows reactivity with all four (pseudo)halides. With $Br^–$, $I^–$, and $SCN^–$, it shows more modest rates than EPO ($10^6 – 10^7$ $M^{-1}s^{-1}$), but it is able to convert $Cl^–$ to HOCl with rate constants at least an order of magnitude greater than EPO (22). Interestingly, across the board, the rates of these reactions increase with decreasing pH; an increase in rate constant of an order of magnitude from pH 7 to pH 5 is typical (23).

The value to mammals for peroxidase-catalyzed peroxygenation of halides is in the antimicrobial properties of the (pseudo)hypohalous acid products. For example, LPO is expressed and secreted in large quantities by the submucosal glands of large respiratory passages (24). Concomitantly, contributing to airway lumen secretions are 1) constant active transport of SCN^- which serves to concentrate it to near mM concentrations (25), and 2) the flavin-dependent H_2O_2 production carried out by Duox 1 and/or 2 (26, 27). Together, this supplies all that is necessary to generate $HOSCN/OSCN^-$, a potent microbiocidal agent with activity against a wide range of organisms, including *Pseudomonas aeruginosa* and *Staphylococcus aereus*. On the continuum of destructive properties $HOSCN/OSCN^-$ is considerably milder than the others (27). It is primarily a thiol modification reagent and appears to have the ability to make respiratory passages inhospitable to colonization by pathogens without causing substantial tissue injury to the host.

On the other end of the continuum is HOCl, a particularly effective product of the tightly controlled MPO-based bacteriocidal system of activated neutrophils. In neutrophils at rest, MPO is sequestered in the azurogranules and the $O_2^{\bullet-}$ generating system, NADPH oxidase (NOX2) complex, is separated into its cytosolic and membrane-embedded components, and as such, it is inactive (28). Proinflammatoy cytokines transition neutrophils to a primed state, and recognition of opsin-bound pathogens by neutrophils initiates the phagocytic response. Coordinate with this is the full assembly and phosphorylation of NOX2 (29). The NADPH oxidase reaction is carried out by flavocytochrome b_{558} (or gp91phox). NADPH oxidation is accomplished on the intracellular side of the membrane by an FAD-dependent cytoplasmic domain. Subsequent electron transfer via a two- heme transmembrane domain results in O_2 reduction to $O_2^{\bullet-}$ on the extracellular or phagosomal side of the membrane (30, 31). The action of SOD rapidly converts $O_2^{\bullet-}$ to H_2O_2, and MPO, introduced into the compartment by degranulation, enables MPO-catalyzed peroxygenation of Cl^- to HOCl (28) (Fig. 1.5).

Generation of RNS from H_2O_2

It is important to point out that these are not the only reactive species generated. Reactive nitrogen species (RNS) can also be formed during normal immune responses. Nitric oxide synthase (NOS) is expressed within macrophages upon activation, initiating the formation of nitric oxide (32). When nitric oxide ($NO^\bullet$) is present, it reacts with $O_2^{\bullet-}$ to form peroxynitrite/peroxynitrous acid ($ONOO^-$/ONOOH) ($pK_a = 6.8$) (33). Close to the diffusion limit, the rates of this reaction rival that of SOD-catalyzed $O_2^{\bullet-}$ disproportionation (33). Holding to the pattern mentioned above, neither $NO^\bullet$ nor $O_2^{\bullet-}$ are particularly reactive in their own right; however, $ONOO^-$/ONOOH is a highly destructive species, carrying out the nitration or oxidation of a broad range of biomolecules, including, incidentally, the oxidative release of iron from the cubane clusters of dehydratases (34, 35). Peroxynitrite is well known to result in the nitration of aromatic amino acids, most especially tyrosine. This is not due to a *direct* reaction of $ONOO^-$, but instead of initial reaction with CO_2, followed by homolysis to form $CO_3^{\bullet-}$ and $^\bullet NO_2$ [Eqs. 7 – 9] (33).

$$NO^\bullet + O_2^{\bullet-} \longrightarrow ONOO^- \qquad \text{[Eq. 1.7]}$$

$$ONOO^- + CO_2 \longrightarrow ONOO\text{-}CO_2^- \qquad \text{[Eq. 1.8]}$$

$$ONOO\text{-}CO_2^- \longrightarrow {}^\bullet NO_2 + CO_3^{\bullet-} \qquad \text{[Eq. 1.9]}$$

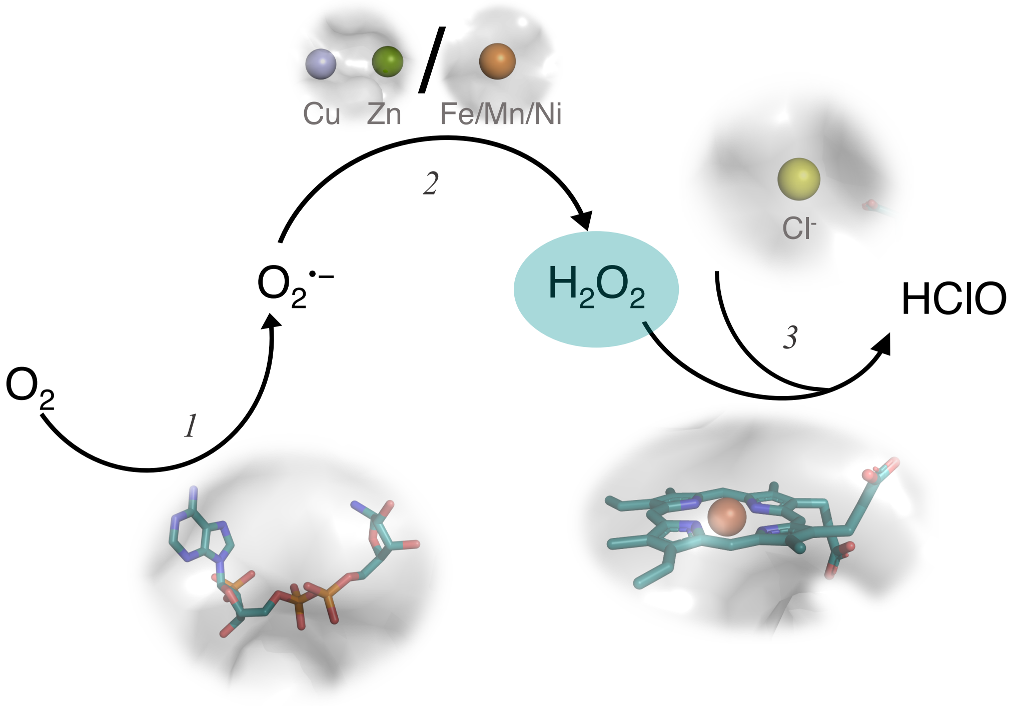

Figure 1.5. Weaponizing H_2O_2 to generate stronger ROS within neutrophils. Upon neutrophil activation of the mammalian innate immune response, myeloperoxidase is relocated by degranulation where superoxide is generated by NOX [step 1]. Naturally, superoxide dismutase is converting superoxide to H_2O_2 (and O_2) [step 2]. Myeloperoxidase can then facilitate the formation of hypochlorous acid by reacting H_2O_2 and a Cl^- anion [step 3].

1.3. Antioxidant proteins

As pointed out above highly damaging species like HOCl or $ONOO^-$ are very threatening to invading pathogens. Therefore, it is no surprise that pathogens focus efforts on removal of H_2O_2 within cells as opposed to the more damaging, downstream ROS or RNS. Aside from host-pathogen relationships, ROS and RNS, especially H_2O_2, are natural consequences of biological systems, and therefore H_2O_2 regulation is crucial to the survival of biological systems. As such, catalases, peroxidases, and catalase-peroxidases are play a key role across biology.

Catalases

Catalases not only mediate decomposition of the intracellular H_2O_2 that is an unavoidable consequence of aerobic life, but also H_2O_2 that is part of typical host immune responses. Catalases are responsible for the removal of H_2O_2 by disproportionation to water and molecular oxygen [Eq. 1.10].

$$H_2O_2 \xrightarrow{catalase} 2H_2O + O_2 \qquad \text{[Eq. 1.10]}$$

Catalase activity can be achieved by a variety of metal-based cofactors. Besides heme catalases, di- manganese centers are commonly used as cofactors within catalase enzymes (36, 37). Until recently KatG was the only catalase active enzyme identified in *M. tuberculosis*. A novel, di-iron catalase reminiscent of hemerythrin has now been confirmed to be another source of catalatic activity for *M. tuberculosis* (38, 39). The catalases that will be considered most heavily in this work are heme-dependent catalases.

Peroxidases

Like catalases, peroxidases are involved in H_2O_2 remediation within the cell, but the chemistry by which this is accomplished is different. Heme peroxidases are capable of the reduction of H_2O_2 only [Eq. 1.11]. After reaction with H_2O_2, the heme peroxidase undergoes two, one-electron reductions by a peroxidatic electron donor (PxED).

$$H_2O_2 + 2(PxED)H \xrightarrow{peroxidase} 2H_2O + 2(PxED)^{\bullet} \qquad \text{[Eq. 1.11]}$$

The identity of PxEDs vary substantially across heme peroxidases. Heme peroxidase PxEDs can vary from small inorganic complexes like: Mn-oxalate; large, irregular structures such as lignin; phenolic compounds such as ferulic acid; to small proteins like cytochrome *c* (Fig. 1.6). Larger, organic compounds such as *o*-dianisidine and ABTS are used for colorimetric determination of peroxidatic turnover *in vitro* due to their ability to easily stabilize their respective oxidized radical forms which often carries intense visible absorption spectra. Further discussion on heme peroxidases, particularly the peroxidase-catalase superfamily can be found in Chapter 2.

Catalase-peroxidases

Catalase-peroxidases (KatGs) are bifunctional enzymes, capable of both disproportionation of H_2O_2 and oxidation of peroxidatic electron donors. Traditional heme peroxidases, capable of low catalase reaction rates (k_{cat} ~ 10 s^{-1}), have catalase activity orders of magnitude lower than KatGs (k_{cat} ~ 3,000 s^{-1}), which are nearer to traditional

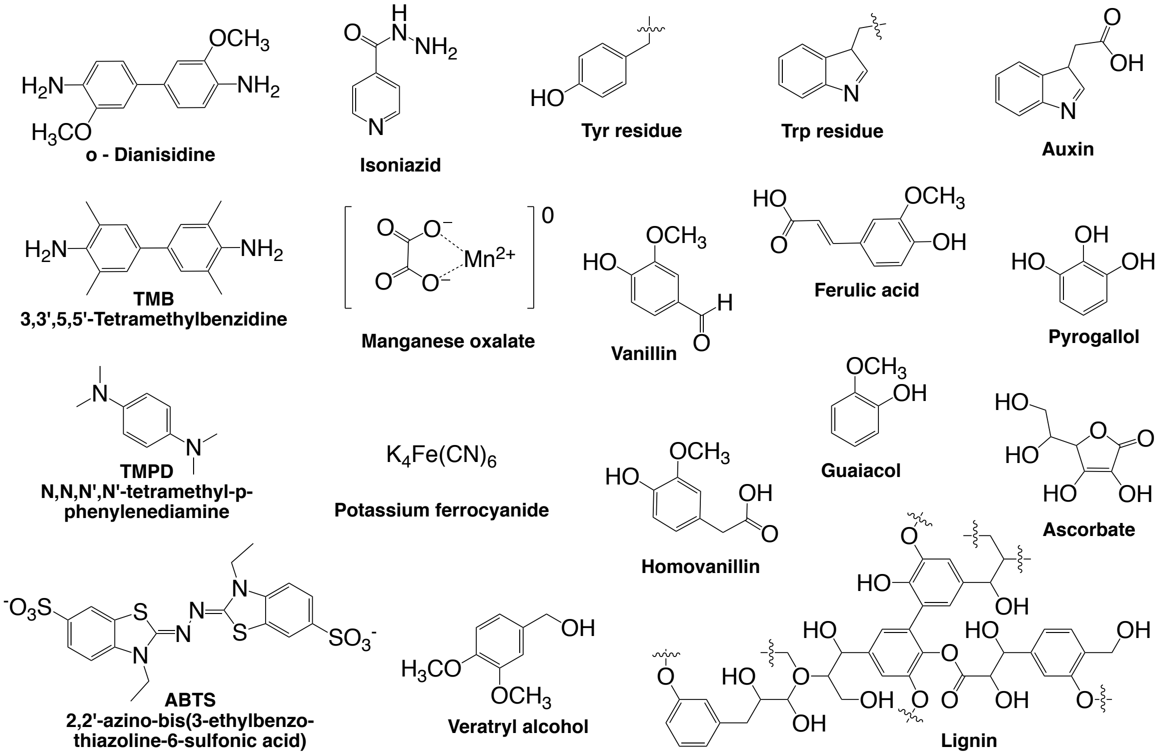
o - Dianisidine
Isoniazid
Tyr residue
Trp residue
Auxin
TMB
3,3',5,5'-Tetramethylbenzidine
Manganese oxalate
Vanillin
Ferulic acid
Pyrogallol
TMPD
N,N,N',N'-tetramethyl-p-phenylenediamine
$K_4Fe(CN)_6$
Potassium ferrocyanide
Homovanillin
Guaiacol
Ascorbate
ABTS
2,2'-azino-bis(3-ethylbenzo-thiazoline-6-sulfonic acid)
Veratryl alcohol
Lignin

Figure 1.6. Examples of common peroxidatic electron donors of heme peroxidases. The wide range of possible peroxidatic electron donors of heme peroxidases from the peroxidase-catalase superfamily is illustrated above with biologically relevant donors on the right side and non-biological, colorimetric electron donors given along the left side.

heme catalases. KatG catalase activity is facilitated by both a heme *b* cofactor and a protein-derived cofactor called the MYW adduct. The unique active-site configuration of KatGs supports robust catalase turnover within the structure of a peroxidase. This work is focused on *Mycobacterium tuberculosis* KatG and will cover four of the many activities that this enzyme is capable of catalyzing: catalase, peroxidase, MYW cofactor biosynthesis, and anti-tubercular, prodrug isoniazid activation. Other activities that KatGs have been observed to exhibit include $ONOO^-$ decomposition (40), and NADPH oxidation (41, 42). Further discussions about these enzymes will be presented in the remaining chapters of this work.

1.4. Pathogens and ROS-eliminating enzymes

Pathogenicity and antioxidant proteins

Clearly the stakes are raised for the organisms that seek to colonize higher eukaryotic hosts. It is fair to say that antimicrobial defenses like the innate immune system of mammals (e.g., neutrophils, etc.) operate a multipronged approach to killing would-be invaders. Not surprisingly, successful pathogens have evolved mechanisms to evade host defenses in a number of ways. A near universal response of higher eukaryotes to infection is to produce large amounts of $O_2^{\bullet-}$, and by virtue of the SOD present as well as the pH of the environment, copious H_2O_2 production is a foregone conclusion. The DUOX and NOX systems mentioned above are but two examples of how this occurs. However, as is illustrated above, it is not the H_2O_2 that presents the primary challenge to microbial invaders, but rather the fact that H_2O_2 can be converted to highly microbiocidal species like $HOSCN/OSCN^-$ or even $HOCl/OCl^-$. The capacity to safely detoxify H_2O_2 before it can be leveraged to much more destructive metabolites would present a significant advantage in this conflict. Not surprisingly, pathogens have at their disposal a wealth of H_2O_2 detoxifying enzymes some of which have already been mentioned

KatG as a virulence factor

KatG is a heme-dependent catalase *and* peroxidase found, thus far, only in prokaryotes and lower eukaryotes (e.g., fungi). Although it is far from the only H_2O_2 detoxifying enzyme found in these organisms, KatG is prominent in its distribution among a wide range of pathogens. Examples of KatG-carrying pathogens are found among bacteria and fungi, and among these are organisms that attack across the range of higher eukaryotes from plants to mammals. Among KatG-dependent mammalian pathogens, a common pattern is that they are bacterial and intracellular. That is, they colonize and propagate from within host immune cells such as macrophages and neutrophils; *M. tuberculosis* is a notorious example (43, 44). Though not essential for initial infection or virulence, KatG has been reported to be essential for the survival in host macrophages (45, 46). The same has been shown for another mycobacterial mammalian pathogen, *M. bovis* (47). *Francisella tularensis* is regarded as one of the most highly infectious bacterial pathogens known, able to cause disease with as few as 25 colony-forming units (48). Along with *Yersinia pestis*, it is classified as a Tier-1 Select Agent as a potential bioterrorism threat. It has been shown that a *ΔoxyR/ ΔkatG* deletion mutant of *F. tularensis* has almost no capacity to propagate within a macrophage cell line, indicating KatG may play a more central role in infection by *F. tularensis* than observed in *M. tuberculosis* (49). There are numerous organisms for which clear evidence for KatG itself as a virulence factor has not yet been established, yet the enzyme is clearly associated with other virulence and pathogen-specific factors. For example, in *Yersinia pestis*, KatG is only expressed with other virulence factors in connection with an increase in temperature from 28 to 37 °C, an event that corresponds to a transition from the flea vector to mammalian host (50–52). In enterohemorrhagic *E. coli* (O157:H7), a periplasm-targetted KatG (KatP) is carried on a large plasmid which is absent from non-pathogenic strains. In *E. coli* O157:H7, KatGs (periplasmic and especially intracellular) contribute the large majority of the H_2O_2 scavenging capacity of the organism, particularly in the exponential phase of growth (53).

It is important to note that KatG has also been implicated in the virulence of several pathogens of agricultural significance that together account for billions of dollars of crop and livestock losses on an annual basis. Some are bacterial as in *Aeromonas hydrophila* a notorious fish pathogen that can have a devastating impact on aquaculture. Here, it has been shown that KatG is essential for the intracellular survival of the organism in host macrophages (54, 55). Similarly, KatG is a virulence factor for the bacterial plant pathogen *Xanthomonas campestris* (cruciferous vegetable black rot) (55). Among plant pathogens a large proportion are fungal in origin, and it is interesting to note that both pathogenic and nonpathogenic fungi produce an intracellular version of KatG, usually designated as KatG1; however, *all* of the fungi that produce an extracellular version of KatG (i.e., KatG2) are pathogens (56). Examples include *Fusarium verticillioides* and *F. graminearum*, which are pathogens of wheat and maize and the cause of Fusarium head blight. Colonization of plant tissue results in an increase in expression of KatG2 as well as a noteworthy a distribution of KatG2 to the hyphal/plant cell boundary (57, 58). Further, deletion of KatG2 produces a decrease in *F. graminearum* virulence (57). Finally, two of the most prolific and destructive plant pathogens, *Magneporthe grisea* and *M. oryzae* (rice blast disease), also rely on extracellular KatG2 for degradation of H_2O_2 produced by plant defenses, particularly in the early stages of infection (59, 60).

Evidently KatG has a robust capacity to decompose H_2O_2. It is widely used among bacteria and lower eukaryotes for responding to the oxidative stress that comes with daily aerobic life. However, it is noteworthy that KatG is also frequently called upon by pathogens for detoxification of the substantially higher concentrations of H_2O_2 that are invariably produced by activated host immune responses. This context also produces other reactive peroxides (e.g., $ONOO^-/ONOOH$) which KatG has shown a capacity to degrade (40). However, most importantly, in this context the failure to adequately and preventively intercept and remove H_2O_2 permits the production of far more destructive species for which there is little defense. Not least among these is HOCl.

As a H_2O_2-detoxifying enzyme, KatG demonstrates not only how organisms can confront O_2 activation with a highly oxidized redox-active transition metal cofactor, but also how such enzymes protect themselves from the inherent danger of such highly reactive intermediates. Recent studies have indicated that KatG may undergo self-oxidation of Tyr, Trp, and Met residues that can participate in redox chemistry in order to preserve viability of the heme and MYW cofactors. Therefore, the relationship between structure and function of KatG presents a remarkable example for the utilization of highly reactive heme intermediates and also self-preservation to limit damage caused by these highly reactive intermediates (more on this in Chapters 2 and 3). While KatG is utilized for protection of cells not only against harm from the ROS that result from ordinary daily aerobic life, it also finds wide use among pathogenic bacteria and fungi, which must face the oxidative stress generated by host immune responses.

Drug resistant tuberculosis and KatG

The *Mycobacterium* genus relies on a cell wall structure which includes a substantial proportion of mycolic acids, long-chain branched fatty acids (e.g., ≥60 carbons) with methyl, cyclopropyl-, keto, and methoxy- modifications. This mycolic acid coating provides a unique source of structural protection (61). The thick mycolic acid layer, which comprises almost half of the mycobacterial weight, is responsible for the pathogen's impermeability and resistance to many antibacterial medications (62). InhA is the enoyl-acyl carrier protein reductase of fatty acid synthase II which catalyzes a key step in mycolic acid biosynthesis. It has been determined that *M. tuberculosis* is inhibited by treatment with pro-drug isoniazid (INH), specifically due to the inhibition of InhA. Consistent with these observations, inhibition of InhA by an isonicotinoyl-nicotinamide adenine dinucleotide adduct (IN-NAD adduct) produces defects in cell wall structure and is ultimately bactericidal (63, 64). Furthermore, KatG has been confirmed as the biological activator of the pro-drug, INH (65–69). Though the full mechanism of INH activation by KatG is unknown, it is presumed that INH is oxidized by KatG to form an isonicotinoyl radical ($IN^\bullet$). This radical then reacts with NAD^+ to generate the InhA-inhibitory IN-NAD adduct.

Mutations to the *katG* gene strongly correlate with INH-resistance. Indeed, roughly 70% of INH resistant *M. tuberculosis* produce KatG variants compromised in their ability to activate INH. By far, the most common resistance-conferring *katG* mutation results in a threonine for serine substitution at position 315 (i.e., S315T KatG). Serine 315 lies at the outer entrance of a narrow access channel to the active site heme and is well known to inhibit KatG-catalyzed formation of IN-NAD (70–72). Interestingly, S315T KatG appears to maintain its other catalytic capabilities (e.g., catalase and peroxidase activities) in spite of the disruption of INH activation. Inhibition of mycolic acid synthesis is an effective mycobateriocidal mechanism and remains a fascinating route for drug development; further studies are needed to confirm the location and mechanism of interaction between INH and KatG.

1.5. Techniques for investigation of heme proteins

Reactivity of heme proteins and specifically KatG can be monitored by an array of techniques due to the unique structural and electronic features of its heme cofactor. The rare ability to monitor *both* substrate degradation and product formation by KatG directly (i.e., without the need to couple enzymatic reactions for detection) facilitates a broad array of steady-state kinetic experiments. In addition, a collection of instrumentation can be used to gather evidence for specific steps in the catalytic mechanisms of KatG. Optical spectroscopic of changes in the heme cofactor, O_2 production by Clark-type electrode detection, electron paramagnetic resonance (EPR) spectroscopy, and Mössbauer spectroscopy each provide information on the intermediates of KatG catalysis and their reactivity that can then be combined to give a wider view of the synergy between the two activities of KatG.

Utilization of heme b as a cofactor

Heme peroxidases, heme catalases, and catalase-peroxidases all utilize heme *b* as a

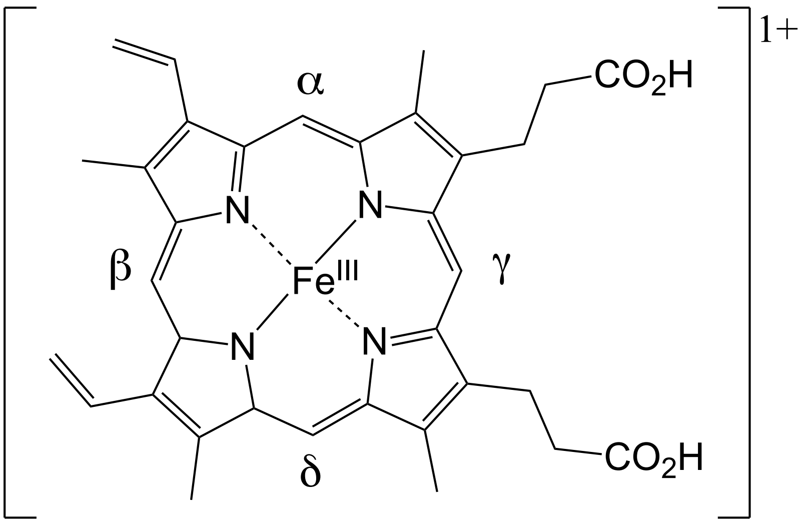
α
β
γ
δ
N
N
N
N
Fe^III
CO2H
CO2H
1+

heme *b*

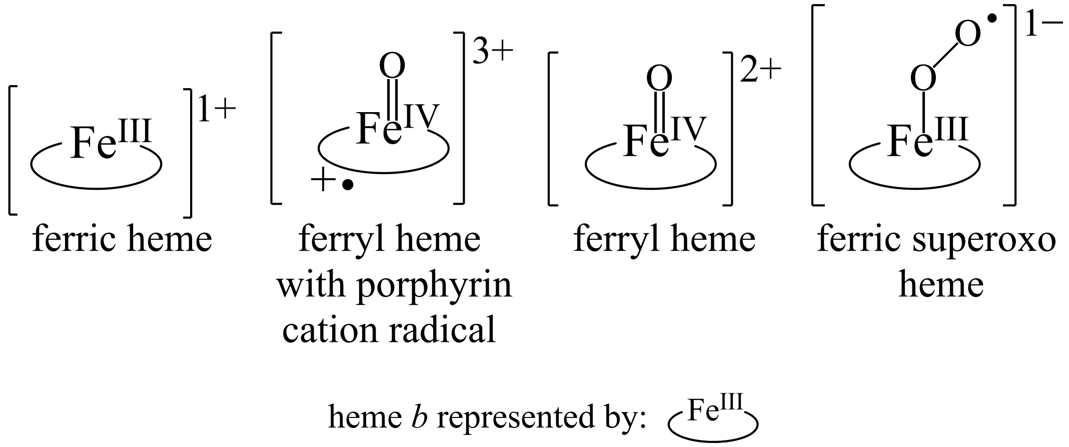
Fe^III
1+
O
Fe^IV
+•
3+
O
Fe^IV
2+
O•
O
Fe^III
1−
ferric heme
ferryl heme with porphyrin cation radical
ferryl heme
ferric superoxo heme
heme b represented by:
Fe^III

Figure 1.7. Structure and common intermediates of heme in catalases and peroxidases. The structure of heme *b* is provided with the meso edges of porphyrin ring labeled above. Heme states common to both heme peroxidases and catalases are shown below with their formal chemical title. As seen here, the ferryl-oxo heme intermediate is abbreviated to simply ferryl heme state.

cofactor to drive H_2O_2 elimination, and as such also share common heme reaction intermediates (Fig. 1.7). In both catalatic and peroxidatic mechanisms, the first intermediate formed upon reaction with H_2O_2 is a ferryl-oxo [porphyrin]$^{\bullet+}$ heme intermediate (Figs. 1.8 and 1.9). This heme state is two oxidizing equivalents above the resting, Fe^{III} enzyme. This is the only heme intermediate identified for heme catalases because this heme state is able to directly react with a second equivalent of H_2O_2 and return to the ferric state. In contrast, peroxidases often undergo two sequential, one-electron reductions to progress back to the resting state via a ferryl-oxo heme intermediate which is formed by one-electron reduction by a PxED. Finally, when overwhelmed by H_2O_2, heme peroxidases have been demonstrated to form a ferric-superoxo heme complexes which is inactive with respect to peroxidase activity. The release of oxygen from this complex is extremely slow, but once it occurs, the enzyme is able to resume peroxidatic turnover.

The electronic configuration of each heme *b* complex greatly influences its reactivity. Heme *b* is a complex between an Fe^{III}, a $3d^5$ metal, and protoporphyrin IX, a ring structure comprised of four, methylene bridged pyrrole rings with four methyl, two vinyl, and two propionyl side chains. The five $3d$-electrons of an uncoordinated Fe^{III} ion would be considered degenerate. As octahedral coordination complexes are formed between the Fe ion and six ligands, the energies of the five *d* orbitals split into three t_{2g} orbitals and two, higher energy e_g orbitals due to interactions with the metal ion's ligands. The electron-electron repulsion of an octahedral (O_h) complex results in the d_{x2-y2} and d_{z2} orbitals increasing in energy as they are oriented along the Fe^{III} z axis. The distance between the t_{2g} and e_g orbitals depends on the identity and nature of the ligand(s) coordinated to the metal. Strong-field ligands interact weakly with the *d*-orbitals of the Fe, are often ligands

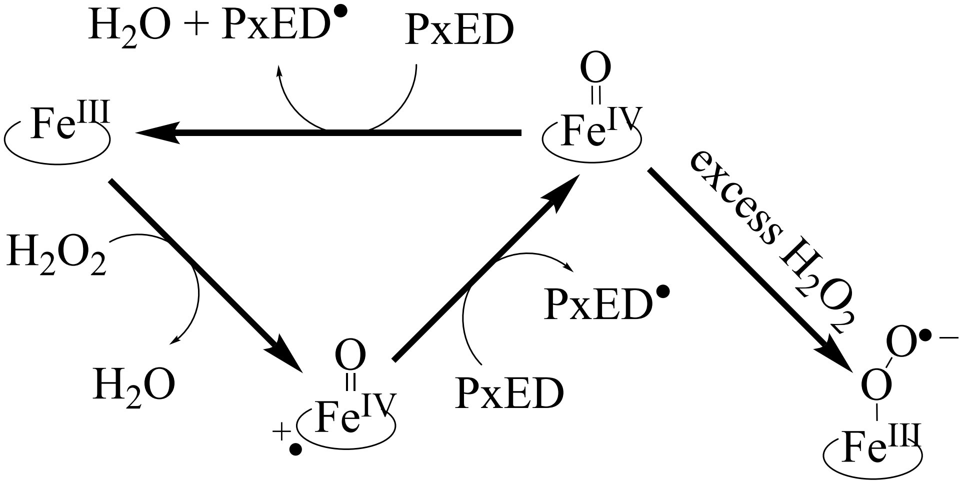
H_2O + PxED•
PxED
Fe^{III}
O
Fe^{IV}
excess H_2O_2
H_2O_2
H_2O
PxED•
O
Fe^{IV}
+•
PxED
O•−
O
Fe^{III}

Figure 1.8. Peroxidatic mechanism of a typical heme peroxidase.

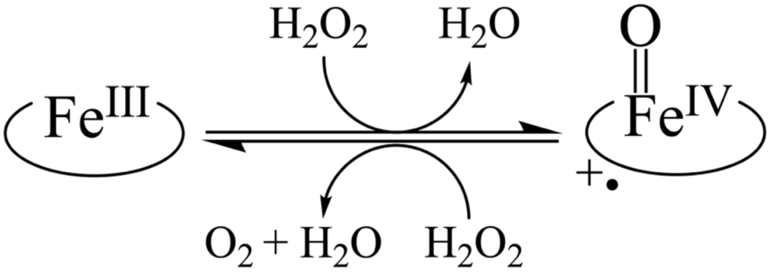
H_2O_2
H_2O
O
Fe^{III}
Fe^{IV}
+•
$O_2 + H_2O$
H_2O_2

Figure 1.9. Catalatic mechanism of a typical heme catalase.

defined as π acceptors, and result in a large energy difference between the t_{2g} and e_g orbitals (e.g., CO, CN^-, NO_2^-). Likewise, weak-field ligands result in less splitting between the the t_{2g} and e_g orbitals, are often classified as π donors, and do not interact strongly with the *d*-orbitals of the Fe ion (e.g., halides, OH^-) (Fig. 1.10).

The coordination of the Fe^{III} atom within the porphyrin ring (i.e., heme) results in even further splitting of the the t_{2g} and e_g orbitals due to the D_{4h} symmetry of the complex. The four pyrrole nitrogen atoms provide the four equatorial ligands (i.e., ~ 1.95 Å bond length) of the octahedral Fe^{III} atom and are usually closer than the axial ligands (i.e., > 2.0 Å for the protein-derived ligand and ~ 1.7 – 1.9 Å for sixth ligand, depending on the identity) resulting in further destabilization, and corresponding increase in energy, of the $d_{x2\text{-}y2}$ orbital (73). Furthermore, conjugation within the porphyrin ring system results in the destabilization of the d_{xz} and d_{yz} orbitals relative to d_{xy} (Fig. 1.10). Strong- and weak-field ligands effect the D_{4h} *d*-orbital splitting of heme similarly as described before for octahedral complexes with O_h symmetry. The electronic structure of heme supports the formation of reaction intermediates with high reduction potentials capable of facilitating a vast array of chemistries. The environment of the heme within active site of heme proteins, including the protein-derived axial ligand, greatly influences the basicity and reduction potential, and therefore, the reactivity of heme (74).

UV-visible spectroscopy of heme proteins

UV-visible spectroscopy enables observation of electronic transitions that can be used to identify molecules and sometimes monitor interactions between a metal and its ligand(s). As a molecule is irradiated by photons, those with the energy equal to that of the

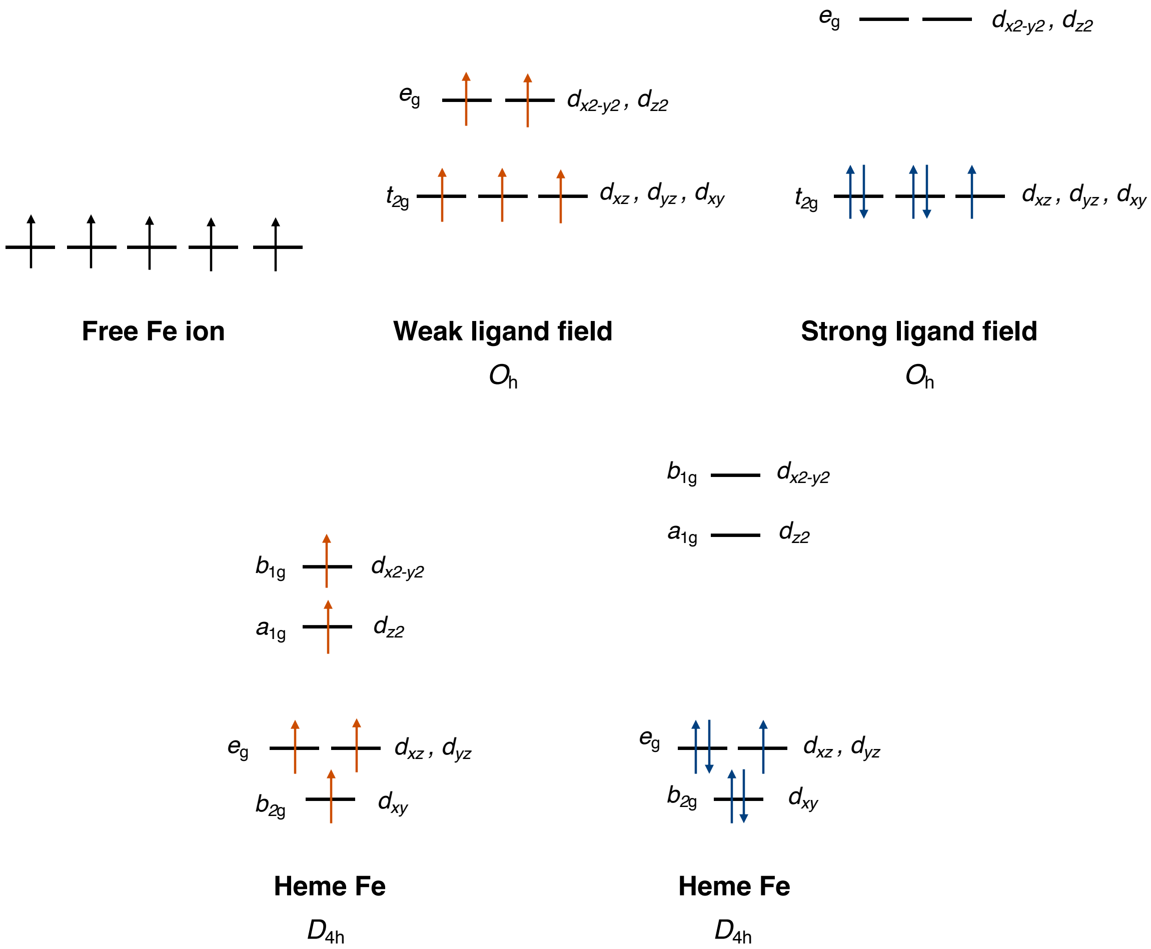
eg
dx2-y2 , dz2
eg
dx2-y2 , dz2
t2g
dxz , dyz , dxy
t2g
dxz , dyz , dxy
Free Fe ion
Weak ligand field
Oh
Strong ligand field
Oh
b1g
dx2-y2
a1g
dz2
b1g
dx2-y2
a1g
dz2
eg
dxz , dyz
b2g
dxy
eg
dxz , dyz
b2g
dxy
Heme Fe
D4h
Heme Fe
D4h

Figure 1.10. Effect of ligands on *d*-electrons of iron. Complexation of the Fe atom causes splitting in the energies of the *d*-orbitals. As a result, according to Hund's rule, the Fe complex can either be a high-spin (HS), 5/2 spin complex (orange arrows) or a low-spin (LS), 1/2 spin complex (blue arrows).

excitation of a ground state electron to an excited state within the molecule are absorbed. This transition is observed by an absorption band at the corresponding wavelength of the resonant photons that were absorbed. The spectrum of a given molecule is influenced by the electronic structure, conjugation within the molecule, other attainable transitions (i.e., multiple absorption bands), and the molar absorptivity of each absorption band. Using the Beer-Lambert law [Eq. 1.12], UV- visible absorption (A) can be used to determine the concentration (c) of a given molecule with a given molar absorptivity (ε). As such, this technique has very wide application within the field of enzymology, especially investigation of KatG, from determination of protein concentration, monitoring a reaction product or reactant, determining reaction kinetics, to monitoring changes in the cofactor spectrum throughout catalysis.

$$log\frac{I_o}{I} = A = \varepsilon lc \quad \text{[Eq. 1.12]}$$

The concentration of a protein can be estimated based on the number of Trp, Tyr, and Cys residues within the protein, given their respective molar absorptivities at 280 nm (75). Additionally, especially with heme proteins, UV-visible spectroscopy can be used to determine the ratio of total protein to coordinated heme by Abs_{Soret}/Abs_{280} which can be considered a purity ratio (also known as the reinheitzahl or RZ value).

The UV-visible absorption of a reactant or product of a reaction can be exploited to determine enzyme kinetics. If none of the products or reactants have detectible absorption features, kinetic experiments can be carried out by the coupling of the reaction of interest to other enzymatic reactions that do produce molecules with detectible absorption features (i.e., a coupled-enzyme assay). For heme catalases and peroxidases, coupled-enzyme assays are not necessary; H_2O_2 degradation can be monitored at 240 nm ($\varepsilon = 39.4\ \mu M^{-1}cm^{-1}$) and a wide array of oxidized PxEDs have unique absorption signatures that can be monitored to determine enzymatic activity.

General determination of oxidation state and coordination of heme cofactors can be derived by the changes in absorption peaks of the heme protein throughout catalysis. The observable electronic transitions of heme are provided in Figure 1.11. The transition that requires the most energy, and accordingly, is observed at the shortest wavelength, is the Soret (γ) band. Other main features of the heme spectrum are the charge transfer (CT) bands. These are indicative of excitation of an electron from the porphyrin ring to the e_g orbitals of the Fe.

Though UV-visible spectroscopy is a powerful and useful technique for rapid data collection (to be further expounded upon later specifically for stopped-flow spectroscopy), there are disadvantages when it comes to understanding the overall electronic structure around the heme Fe (i.e., assigning formal oxidation and spin states of the heme Fe) based solely on UV-visible absorption features.

Stopped-flow spectroscopy

Stopped-flow spectroscopy permits rapid kinetic analyses by combining a sub-millisecond rapid mixing apparatus to mix enzyme with other reactants (i.e., substrates, inhibitors, etc.) and move them into an optical cell for observation by UV-vis, fluorescence, or circular dichroistic feature changes during reaction (Fig. 1.12). For our investigations, we focus on UV-visible absorption changes using either a fiberoptic photodiode array for

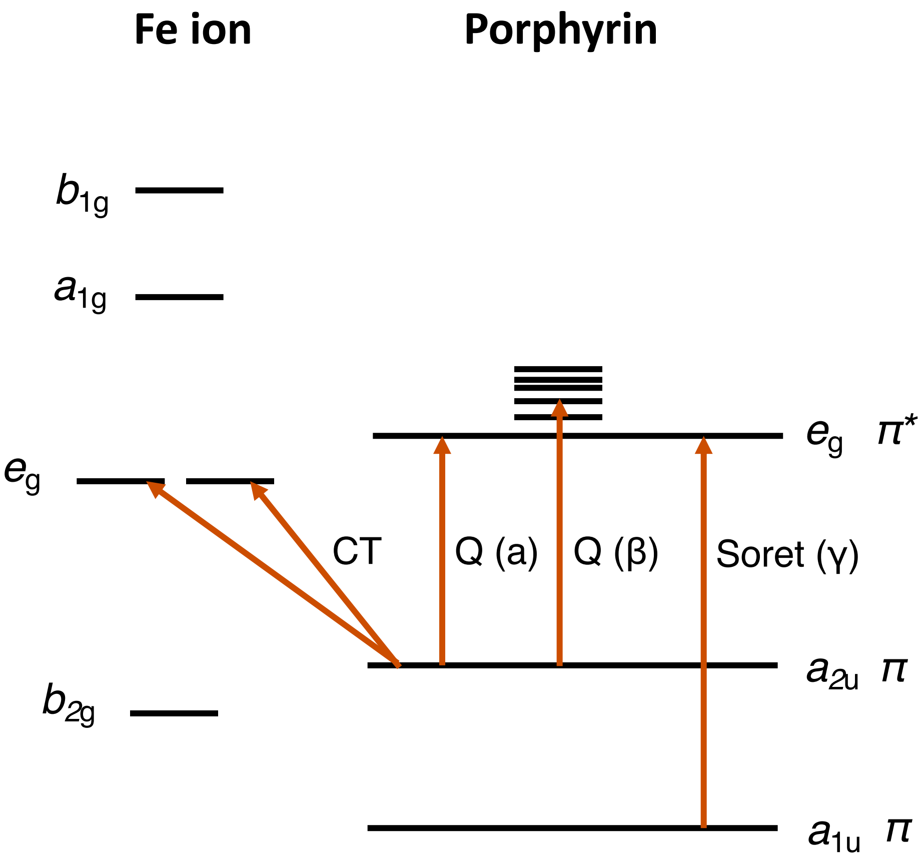
Fe ion
Porphyrin
b_{1g}
a_{1g}
e_g
b_{2g}
e_g π^*
a_{2u} π
a_{1u} π
CT
Q (a)
Q (β)
Soret (γ)

Figure 1.11. Electronic transitions responsible for heme absorption.

full spectral observation or a photomultiplier tube for single-wavelength detection. After the flow is stopped by filling the stop syringe, data collection begins and the instrument collects spectra over the whole wavelength range (for data collected by photodiode array) across the whole reaction time, which can be anywhere from tens of milliseconds to hundreds of seconds. The resulting data is a collection of 3D information of the enzyme's activity given in absorbance v. wavelength v. time (Fig. 1.12 inset). This can be plotted either as absorbance v. wavelength where overlapping spectra correspond to different times after initiation of the reaction or as absorbance v. time for a given wavelength. Such data is extremely useful as it not only provides information about holistic spectral changes in the heme cofactor upon reaction, but also allows for directed investigation at a particular wavelength through time which can corroborate with data collected by other methods. Given the molar absorptivity of the protein-bound heme, optical spectroscopy is not a highly material-intensive technique with respect to the KatG enzyme, only low micromolar concentrations are required. Though stopped-flow spectroscopy is often used for single-turnover kinetic studies, reaction conditions can be adjusted to enable multiple-turnover conditions. Depending on the substrate concentrations used relative to enzyme, a pre-steady state phase can give way to a monitorable steady-state turnover phase of the reaction.

Electron paramagnetic resonance spectroscopy

As the name indicates, electron paramagnetic resonance (EPR) spectroscopy enables the exploration of paramagnetic systems (i.e., those with unpaired electron(s)). Detection of the paramagnetic system depends on the absorption of microwaves used to

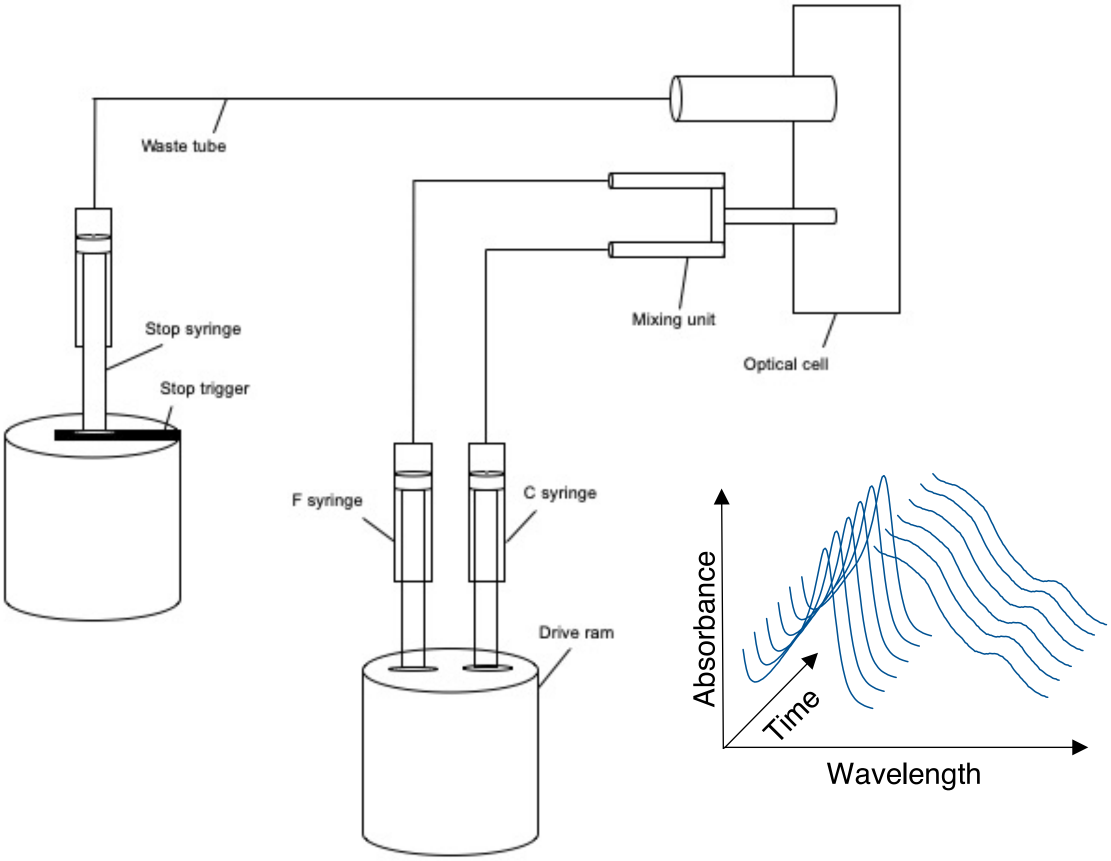
Waste tube
Mixing unit
Optical cell
Stop syringe
Stop trigger
F syringe
C syringe
Drive ram
Absorbance
Time
Wavelength

Figure 1.12. Diagram of stopped-flow spectrometer. Rapid mixing of enzyme and substrate occurs within milliseconds before entering the optical cell for rapid kinetic evaluation.

irradiate the sample within a magnetic field. The instrument is set to a given microwave frequency to irradiate the sample while the magnetic field is swept (Fig. 1.13). Absorption of the microwaves causes the electron to transition to an excited state with an energy resonant with that of the set frequency. The magnetic field (B_o) around the sample induces the splitting of the electron's energy level to two separate levels based on the spin of the electron and its alignment with B_o (Fig. 1.14). The energy of absorption can be defined by:

$$\Delta E = h\nu = g_e \beta B_o \qquad \text{[Eq. 1.13]}$$

Eq. 1.13, where g_e is system-specific EPR parameter called the g-value and β is the Bohr magneton. The final EPR spectrum is presented as the 1st derivative of the absorption (Fig. 1.14). The energy absorption of a given complex is determined by a sweep of the magnetic field, and the corresponding absorption peak can be used to determine *g* [Eq. 1.14].

$$g = \frac{h\nu}{\beta B_o} = \frac{\left(6.626\times10^{-34} Js\right)\times \nu(GHz)}{(9.274\times10^{-28} JG^{-1})\times B_o(Gauss)} \qquad \text{[Eq. 1.14]}$$

Interaction with a nucleus of $I = ½$ spin results in further splitting of the energy levels with $2I+1$ allowed transitions, resulting in an EPR spectrum with two peaks instead of one (Fig. 1.15). Of course, the number of peaks increases as the spin of the nucleus increases (e.g., nucleus with $I = 5/2$ will result in 6 allowed transitions).

EPR spectroscopy can provide insight of the electron configuration of metal cofactors in addition to any radicals isolated on residues within the protein matrix. The ligands of the metal influence the environment of the unpaired electrons(s) within the *d*-

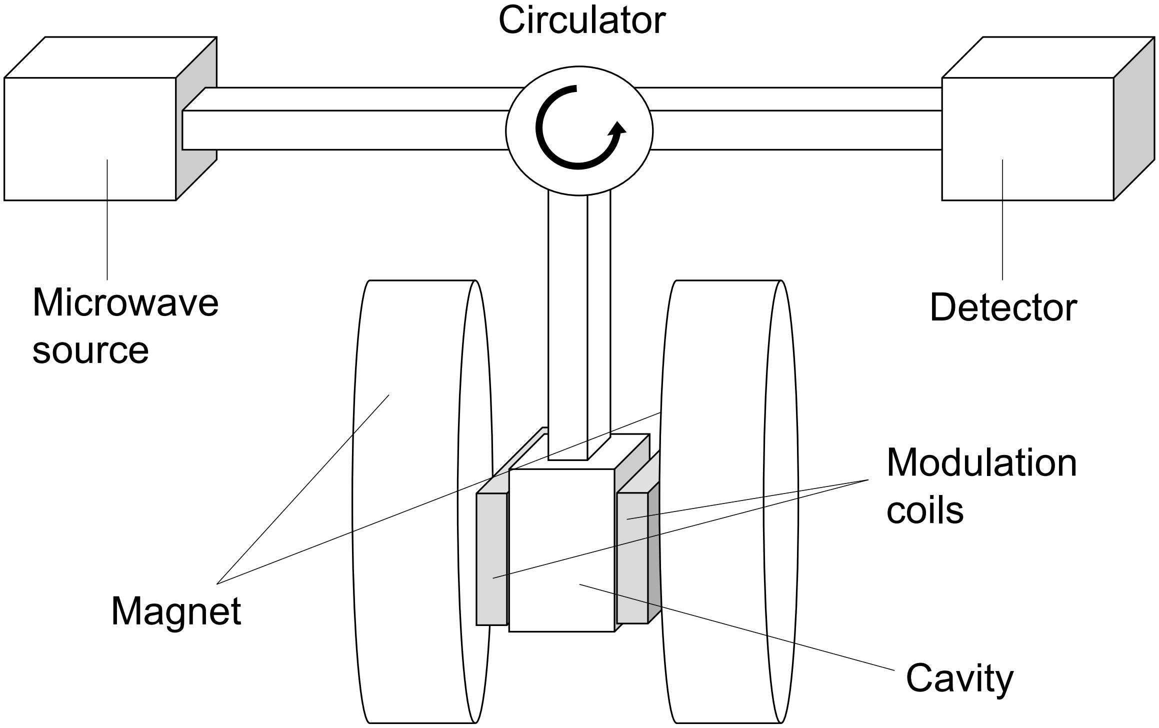
Circulator
Microwave source
Detector
Modulation coils
Magnet
Cavity

Figure 1.13. Diagram of electron paramagnetic resonance spectrometer.

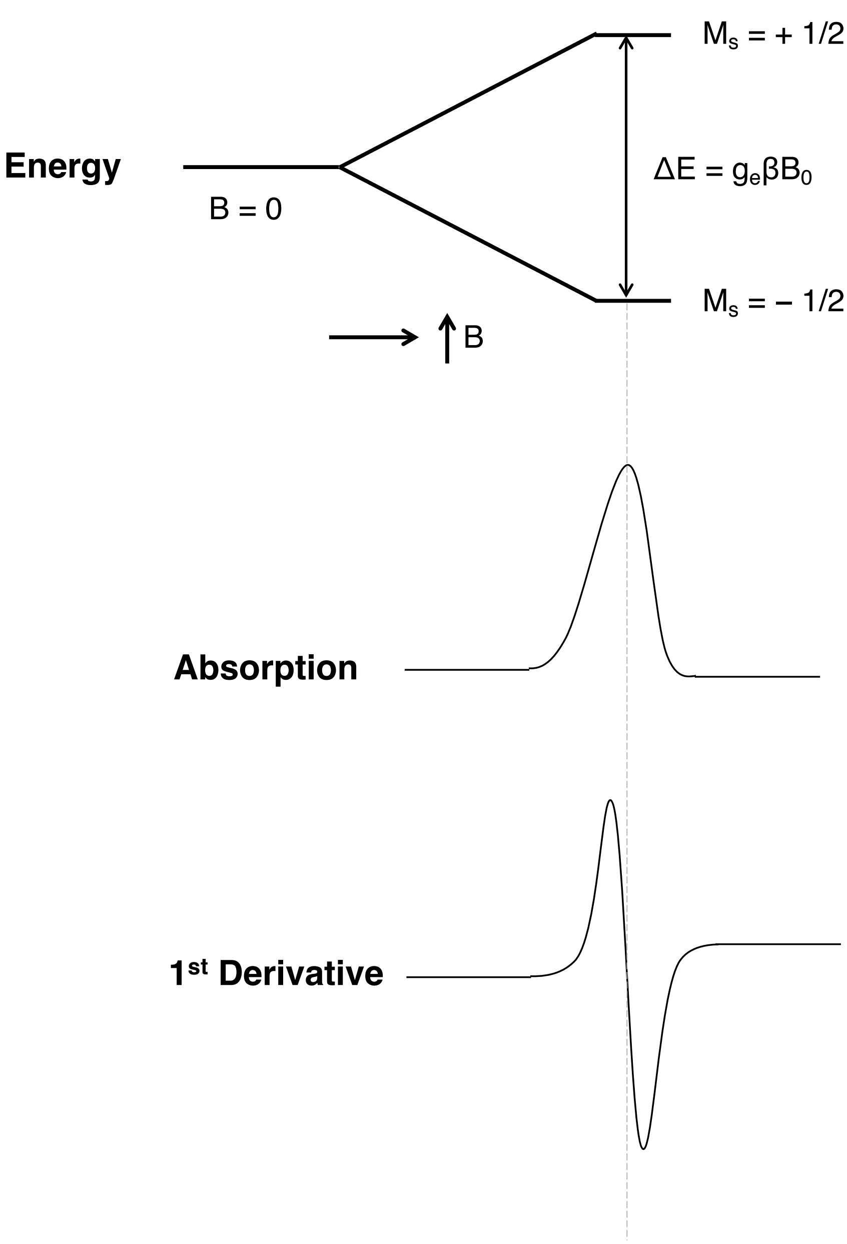
Energy
B = 0
$M_s = + 1/2$
$\Delta E = g_e \beta B_0$
$M_s = - 1/2$
B
Absorption
1st Derivative

Figure 1.14. Schematic representation of Zeeman effect in EPR spectroscopy.

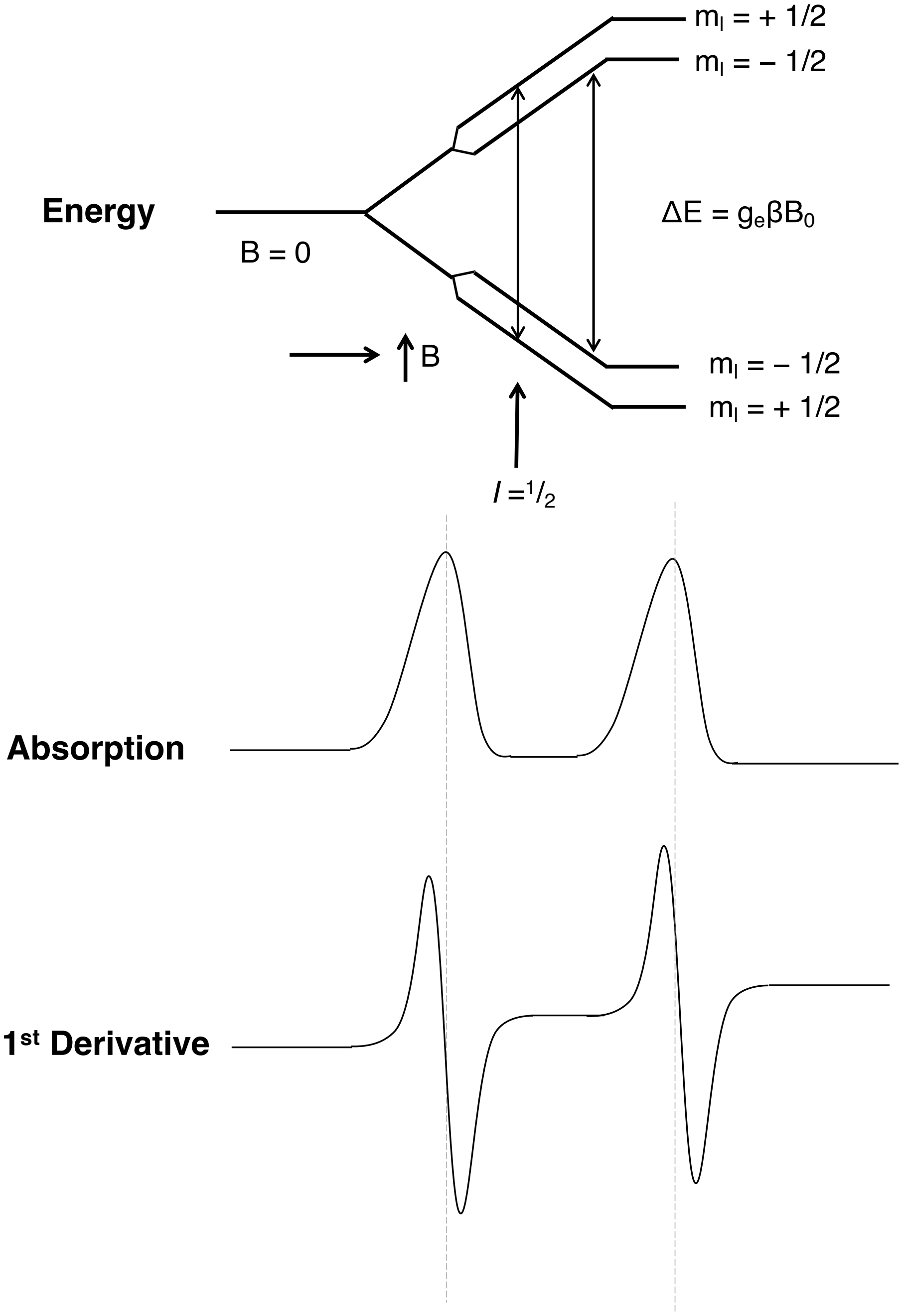
m$_I$ = + 1/2
m$_I$ = − 1/2
Energy
B = 0
ΔE = $g_e\beta B_0$
B
m$_I$ = − 1/2
m$_I$ = + 1/2
$I = {}^1/_2$
Absorption
1st Derivative

Figure 1.15. Diagram of hyperfine splitting of EPR signal from nucleus with *I* = ½.

orbitals of the metal, resulting in distinct EPR spectra for various ligand configurations around the metal (Fig. 1.16). When the ligands around the metal center are highly similar or identical, the electronic field around the paramagnetic center is isotropic, indicating that the interactions with the orbital moment of the un-paired electron is equal in all directions, and there is only one value of the external field where resonance is achieved (i.e., $g_x = g_y = g_z$). When the two axial ligand interactions (along the *z* axis) differ from the four equatorial ligand interactions (those along the *x* and *y* axes) the metal center is described as axial. Here, there are two values at which resonance occurs one corresponding to the g_z and the other to g_x and g_y. Finally, when interactions with the *d*-electrons differ in every direction, the paramagnetic center is rhombic, and each principal axis has a distinct value of the external field where resonance is achieved. As can be anticipated, heme proteins often have axial or rhombic Fe^{III} EPR spectra. The four, pyrrole nitrogen atoms of the porphyrin ring make up the equatorial ligand environment provide unique interactions from that of the protein-derived, axial ligand, and any other ligand to the heme, such as water, will result in a different interaction with the *d*-electrons of the Fe. For KatG in particular, the mature, ferric, resting enzyme exhibits a mixture of axial and rhombic features. This is due to the natural mixture of 5-coordinate and 6-coordinate heme within a given population of KatG. The 5-coordinate heme gives a rhombic EPR spectrum whereas the heme that coordinates water (i.e., 6-coordinate) provides an axial EPR spectrum. The resulting EPR spectrum is therefore the sum of the overlaid axial and rhombic features, which is most clear by the manifestation of two g_z values. The value of the g-tensor can indicate the spin-state of the metal system. For example, low-spin Fe systems with $S = 1/2$ have the largest g-values near 4, whereas high-spin Fe systems of $S = 3/2$ and $S = 5/2$ exhibit their largest

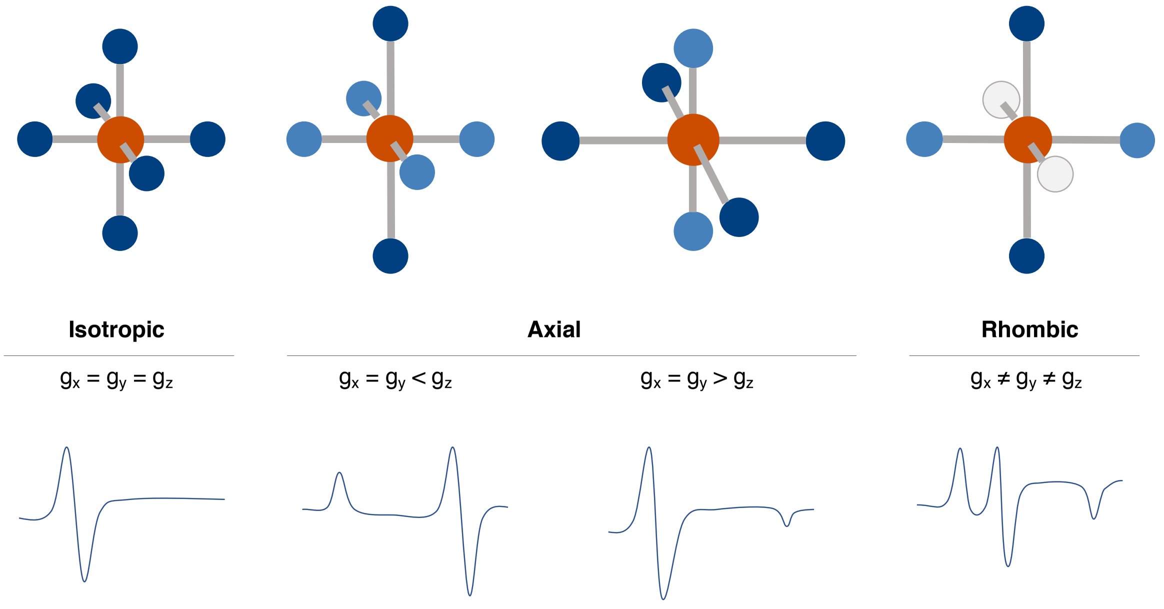
Isotropic
Axial
Rhombic
$g_x = g_y = g_z$
$g_x = g_y < g_z$
$g_x = g_y > g_z$
$g_x \neq g_y \neq g_z$

Figure 1. 16. Effect of ligand field on g-tensors and resulting EPR spectra.

g-values around 6 and 10, respectively. As such, the KatG Fe^{III} enzyme is understood to have a mixture of axial and rhombic high-spin heme with g-values around 6.63, 5.90, 4.98, 1.99, and 1.95.

The catalase and peroxidase reaction intermediates of KatG are often EPR-silent. In particular, the $Fe^{IV}=O$ state and therefore the resting, Fe^{III} state of KatG is the only metal derived EPR spectrum that can be detected. This can be useful to observe the coordination and oxidation state of the Fe^{III} heme. Perhaps more powerful, however, is the utilization of EPR spectroscopy to observe protein-based radicals that are formed within KatG during catalysis. In the same way as described above, the excited un-paired electron, in this case isolated on the side chain of a residue within the active site, with its particular environment has a unique value of the external field which matches the energy of the splitting due to the influence from the magnetic field (its g-value). Interactions with nuclear spin from nearby atoms result in splitting of the electron's energy levels resulting, as described above, concomitant splitting of the EPR spectrum (Fig. 1.15). Additionally, broadening of EPR signal from an organic, protein-based radical can provide information on interactions with metal centers, such as exchange coupling. There are two distinct protein-based radicals that are commonly observed during KatG catalytic turnover: the narrow doublet signal and the exchange-coupled radical signal. These signals and their identities will be discussed at length in Chapter 3.

The nature of EPR causes it to be a less sensitive method than optical spectroscopy, requiring about higher micromolar (150 μM) concentrations for the samples of 300 μL volume. A sample preparation technique called rapid freeze-quench (RFQ) is often implemented in order to observe transient radical intermediates. In this procedure, equal amounts of enzyme and substrate are pushed through a stopped-flow-type instrument, allowed to react together in tubes calibrated to specified reaction times, and then ejected out of the tube into cryogenic fluid where the reacted mixture freezes upon impact. The solid, frozen reaction mixture is then packed into a small, quartz EPR tube that is submerged in a liquid nitrogen-isopentane mixture (Fig. 1.17). Though the typical cryogenic medium for RFQ is isopentane, KatG samples are typically frozen in liquid ethane as it results in frozen KatG reaction mixtures that pack more readily.

Mössbauer spectroscopy

The most direct method for elucidation of iron oxidation and spin states, including those of heme centers, is Mössbauer spectroscopy. Unlike EPR spectroscopy, Mössbauer spectroscopy is able to detect and distinguish all oxidation states of Fe. The spectroscopy is founded on the principles of recoilless absorption of γ rays by isotopically enriched ^{57}Fe atom and the Doppler effect. A beam of 14.4 eV γ rays emitted from a radioactive ^{57}Co source pass through the solid (either crystalline or frozen) ^{57}Fe-enriched sample and the transmittance of the γ rays is acquired by a detector (Fig. 1.18). The Doppler effect is employed when the source emission is modulated by shifting the position of the source relative the sample in order to achieve resonance absorption frequency of the sample (76). And the conversion factor from velocity to energy is given by Eq. 1.15.

$$1\, mm/s \leftrightarrow 11.6\, MHz \leftrightarrow 3.87 \times 10^{-4}\, cm^{2} \leftrightarrow 4.81 \times 10^{-8}\, eV \quad \text{[Eq. 1.15]}$$

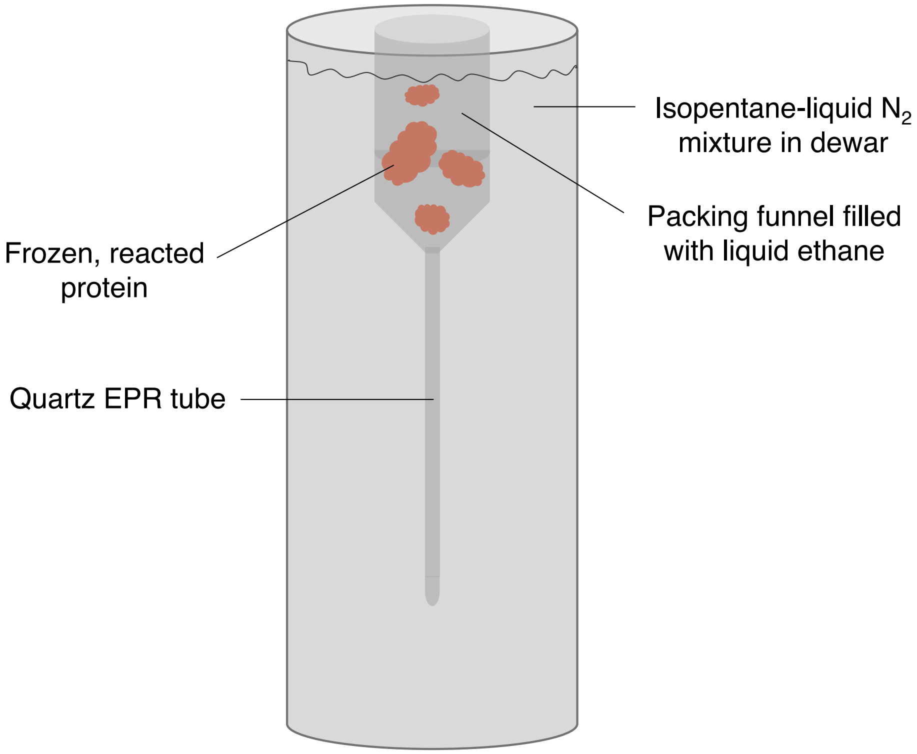
Isopentane-liquid N_2 mixture in dewar
Packing funnel filled with liquid ethane
Frozen, reacted protein
Quartz EPR tube

Figure 1.17. Schematic representation of rapid freeze-quench EPR sample preparation. The above scheme depicts how reacted KatG is frozen upon impact with liquid ethane and packed into a quartz EPR tube for later analysis by EPR spectroscopy.

The absorption of the γ ray by the ^{57}Fe atom results in nuclear eigenstate transitions, specifically to the 14.4-keV excited state (77). Mössbauer spectroscopy provides information on the ^{57}Fe nucleus monopole, dipole, and quadrupole moments, though the most informative are the monopole and quadrupole moments. From this information, two key Mössbauer parameters are determined: the isomer shift and the quadrupole splitting constant. The isomer shift (δ_{Fe}) is derived from the monopole moment of the ^{57}Fe nucleus within the sample and informs of its *s*-electron density (Fig. 1.19). The shift in the Mössbauer spectrum of a Fe complex (relative to ^{57}Fe metallic powder) indicates the change in Coulombic interactions between the nucleus and the *s*-electrons due to shielding by *d*-electrons or a decrease in electron density. The isomer shift is calculated by:

$$\delta_{Fe} = \delta_0 + \left(-\frac{E_\gamma\langle v^2\rangle}{2c^2}\right) \qquad \text{[Eq. 1. 16]}$$

where δ_0 is the ^{57}Fe metallic standard, E_γ is the energy of the γ ray absorbed, $\langle v^2\rangle$ is the mean-square velocity of the Fe, and *c* is the speed of light (77). The quadrupole splitting constant (ΔE_Q) is informed from the quadrupole moment of the ^{57}Fe nucleus (Fig. 1.19). This provides insight to the electric field gradient (EFG) at the nucleus influenced by nearby charges. ΔE_Q can be described by Equations 1.17 and 1.18.

$$\Delta E_Q = \frac{1}{2}eQ|V_{zz}|\sqrt{1 + {\eta^2}/{3}} \qquad \text{[Eq. 1.17]}$$

$$\eta = \frac{V_{xx} - V_{yy}}{V_{zz}} \qquad \text{[Eq. 1.18]}$$

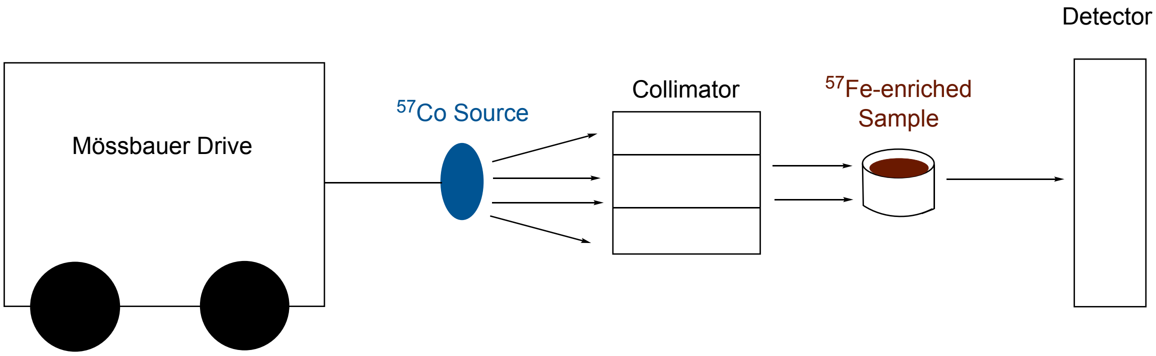
Detector
Mössbauer Drive
^{57}Co Source
Collimator
^{57}Fe-enriched Sample

Figure 1.18. Diagram of instrumental setup for Mössbauer spectroscopy. The sample isotopically enriched with ^{57}Fe is able to absorb energy emitted from radioactive ^{57}Co source. The source is moved back and forth towards and away from the sample, and the velocity at which the sample absorbs is monitored by the detector.

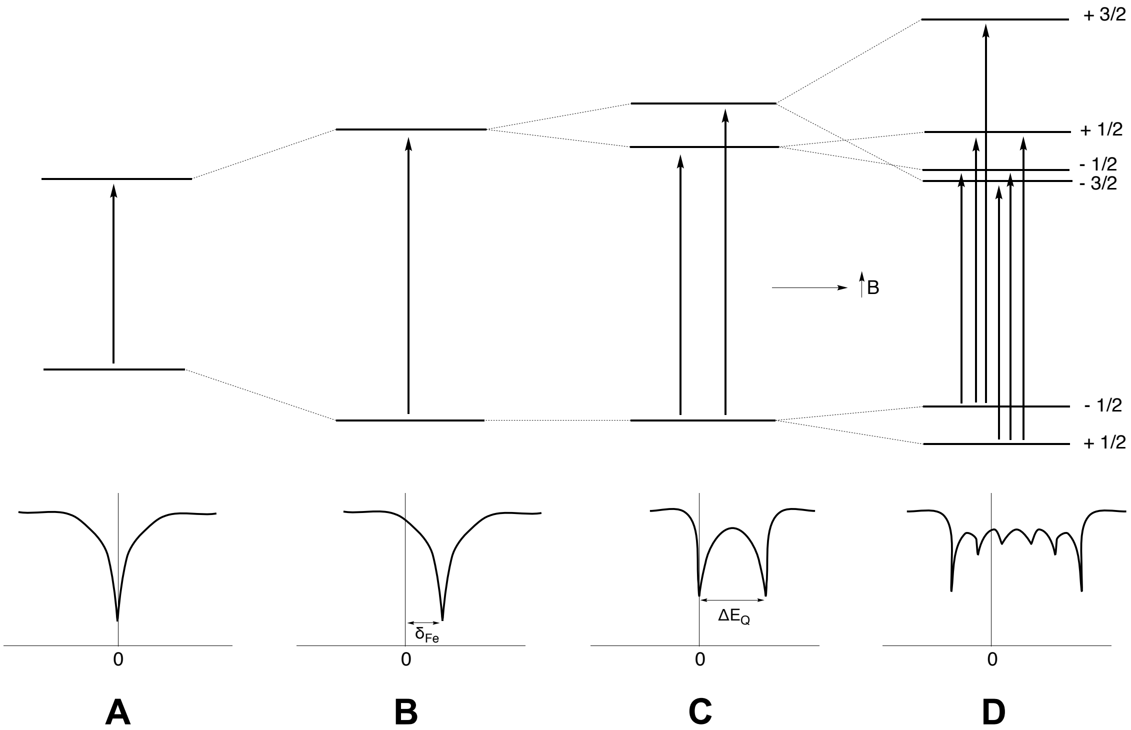
+ 3/2
+ 1/2
- 1/2
- 3/2
B
- 1/2
+ 1/2
δFe
ΔEQ
0
0
0
0
A
B
C
D

Figure 1.19. Schematic representation of Mössbauer spectrum. The electronic structure around the isotopically labeled Fe atom gives rise to the peaks in the Mössbauer spectrum.

For these equations, e is the charge of an electron, Q is the quadrupole moment of the ^{57}Fe, and η is called the asymmetry parameter and it describes the EFG where V_{zz} is the largest component of the EFG.

Mössbauer spectroscopy has a wide range of applications for any Fe-containing enzyme. As such, it has been heavily utilized in the early determination of reaction mechanisms of both heme peroxidases and heme catalases. Figure 1.20 provides a schematic depiction of the many Fe states that can be identified by Mössbauer spectroscopy. From these, those of particular interest for the research presented in this work are the ferrous $3d^6$ S = 0, ferryl $3d^4$, S = 1, and the ferric $3d^5$ states. The $Fe^{IV}=O$ intermediates of heme peroxidases typically have small δ_{Fe} values, ΔE_Q values ranging from 1 to 1.6 mms^{-1} with asymmetric peak splitting (76, 77). Ferrous S = 0 heme states complexed with O_2 (which is isoelectric to a ferric superoxo complex) typically stands out due to their very large and negative quadrupole splitting values (around -2.0 mm/s). Additionally, this quadrupole splitting is temperature dependent. A more thorough conversation about KatG reaction intermediates and their potential Mössbauer parameters can be found in Chapter 4.

Though informative, Mössbauer a very insensitive technique necessitating samples contain ^{57}Fe concentration of 1 mM for a sample 400 – 500 µL in volume and scan times on the magnitude of tens of hours. Given the natural abundance of ^{57}Fe is just over 2%, preparation of enzymatic samples, especially heme proteins, for Mössbauer necessitates the protein be enriched with ^{57}Fe. Similarly as described for EPR spectroscopy, samples can be prepared by RFQ to capture transient reaction intermediates for Mössbauer

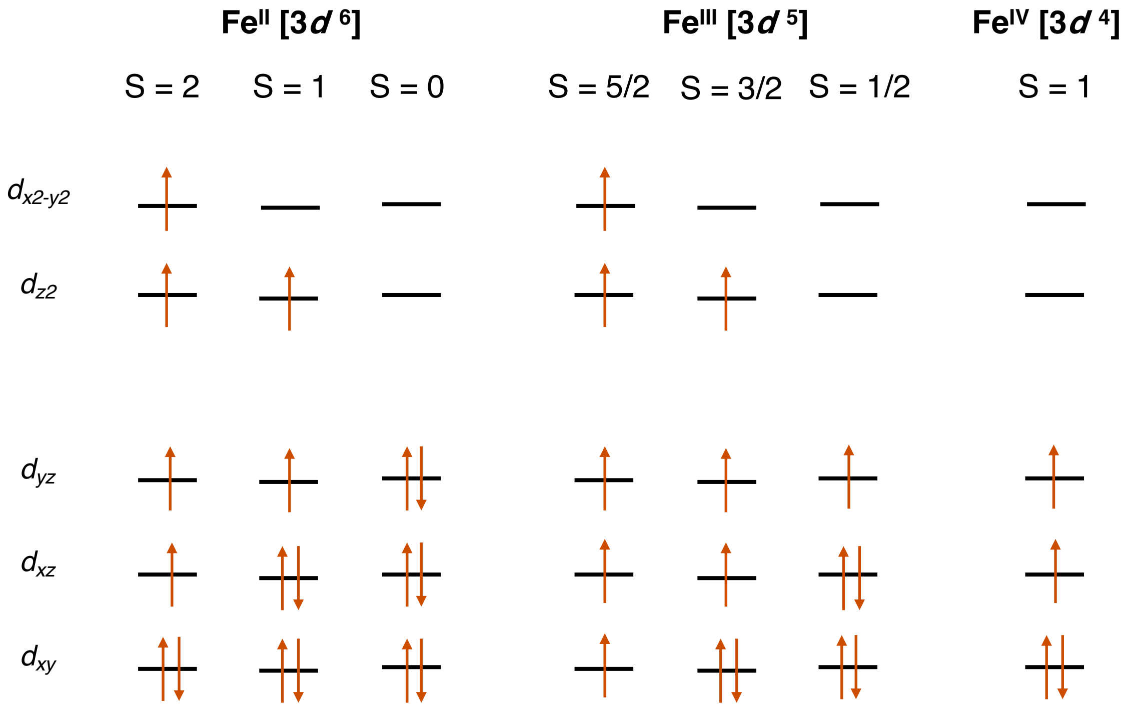
Fe^{II} [3d^6]
Fe^{III} [3d^5]
Fe^{IV} [3d^4]
S = 2
S = 1
S = 0
S = 5/2
S = 3/2
S = 1/2
S = 1
d_{x2-y2}
d_{z2}
d_{yz}
d_{xz}
d_{xy}

Figure 1.20. Electronic configuration of common heme-Fe oxidation and spin states.

spectroscopy. In this case, a custom funnel has been created for the facile addition of the Mössbauer sample cup to the bottom of the neck of the funnel.

Oxygen production by Clark electrode

Monitoring oxygen production is an invaluable way to distinguish catalase activity from peroxidase activity, given only the catalase reaction involves disproportionation of H_2O_2 generating O_2. The Clark electrode, fitted with a platinum (Pt) cathode and silver (Ag) anode and relies on potassium chloride (KCl) as an electrolyte (Fig. 1.21), is encapsulated in a reaction chamber unit allowing real-time O_2 production readings. Reduction of O_2 at the Pt cathode, and the potential builds to 0.7 V, the subsequent reduction of H_2O_2 initiates a current that is then proportional to the amount of O_2 produced by the enzyme in the reaction chamber above the membrane (Fig. 1.22). Accordingly, full *catalatic* degradation of H_2O_2 results a 1:2 molar ratio of O_2 produced to moles of H_2O_2 consumed to the reaction. The Clark electrode set-up (or oxygraph) enables *direct* observation of product formation by KatG even when varying reaction conditions such as pH or inclusion of exogenous peroxidatic electron donors.

Kinetics

Mechanistic investigation of nearly any enzyme system necessitates the use of steady-state kinetics. Generally, catalase enzyme activity, measured at pH 7, can be determined either by the degradation of H_2O_2, monitored at 240 nm on a spectrometer ($\varepsilon = 39.4\ \mu M^{-1}cm^{-1}$), or by O_2 production, monitored by a Clark-type electrode. Peroxidase activity, measured at pH 5, is often monitored by oxidation of PxEDs. Often PxEDs like

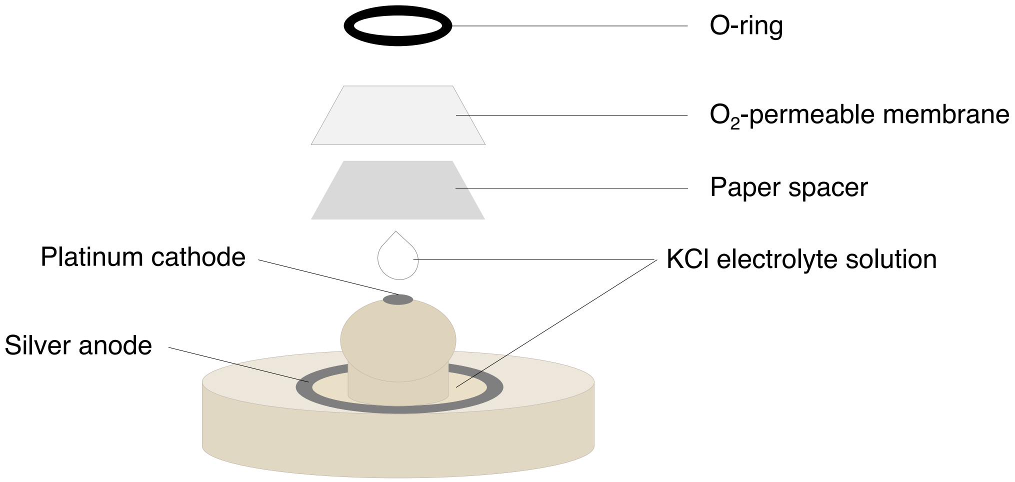
O-ring
O_2-permeable membrane
Paper spacer
Platinum cathode
KCl electrolyte solution
Silver anode

Figure 1.21. Diagram of Clark electrode. The oxygen-sensitive electrode is encased by a reaction chamber allowing enzymatic reactions to take place above the O_2 permeable membrane. The electrical current is stoichiometric to the O_2 consumed or produced at the cathode.

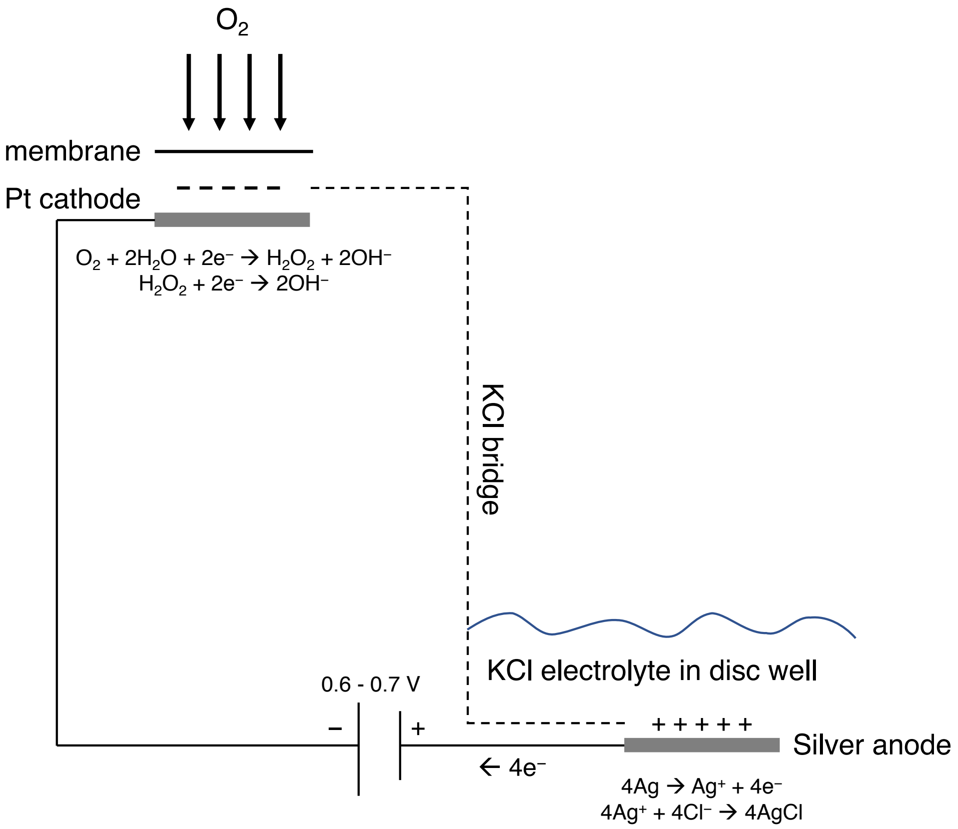
O_2
membrane
Pt cathode
$O_2 + 2H_2O + 2e^- \rightarrow H_2O_2 + 2OH^-$
$H_2O_2 + 2e^- \rightarrow 2OH^-$
KCl bridge
KCl electrolyte in disc well
0.6 - 0.7 V
–
+
+ + + + +
Silver anode
← $4e^-$
$4Ag \rightarrow Ag^+ + 4e^-$
$4Ag^+ + 4Cl^- \rightarrow 4AgCl$

Figure 1.22. Electrochemical diagram of Clark electrode. This system allows for detection of oxygen production by enzymatic systems in solution.

ABTS, 3,3’,5,5’-tetramethylbenzidine (TMB), o-dianisidine and N,N,N’,N’-tetramethyl-p-phenylenediamine (TMPD) (Fig. 1.4) are used instead of physiological donors due to the stability of the radical or otherwise oxidized species of these compounds, and therefore the ease of spectrophotometric detection of peroxidatic turnover.

Investigations of the catalase and peroxidase mechanisms of KatG were generally carried out in the same manner. The bifunctionality of KatG, however, must be kept in mind during experimental planning and data analyses. The initial rates of H_2O_2 degradation or formation of $ABTS^{\bullet+}$ ($\varepsilon_{417} = 34.7\ mM^{-1}cm^{-1}$) across a range of H_2O_2 concentrations were determined and fit to an appropriate kinetic equation. KatG catalase and peroxidase activities were evaluated to obtain a k_{cat}, which is defined as mole of product generated per mole of enzyme active site per unit of time under saturating substrate conditions, and k_{on} or k_{cat}/K_M, which is the catalytic efficiency of the enzyme. The K_M or Michaelis constant is the concentration of substrate required to reach half the maximum catalytic output of the enzyme, and it reflects the sensitivity of the enzyme to its substrate. It must be remembered that the K_M is a collection of rate constates that together give the appearance of a dissociation constant. However, this does not translate to a physical interpretation of properties like the turnover number or enzymatic efficiency. Additionally, determination of k_{on} by first determining K_M increases error of the k_{on} determination unnecessarily. Therefore, a rearranged Michaelis-Menten equation was used to solve directly for k_{on} [Eq. 1.19].

$$ {}^{v_o}/_{[E]_T} = \frac{k_{cat}[S]}{{}^{k_{cat}}/_{k_{on}} + [S]} \qquad \text{[Eq. 1.19]} $$

wt KatG exhibits a biphasic response to H_2O_2 when characterizing catalase activity at pH 5 and is therefore fit using Equation 1.20.

$$v_o/[E]_T = \frac{k_{cat}[S]}{\left(k_{cat}/k_{on}\right)+[S]} + k_i([S]+b) \qquad \text{[Eq. 1.20]}$$

Other methods utilized for mechanistic determination

Reaction conditions can provide an advantage when attempting to perform enzymatic characterization. Especially in the investigation of a bifunctional enzyme, such as KatG, reaction conditions such as buffer pH, presence of a PxED, identity of substrate, substrate concentration, and even site-directed mutagenesis are tools that can be used to gain a better understanding of KatG reactivity. For example, all previous research indicates that inclusion of PxED prevents the accumulation of inactive species. Therefore, we can assume and have confirmed the presence of a PxED will decrease or even eliminate accumulation of and contributions from catalase-inactive states, and correspondingly, spectral signals of catalase-*active* states will be enhanced. The stimulation of catalase activity by PxEDs is more prominent at pH 5.0, and therefore this pH will be used to more definitively determine catalase-active intermediates. Site-directed mutagenesis can also be used to discern the roles that various residues sustain within the enzyme as a whole. Substrate concentration can be adjusted to indicate what kind of species are present. When we react KatG with 667 equivalents of H_2O_2, we are able to visualize the point of substrate depletion. However, when larger concentrations of H_2O_2 are used in reaction with KatG (e.g., 100,000 equivalents), the enzyme experiences inactivation before reacting with all substrate present. Additionally, use of a non-catalytic, alkyl peroxide substrate such as peracetic acid (PAA) or *m*-chloroperoxybenzoic acid (*m*-CPBA) we can identify binding constants and even inactive intermediates of KatG. By manipulating these factors, the accumulation of key intermediates (i.e., catalase-active or catalase-inactive) is maximized for detection by stopped-flow, EPR, or Mössbauer spectroscopy.

Chapter Two

Understanding the Unique Peroxidase Activity of KatG

2.1. Introduction

Typical heme peroxidases enable the utilization of H_2O_2 for the oxidation of large, mainly phenolic, organic compounds (reference Fig. 1.6). In these enzymes, the resting, ferric heme center reduces H_2O_2 to water; this results in a 2-electron oxidation of the heme cofactor. The heme Fe is oxidized (i.e., to Fe^{IV} or ferryl) as is the porphyrin macrocycle, resulting in what is called a ferryl-oxo porphyrin-based cation radical heme intermediate (i.e., $Fe^{IV}=O[por]^{\bullet+}]$) (Fig. 2.1). This ferryl form of the cofactor is then reduced back to the ferric enzyme by two sequential, one-electron reductions at the expense of an exogenous peroxidatic electron donor (PxED) through a $Fe^{IV}=O$ heme intermediate (Fig. 2.1). As previously mentioned in Chapter 1, the majority of PxEDs are oxidized at or near the heme edge, necessitating a larger active-site access channel. The access channel of KatG is significantly more restricted, allowing only water, H_2O_2, and similarly sized molecules entry to the enzyme's active site. The oxidation of PxEDs by KatG, therefore, must take place at the protein's exterior surface because the PxEDs are too large to directly access the heme. Despite this, KatG is able to oxidize PxEDs, including 2,2'-azino-bis(3-ethylbenzthiazoline-6-sulfonic acid) (ABTS), 3,3',5,5'-tetramethylbenzidine (TMB), N,N,N',N'-tetramethyl-p-phenylenediamine (TMPD), and o-dianisidine. In fact, the

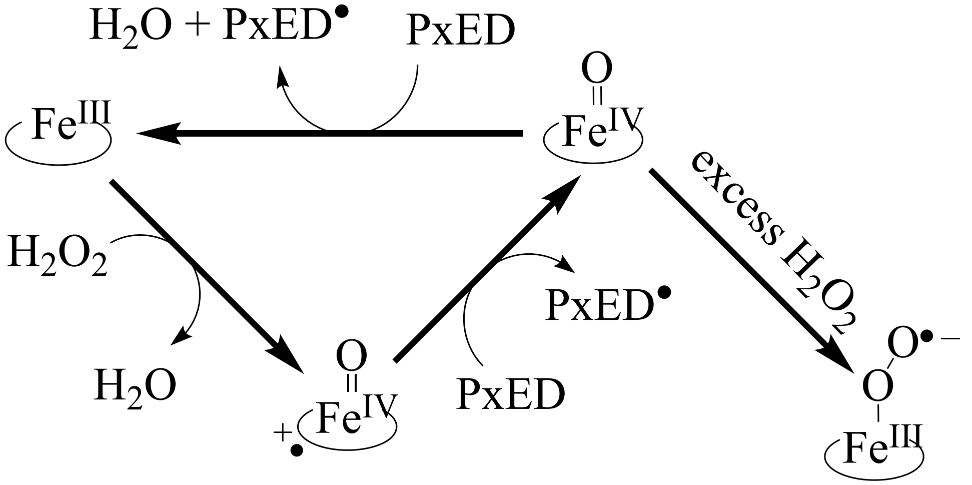
H2O + PxED•
PxED
FeIII
FeIV
excess H2O2
H2O2
H2O
FeIV
PxED•
PxED
O•−
FeIII

Figure 2.1. Typical heme peroxidase mechanism.

Goodwin lab has shown that inclusion of PxEDs in reactions of KatG with H_2O_2 unexpectedly stimulates *catalase* activity (78). For this to be the case, it is certain that KatG must utilized a peroxidase mechanism distinct from typical heme peroxidases.

Despite its different peroxidase mechanism, KatG has an active site nearly identical to typical heme peroxidases (Fig. 2.2). Distal and proximal residues responsible for heme ligation, reaction with H_2O_2, and stabilization of key heme intermediates are all strictly conserved. The only difference is that KatG has additional features: 1) a protein-derived cofactor generated by the post-translational modification of a Met, Tyr, and Trp (MYW cofactor) and 2) a conformationally dynamic Arg residue (i.e., the Arg switch) that helps to direct electron transfer within the active site (Fig. 2.2). Notably, there are also two aromatic residues widely conserved within heme peroxidase active sites, one distal to the heme and the other proximal. The identity of these aromatic residues is not strictly conserved across the peroxidase-catalase superfamily. In KatG and its closest relatives, cytochrome *c* peroxidase (C*c*P) and ascorbate peroxidase (APx), these aromatic residues are both Trp's. In the majority of the other peroxidase-catalase superfamily members, these two residues are Phe's. The proximal Trp (^{Px}W) of C*c*P is critical for catalysis. The electronic structure of the active site is such that the traditional Fe^{IV}=O[por]$^{\bullet+}$ intermediate is not stable, and very rapid intramolecular electron transfer results in formation of a Fe^{IV}=O[^{Px}W]$^{\bullet+}$ intermediate. Interestingly, the Fe^{IV}=O[^{Px}W]$^{\bullet+}$ form of APx is not observed because the coordination of a K^+ ion near the proximal Trp residue. In order to study the role of the proximal Trp of KatG (Trp321 by *Mycobacterium tuberculosis* numbering), a non-oxidizable, Phe was incorporated at position 321 using site-directed mutagenesis (i.e., W321F KatG was generated).

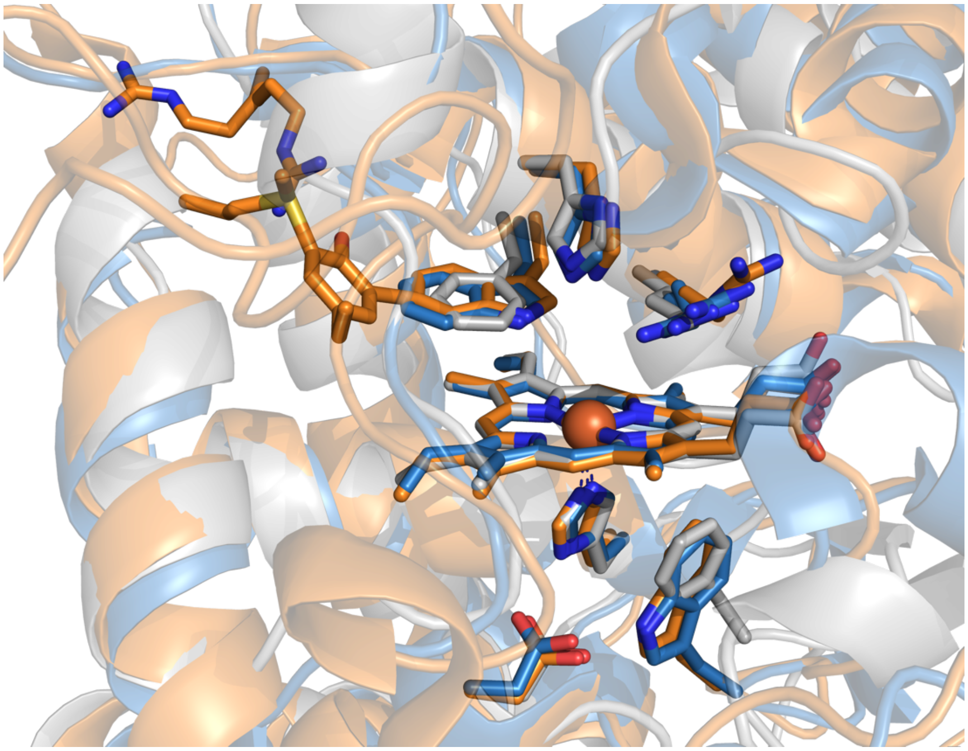

Figure 2.2. Heme peroxidase active site of KatG. The active site of KatG (orange) overlaid with C*c*P (blue) and HRP (light gray). The identities of the aromatic residues of the active site are not strictly conserved across the entire peroxidase-catalase superfamily. This figure was made using the PDB accession numbers: 2CCA (KatG), 4XVA (C*c*P), and 1ATJ (HRP).

In addition to the distal and proximal Trps in the active site of KatG, there are two other Trp residues within 10 Å of the heme cofactor (W412 and W91) (Fig. 2.3A). Each of these four Trp residues (W107, W321, W412, and W91) are within 10 Å of other oxidizable residues (i.e., Met, Tyr, or Trp residues). The abundance of Met, Tyr, and Trp residues within the KatG N-terminal is astounding and facilitates a scaffold for intraprotein electron transfer (or hole-hopping). About 11% of the N-terminal of KatG is comprised of Met, Tyr, or Trp residues – this is over 70% higher than the average protein. These residues have been suggested to support intraprotein hole hopping in other oxidoreductases (79–81). Using the Redox Chain Database generated by Drs. Gray and Winkler (82) potential hole-hopping pathways throughout KatG have been predicted (Fig. 2.3B). Given the oxidation of PxEDs by KatG must occur at the protein surface, due to the restriction of the active-site channel, such a hole-hopping pathway would offer a reasonable mechanism for the peroxidase activity of KatG. Additionally, such a mechanism could explain how synergy can exist between the catalase and peroxidase activities of KatG. Figure 2.4 provides a proposed scheme for the peroxidase activity of KatG by way of intraprotein hole transfer through Met, Tyr, and Trp residues. Within this proposed mechanism, only one predicted hole-hopping pathway is explored simply as an example, however, it should be noted that there are numerous other hole-hopping pathways that may be utilized and that hole transfer through these pathways may not be ordered or systematic. The work presented in this chapter is aimed to understand the participation of Trps near within KatG's active site (particularly W321), how the peroxidase activity of KatG prolongs its catalase turnover, and the role that exogenous electron donors play in enzyme preservation.

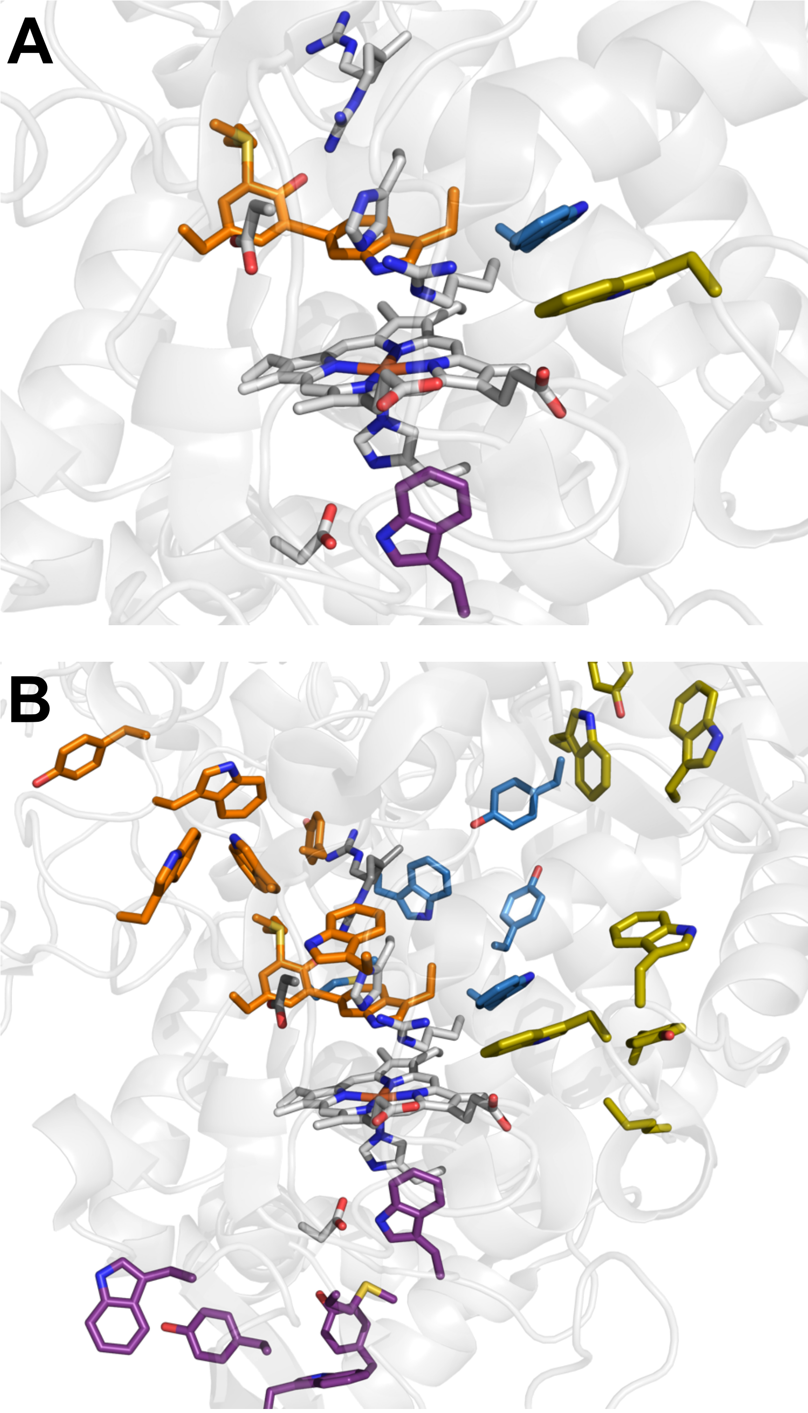

Figure 2.3. Hole-hopping pathways through KatG enable PxED oxidation. The four Trps within 10 Å of the heme center are positioned for facile heme reduction and possibly as origin sites for hole-hopping through KatG. (A) A number of other redox-active residues are positioned throughout the N-terminal of KatG within reasonable electron transfer distances, and therefore can act as hole-hopping pathways to the KatG surface.

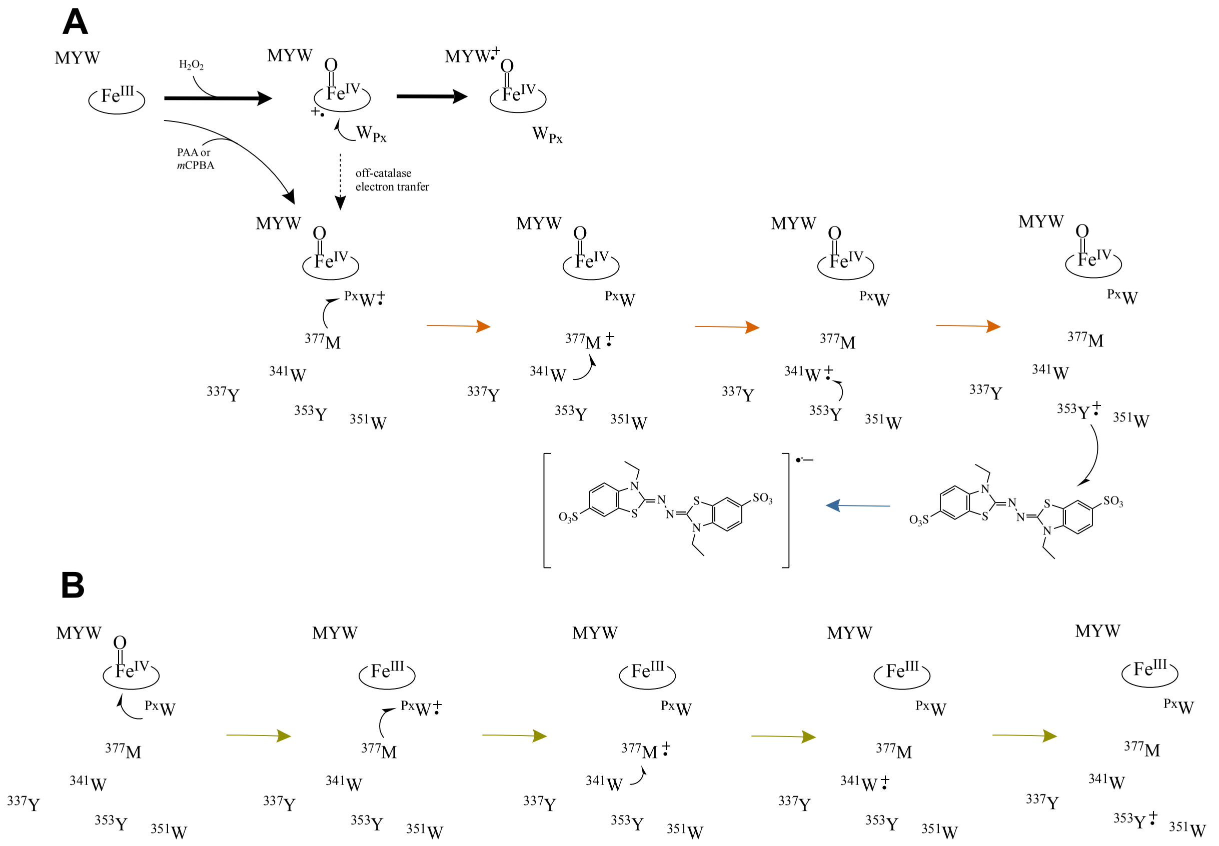
A
MYW
Fe^III
H2O2
PAA or mCPBA
MYW
Fe^IV
W_Px
off-catalase electron tranfer
MYW+
Fe^IV
W_Px
PxW
377M
341W
337Y
353Y
351W
O3S
SO3
B
MYW
Fe^IV
Fe^III
PxW
377M
341W
337Y
353Y
351W

Figure 2.4. Possible mechanism of KatG peroxidase activity. (A) When reacted with H_2O_2 (bolded arrows), peroxidatic turnover can be initiated by periodic off-catalase electron transfer (dotted arrow). Reaction with other peroxides such as PAA or *m*CPBA (regular arrows), peroxidatic turnover is the only possible route. Reduction of the ferryl heme by the proximal Trp can initiate hole-hopping through KatG (orange arrows). Nearby Met, Tyr, and Trp residues are near enough to initiate subsequent reduction, resolving the protein-based radical previously formed. Once the radical has migrated to the outside surface of the protein, the exogenous electron donor (such as ABTS) can resolve the surface radical, becoming a radical species itself (blue arrow). (B) This same hole-hopping pathway can again be exploited in order to reduce the ferryl heme back to its ferric state (yellow arrows).

2.2. Materials and Methods

Site-directed mutagenesis

Site-directed mutagenesis was carried out by applying the “Round-the-Horn” approach (83) to the construct we use for the expression of wild-type *Mt*KatG. This construct, pMRLB11, is a pET23b-derived plasmid bearing the *M. tuberculosis katG* gene and was obtained from the TB Vaccine Testing and Research Materials Contract at Colorado State University. The sense strand primers designed for W321F substitution (5’-GAG*G*TGGTA**TTT**ACGAACACCCCGACGAAATGGGAC-3’) included a site for codon replacement (bold) as well as mutations designed to introduce diagnostic restriction digest sites for screening (underlined). This approach allowed us to generate reverse primers without substitutions for W321F 5’-GATGCCGCTGGTGATCGCGTCCTTA-CCG-3’. Both primers were modified by 5’-phosphorylation to allow for blunt-end ligation of PCR products. PCR for generation of the variant was carried out using *Phu*sion High Fidelity polymerase (New England Biolabs, Beverly, MA) in GC Buffer-containing Master-Mix and 3% DMSO. The PCR products were treated with *Dpn*1 to eliminate the starting template and ligated using T4 DNA ligase. The ligation products were used to transform *E. coli* XL-1 Blue cells by a standard heat shock procedure. Transformants were selected using ampicillin-containing media, and candidate plasmids were screened by *Bsa*AI restriction digest. Successful candidates were sent for full DNA sequence analysis (Davis Sequencing, Davis, CA) to verify that the intended mutations were present and that no unintended mutations were created.

Protein expression

E. coli C41 (DE3) cells containing the pHPEX3 plasmid were transformed with the PCR products from W321F constructs. Transformants were then selected on the basis of ampicillin and tetracycline resistance. Expression cultures were grown in Luria Bertani, Miller broth supplemented with ampicillin and tetracycline at 37 ºC until an OD_{600} of 0.30-0.45 was reached, at which time the cultures were then induced using the addition of 1 mM IPTG. The cultures were grown for 4 hours before cells were harvested at 5,000 rpm for 20 mins at 4-8 ºC. Harvested cells were frozen at -20 ºC until prepared for purified. Overexpression of W321F KatG was verified by TCA precipitation and SDS-PAGE analysis.

Protein purification

The frozen, harvested cells were then resuspended in 5 mL/expression-volume 50 mM sodium phosphate, 200 mM NaCl, pH 7. 200 μL/expression-volume of 50 mM phenylmethylsulfonylfluoride (PMSF) was added to the resuspended cells. The cell mixture was then homogenized using a glass tissue grinder. The homogenized cell solution was then lysed by 8 sonication cycles (42 s on, 42 s off) using a Branson 250 Sonifier (Danbury, CT) equipped with a standard tip by sonication at 3.5 duty and constant output. 2 μL/expression volume of Benzonase Nuclease was added to the cell lysate and the mixture was allowed to stir at 4 ºC for 4 hours. The cell lysate was then centrifuged at 8,600 rpm for 1 hour (with slow deceleration) at 4 ºC to separate protein solution from cell matter. The protein supernatant was added then added to pre-washed Ni-NTA resin in multiple 50 mL conical tubes and allowed to bind on rotator at 4 ºC for 12 hours. The Ni-NTA column was then washed with: 50 mM tris buffer, pH 8; 50 mM sodium phosphate, 200 mM NaCl, pH 7; and 20, 50, 100, 200, and 500 mM imidazole in 50 mM sodium phosphate, 200 mM NaCl, pH 7. The KatG proteins were eluted in the 100 mM imidazole fraction. After confirmation by SDS-PAGE, the fraction(s) containing KatG were combined and concentrated using centrifugal filters with a 30 kDa cutoff limit. The concentrated protein was then added to Econo-Pac 10DG desalting columns (BioRad) for buffer exchange into 50 mM sodium phosphate, pH 7. After buffer exchange, a diagnostic spectrum was taken of the protein, and the protein was further concentrated in preparation for anion exchange chromatography. Macro-Prep High Q resin (BioRad) was used to purify the protein by anion exchange. KatG was purified from remaining contaminating proteins by elution using a linear gradient between 50 mM sodium phosphate, pH 7 and 50 mM sodium phosphate, 500 mM NaCl, pH 7. After analysis by SDS-PAGE and UV-visible spectroscopy, the most-pure and most heme-containing KatG fractions were combined and concentrated. Next, buffer exchange to 5 mM sodium phosphate, pH 7 was achieved by concentrating the protein by centrifugal filtration (30 kDa cut-off filters, Pall Laboratory), diluting with new buffer, and repeating ~3-5 times to ensure maximum buffer exchange. The appearance of the protein was assessed by taking a spectrum of the resulting, purified protein and the integrity of the protein was verified by a quick test of enzymatic activity. The purified protein was then properly aliquoted and frozen for future experimental investigation.

Stopped-flow spectroscopy

Spectral changes of the heme cofactor were monitored on a PC-upgraded SX18.MV rapid reaction analyzer from Applied Photophysics (Surrey, UK) equipped with a photodiode array detector. Reactions of KatG with antibiotics and sugars were carried out with 3 μM KatG, 5 equivalents PAA in 100 mM phosphate, pH 7 at 23 °C. Reactions of KatG with PAA or *m*CPBA alone were carried out with 3 μM KatG, 10 equivalents of substrate in 100 mM phosphate, pH 7 at 4 °C.

Rapid freeze-quench (RFQ) electron paramagnetic resonance (EPR) spectroscopy

Purified KatG protein was concentrated to 300 μM for RFQ-EPR sample preparation, for a final concentration of 150 μM in a final volume around 300 μL in an EPR tube (Wilmad Glass, Vineland, NJ). H_2O_2 (667 molar equivalents when present) or PAA (20 molar equivalents when present) were prepared fresh in ddH_2O, and when included, a concentration of 0.1 mM was used for ABTS and ascorbate. Samples were prepared using a KinTek RFQ-3 Quench-Flow Instrument (KinTek Corporation, Snow Shoe, PA). The enzyme-substrate mixture ejected from the KinTek Quench-Flow instrument was caught in a funnel with a quartz EPR tube attached, filled with liquid ethane, and surrounded with liquid nitrogen-isopentane mixture at ~120 K. Samples were then packed using metal packing rods in a KinTek temperature-controlled packing apparatus regulated by liquid nitrogen-isopentane mixture ~120 K. Residual ethane was quickly slung out from the EPR tubes, and samples were then stored at 77 K in liquid nitrogen until read on the EPR spectrometer.

EPR spectra were collected on a Bruker EMX X-band spectrometer operating in perpendicular mode. The parameters used, unless otherwise specified are as follows: 4.5 K temperature, 9.392 GHz frequency, 1.00 × 10^4 receiver gain, 100 kHz modulation frequency, 1.0 G modulation amplitude, 0.630 mW power, 327.680 ms conversion, 327.680 ms time constant, 335.544 s sweep time, and resolution of 1024 points. For comparison of spectra across various time points, 0.630 mW power was used even if the EPR signal was slightly saturated; temperature- and power-saturation studies were additionally performed to determine non-saturating conditions for various species.

Extent of O_2 production experiments

Catalase activity and catalase-dependent inactivation was evaluated by monitoring extent of O_2 production as detected by a Clark, O_2-sensitive electrode. To observe the full capacity of O_2 production for *wt* and W321F KatG proteins, 5 nM KatG was reacted with 500 μM H_2O_2 (100,000 molar equivalents) in either 100 mM phosphate, pH 7 or 50 mM acetate, pH 5 with 0.1 mM ABTS, when included. The cause of inactivation was further investigated by either adding an additional volume of either substrate or enzyme to the reaction upon the cessation of O_2 production. The time-dependent effects of PxEDs on O_2 production were evaluated in the same way, but by adding PxED at various time points after the reaction between KatG and H_2O_2 had already begun.

2.3. Identification of catalase inactive states of KatG

Kinetic studies of W321F KatG

During early investigations of W321F, this variant appeared to show higher catalase activity than the *wt* enzyme. Reaction of W321F with 2 mM H_2O_2 (667 molar equivalents) resulted in a more rapid depletion of H_2O_2 and subsequent return of the ferric enzyme (Fig.

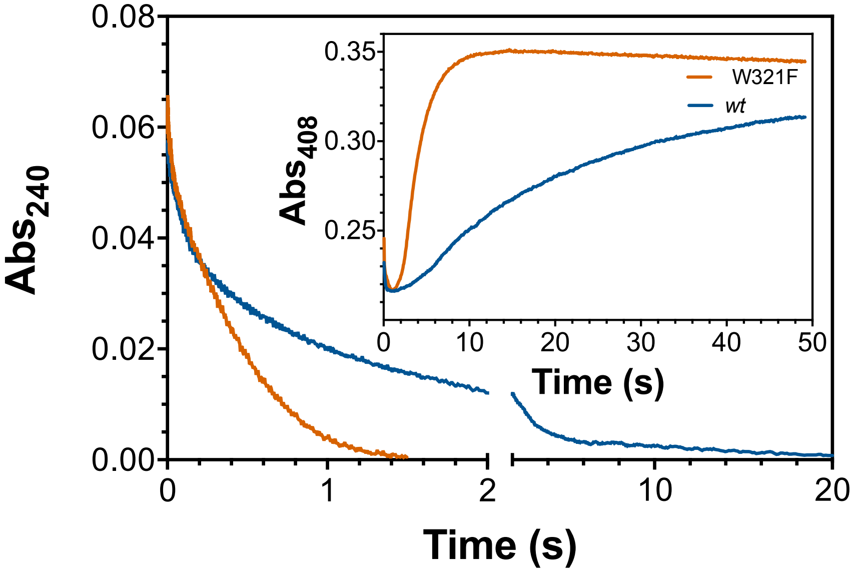

Figure 2.5. Comparison between *wt* and W321F reactivity. Depletion of H_2O_2 (240 nm) return of the resting enzyme (408 nm) and were monitored by stopped-flow spectroscopy with 667 molar equivalents of H_2O_2 in 50 mM acetate, pH 5 for both *wt* (blue) and W321F (orange) KatG proteins.

2.5). Congruent with this, we see a 12-fold decrease in time required to fully consume the H_2O_2 substrate was observed (Fig. 2.5). Not until the full course of catalase activity is monitored by O_2 production does the compromised *catalatic* output of the variant become apparent. Consistent with stopped-flow spectroscopic observations, the *initial rate* of O_2 production by W321F is greater than *wt* KatG (Fig. 2.6). The full extent of O_2 production of *wt* compared to W321F, however, demonstrates that the robust rate of catalase activity exhibited by W321F comes at a high expense because the W321F variant is capable of only 1/3 the catalase turnovers. For both *wt* and W321F KatG, O_2 production was not sustained until full substrate depletion. If 500 μM H_2O_2 is added to a reaction, it should result in the production of 250 μM O_2, according to catalase stoichiometry. The cause for cessation of O_2 production was investigated by monitoring O_2 production after the addition of another aliquot of enzyme or substrate. At pH 5 for both *wt* and W321F KatG, the initial cessation of catalase turnover is a result of enzyme inactivation because O_2 production is resumed only when fresh enzyme is added to the reaction; no activity is observed upon the addition of fresh substrate.

Inclusion of ABTS resulted in a 2.5-fold and 8.3-fold increase in extent of O_2 production for *wt* and W321F. Though both *wt* and W321F are able to consume all 500 μM H_2O_2 present, *wt* KatG has a higher rate upon a second addition of enzyme to the reaction, indicating the absence of the proximal Trp hinders the enzyme from efficient rescue by the PxED (Fig. 3.6B). In the presence of ABTS, *wt* KatG is not only able to sustain full conversion of 500 μM to 250 μM O_2, but also able to continue catalase turnover upon a fresh addition of substrate. Despite full conversion of H_2O_2 to O_2 by W321F, addition of a second H_2O_2 aliquot results in only slow catalase activity – indicating W321F, to a greater

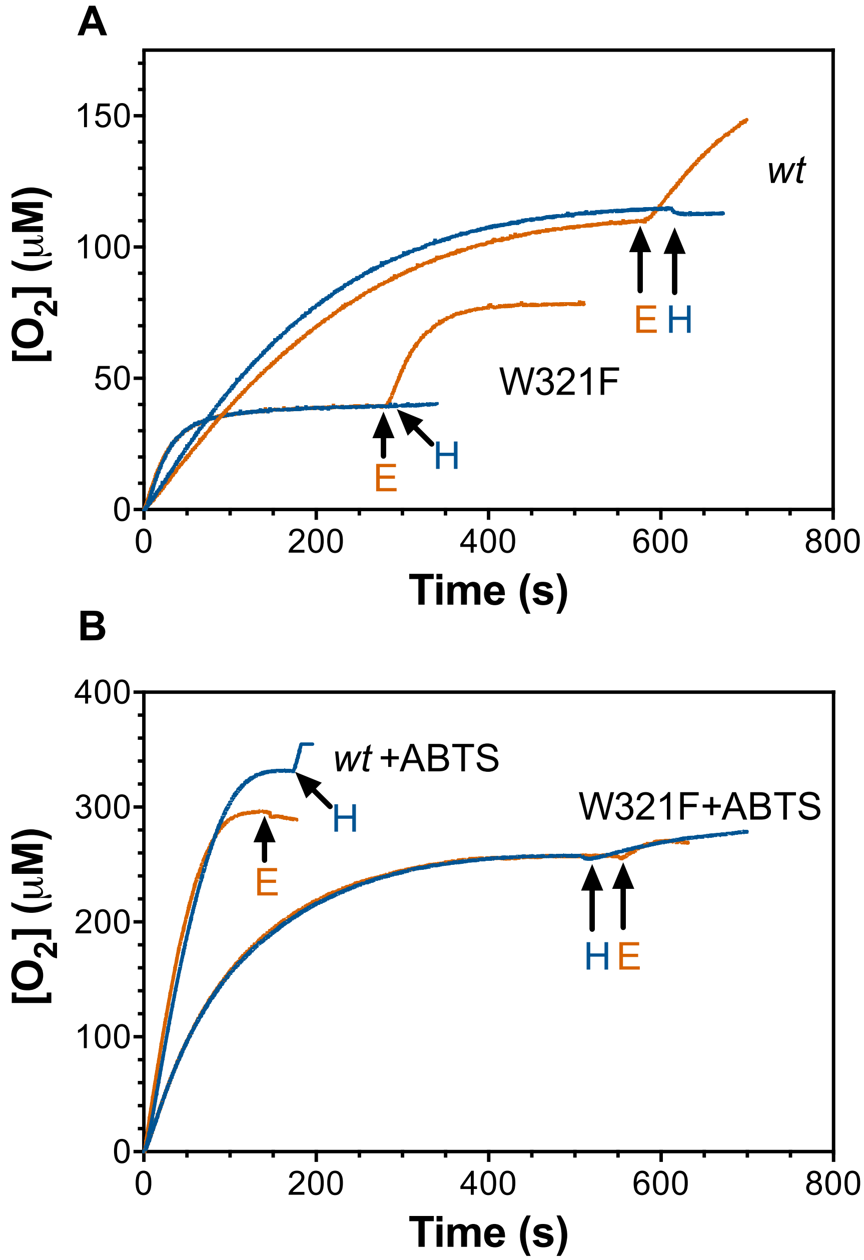

Figure 2.6. Effect of PxED on O_2 production by *wt* and W321F KatG. Production of O_2 by *wt* and W321F KatG was examined in the absence (A) and presence (B) of 0.1 mM ABTS. In each reaction, enzyme inactivation and substrate depletion were differentiated by the addition of fresh enzyme (E) or H_2O_2 (H), respectively.

degree than *wt*, has experienced some level of inactivation, even if not complete inactivation (Fig. 2.6). Together, these results suggest that PxEDs such as ABTS may play some role in prevention of inactivation of the enzyme. Furthermore, the presence of W321 appears important to this mechanism of preservation of KatG's catalase activity as evidenced by the response W321F O_2 production upon inclusion of 0.1 mM ABTS in the reaction. The loss of W321 as a viable oxidation site results in an enzyme only capable of 8,000 catalase turnovers compared to *wt* KatG which is able to sustain 20,000 turnovers before inactivation (Table 2.1). The decreased rate of O_2 production exhibited by W321F upon the addition of enzyme after initial cessation of O_2 production the presence of ABTS suggests that the absence of the proximal Trp results in a decrease in PxED-dependent preservation of catalase turnover.

Heme and protein-based radical intermediates associated with proximal Trp

The slow return of the Fe^{III} (i.e., resting) enzyme of *wt* KatG after reaction with H_2O_2 (Fig. 2.7) indicates possible accumulation of inactive species. The identity of these inactive states of the enzyme was interrogated using RFQ-EPR in parallel with optical stopped-flow kinetic methods. Reaction of *wt* KatG with 667 equivalents of H_2O_2 at pH 5 resulted in heme spectral features consistent with a Fe^{III}-$O_2^{\bullet-}$ intermediate. Specifically, there was a Soret peak at 416 nm and two other $\pi \rightarrow \pi^*$ transitions at 545 nm and 578 nm. (Q_{00} and Q_{01}. respectively) These Fe^{III}-$O_2^{\bullet-}$-like features then transition to those consistent with Fe^{IV}=O spectral features. Here, the Soret maximum was observed at 420 nm and Q_{00} and Q_{01} bands were observed at 530 nm and 560 nm (Fig. 3.7A). Once the H_2O_2 substrate was depleted, the Fe^{IV}=O-like spectral features slowly transitioned to those of the Fe^{III} (i.e.,

Table 2.1. Number of turnovers before inactivation by *wt* and W321F KatG.

KatG protein	[O_2] (μM) produced before inactivation	Number of turnovers performed	H_2O_2 (μM) consumed before inactivation
wt	100	20,000	200
W321F	40	8,000	80
wt + ABTS	250	50,000	500
W321F + ABTS	250	50,000	500

All traces were collected on a Clark electrode in 50 mM acetate buffer at pH 5.0 with 5 nM enzyme, 500 μM $H_2O_{2,}$, and when present, 0.1 mM ABTS.

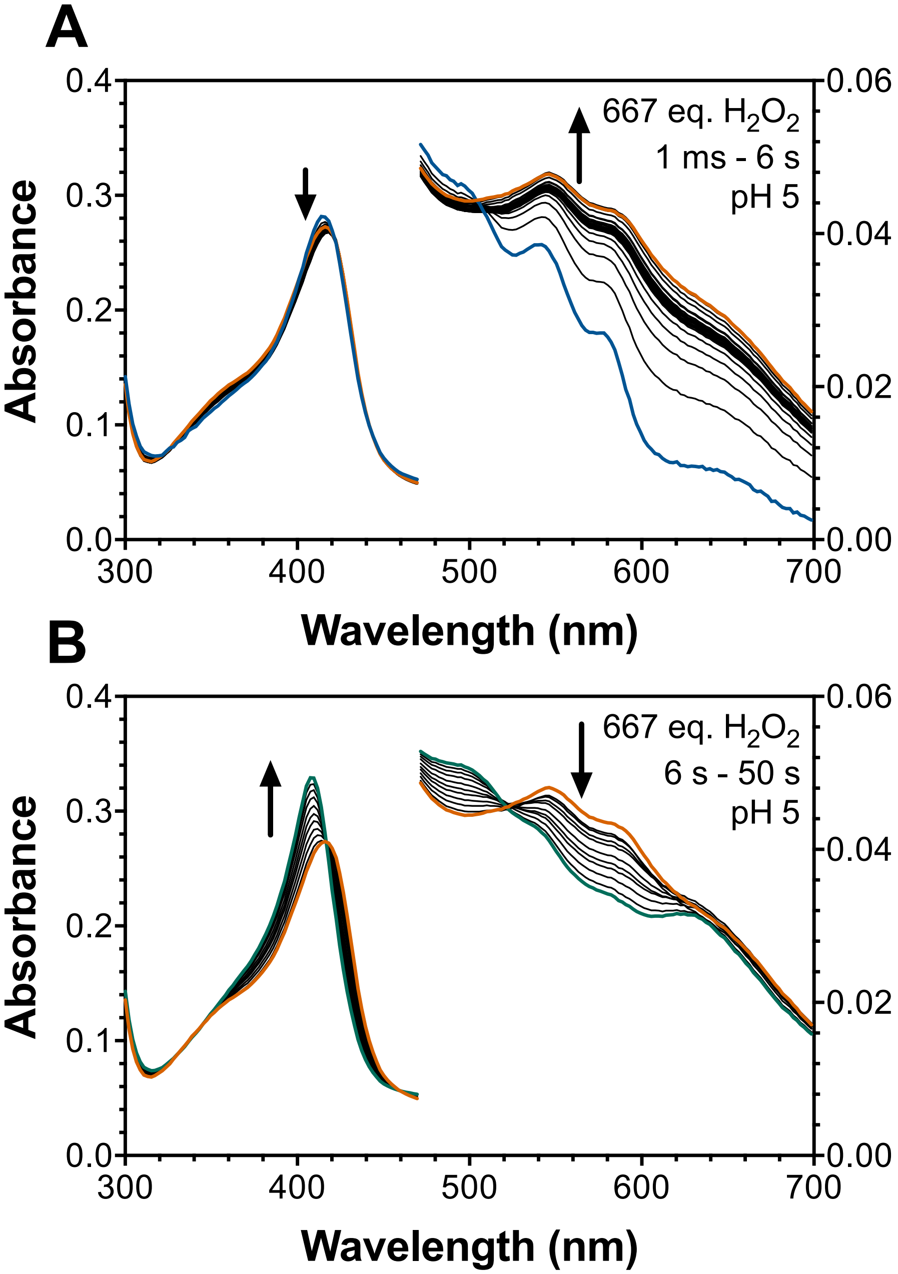

Figure 2.7. Heme intermediates observed during *wt* KatG reaction with H_2O_2. Spectral features consistent with a Fe^{III}-$O_2^{\bullet-}$ state (418, 545, and 578 nm) (blue) are prominent from the first measurement at 1.2 ms until the point of substrate depletion, 6 s (A). After H_2O_2 is depleted, the features consistent with a Fe^{IV}=O heme state (417, 546, and 588 nm) (orange) transition back to the resting enzyme (teal) over the next 50 seconds (B).

resting) enzyme (Fig. 2.7B). When 0.1 mM ABTS and ascorbate were present in the reaction, the only observed heme spectra are those consistent with the Fe^{III}-$O_2^{\bullet-}$-like features transitioning to the Fe^{III} enzyme within 500 ms (Fig 2.8). With the knowledge that PxEDs not only promotes catalase activity of KatG, but also prevents enzyme inactivation, the Fe^{III}-$O_2^{\bullet-}$-like heme spectra are assigned as catalase active. This is striking given the reputation of the Fe^{III}-$O_2^{\bullet-}$ state to be inactive for conventional heme peroxidases – this will be addressed in the next chapter in the discussion of KatG's catalase activity. The optical spectral features present after the point of substrate depletion are congruent with a Fe^{IV}=O heme state. In the presence of ABTS and ascorbate, catalase turnover is promoted and inactivation is avoided, and consistent with this contribution of Fe^{IV}=O states are absent, suggesting the ferryl-oxo intermediate is catalase-inactive heme state.

EPR spectra were collected of *wt* KatG reaction with 667 molar equivalents of H_2O_2 freeze-quenched at time points corresponding to heme spectra collected by stopped-flow spectroscopy. Concomitant with the transition from Fe^{III}-$O_2^{\bullet-}$-like to Fe^{IV}=O-like heme spectra, is a progression from a narrow doublet radical signal to an exchange-coupled radical signal (Fig. 2.9). Upon the inclusion of ABTS and ascorbate to the freeze-quench reaction, only the narrow doublet signal is prominent, suggesting this signal is solely associated with catalase activity (Fig. 2.10). Previously our lab has reported the presence of a narrow doublet signal of the $MYW^{\bullet+}$ radical at 10 ms and an exchange-coupled signal of the $^{Px}W^{\bullet+}$ at 6s (84). Additionally, we have shown that the exchange-coupling features are absent in the W321F singlet signal at the point of substrate depletion (84). Altogether, Here, we present greater time resolution of the protein-based radicals present during *wt* KatG catalase turnover with additional quench times at 4.6 ms, 40 ms, and 1 s in attempt

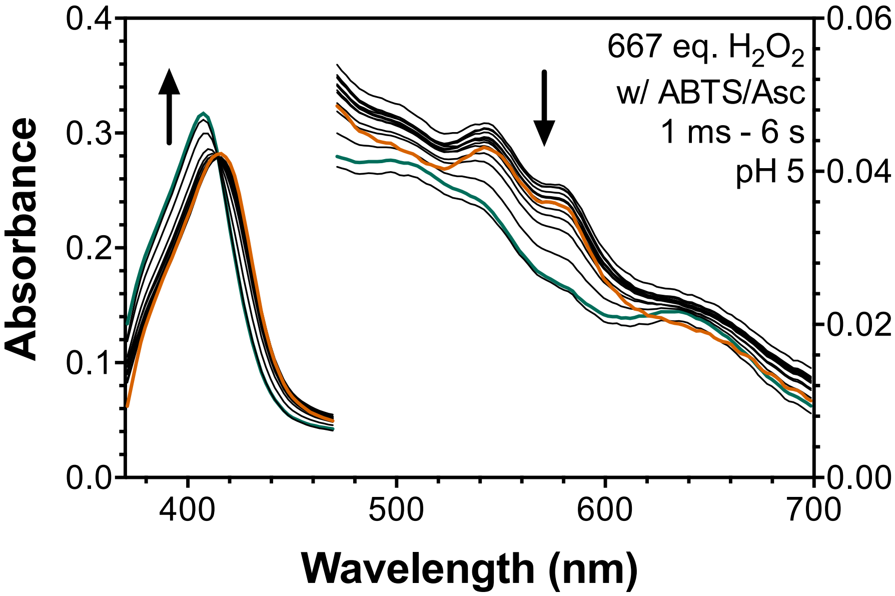

Figure 2.8. Heme intermediates observed during *wt* KatG catalase turnover in the presence of PxED. Upon the addition of 0.1 mM ABTS and 0.1 mM ascorbate (Asc) to the reaction, the only spectral features observed are those consistent with a Fe^{III}-$O_2^{\bullet -}$ heme state (408, 545, and 578 nm) (orange). Additionally, the resting enzyme (teal) returns by 6 s in the presence of PxED.

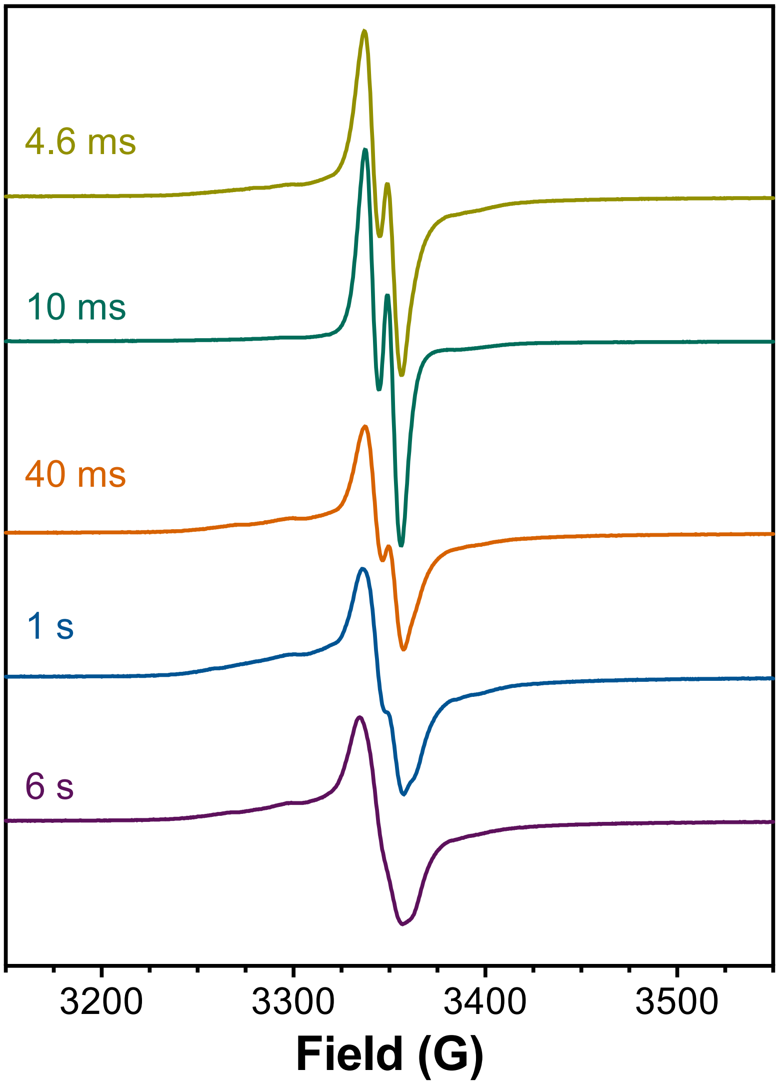

Figure 2.9. Protein-based radical intermediates identified for *wt* KatG. When reacted with 667 molar equivalents of H_2O_2, a narrow doublet is the observed as early as 4.6 ms into the reaction. Broadening features are observed in the EPR spectrum as early as 40 ms. At the point of substrate depletion (6 s), the exchange-coupled radical is the dominant radical species observed.

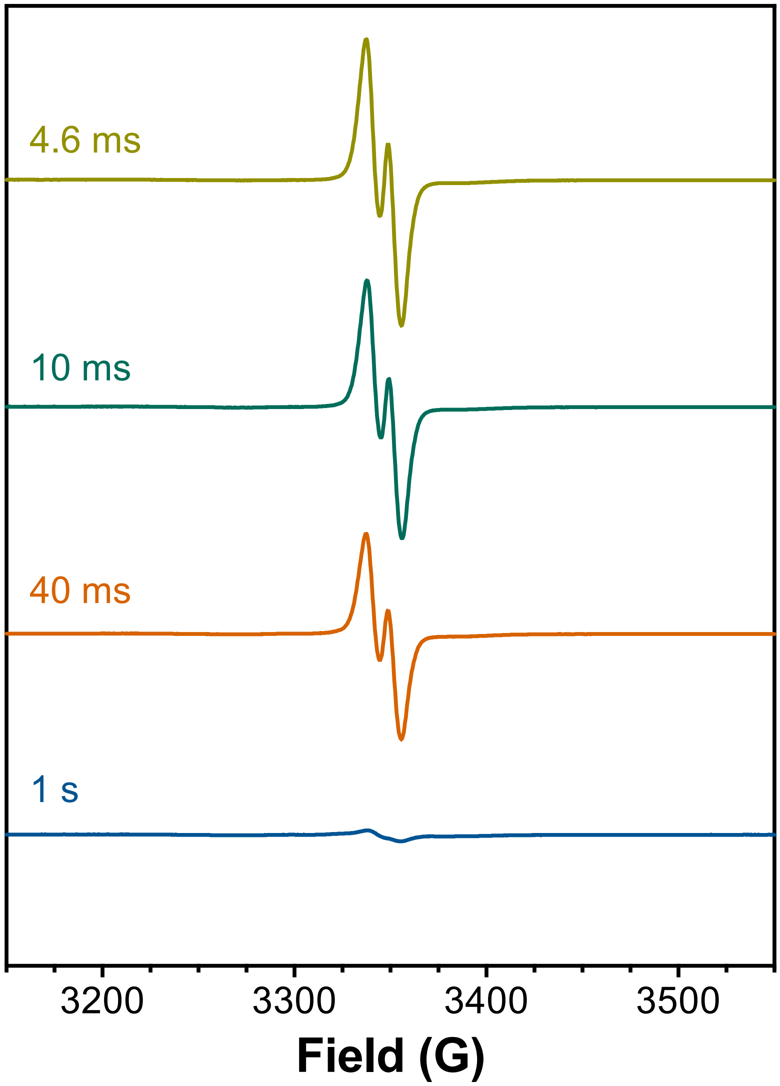

Figure 2.10. Protein-based radial intermediates of *wt* KatG in the presence of PxED. Reaction with 667 molar equivalents of H_2O_2 in the presence of ABTS and ascorbate yields spectra dominated by the narrow doublet species. It isn't until 1s, which after substrate depletion (500 ms), that there is a singlet species observed. This singlet, however, does not exhibit any exchange-coupled broadening.

to provide insight to the appearance of the $^{Px}W^{\bullet+}$ signal. The exchange-coupling features of the $^{Px}W^{\bullet+}$ are evident as early as 40 ms into the reaction. Presence of ABTS in the reaction results in the decrease of broadening due to exchange coupling in the 40 ms and 1 s EPR signals (Fig. 2.11). Appearance of broadened EPR features at such early reaction times, agrees with previously presented inactivation studies, suggest reaction with H_2O_2 facilitates rapid off-catalase turnover that will most-likely result in oxidation of the proximal Trp residue.

Power saturation characteristics of this 40 ms sample were examined by collecting spectra from 0.3159 μW to 50.060 mW (Fig. 2.12A). At least two radical signals were observed with distinct power saturation characteristics out by monitoring distinct features of the respective radical signals (i.e., monitoring 3300.146 G which corresponds to the exchange-coupling "shoulder" and 3349.85 G which corresponds to the middle peak of the narrow doublet signal) (Fig. 2.12B). The results of this power saturation plot are consistent with previous conclusions that there is a combination of radical species present at this time and the exchanged coupled radical species ($^{Px}W^{\bullet+}$) is highly resistant to power.

Reaction with PAA and mCPBA

Peracetic acid (PAA) and *m*-cholorperoxybenzoic acid (*m*CPBA) are strongly oxidizing peroxides that can bind to the active-site heme of KatG and promote peroxidatic *but not* catalatic turnover. PAA has been used within the KatG field as a substitute for H_2O_2 due to the difficulty of examining rapid enzyme kinetics with the enzyme's true substrate. KatG's response to PAA, however, is vastly different than to H_2O_2. In this work, PAA and *m*CPBA were used as a substrate to simulate inactive forms of KatG. Upon reaction with

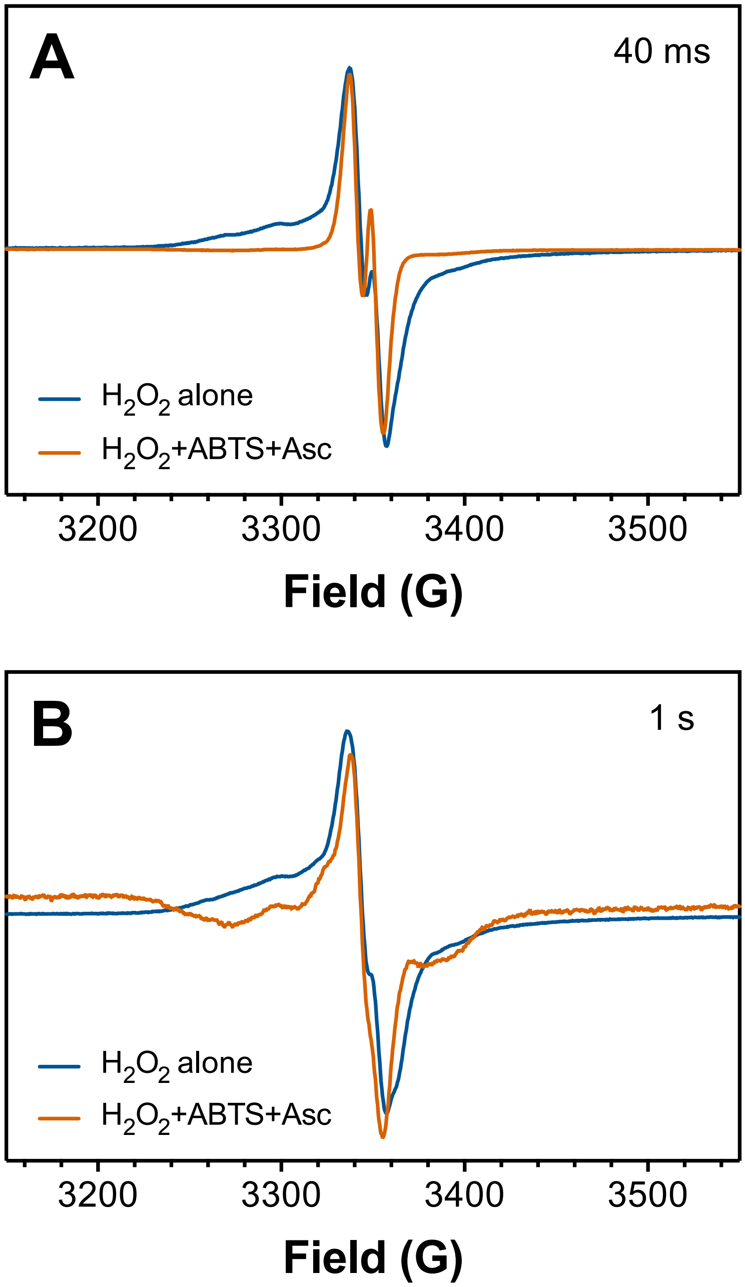

Figure 2.11. Absence of signal broadening upon inclusion of ABTS and ascorbate. Comparison of reactions with and without ABTS and ascorbate quenched at 40 ms (A) and 1 s (B) indicate that the presence of ABTS and ascorbate prevents accumulation of species that exhibit exchange-coupling (broad) features. All spectra were collected at 0.630 μW and 4.5 K.

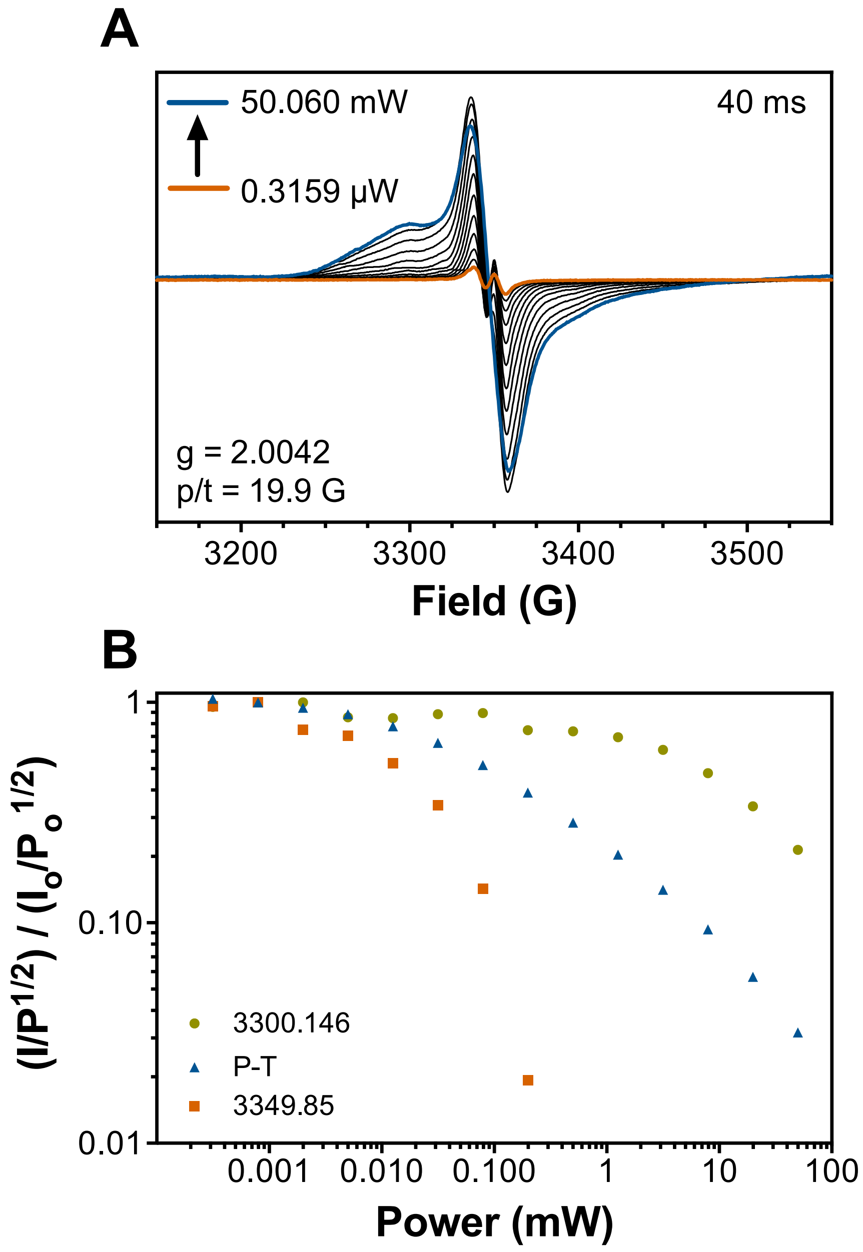

Figure 2.12. Power saturation of 40 ms RFQ-EPR sample of *wt* KatG with 667 eq. H_2O_2 at pH 5. The power-dependence of the 40 s RFQ-EPR sample of *wt* reacted with 667 eq. H_2O_2 at pH 5 was tested by collecting spectra from 0.3159 µW (orange) to 50.060 mW (blue) at 4.5 K (A). The two components of this EPR signal can be distinguished by following the saturation of particular spectral features that are distinct for the two prominent features: the narrow doublet (3349.85 G, orange) and the exchange-coupled radical (3300.146 G, yellow).

20 molar equivalents of PAA, KatG exhibits spectral features consistent with a $Fe^{IV}=O[por]^{\bullet+}$ heme state including the hypochromic shift of the Soret peak at 407 nm and the broad, non-descript features of the visible region (Fig. 2.13A). After the formation of this heme state, the enzyme begins its return to the resting enzyme. W321F KatG exhibits similar spectral features with changes particular in the visible region (Fig. 2.13B)

EPR spectra of *wt* mixed with 20 molar equivalents of PAA and then freeze-quenched after 10 ms or 8 s reaction times show nearly identical spectra dominated by exchange-broadened features (Fig. 2.14). This exchange-coupled radical signal is very similar to that observed upon reaction of *wt* with H_2O_2 and freeze-quenched at 6 s, or the point of substrate depletion (Fig. 2.14B). The absence of any narrow doublet signal here is noteworthy; reaction with PAA does not result in the active form of the enzyme either in terms of heme or protein-based radical states. Power saturation of the exchange-coupled radical signals of *wt* reacting with PAA was performed for a more rigorous comparison to previously identified exchange-coupled EPR signals. The power saturation characteristics of this PAA exchange-coupled radical strongly resemble the H_2O_2 exchange-coupled radical signal (Fig. 2.15B). In all, we were able to confirm the use of non-catalytic substrates, PAA, as a method to explore the catalase inactive states of KatG.

Reaction between W321F KatG and *m*CPBA result in similar $Fe^{IV}=O[por]^{\bullet+}$-like spectral features to those observed upon reaction with PAA (Fig. 2.16). Additionally, the heme spectra observed for *wt* and W321F KatG are more similar to each other than when reacted with PAA. This may indicate a more selective oxidation of the protein takes place during reaction with *m*CPBA. Unlike that for PAA, the RFQ-EPR spectra of *wt* KatG reacted with 20 eq. *m*CPBA quenched at 10 ms and 24 s are strikingly distinct from one

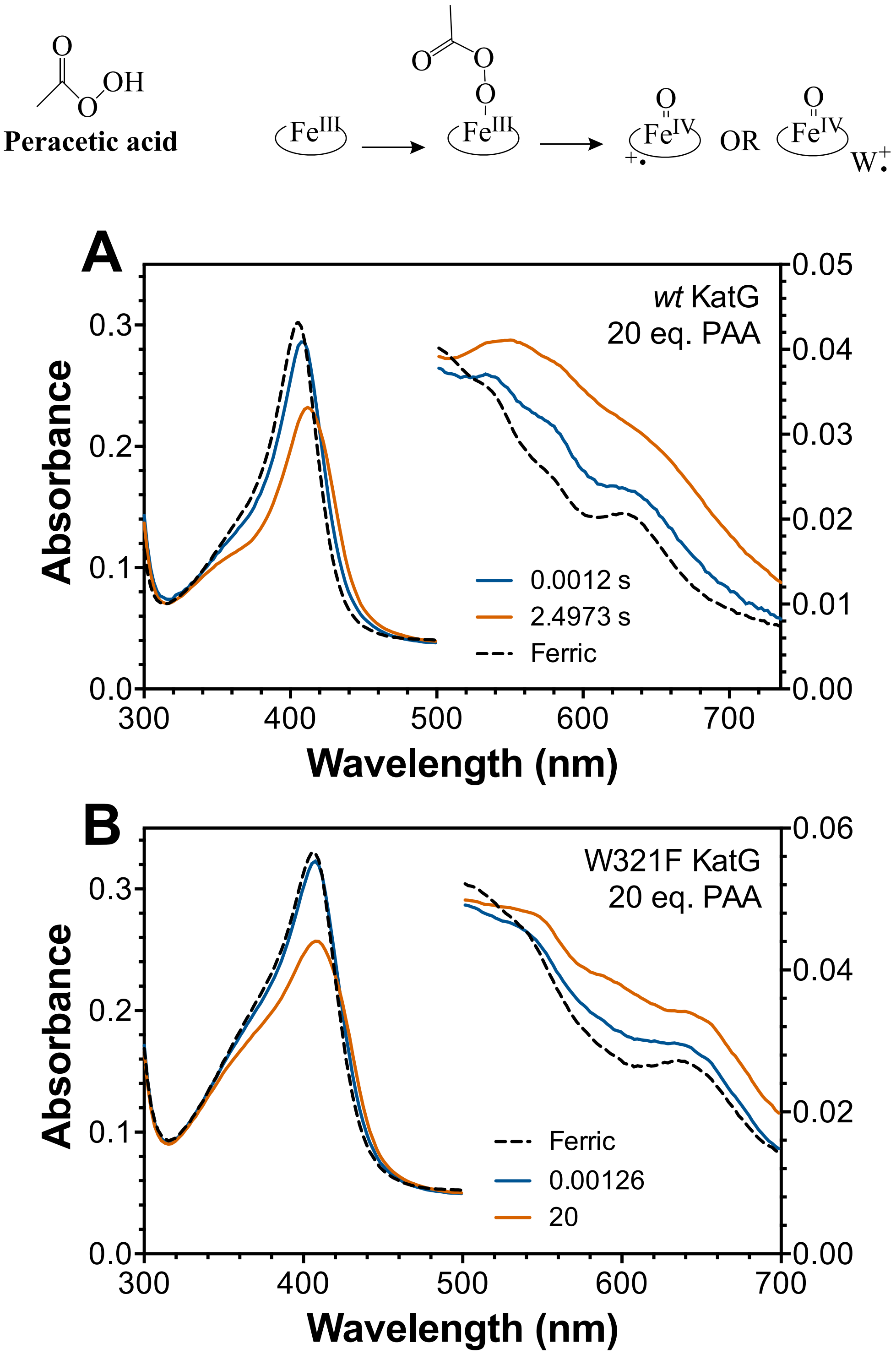

Figure 2.13. Heme spectral features of *wt* and W321F KatG when reacted with PAA. Reaction with 20 eq. of PAA, the non-catalytic substrate, with *wt* KatG (A) and W321F KatG (B) results in spectral features consistent with a mixture of Fe^{III} and Fe^{IV}=O[por]$^{\bullet +}$ heme states.

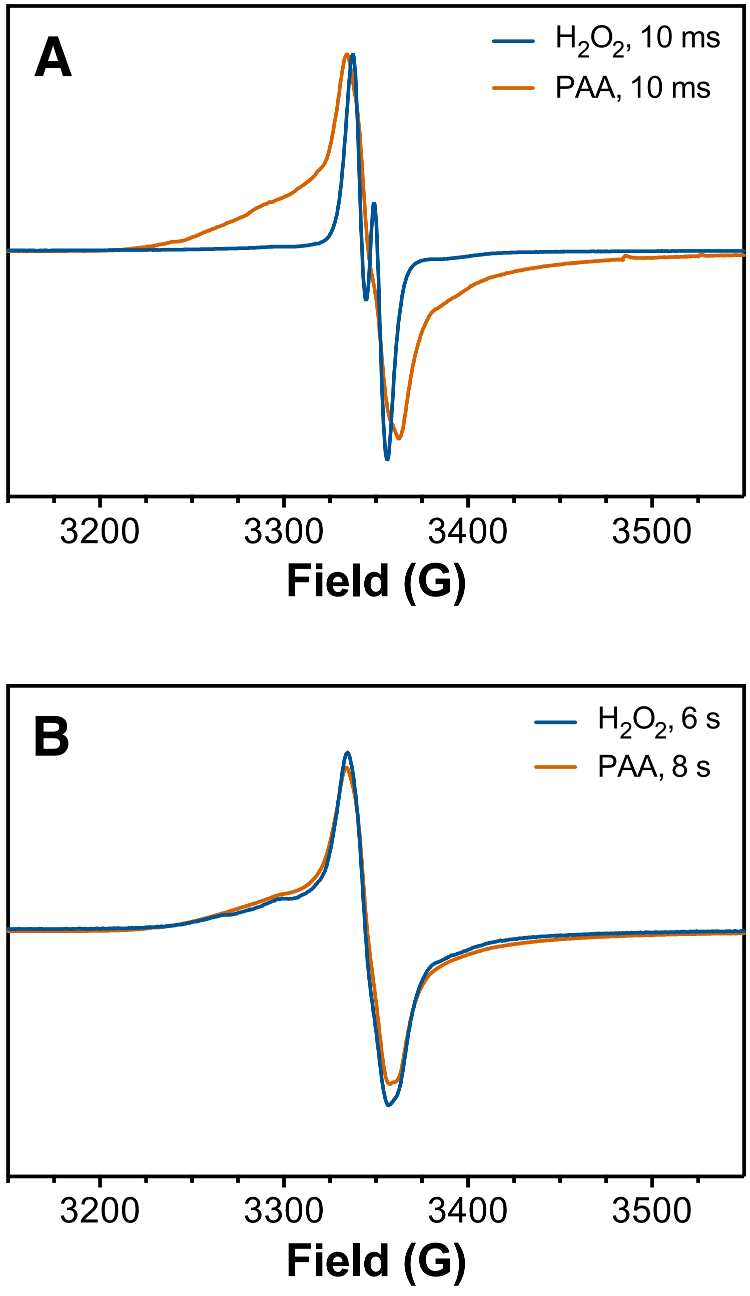

Figure 2.14. Comparison of protein-based radicals present when reacting *wt* KatG with H_2O_2 and PAA. RFQ-EPR samples were prepared by reacting *wt* KatG with 667 eq. H_2O_2 or 20 eq. PAA for 10 ms (A) and 6 s or 8 s, respectively (B).

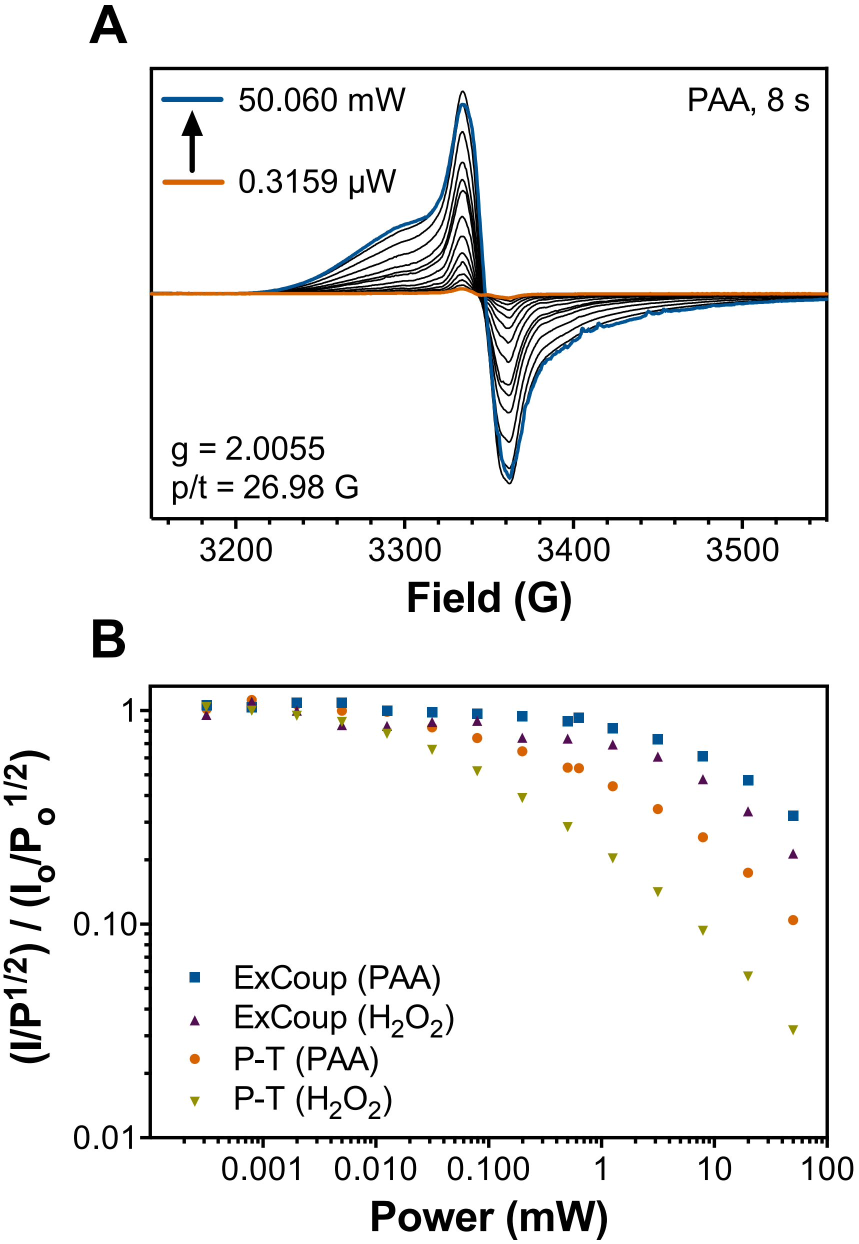

Figure 2.15. Power saturation of EPR signal observed upon *wt* KatG reaction with PAA at 8 s. Spectra were recorded from 0.3159 μW (orange) to 50.060 mW (blue) at 4.5 K (A). Power saturation characteristics of the PAA exchange-coupled signal was compared to that of *wt* reacting with H_2O_2 (B).

another (Fig. 2.17). Not only are the radical species resulted from reaction with *m*CPBA distinct from those observed upon reaction with PAA or H_2O_2, but specifically, the signal quenched after 10 ms reaction time with *m*CPBA is unlike any EPR signal we have observed to date. The exchange-coupled features (around 3300 G) are uniquely prominent in this spectrum; the power saturation characteristics of this radical also are distinct from previously observed radicals (Fig. 2.18). Power saturation characteristics of the EPR sample quenched after 24 s after reaction with *m*CPBA, however, look very similar to those of other exchange-coupled radicals observed upon reaction with PAA or H_2O_2 (Fig. 2.19).

Reacting *wt* and W321F KatG with substrates that do not support catalase activity such as PAA and *m*CPBA provide insight to the spectral characteristics of catalase-inactive species. In general, it can be expected that these catalase-inactive species are capable of KatG-unique peroxidase activity, that is, intraprotein hole-hopping for the relocation of oxidizing equivalents from the core of the protein out to the surface. As such, these intermediates are characterized by exchange-coupled broadening EPR spectral features and ferryl-type optical spectral features. The distinctions between *wt* and W321F heme spectra observed upon reaction with PAA might suggest that this substrate favors the oxidation of the proximal Trp, which is also supported by the comparison of PAA-generated protein-based radicals with the proximal Trp radical identified upon reaction with H_2O_2. Reaction with *m*CPBA, however, does not result in such stark differences in the heme spectra exhibited by *wt* and W321F KatG. Perhaps the minute changes in heme spectra and the vastly different changes in EPR spectra for proteins reacted with *m*CPBA suggest that reaction with *m*CPBA supports residue oxidization other than W321. Further investigation such as investigation of the peroxidase activity of these proteins using PAA and *m*CPBA

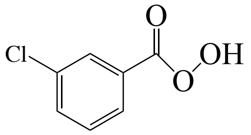

m-Chloroperoxybenzoic acid

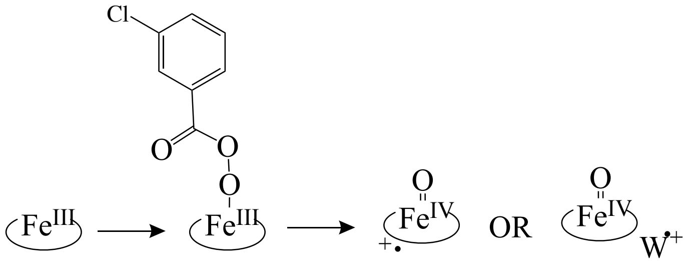

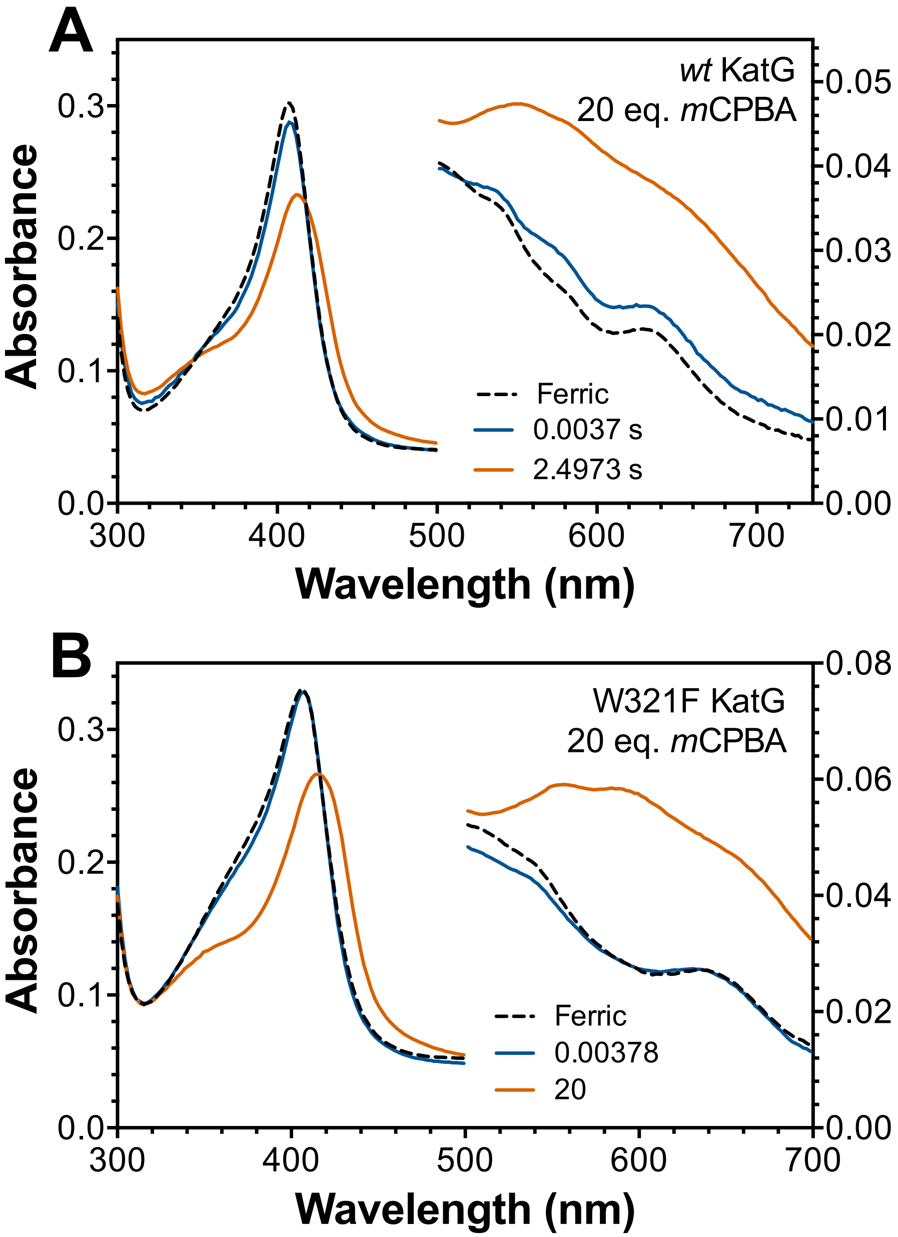

Figure 2.16. Observed heme state of *wt* and W321F KatG reacted with *m*CPBA. Reaction with 20 eq. of the non-catalase supporting substrate, *m*CPBA, and *wt* KatG (A) and W321F KatG (B) results in spectral features consistent with a mixture of Fe^{II}=O and Fe^{IV}=O[por]$^{\bullet+}$ heme states.

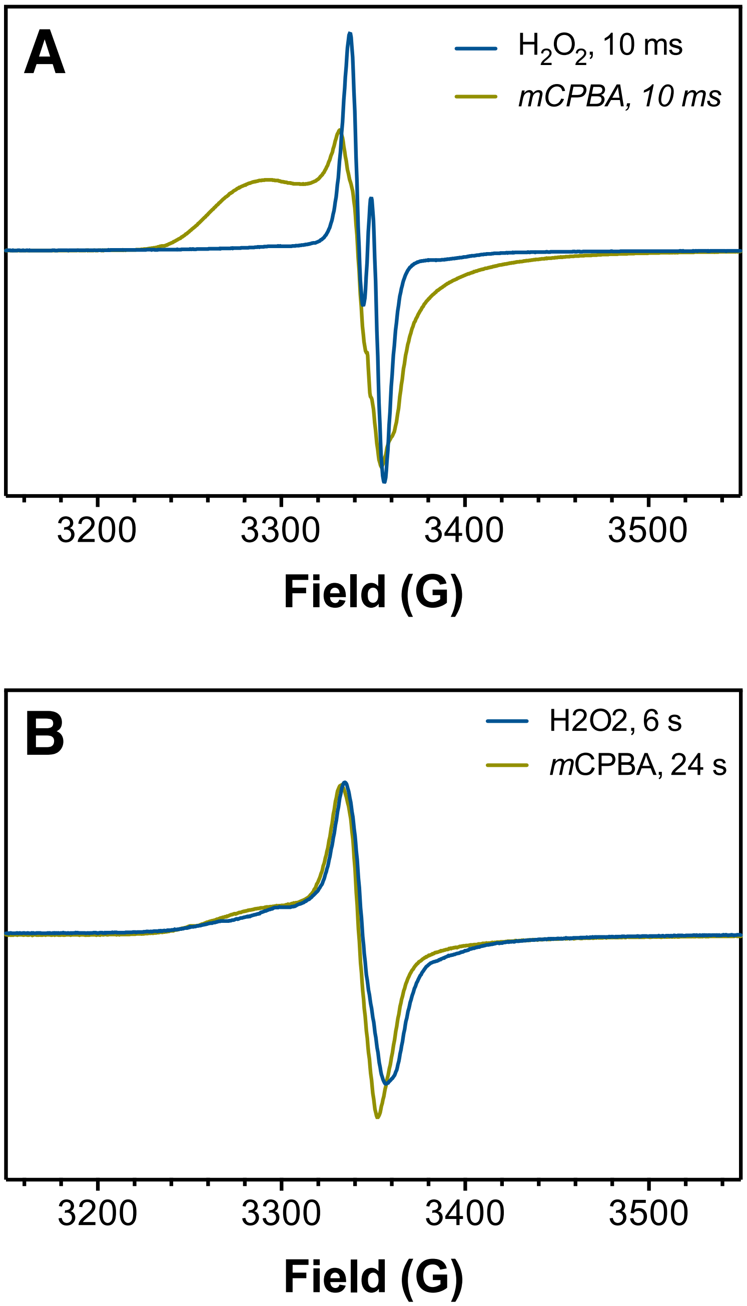

Figure 2.17. Comparison of protein-based radicals present when reacting *wt* KatG with H_2O_2 and *m*CPBA. RFQ-EPR samples were prepared by reacting *wt* KatG with 667 eq. H_2O_2 or 20 eq. *m*CPBA for 10 ms (A) and 6 s or 24 s, respectively (B).

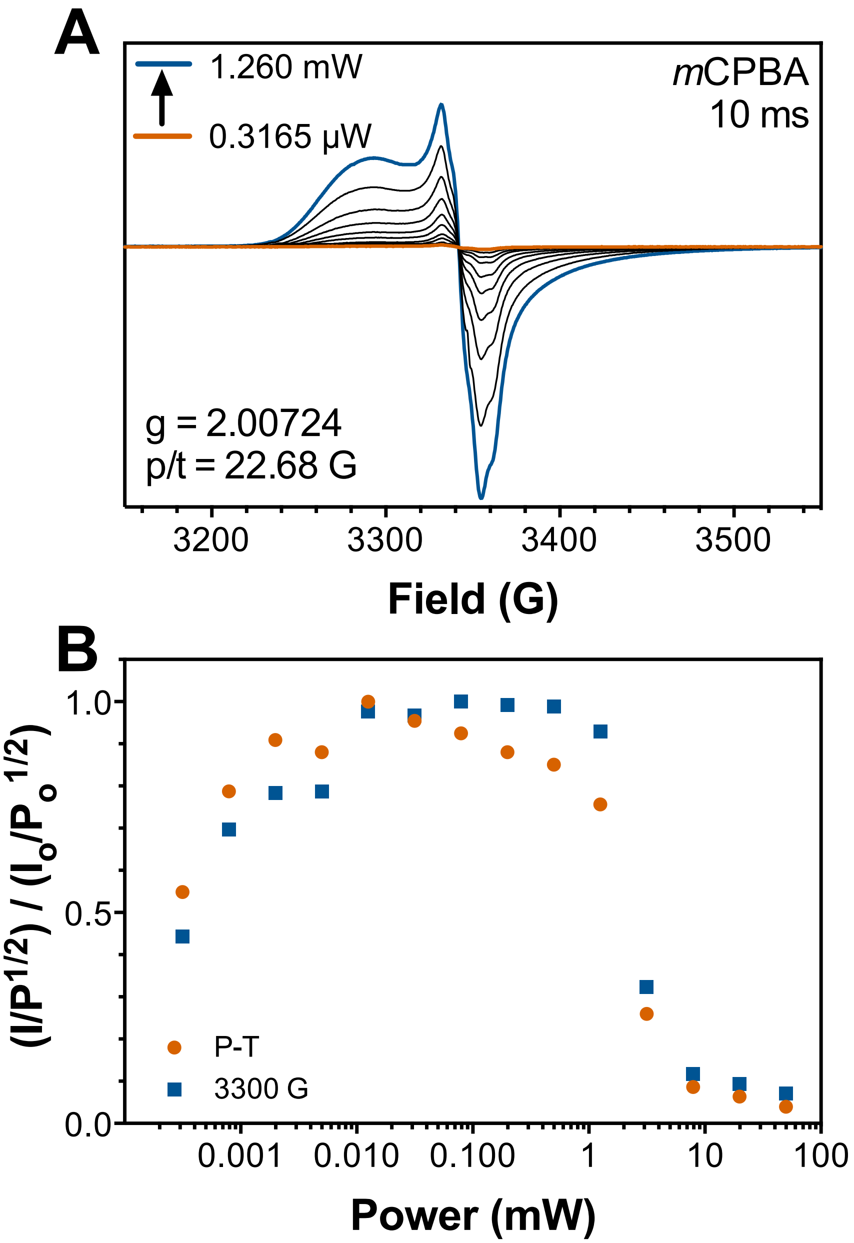

Figure 2.18. Power saturation of EPR signal observed upon *wt* KatG reaction with *m*CPBA at 10 ms. Spectra were recorded from 0.3165 μW (orange) to 1.260 mW (blue) at 4.5 K (A). Power saturation characteristics of the peak-to-through and 3300 G features of the *m*CPBA radical (B).

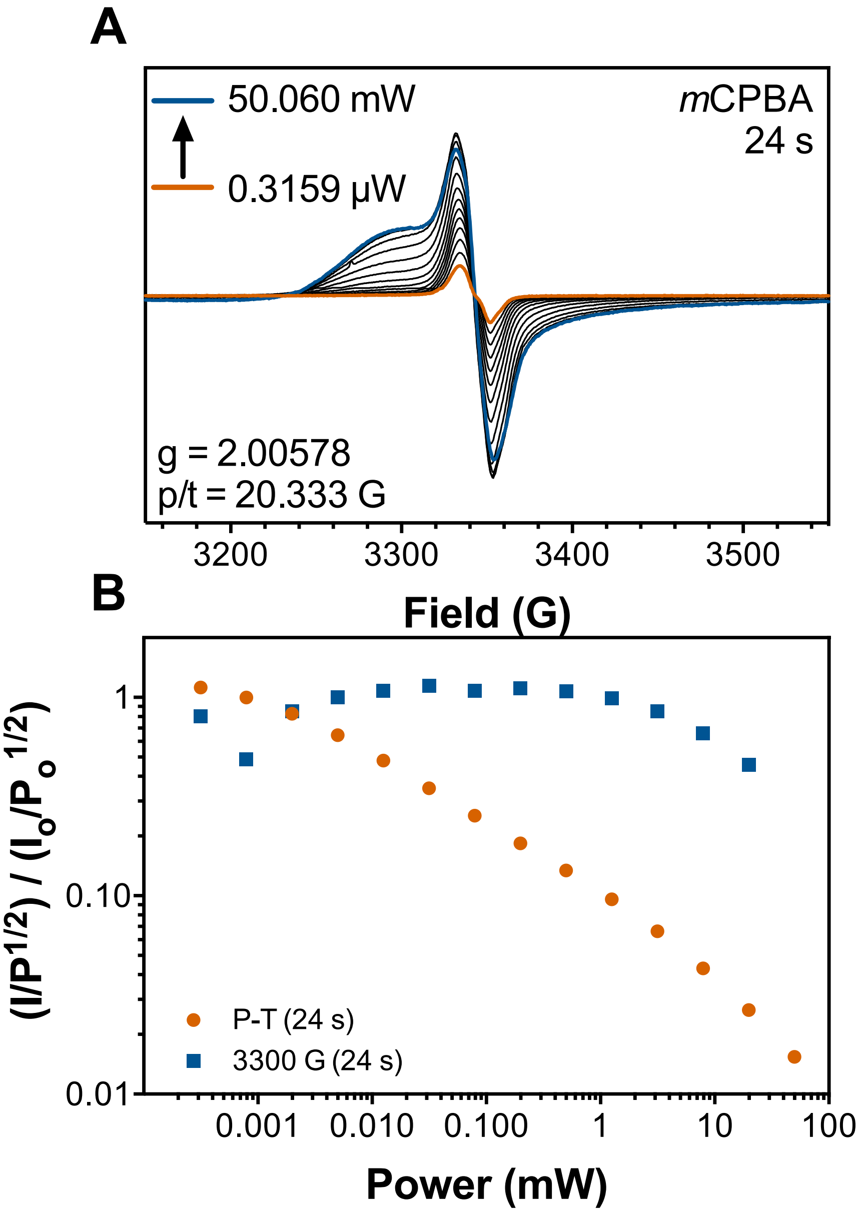

Figure 2.19. Power saturation of EPR signal observed upon *wt* KatG reaction with *m*CPBA at 24 s. Spectra were recorded from 0.3159 µW (orange) to 50.060 mW (blue) at 4.5 K (A). Power saturation characteristics of various features of the *m*CPBA radical (B).

as a substrate and characteristics of protein-based radicals present upon W321F reaction with PAA and *m*CPBA would provide additional insight to the reactivity and variability of residue oxidation that may routinely occur during KatG peroxidase activity.

2.4. Understanding enzyme rescue by PxEDs

Inactivation of KatG and preservation of catalysis by PxEDs

Experiments evaluating the extent of O_2 production while PxEDs (e.g., ABTS or TMPD) were added at various times to an ongoing reaction between KatG and H_2O_2 were performed to understand the inactivation of KatG and the enzymatic preservation afforded by the presence of PxEDs. Addition of ABTS to reactions between *wt* and W321F and H_2O_2 resulted in lower rates of O_2 production as the reaction proceeded (Fig. 2.20). This is presumed to be a cause of the decreasing population of active KatG protein in solution as catalase turnover persists. Given the rapid rate of inactivation of W321F (reference Fig. 2.6), it is no surprise that there is a much smaller stimulation in rate of O_2 production upon the addition of ABTS as there is expected to be less active protein present to preserve. Measuring the O_2 production rate after addition of ABTS can represent the remaining catalase activity of the enzyme. In comparison to extent of O_2 production curve without ABTS present, the rates of inactivation agree with each other (Fig. 2.21). The observed rate constant derived from the decrease in stimulated O_2 production rate over time ($0.009 \pm 0.0004\ s^{-1}$) corresponds with the rate of inactivation of O_2 production overall ($0.012 \pm 1.20 \times 10^{-5}\ s^{-1}$) for *wt* KatG. When TMPD is used as a PxED to prevent enzyme inactivation, similar trends to that of ABTS are observed, specifically the stimulated rate of O_2 production after the addition of TMPD decreases as the reaction progresses (Fig. 2.22).

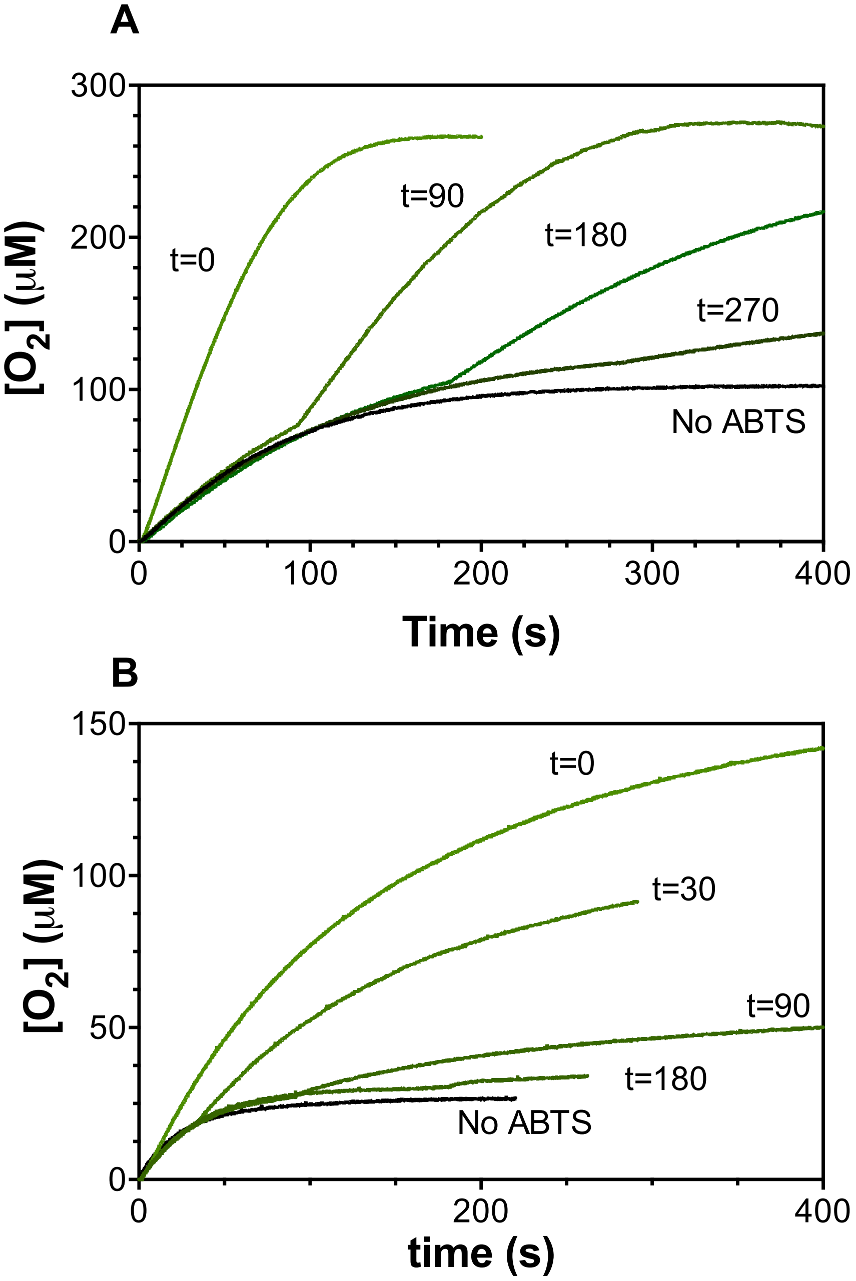

Figure 2.20. Time-dependent rescue of *wt* and W321F by ABTS. A decrease in stimulated rate after addition of ABTS at the given times during reaction of *wt* (A) or W321F (B) KatG and 500 µM H_2O_2 indicates inactivation by both enzymes. All reactions were conducted with 5 nM enzyme, 500 µM H_2O_2, and 0.1 mM ABTS when present in 50 mM acetate, pH 5.

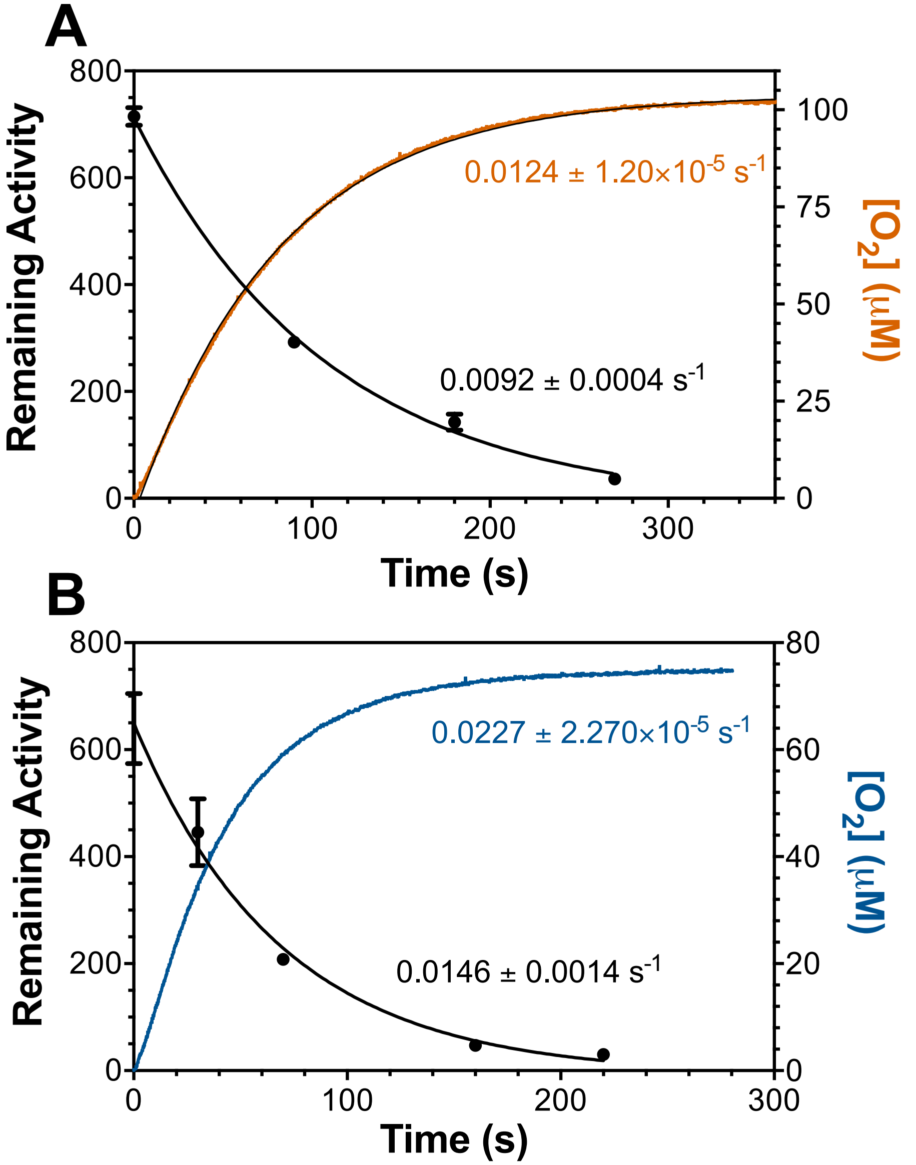

Figure 2.21. Remaining catalase activity compared to O_2 production. Inactivation of *wt* (A) and W321F (B) KatG proteins was investigated by the cessation of O_2 production (orange and blue, respectively) and remaining catalase activity observed upon the addition of 0.1 mM ABTS to the reaction mixture (black).

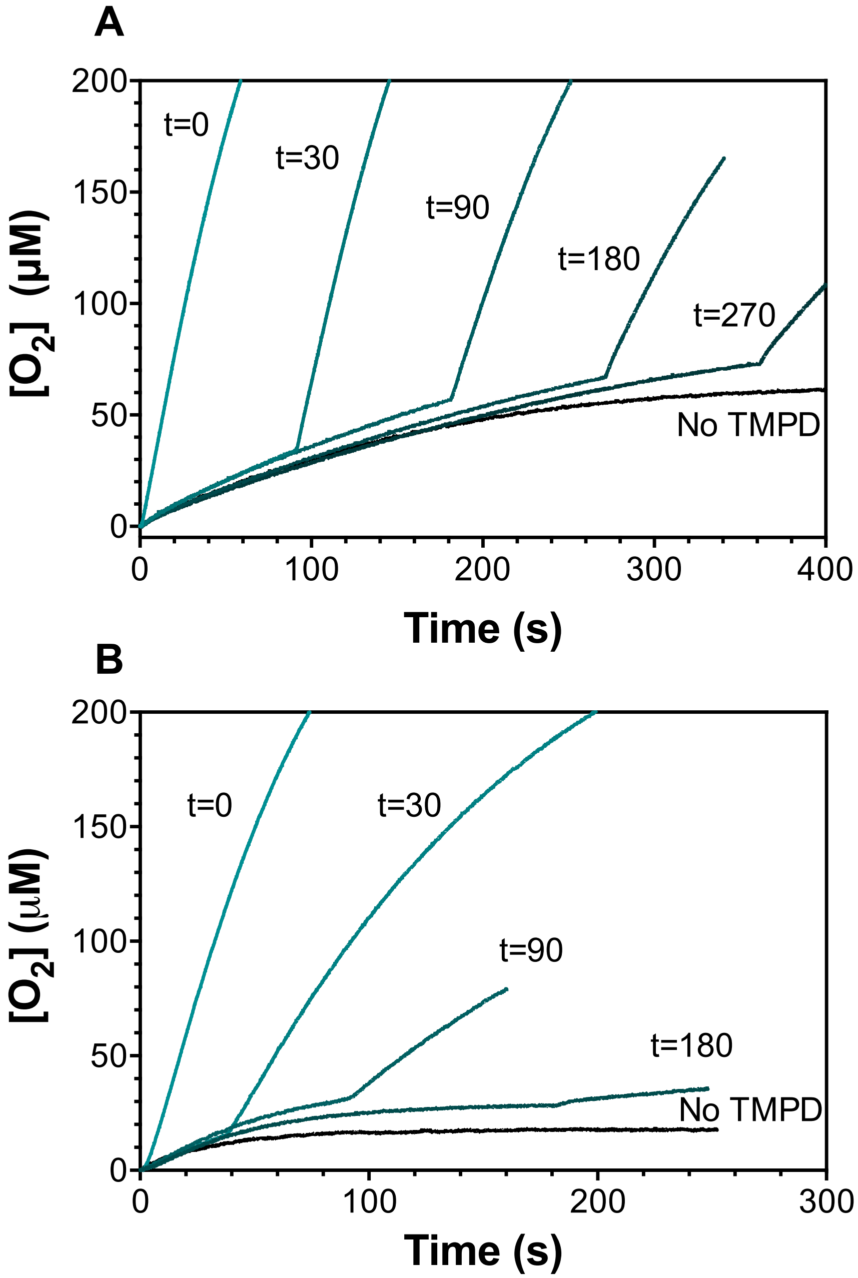

Figure 2.22. Time-dependent rescue of *wt* and W321F by TMPD. A decrease in stimulated rate after addition of TMPD at the given times during reaction of *wt* (A) or W321F (B) KatG and 500 µM H_2O_2 indicates inactivation by both enzymes. All reactions were conducted with 5 nM enzyme, 500 µM H_2O_2, and 0.1 mM ABTS when present in 50 mM acetate, pH 5.

Overall, TMPD seemed to provide greater stimulation of catalase activity for both *wt* and W321F, with increases in stimulated O_2 production rate compared to ABTS for *wt* and W321F, respectively.

Despite the identity of the PxED, *wt* experienced more stimulation than W321F, which again suggests *wt* seems to be able to more efficiently use the PxED for catalase activity stimulation due to the presence of the proximal Trp. As clarified by this experiment, PxEDs are not able to recover inactive protein back to catalase turnover. Indeed, PxEDs must be present at the onset of inactivation events in order to facilitate recovery of catalase turnover. The presence of PxED at the beginning of the reaction not only provides significant stimulation in rate, but also the prevents the accumulation of inactive states of the enzyme. PxEDs exerted the same effect on *wt* and W321F KatG, but their presence appeared to have a lesser ability to protect W321F activity relative to *wt* KatG, as observed in previous extent O_2 production experiments where ABTS was present from the beginning of the reaction. Consequently, the absence of the proximal Trp greatly impacts the ability of the enzyme to utilize exogenous electron donors, when they are present. Together with previous spectroscopic evidence, these data suggest W321 not simply takes part in, but plays a key role in the efficacy of the unique peroxidase activity of KatG. It is anticipated, due to its proximity to the heme cofactor, that W321 is a primary site for off-catalase oxidation, initiating hole-hopping to relocate the unpaired electron to the protein surface for PxED oxidation. Given the proposed mechanism by which KatG carries out peroxidase activity, that is, oxidation of the compound at the protein's surface as a result of intraprotein hole transfer, KatG is expected to oxidize a wide range of PxEDs. Figure 2.23 and Table 2.2 provide data on a variety of PxEDs that result in prolonged

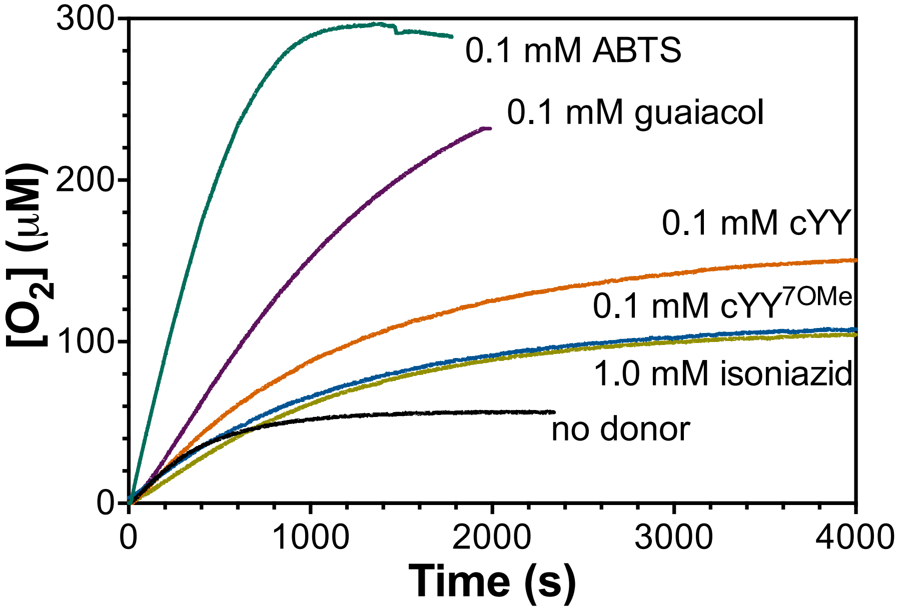

Figure 2.23. Extent of O_2 production with various PxED.

Table 3.2. Effects of Electron Donors on Initial Rate and Extent of O_2 Production

	$\nu_o/[E]_T$ (s^{-1})[†]	% Increase observed	$[O_2]$ produced (μM)	% Increase observed
wt, no donor	63.6 (5.8)	---	52 (3)	---
ABTS	900 (200)	1300%	312 (23)	500%
Pyrogallol	138.7 (7.1)	120%	256 (9)	390%
Guiacol	93.0 (2.7)	46%	~250	380%
cYY	70.5 (3.2)	11%	153 (8)	190%
cYY^{7OMe}	59.0 (3.5)	-7%	118 (7)	130%
INH	37.0 (14.0)	-42%	95 (13)	85%

All experiments were performed with 5 nM *wt* enzyme and 0.5 mM H_2O_2 in 50 mM acetate, pH 5.0 on oxygen sensitive electrode.

[†] initial rate divided by total enzyme concentration

catalase turnover. This group consists of colorimetric PxED, ABTS, Tyr-Tyr crosslinked adduct with an OMe Tyr-Tyr derivative, and biologically relevant electron donors such as guaiacol and isoniazid. Of all the electron donors, ABTS supports the highest rate and the longest sustainability of O_2 production.

Exploring range of effective exogenous electron donors

Though an exact mechanism has not been determined, it is presumed that KatG carries out INH activation by way of peroxidase activity. Previous investigations by Loewen and coworkers regarding predisposition of antibiotic resistance due to the presence of KatG lead to the investigation of the aminoglycoside antibiotic, kanamycin (85). Loewen, *et.al.* concluded that kanamycin was oxidized by direct interaction with KatG. Following this, aminoglycosides (e.g., kanamycin, gentamycin and amikacin) were investigated as potential electron donors. Similarly, glucose, sucrose, and maltose were examined as potential exogenous electron donors due to their similarity in structure and binding location to the aminoglycosides, specifically kanamycin (Fig. 2.24).

Gentamycin and amikacin were not effective PxEDs to reduce the Fe^{IV}=O[por]$^{\bullet+}$ state of KatG that is formed after reaction with 5 molar equivalents of PAA. Only when increased to 2.5 mM and 50 mM, respectively, were gentamycin and amikacin able to support reduction of Fe^{IV}=O[por]$^{\bullet+}$ KatG to a degree comparable to kanamycin at 0.75 mM (Fig. 2.25). These high concentrations needed for effective Fe^{IV}=O[por]$^{\bullet+}$ reduction renders gentamycin and amikacin impractical as *in vivo* exogenous electron donors. Among the three sugars tested, only maltose was effective at the reduction of Fe^{IV}=O[por]$^{\bullet+}$ KatG (Fig. 2.26). The concentration required for effective Fe^{IV}=O[por]$^{\bullet+}$ reduction, however, was far

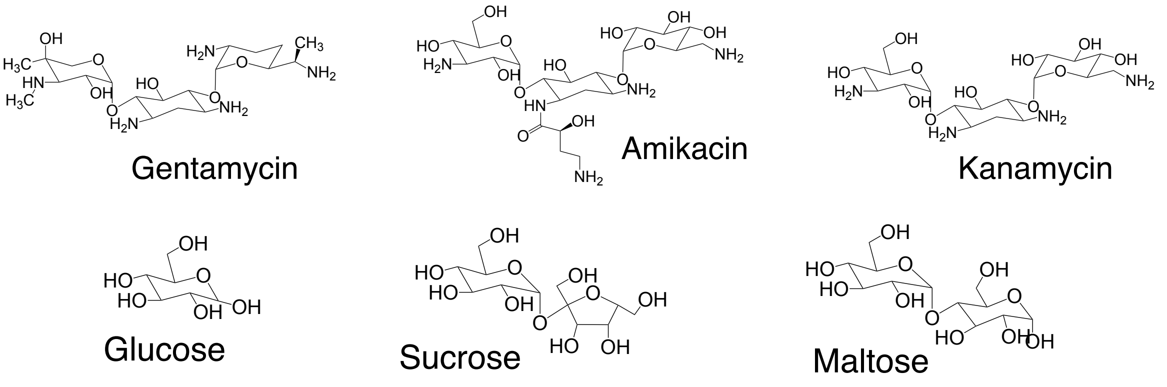
Gentamycin
Amikacin
Kanamycin
Glucose
Sucrose
Maltose

Figure 2.24. Aminoglycoside antibiotics and disaccharides.

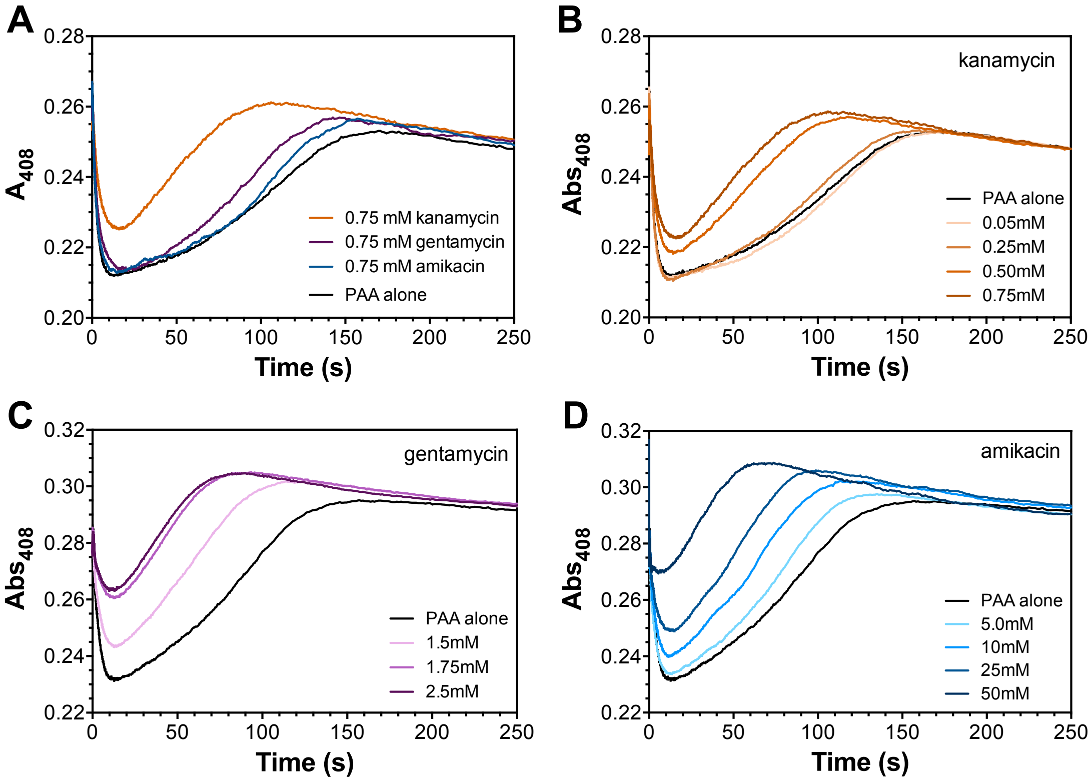

Figure 2.25. Antibiotics as electron donors with *wt* KatG. The return of ferric KatG after reaction with PAA was compared across a range of gentamycin (A), amikacin (B), and kanamycin (C) concentrations. All reactions were conducted with 3 µM enzyme, 5 eq. PAA in 100 mM phosphate, pH 7 by sequential mixing stopped-flow spectroscopy.

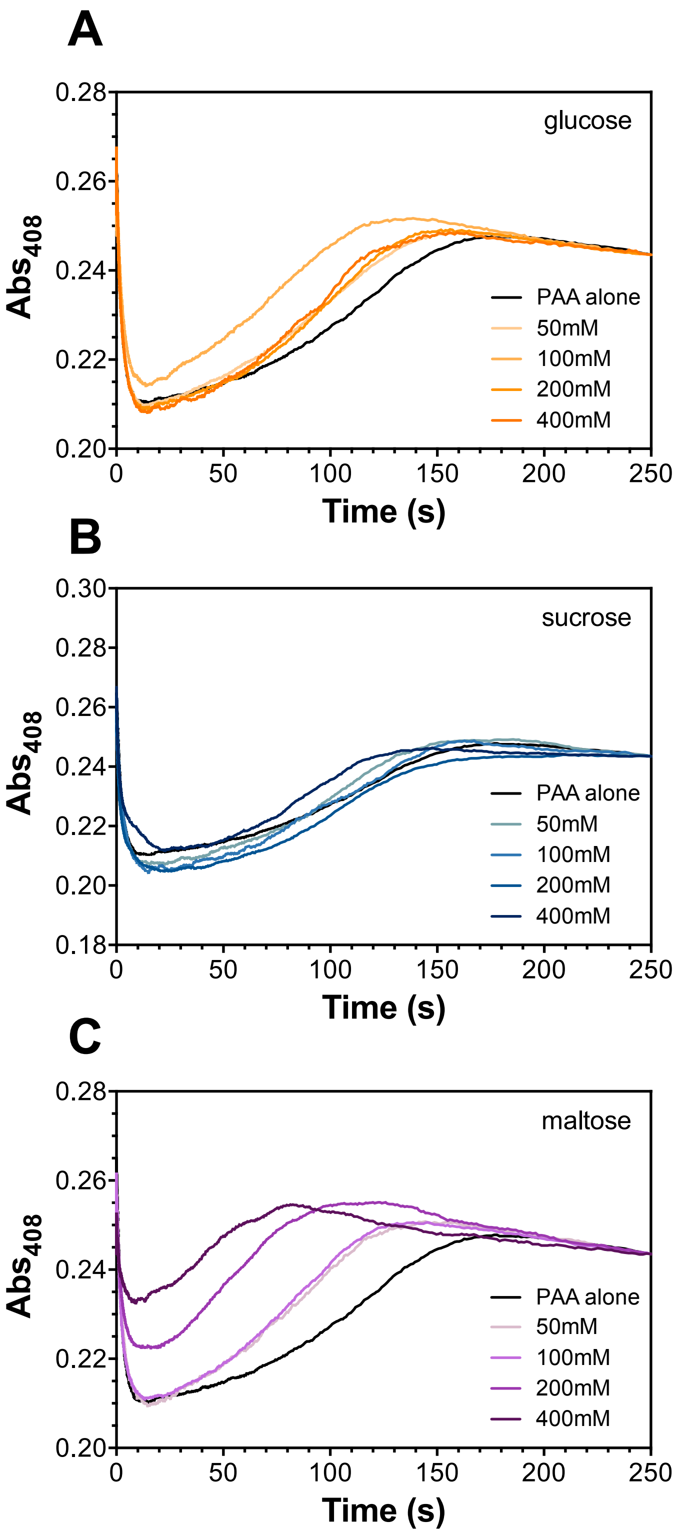

Figure 2.26. Sugars as electron donors for *wt* KatG. The return of ferric KatG after reaction with PAA was compared across a range of glucose (A), sucrose (B), and maltose (C) concentrations. All reactions were conducted with 3 μM enzyme, x eq. PAA in 100 mM phosphate, pH 7 by sequential mixing stopped-flow spectroscopy.

too high for practical *in vivo* application at 400 mM maltose. Higher concentrations of glucose and sucrose were not investigated because no matter the results, the concentration would be too high to be practical for treatment. In general, only the compounds already investigated, kanamycin and maltose, showed any appreciable electron donor capacity.

2.5. Discussion

The work presented here supports the findings already reported by our lab that the proximal Trp of KatG is a prominent, and most likely the primary, site for off-catalase oxidation. The narrow active site to the heme center restricts PxED oxidation to the surface of the protein, which necessitates electron transfer through the protein matrix. Given the multitude of Tyr, Met, and Trp residues near the heme leading out to the protein surface, it is expected that this is the typical mechanism of KatG peroxidase activity. As such, peroxidase activity acts as a method for preserving the integrity of the catalytic core of KatG, explaining the synergy that has been observed between the catalase and peroxidase activities of KatG (Fig. 2.27). Peroxidase activity of KatG, especially in the absence of an exogenous electron donor, is a self-sacrificial method of preservation where the redox active residues (i.e., Trp, Tyr, and Met residues) throughout the protein act as *endogenous* electron donors that are sacrificially oxidized for the promotion of catalase activity. However, in the presence of PxEDs the oxidized residues can be restored, preventing long-term damaging effects of the hole-hopping process and prolonging catalatic turnover.

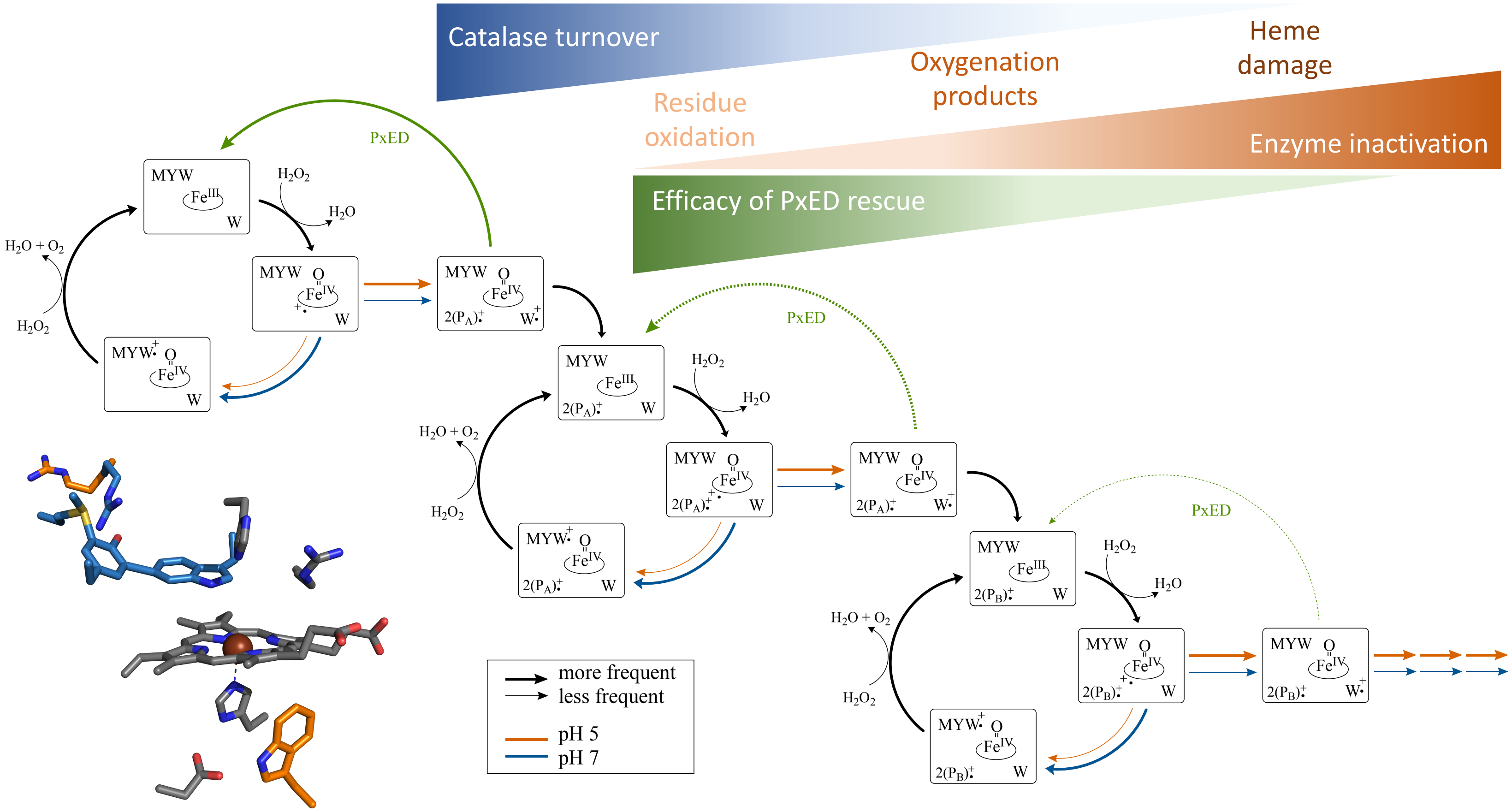
Catalase turnover
Residue oxidation
Oxygenation products
Heme damage
Enzyme inactivation
Efficacy of PxED rescue
PxED
MYW
Fe^{III}
Fe^{IV}
W
H_2O_2
H_2O
$H_2O + O_2$
$2(P_A)^{+}$
$2(P_B)^{+}$
more frequent
less frequent
pH 5
pH 7

Figure 2.27. Synergistic scheme of the KatG bifunctional mechanism. The figure below shows how the peroxidase and catalase mechanisms of KatG work together to make a more effective enzyme. Additionally, the pH-dependence of these functions and the involvement of any PxED present are presented.

Chapter Three

Toward Identification of Iron States in the Unique Catalase Mechanism of KatG: Protocols for Labeling Enzyme with ^{57}Fe

3.1. Introduction

KatG's unique catalase activity

As discussed in the preceding chapter, though KatG is a bifunctional enzyme, the peroxidase activity of the enzyme appears to play a substantial role in the preservation of its primary function, H_2O_2 decomposition by it catalase mechanism. As a reminder, KatG is the only member of its superfamily that is capable of any appreciable catalase activity. When the active site of KatG is directly compared to the active sites of a typical catalase and a typical peroxidase, it is clear that though KatG's primary function is catalase activity, structurally it is a heme peroxidase (Fig. 3.1). The ability to support catalase turnover as the primary chemistry within the core structure of a heme peroxidase is derived from KatG-unique structural features near the active-site heme: a plethora of oxidizable residues that enable a peroxidase activity that maintains the active site in a condition to continue catalase activity, a protein-derived cofactor called the Met-Tyr-Trp (or MYW) covalent adduct, and a conformationally dynamic Arg residue (Arg switch) that appears to regulate electron flow through the active site (Fig. 3.2).

A typical catalase mechanism is shown in Figure 3.3. Similar to what is observed for peroxidase activity, the reaction with the first equivalent of H_2O_2 results in the formation of a ferryl-oxo heme state with a porphyrin-based cation radical (i.e., Fe^{IV}=O

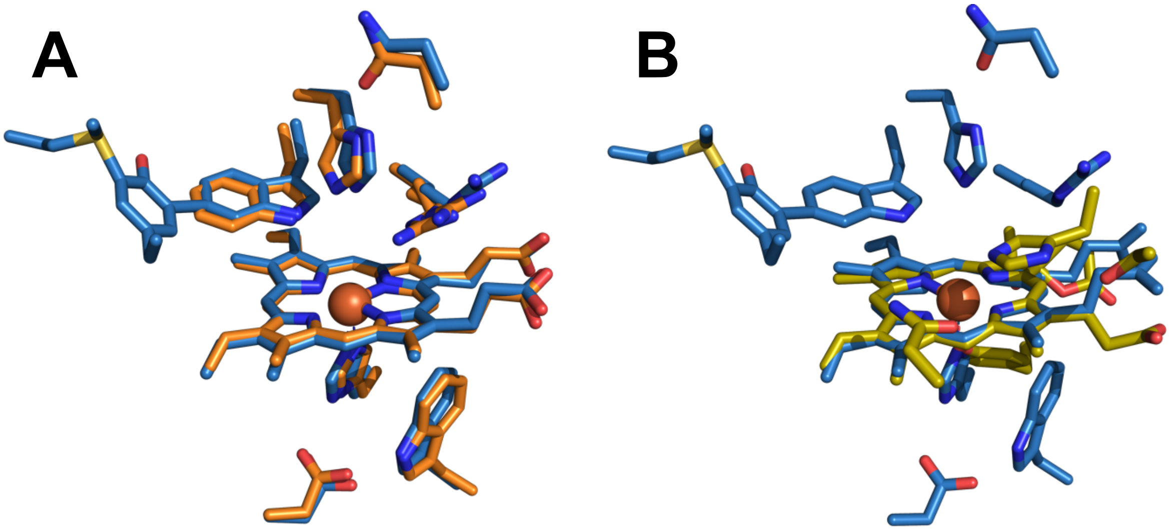

Figure 3.1. Comparison between a typical catalase and a typical peroxidase with KatG. A direct comparison of the conserved active site residues of KatG (blue) and those of a typical heme peroxidase (orange) (A) and typical heme catalase (yellow) (B) make it clear that KatG is a structure-function anomaly that is able to support catalase turnover within the scaffold of a peroxidase. PDB accession numbers: KatG (2CCA), *E.coli* catalase (1GGE), and C*c*P (4XVA).

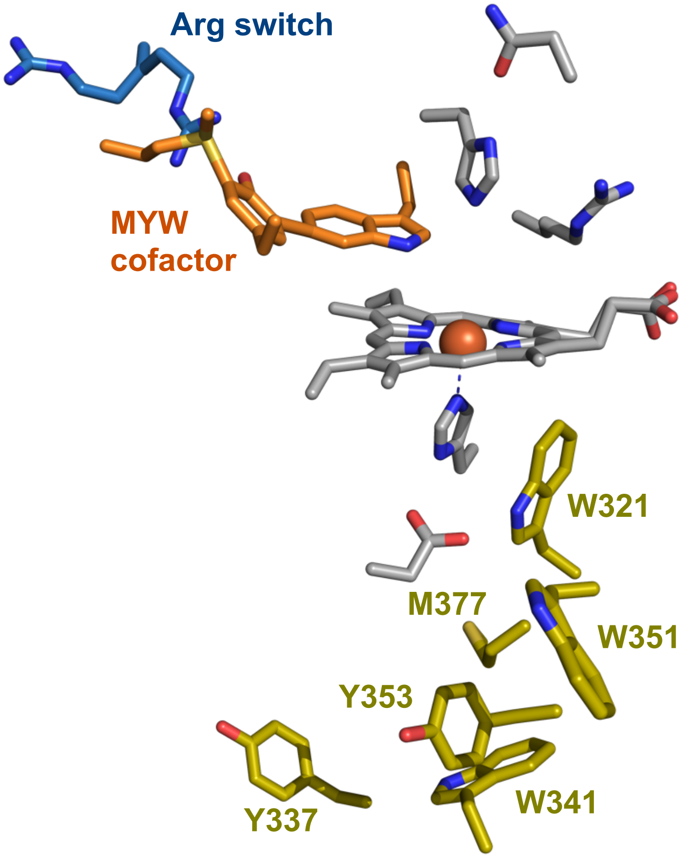
Arg switch
MYW
cofactor
W321
M377
W351
Y353
Y337
W341

Figure 3.2. KatG-unique structural features that enable unexpected robust catalase activity in a peroxidase active site. The MYW cofactor (orange), the Arg switch (blue), and a select few of the redox-active residues near the active site (yellow) all contribute to KatG's ability to leverage the active site of a peroxidase for robust catalase activity. PDB accession number 2CCA.

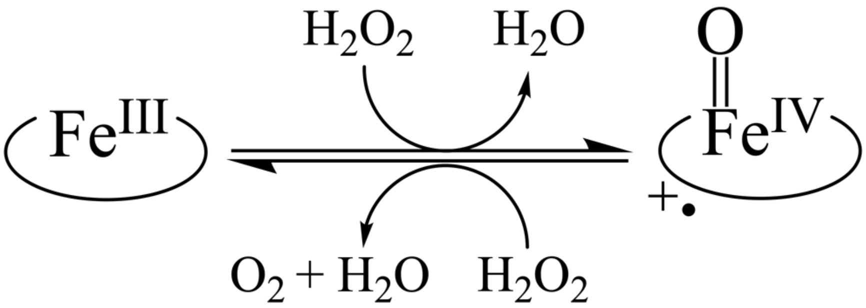
H2O2
H2O
O
FeIII
FeIV
+•
O2 + H2O
H2O2

Figure 3.3. Mechanism of a typical heme catalase. A typical heme catalase is capable of using a single, high-valent heme intermediate to react with a second equivalent of hydrogen peroxide to return back to the resting enzyme.

$[\text{porphyrin}]^{\bullet+}$). This intermediate is oxidized by two electrons relative to the Fe^{III} enzyme. This intermediate can directly react with another equivalent of H_2O_2 to return the enzyme back to its resting, Fe^{III} state in a typical catalase. KatG, however, utilizes another mechanism for catalase activity. It has been observed that any KatG variant lacking the MYW cofactor (i.e., variants targeting any of the three amino acids of the structure) results in an enzyme that shows little, if any, catalase activity, in essence reverting the enzyme to the peroxidase-only activity of the rest of the members of the superfamily (86–89). Participation of the MYW cofactor in the catalase activity of KatG, therefore, necessitates a completely novel catalase mechanism which remains to be fully elucidated. Identifying the intermediates of the catalase mechanism of KatG is imperative to fully understanding the enzyme and its functionality within pathogenic organisms.

Proposed catalase mechanisms of KatG

Though many features of KatG's catalase mechanism remain unknown, most investigators in the field agree that th KatG MYW cofactor participates in a one-electron reduction of the $\text{Fe}^{\text{IV}}\text{=O}[\text{porphyrin}]^{\bullet+}$ heme center, resulting in a $\text{Fe}^{\text{IV}}\text{=O}[\text{MYW}]^{\bullet+}$ intermediate. How this state then reacts with a second equivalent of H_2O_2 and ultimately returns to its resting (i.e., Fe^{III} state), including the enzyme intermediate(s) involved is where many questions remain. Three basic hypotheses have been put forward suggesting putative intermediate(s) in the KatG catalase mechanism (Fig. 3.4). One hypothesis involves the formation of a Fe^{III}-OH [MYW-OOH] structure that transitions to a MYW-OO-Fe^{III} bridged-peroxo intermediate which is supported by the reproducible peroxy derivatization of the distal Trp of *Bp*KatG (Fig. 3.4A) (90). A second proposes a proton-

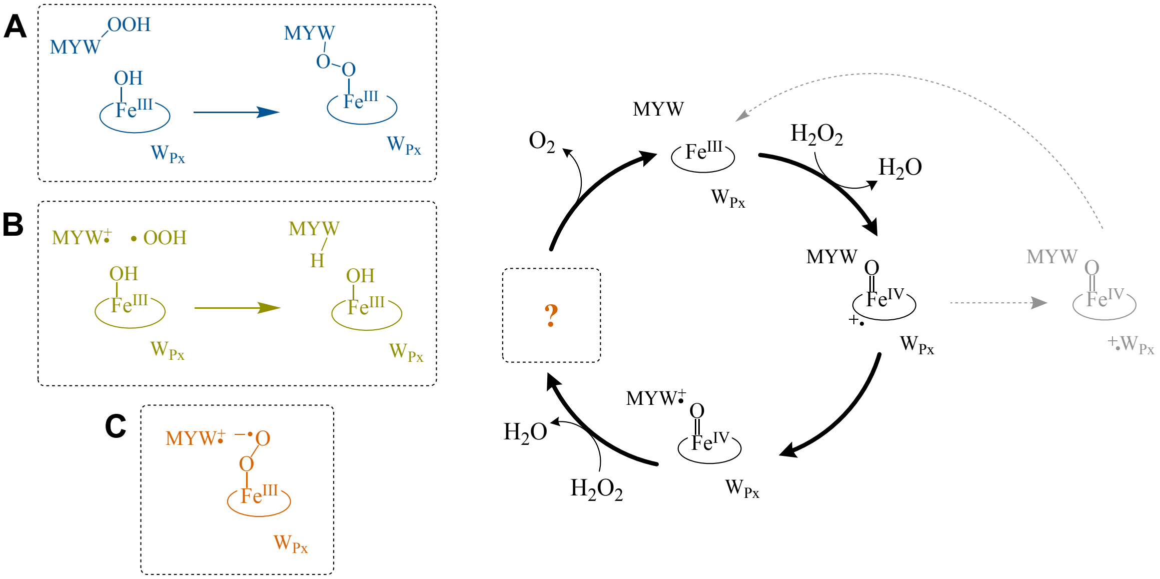
A
MYW
OOH
OH
FeIII
WPx
MYW
O
O
FeIII
WPx
B
MYW+•
• OOH
OH
FeIII
WPx
MYW
H
OH
FeIII
WPx
C
MYW+•
−•O
O
FeIII
WPx
?
O2
MYW
FeIII
WPx
H2O2
H2O
MYW
O
FeIV
+•
WPx
MYW+•
O
FeIV
WPx
H2O
H2O2
MYW
O
FeIV
+•WPx

Figure 3.4. Proposed mechanisms for the KatG catalase mechanism. The three proposals for the unknown intermediate(s) of the catalase mechanism are given the the left (A, B, and C) while intermediates that are established as catalase intermediates are provided in black on the right. The proposed first step of the catalase-preserving peroxidase activity of KatG through the oxidation of the proximal Trp is then shown in gray on the right.

coupled electron transfer (PCET) between Fe^{III}-OH[$HOO^{\bullet}$] and Fe^{III}-OH[$MYW^{\bullet+}$] radical intermediates and is supported by QM/MM calculations (Fig. 3.4B) (91). The final hypothesis depends on the reactivity of a Fe^{III}-$O_2^{\bullet-}$[$MYW^{\bullet+}$] intermediate and is supported by optical spectral features (416, 545, and 578 nm) comparable to those of a ferri-superoxo (Fe^{III}-$O_2^{\bullet-}$) (Fig. 3.4 C) heme state, this kind of intermediate is commonly observed in typical heme peroxidases upon their reaction with excess H_2O_2 in the absence of a substrate to act as an electron donor (84, 92–94). With favorable positioning near the heme (i.e., within 5 Å) and a highly resonant structure the MYW adduct is able to act as an intrinsic electron donor. Furthermore, formation of Fe^{IV}=O[MYW]$^{\bullet+}$ (upon reduction of Fe^{IV}=O[porphyrin]$^{\bullet+}$) is proposed to easily couple with the superoxide radical, releasing O_2. In doing so, not only does the MYW radical keep the ferri-superoxo intermediate from being a dead-end, but it enables a novel mechanism for catalase activity within the structure of a peroxidase.

Ambiguity of optical spectra of heme proteins

The results from our lab strongly support the participation of a ferric superoxo heme state in KatG catalase turnover. It is reasonable to suggest that the unique structural features that enabling catalase turnover within the peroxidase core of KatG can also facilitate unprecedented functionalization of this heme state that is inactive for typical peroxidases. Figure 3.5 presents the Fe^{III}-$O_2^{\bullet-}$ intermediate of horseradish peroxidase (HRP) directly compared to the steady-state intermediate of KatG catalase turnover. There are distinct differences between the two spectra including small (~ 2 – 4 nm) shifts in the absorption maxima of the Soret (γ) band and the α and β bands, but the majority of the differences are

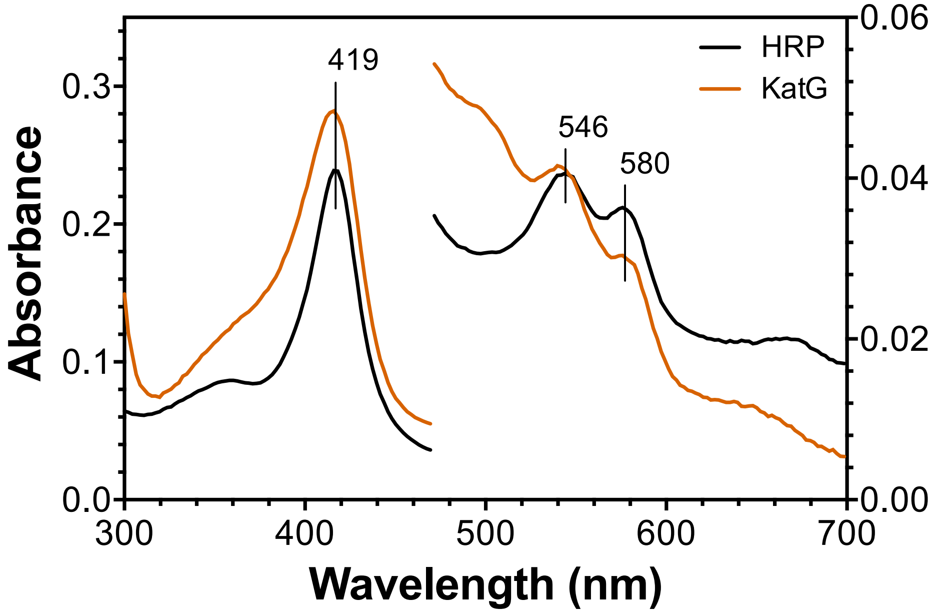

Figure 3.5. Comparison of KatG with ferric superoxo intermediate of HRP. The steady-state intermediate of KatG's (orange) catalase turnover resembles that of HRP (black) reacted with 1 mM of H_2O_2 at pH 7, which results in the formation of a ferric superoxo complex. Wavelengths highlighted in the figure designate peaks of the HRP spectrum. Both proteins were reacted at 3 µM by stopped-flow spectroscopy at 4 °C.

most likely influenced by active-site and overall protein structure. Nevertheless, these similar heme spectral features, comparison of optical spectroscopy across proteins is not rigorous enough for mechanistic determination of intermediate structure. As previously discussed, small changes in coordination state, solvation effects, and other structural changes can have a large impact the spectral features of heme cofactors. As an additional example, four different forms of a $Fe^{IV}=O$ heme state have been overlaid for comparison in Figure 3.6. KatG was reacted peracetic acid (PAA) or *m*-chloroperoxybenzoic acid (*m*CPBA) at pH 7. As these are not catalytic substrates, reactions with PAA and *m*CPBA result in the two-electron oxidation of the enzyme to form a $Fe^{IV}=O[porphyrin]^{\bullet+}$ heme intermediate that is then rapidly reduced by a nearby residue (e.g., the proximal Trp or some other oxidizable residue in close proximity to the active site), but not the MYW cofactor, resulting in a $Fe^{IV}=O[protein]^{\bullet+}$ state (reference Chapter 2). This persists until the heme is reduced back to its Fe^{III} state (most likely a process driven by hole-hopping within the enzyme). As discussed in Chapter 3, KatG reacted with its catalytic substrate, H_2O_2, accumulates $Fe^{IV}=O[W_{Px}]^{\bullet+}$ states (where the proximal Trp is oxidized) as off-catalase electron transfers occur during catalase turnover. Finally, the second intermediate of HRP catalysis is a $Fe^{IV}=O$ heme state. The comparison of all of these spectra emphasizes that though the heme-Fe and oxygen-ligand oxidation state are the same, the resulting heme spectral features can be vastly different. As such, optical spectroscopy alone is not sufficient for formal assignments of the heme intermediates responsible for KatG's unique catalase mechanism.

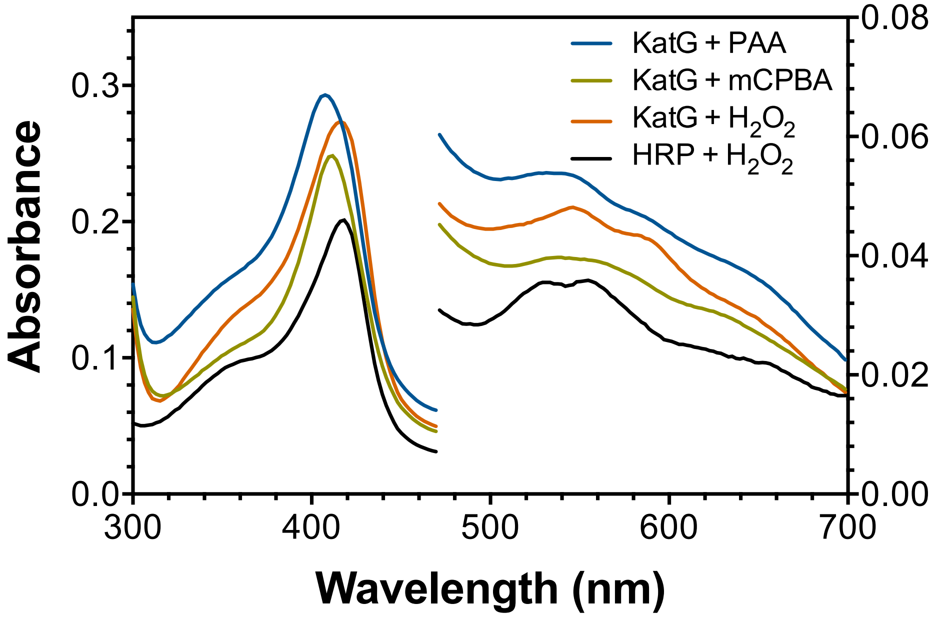

Figure 3.6. Ferryl-oxo intermediates across two proteins and various substrates. Active-site structural differences, coordination, and substrates each effect the spectral features of a Fe^{IV}=O heme state.

Mössbauer spectroscopy and heme peroxidases

Historically, Mössbauer spectroscopy has been a particularly useful tool for elucidation of heme protein mechanistic intermediate structures. It is the most direct method for determination of the oxidation and coordination state of the heme Fe. Briefly, an isomer shift (δ_{Fe}) provides insight to the *s*-electron density around the Fe nucleus which can be used to deduce the oxidation state of the Fe atom. The quadrupole splitting (ΔE_Q) is a result of the interactions between the electric field gradient of the electrons surrounding the Fe and the quadrupole moment of the excited state of the Fe nucleus which can be used to understand the configuration surrounding the ^{57}Fe atom. Chapter 1 can be referenced for more information on the theory and interpretation of these parameters.

The Mössbauer parameters for widely encountered heme states within various proteins tend to be highly consistent (Table 3.1). For example, heme proteins in the Fe^{III} state tend to have δ_{Fe} values ranging from 0.30 – 0.42 mm s^{-1} and quadrupole splitting around 1.24 – 2.60 mm s^{-1}. Interestingly, Fe^{III} heme states of various heme proteins tend to have very similar δ_{Fe} and ΔE_Q values (0.30 – 0.40 and 1.71 – 2.03, respectively). The Fe^{IV}=O[porphyrin]$^{\bullet+}$ heme state exhibits much smaller isomer shifts, ranging from 0.05 – 0.10 mms^{-1}, and quadrupole splitting that spans 1.25 – 1.55 mms^{-1}. The parameters for the Fe^{IV}=O state tend to be very similar and hard to distinguish from those of the Fe^{IV}=O[porphyrin]$^{\bullet+}$ heme state because the Fe has a spin of $S = 1$ and an oxo ligand in both intermediates. Finally, Fe^{III}-$O_2^{\bullet-}$ intermediates, which are isoelectronic with Fe^{II}-O_2 forms (e.g., oxymyoglobin, oxyperoxidase, etc.), exhibits Mössbauer parameters that are unique compared to other heme states. Specifically, these forms show a large, negative, axially symmetric quadrupole splitting that is temperature-dependent (95). Surprisingly,

Table 3.1. Mössbauer Parameters of Various Heme Proteins

		Ferric	Fe^{IV}=O [por]$^{\bullet+}$	Fe^{IV}=O [por]	Fe^{III}-$O_2^{\bullet -}$	Fe^{III}-O_2^{2-}
Horseradish peroxidase (95)	δ_{Fe} (mm s^{-1})	0.40 (4.2 K)	0.08 (4.2 K)	0.03 (4.2 K)	0.23 (4.2 K)	---
	ΔE_Q (mm s^{-1})	1.60 (4.2 K)	1.25 (4.2 K)	1.61 (4.2 K)	-2.31 (4.2 K)	---
Cytochrome *c* peroxidase (96)	δ_{Fe} (mm s^{-1})	0.30 (4.2 K)	0.05 (4.2 K)	0.46 (4.2 K)	---	---
	ΔE_Q (mm s^{-1})	2.10 (4.2 K)	1.55 (4.2 K)	1.23 (4.2 K)	---	---
Japanese radish peroxidase (97)	δ_{Fe} (mm s^{-1})	0.37 (77 K)	0.10 (77 K)	0.11 (77 K)	0.29 (77 K)	---
	ΔE_Q (mm s^{-1})	2.20 (77 K)	1.33 (77 K)	1.46 (77 K)	-2.37 (77 K)	---
Myoglobin (97, 98)	δ_{Fe} (mm s^{-1})	0.42 (4.2 K)	---	0.10 (4.2 K)	0.138 (4.2 K)	0.29 (4.2 K)
	ΔE_Q (mm s^{-1})	1.24 (4.2 K)	---	1.49 (4.2 K)	-2.296 (4.2 K)	1.71 (4.2 K)
Hemoglobin (99)	δ_{Fe} (mm s^{-1})	0.91 (4 K)	---	---	0.24 (1.2 K)	---
	ΔE_Q (mm s^{-1})	2.40 (4 K)	---	---	-2.24 (1.2 K)	---
Heme Oxygenase (98, 100)	δ_{Fe} (mm s^{-1})	0.42 (4.2 K)	---	---	0.26 (4.2 K)	0.29 (4.2 K)
	ΔE_Q (mm s^{-1})	1.24 (4.2 K)	---	---	-2.28 (4.2 K)	2.03 (4.2 K)
Cytochrome P450 (100)	δ_{Fe} (mm s^{-1})	0.31 (200 K)	---	---	0.31 (4.2 K)	
	ΔE_Q (mm s^{-1})	2.66 (200 K)	---	---	-2.15 (4.2 K)	

Temperatures at which the spectra were collected are provided in parentheses.

for all heme states, it is the protein-derived ligand and not the oxygen ligand that has the greatest impact on the isomer shift and quadrupole splitting observed.

Given previous Mössbauer investigations on heme proteins and even small-molecule heme protein mimics, distinct parameters can be expected for the intermediates unique to each of the three proposed catalase mechanisms for KatG. Perhaps the most facile assignment would be for the Fe^{III}-$O_2^{\bullet-}$ intermediate because this heme state has been very well characterized across a number of heme proteins, including heme peroxidases. If this hypothesis is correct, we should expect the steady-state intermediate of KatG's catalase mechanism to have an isomer shift ranging from about 0.20 – 0.30 mms^{-1} and quadrupole splitting that is large, negative and temperature dependent with symmetrical splitting when subjected to a magnetic field (95, 97, 98). The hypothesis proposing PCET within the KatG active site proposes the participation of a Fe^{III}-OH heme state. Though there are not many ferric hydroxyl intermediates that have been previously evaluated, it is anticipated that this heme state would display a δ_{Fe} very similar to the Fe^{III} state (~ 0.30 – 0.40 mm s^{-1}), with quadrupole splitting more like that of the Fe^{IV}=O heme states around 1.3 – 1.6 mm s^{-1}, given that some Fe^{IV}=O states appear to be protonated under certain conditions (95, 98, 101). Lastly, the proposed mechanism including a bridged Fe^{III}-OO-MYW intermediate should exhibit novel Mössbauer parameters due to the peroxo bridge and influence from a linkage to the MYW cofactor. Investigations of inorganic small-molecule mimics indicate that ferric hydroperoxy heme states are characterized by features that are similar to that of the Fe^{III}-$O_2^{\bullet-}$ intermediate (δ_{Fe} ~ 0.20 – 0.30 and ΔE_Q ~ -2.0 – -2.1) (101, 102). The distinguishing factor here would be the response of the quadrupole splitting under the influence of a magnetic field. The Fe^{III}-OO-MYW intermediate should show asymmetric splitting when subjected to a ~ 6 – 7 T magnetic field (101, 102).

Mössbauer sample preparation for KatG

Mössbauer spectroscopy is not a sensitive technique, and therefore not only requires the enzyme to be isotopically enriched with ^{57}Fe, but also requires a final concentration ~1 mM ^{57}Fe within the target sample. The majority of published protocols for heme protein preparation for Mössbauer spectroscopy rely on the reconstitution of apo enzyme with ^{57}Fe-enriched heme cofactor. In the cases of myoglobin, HRP, hemoglobin, and heme oxygenase most studies have expressed the heme protein in the apo form and then reconstituted with ^{57}Fe-enriched heme that had either been purchased or synthesized in-house (95, 98, 103). Alternatively, studies on Japanese radish peroxidase (JRP) indicate that the enzyme was expressed in its holo form, converted to its apo form by acid-acetone heme extraction protocol, and the resulting enzyme was then reconstituted with enriched heme (97, 104). A similar protocol was utilized to prepare cytochrome *c* peroxidase samples for crystallization (105).

Unfortunately, preparing Mössbauer samples with KatG poses additional challenges. The most common method of Mössbauer sample preparation, reconstitution of apo enzyme with ^{57}Fe-labled heme, is not the ideal method of preparation for KatG because mature, fully active KatG requires both the heme and the MYW cofactor in place and the biosynthesis of the MYW cofactor is a heme-dependent process. Our own data suggest that the majority of reconstituted protein has not yet formed the MYW adduct and would therefore not yield mature enzyme. Instead, ^{57}Fe isotopic enrichment of KatG would be accomplished best by ensuring isotopic enrichment takes place during expression. This can be accomplished either by addition of ^{57}Fe-enriched heme to the cell culture for direct insertion, or by supplementing the cell culture an ^{57}Fe salt and the heme precursor, δ-aminolaevulinic acid (δ-ALA), to encourage *in vivo* synthesis of ^{57}Fe-enriched heme which will then be inserted into KatG. Both methods were attempted to determine which method produced the highest yield and best quality of ^{57}Fe-labeled KatG. Commercial heme is prepared by isolation from bovine or porcine hemoglobin. In these cases, the Fe atom is already chelated to the porphyrin and therefore a benchtop chelation technique is necessary for the generation of ^{57}Fe-enriched heme.

3.2. Materials and Methods

Synthesis of heme

A survey of the literature on Mössbauer spectroscopy of heme proteins revealed that the majority of protocols for the synthesis of heme from protoporphyrin IX and a Fe salt referenced one of two main synthetic procedures, those of Caughey, *et.al.* (1966) or Adler, *et.al.* (1970) (106, 107). Each of these synthetic protocols were attempted in order to prepare heme for the enrichment of KatG.

Isotopically enriched ^{57}Fe powder was acquired from IsoFlex USA, San Francisco, CA at 96.14 – 96.18% abundance for ^{57}Fe. Metalation of PpIX with ^{57}Fe^{II} acetate following the Caughey, *et.al.* protocol (106) was accomplished as follows. About 65 mg of ^{57}Fe powder was added to 15 mL of glacial acetic acid in a 20 mL round bottom flask and refluxed at 118 °C under nitrogen until the solution turned a dark red color. Protoporphyrin IX (300 mg), NaCl (300 mg), and 250 mL glacial acetic acid were added to a larger round bottom flask. The ferrous acetate salt solution was then added to the flask containing the PpIX. The mixture was then refluxed together over night. The product was recovered by evaporating off the acetic acid under a stream of N_2 (*g*). After this, the product was dried further in a vacuum oven for 2 – 3 days. Separation of the heme from other side products was carried out by Celite chromatography (5 × 50 cm column). The mobile and stationary phases were prepared by mixing 2.5 L pyridine, 1.25 L chloroform, 1.25 L water, and 125 mL isooctane in a separatory funnel and then allowing the phases separate. The less dense, upper phase (water and pyridine mixture) was used to prepare the Celite column. The more dense, lower phase (chloroform and isooctane mixture) was used as the mobile phase and to dissolve the synthetic product to be added to the column. The red-brown band was reported to be the desired product and so this band was recovered. The resulting fractions were then collected and concentrated in a single round bottom flask for recovery of the product.

Metalation of PpIX with $^{57}Fe^{II}$ acetate following the Adler, *et.al.* protocol (107) was accomplished as follows. Ferrous acetate was prepared as described above; however, the sample was then allowed to evaporate, leaving a dried salt in the flask. To this dried metal salt, 200 mg PpIX and 100 mL of dimethylformamide (DMF) was added. The mixture was then refluxed at 154 °C under nitrogen until the solution turned from a red to green-brown in color. The synthetic product was recovered by evaporating off DMF by gentle heating under a stream of N_2 (*g*).

In an attempt to acquire a better synthetic product for KatG enrichment, a heme synthetic protocol by Erdman, *et.al.* (1947) (108) was attempted. Fe powder (75 – 80 mg) was added to 85 % acetic acid (3 – 5 mL) and stirred while heating to 98.6 °C. Meanwhile, 200 mg PpIX and 100 mg finely powdered NaCl was added to 10 mL glacial acetic acid. This PpIX and NaCl solution was gently heated to 50 °C in a sand bath and mixed vigorously to maximize dissolution of solids. The flask was then taken out of the sand bath and cooled while the ferrous acetate was completing its reaction. When the Fe salt solution was completely reacted, the PpIX solution was placed over the stir plate (without heat) and the ferrous acetate was added dropwise to the stirring PpIX-NaCl solution. Only small amounts of ferrous acetate were added to the pipette so that it would not cool too much before adding to the PpIX solution. Once all the ferrous acetate solution was added to the porphyrin mixture, the reaction was stirred vigorously and left to react for 10 min to complete the oxidation, according to Erdman, *et.al*. After 10 mins, the flask was left to settle for 5 – 10 mins before the product was removed by vacuum filtration. The collected purple powder was washed with 30% acetic acid, deionized water, and finally methanol.

Separation of heme from protoporphyrin IX

The heme product synthesized was separated from unreacted PpIX according to the methods of Vogel, *et.al.* (109) and Dresel and Falk (110). The crude product (100 mg) was then dissolved in ~ 150 mL ethyl acetate (EtOAc). The solution, kept in the dark, was not heated but was vigorously stirred to maximize dissolution of the powder product into EtOAc. The EtOAc-dissolved product was then added to a separatory funnel and ~ 100 mL of 10% HCl was added. The aqueous phase turned pink-purple due to the PpIX being extracted. These washes were repeated 4-5 times to continue removing unreacted PpIX from the product. As the washes proceeded, a purple, metallic slurry formed between the aqueous and organic phases in the funnel. This is expected to be the desired hemin product. The purple, metallic slurry was isolated from the separatory funnel and vacuum filtered.

Characterization of synthesized heme

After the recovery of product from each synthesis, the powder from each was solubilized in 0.1 M KOH solution and 5 uL of each solution was added to a cuvette to record diagnostic spectra. Each spectrum was compared to that from a commercial preparation of heme. Additionally, FTIR spectroscopy was used to compare each synthetic product to its commercial counterpart. Finally, the synthetic products with the closest spectral resemblance to commercial preparations were then analyzed by mass spectrometry to not only to confirm synthesis of the correct porphyrin product, but also the enrichment of ^{57}Fe. Mass spectra were acquired in the Auburn University Mass Spectrometry Center (Department of Chemistry and Biochemistry) on an ultra-performance LC system (ACQUITY, Waters Corp., USA) coupled with a quadrupole time-of-flight mass spectrometer (Waters Q-Tof Premier) with electrospray ionization (ESI) in positive mode using Masslynx software (V4.1). The product was dissolved in 1.3 N ammonium hydroxide solution and 10 μL of this solution was dissolved in 490 μL acetonitrile and directly injected to the source using a syringe pump at a rate of 2-3 μL/min.

Acid-butanone removal of heme cofactor

An alternative method of ^{57}Fe-labeled heme KatG reconstitution involving protein unfolding and removal of the heme by an organic solvent was attempted because of its precedence with horseradish peroxidase and cytochrome *c* peroxidase (105). The protein was denatured by the addition of 0.1 mM HCl drop by drop until the solution reached a pH of 2 in a 100 mL separatory funnel at 4 °C. Immediately after reaching a pH of 2, an equal volume of butanone was added to the protein and then mixed vigorously for 30 sec. Once the phases separated, the organic phase with extracted heme was removed from the funnel, and the process was repeated twice. Heme was then added to the resulting protein solution and the mixture was then dialyzed in 10 mM sodium bicarbonate in attempt to maximize reconstitution, refolding, and to remove any remaining butanone.

Reconstitution of apo KatG with synthesized heme

The most promising products from these procedures as determined by UV-vis, FTIR, and MS were evaluated further by performing a test reconstitution of KatG with each synthetic product. The properties of KatG (i.e., catalase activity and heme spectral features) reconstituted with these products served as the ultimate test of their suitability. The description for apo KatG expression and our full reconstitution protocol is provided in Chapter 5.

Heme synthesis by ferrochelatase

Attempts to synthesize heme using a more biologically based strategy was pursued in order to eliminate possible interference caused by remaining organic solvents. Constructs and strains for the expression of ferrochelatase (*wt* and F110A variant) were obtained by a generous gift from Dr. William Lanzalatta (University of Georgia) (111, 112). These enzymes were expressed, purified, and evaluated for their capacity to synthesize Fe-PpIX from PpIX and Fe salt. The expression and purification protocols were carried out as previously described (113). Reactions were carried out anaerobically in 100 mM Tris, pH 8.0, and 0.5% Tween 20. Final reactions were carried out in a total volume of 5 mL which included 1 μM ferrochelatase, 75 μM ferrous ammonium sulfate with 1 mg/mL ascorbate, and 75 μM PpIX (111, 113–115). Reactions were quenched with and equal volume of 2.6 N HCl to denature protein as a crude purification of the heme and enable characterization of the biosynthetic product(s).

Expression of KatG with δ-ALA and enriched iron salt

Terrific broth (TB) was treated with Chelex-100 Na resin (BioRad, #1432832) for 12-14 hours and then filtered (116). Glycerol (4.5 mL) was added to the filtered TB and then autoclaved. Upon inoculation with 100 mL starter culture, 1 L autoclaved TB was supplemented with 100 mL of a 0.17 M KH_2PO_4, 0.72 M K_2HPO_4 buffer; 2.5 mL of a trace metal solution [3.6 mM $ZnSO_4{\bullet}7H_2O$, 7.6 mM $MnCl_2{\bullet}4H_2O$, 4.9 mM H_3BO_3, 1 mM $Na_2MoO_4{\bullet}2H_2O$, 1 mM $CoCl_2{\bullet}6H_2O$, 0.88 mM $CuSO_4{\bullet}5H_2O$, 2.26 mM EDTA, 7.6 mM $MgCl_2$]; and any necessary antibiotics for bacterial growth (116, 117). All starter cultures were grown at 37 °C. Once expression cultures reached an OD_{600} of 0.5 – 0.7, KatG expression was induced by the addition of IPTG (100 mM) (GoldBio, I2481C200), 60 μM $^{57}Fe^{II}(NH_4SO_4)_2$, and 500 μM δ-ALA (Sigma-Aldrich, A3785). At the time of induction, the temperature was reduced to 20 °C and incubation was allowed to continue for 48 hours in the dark (116). The cells were harvested after expression and frozen at -80 °C before purification.

Purification of KatG

The cell pellet was resuspended in 0.17 M KH_2PO_4, 0.72 M K_2HPO_4 buffer (5 mL/expression L) supplemented with 50 mM PMSF (0.2 mL/expression L). The resulting cell suspension was homogenized using a glass tissue grinder. After homogenization, the cell lysate was sonicated for 8 cycles (42 s on, 42 s off) at 30% duty. Benzonase nuclease (EMD Milipore, #70746) was then added to the lysate (2 µL/expression L) and the solution was incubated for 4 hours at 4 °C with constant agitation. At the end of 4 hours, the lysate is anticipated to have a lower viscosity due to the extensive hydrolysis of nucleic acids by benzonase nuclease, aiding the formation of a firm pellet during centrifugation. The protein solution was separated from the cell matter by centrifugation at 4 °C (8,600 rpm for 45 – 60 mins with a slow deceleration). The supernatant was collected and then added to Ni-NTA resin (5 mL/expression L) prewashed with 50 mM Tris, pH 8.0. The supernatant-resin slurry was then subjected to constant aggitation at 4 °C for 12 hours to maximize binding of KatG to the Ni-NTA based resin. KatG was first purified by Ni-NTA chromatography (G-Biosciences, 786-407), where KatG eluted in the 60 mM, 75 mM, and 100 mM imidazole fractions. KatG was then subjected to buffer exchange into 50 mM phosphate, pH 7 using 10DG desalting columns (BioRad, 732-2010). Further purification of KatG was accomplished by anion exchange chromatography as previously described in Chapter 2 (BioRad, 156-0040). Fractions from anion exchange chromatography with least contamination by SDS-PAGE analysis and the highest purity value (A_{406}/A_{281}) were collected together and concentrated by centrifugal filtration with 30 kDa cutoff (Pall Laboratory, MCP030C41). Protein concentration and purity were determined by absorbance values from final spectrum of purified enzyme. Additionally, the activity of the purified enzyme was tested to ensure vitality.

Preparation of ^{57}Fe ammonium sulfate

^{57}Fe-enriched ferrous ammonium sulfate was prepared in order to supplement KatG cultures with the isotopically enriched salt for the *in vivo* synthesis of heme within the culture during expression. First, 3 mL of 2 M sulfuric acid was briefly heated to ~120 °C in a 20 mL scintillation vial on a hot plate. Once removed from the hot plate, the hot acid solution was slowly added to the 20.5 mg of ^{57}Fe powder in another 20 mL scintillation vial. The Fe and sulfuric acid were left to react, H_2 (g) is created during this process, so great care must be given to the environment where this reaction is taking place. While the Fe and sulfuric acid continue to react, 3 mL of a 2 M ammonium sulfate solution (pH 8) was heated to ~120 °C in a 20 mL scintillation vial on a hot plate. Once H_2 (*g*) production ceased, the ammonium sulfate solution was slowly added to the ferrous sulfate solution and gently swirled. This stock of isotopically enriched ferrous ammonium sulfate was added to KatG expression cultures for a final concentration of 60 μM.

Rapid freeze-quench sample preparation

Purified KatG enzyme was concentrated to 2 mM using centrifugal filters with 30 kDa cutoff in preparation for rapid freeze-quench (RFQ) Mössbauer sample preparation, for a final enzyme concentration of 1 mM at 500 μL total volume. A KinTek RFQ-3 Quench-Flow Instrument was used for mixing reaction components. 2 mM KatG with substrate and ejected into a funnel filled with liquid nitrogen to freeze the reaction mixture on impact. The frozen reaction mixture was packed into the Mössbauer cup (LAContainer, Polyvial EP2100) attached by ½ inch inner diameter vinyl tubing to the end of a custom glass funnel using a custom-built packing utensil in liquid nitrogen. The Mössbauer cups were then caped with silicon stoppers for storage in liquid nitrogen until analysis.

3.3. Results and Discussion

Comparison of heme synthetic protocols

The products of the three synthetic protocols were directly compared using UV-visible spectroscopy (Fig. 3.7). Each synthesis yielded a product with slightly different spectra. Notably, two of the three protocols, namely Caughey and Adler, generated products with strong absorption features at wavelengths below 300 nm.

The indistinct absorbance ≤ 300 nm in these two spectra also correspond with a general increase in absorbance progressing from the visible to the ultraviolet which is indicative of light scattering; this could be due to the presence of insoluble particulate matter, organic solvent in solution, or degradation of the heme product. Both synthetic products were re-washed with volatile solvents and then dried under vacuum in attempts to displace, wash out, and ultimately remove any lingering organic solvents from the recovered product. These attempts were not successful to remove the contributing background components in the recovered products. In contrast, the product from the Erdman synthesis does not seem to have these types of spectral features below 300 nm. Additionally, there are more defined peaks in the visible region of the Erdman product spectrum (Fig. 3.7). These distinct peaks may be indicators that PpIX is still present in the product recovered from the synthesis. Perhaps most noteworthy from the comparison of these syntheses is the distinct features of the absorption maxima (350 – 400 nm region).

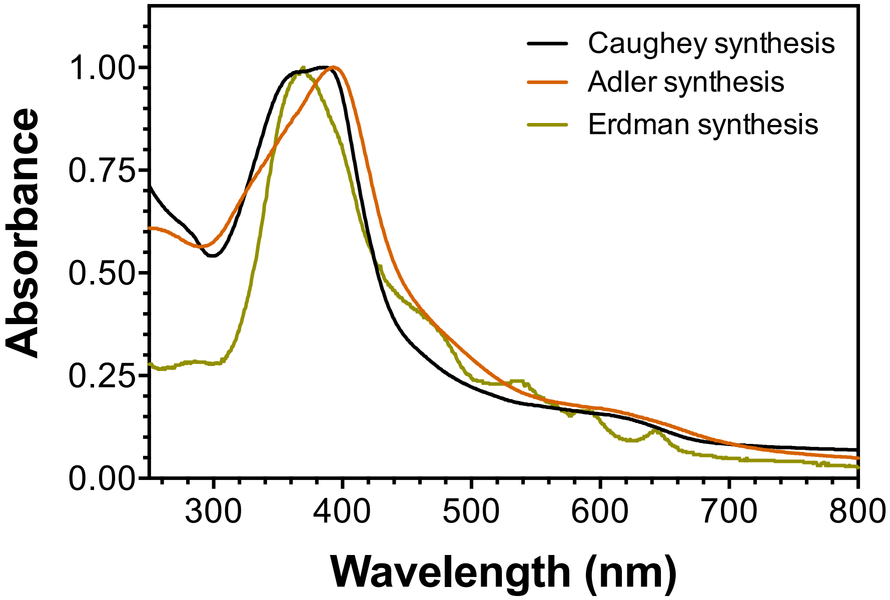

Figure 3.7. Spectral comparison of products from various heme syntheses. The three attempted synthetic methods were tested and their respective products are presented above.

Comparison of synthesized heme and commercial heme

The Caughey synthesis yielded a product with an absorption maximum and spectral line shape most similar to commercial preparations of hemin (Fig. 3.8). The Erdman synthesis was next closest to the commercial heme target. When comparing the Caughey and Adler synthetic products to commercial heme and PpIX by Fourier-transform infrared resonance (FTIR) spectroscopy, it appears that the Caughey product may exhibit features similar to the PpIX sample ~3400 cm^{-1} (Fig. 3.9). This feature, as it is mainly present in the PpIX sample, may pertain to the two pyrrole protons that are absent upon chelation of Fe in the heme porphyrin, and the presence of these features in the Caughey protocol may indicate trace presence of unchelated PpIX. Analysis by mass spectrometry, however, shows that product recovered is consistent with commercial heme ionization (Fig. 3.10). Additionally, the synthesized heme exhibits MS ions consistent with the incorporation of ^{57}Fe.

Reconstitution of aKatG with synthesized heme

The quality of heme product from Caughey synthesis was tested by performing parallel reconstitutions of purified apo KatG with this heme and commercial heme. The distinctions in the Soret (γ) band between the two reconstitutions is striking (Fig. 3.11). Reconstitution with commercial heme resulted in a purity index (Abs_{406}/Abs_{281}) of 0.373 and a Soret band with a λ_{max} at 406 nm. These features are highly similar to the KatG expressed in the presence of heme and purified in its mature form. In contrast, the reconstitution with the Caughey synthetic product resulted in a purity index of 0.167 and a

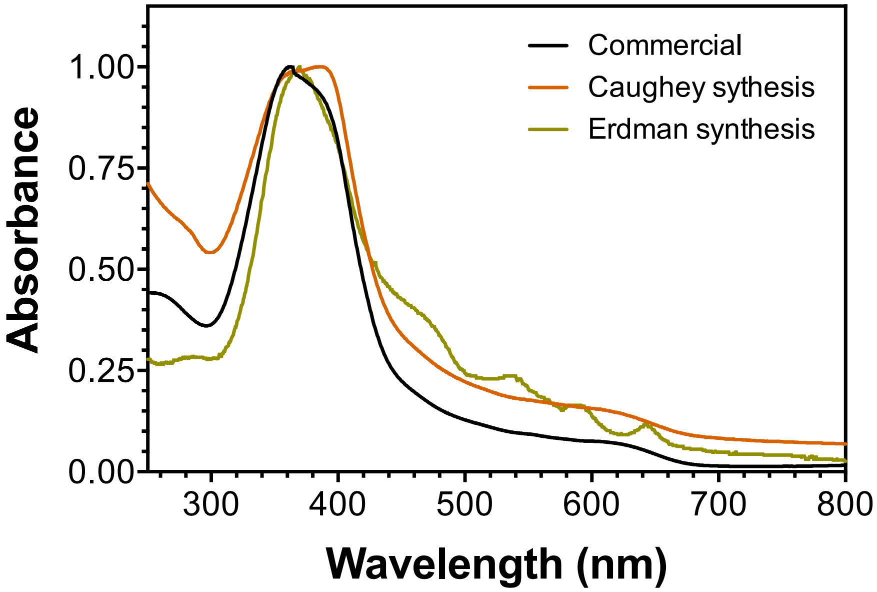

Figure 3.8. Comparison between commercial heme and synthesized heme. The heme spectra where normalized to their respective absorption maxima.

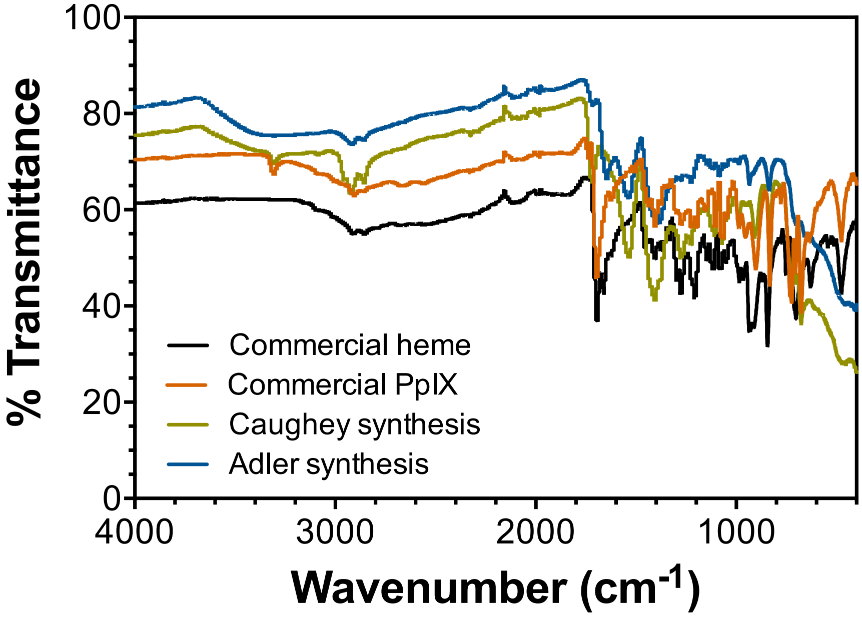

Figure 3.9. Comparison of commercial heme, PpIX, and synthesized heme by FTIR.

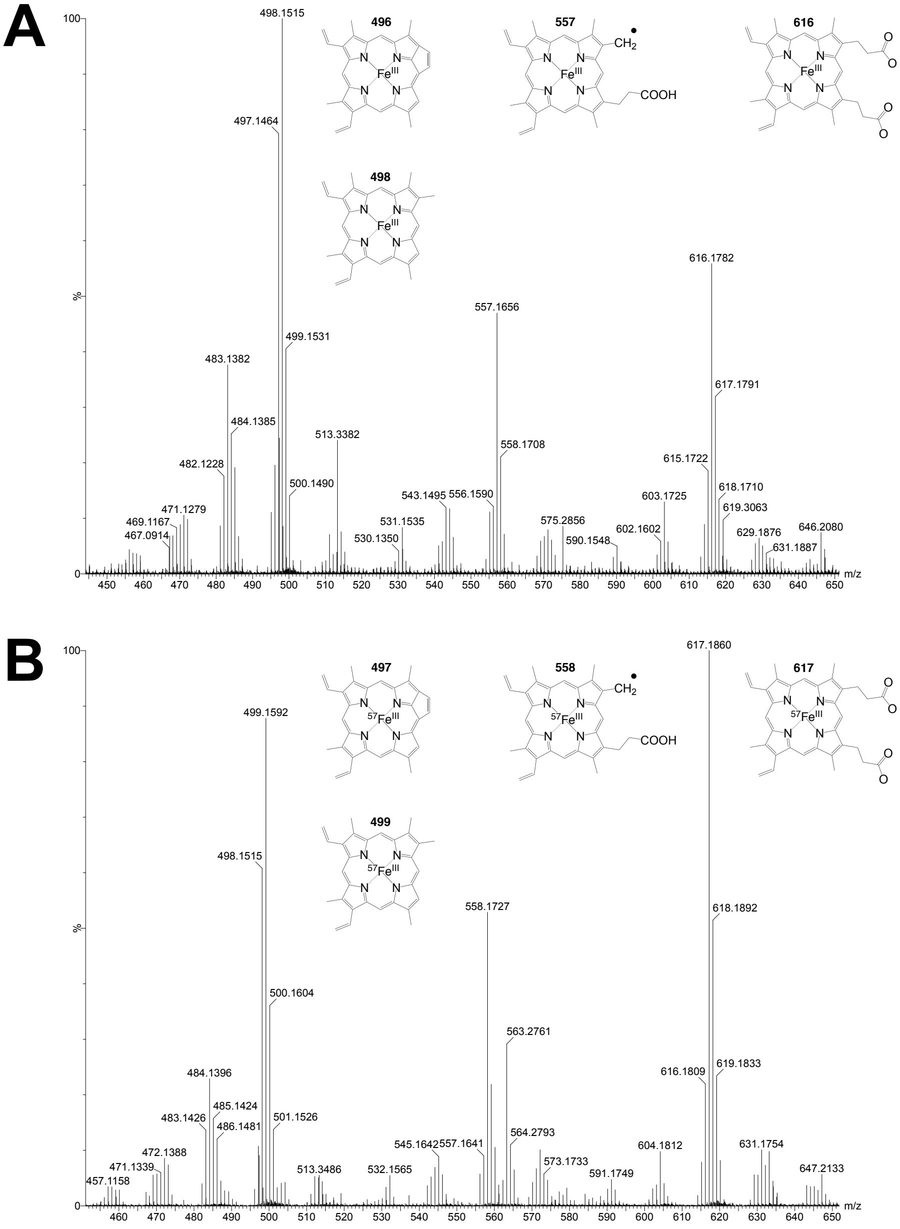

Figure 3.10. Mass spectrometry analysis of commercial heme and ^{57}Fe-enriched heme. Analysis of ^{57} Fe-enriched heme by mass spectrometry shows typical fragmentation for heme and indicates the proper shift in m/z corresponding to isotope enrichment (7).

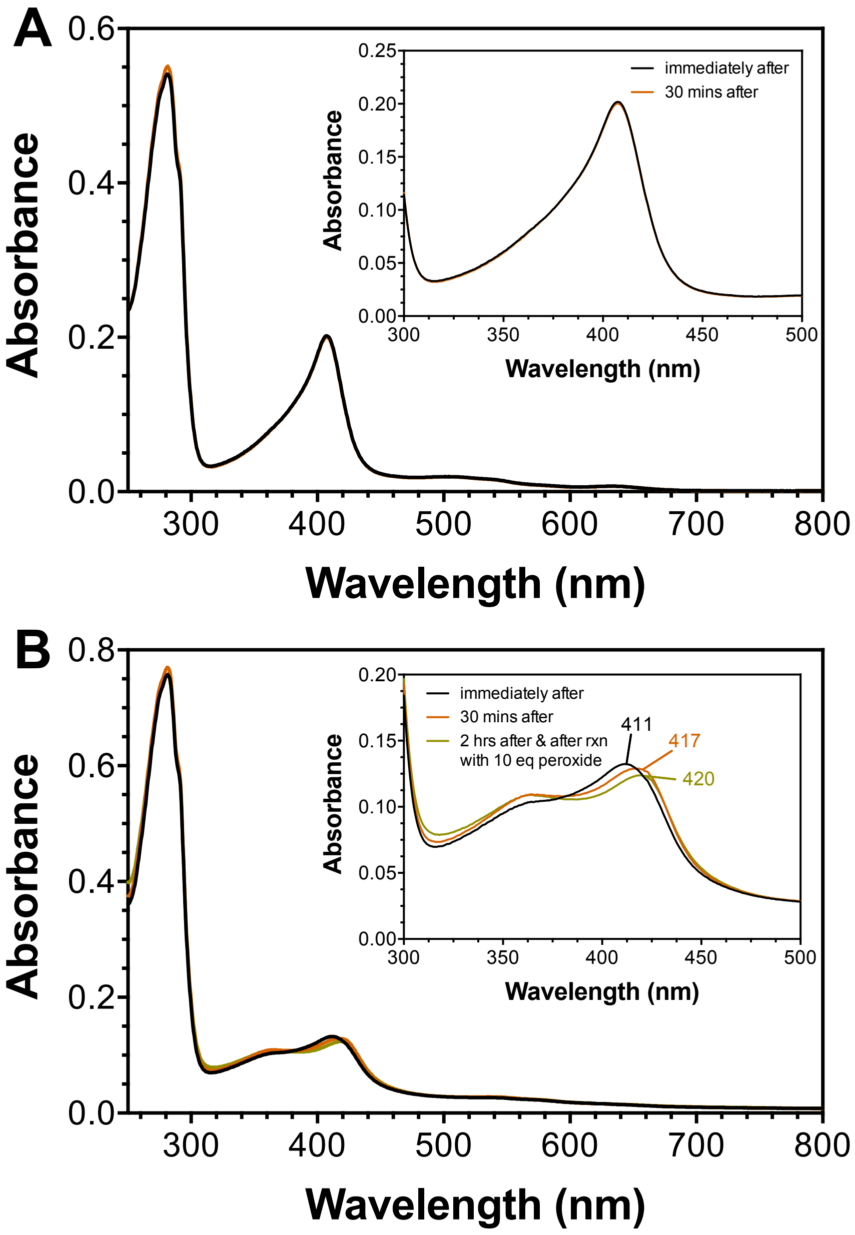

Figure 3.11. Contrast of KatG reconstitution with commercial heme and synthesized heme.

Soret peak maximum around 420 nm. In this case, it isn’t even clear if the absorption features from 350 – 420 nm are indicating incorporation of the synthesized heme into the active site or simple adventitious binding of the heme to the protein. Reconstitution with the heme prepared using the Erdman synthesis resulted in a KatG protein with a Soret band at 408 nm with a purity index of 0.316 and with excellent catalase activity (Fig. 3.12).

Heme synthesis by ferrochelatase

The reactions of heme from ferrous acetate and PpIX using either *wt* and F110A ferrochelatase did not result in large yields of heme. First, synthesis of heme by F110A was tested in the presence and absence of β-mercaptoethanol (Fig. 3.13) as described by Najahi-Missaoui and Dailey (113). The resulting product did have distinct features from the starting PpIX porphyrin ring, but an intense absorption feature at 552 nm resulted from a blue shift of the typical 580 – 590 nm peak indicates reaction between the thiol and the vinyl groups of PpIX (114). In previous studies this artifact is not observed with mesoheme where the vinyl groups are absent. Because of this, further reactions with thiols present were not attempted, even anaerobically. Ferrochelatase *wt* was chosen for subsequent heme biosynthetic reactions because the generated heme product can be released from the active site. The F110A ferrochelatase variant, once facilitating metalation of the porphyrin macrocycle, binds the heme tightly, limiting reactivity to one heme generated per active site. Though this can protect the heme from further reactions in solution, it also limits the amount of heme that can be synthesized to the amount of F110A ferrochelatase present. The first attempt of anaerobic synthesis by *wt* ferrochelatase on a small scale yielded spectral features that were consistent with heme coordinated in the ferrochelatase active

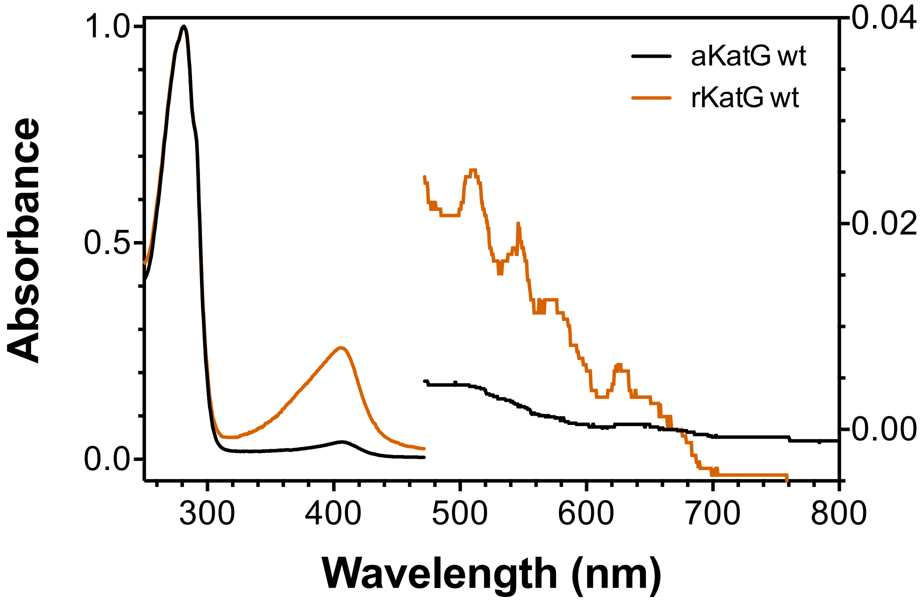

Figure 3.12 Reconstitution from heme recovered from Erdman synthesis.

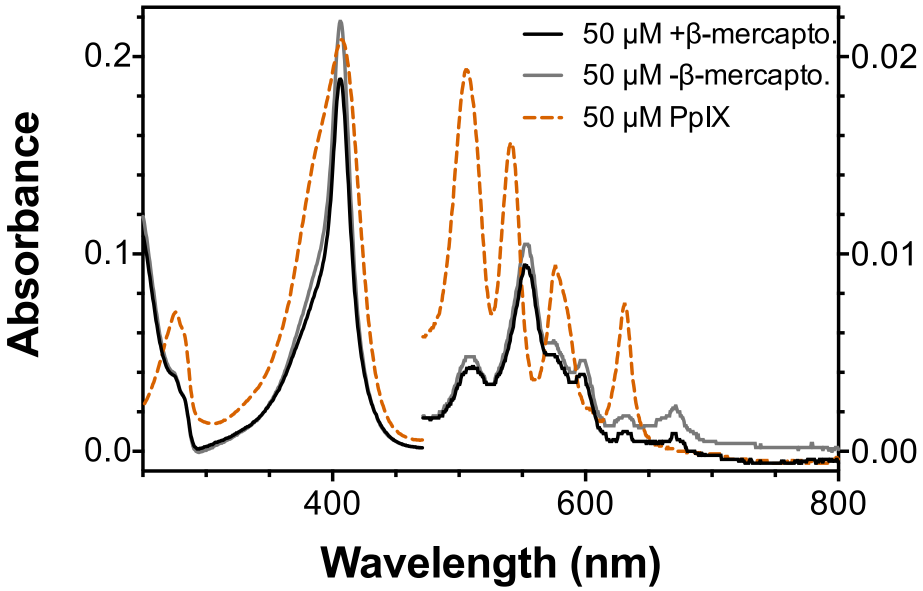

Figure 3.13. Heme synthesis by ferrochelatase F110A with β-mercaptoethanol. Reaction was performed with 1 µM ferrochelatase F110A, 50 µM PpIX, 50 µM Fe with 0.1 mg/mL ascorbate in solution, and 1 mM β-mercaptoethanol.

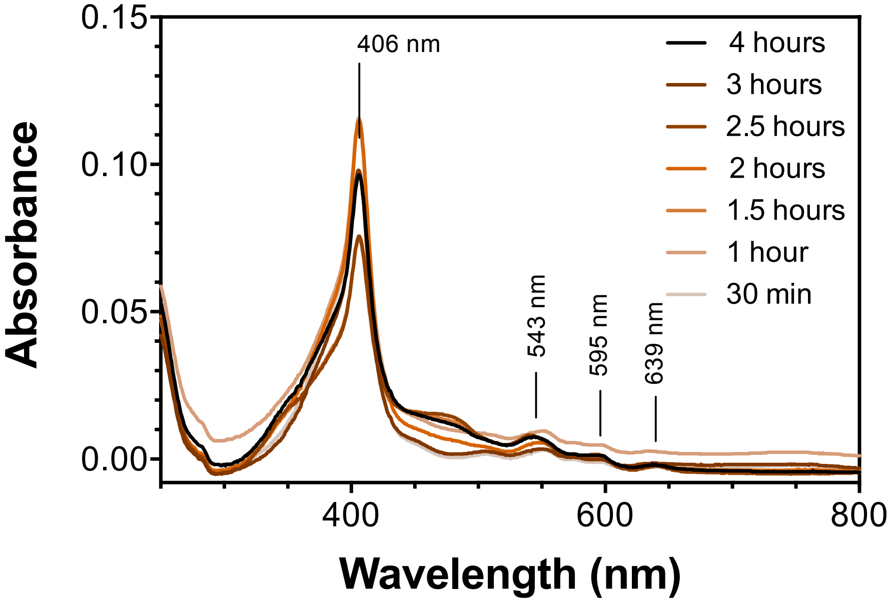

Figure 3.14. Heme synthesis by ferrochelatase *wt* 75 µM Fe and PpIX (with ascorbate). Small-scale anaerobic reactions were performed with 1 µM ferrochelatase *wt*, 75 µM PpIX, and 75 µM Fe with 1 mg/mL ascorbate in solution over 4 hours incubation time. Spectra were collected by reacting with equivalent volumes of 2 N HCl to denature ferrochelatase enzyme.

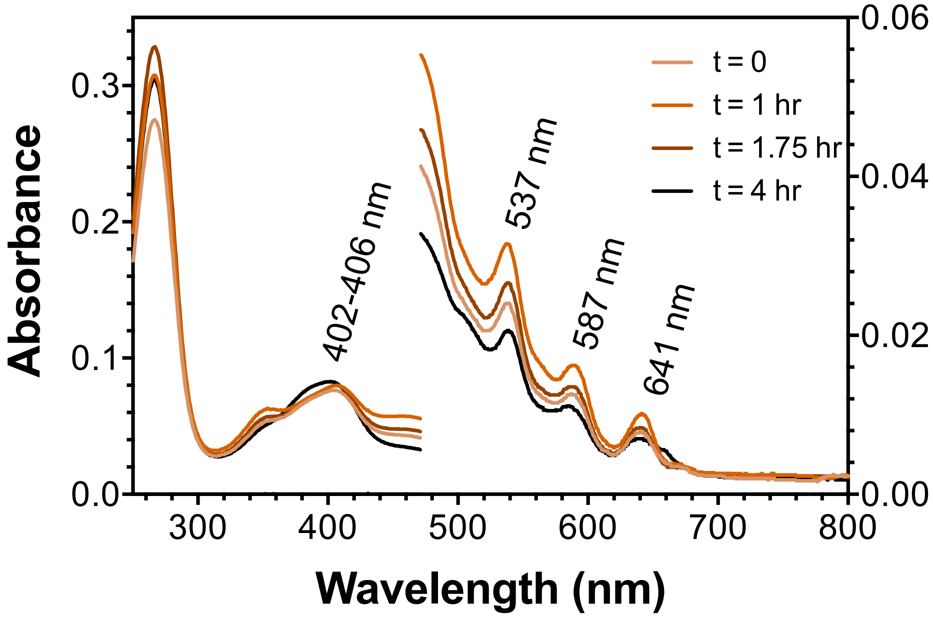

Figure 3.15. Heme synthesis by Ferrochelatase *wt* with 450 µM Fe and PpIX (ascorbate in solution). Larger-scale anaerobic reactions were performed with 6.4 µM ferrochelatase *wt*, 450 µM PpIX, and 450 µM Fe with 5 mg/mL ascorbate in solution over 4 hours incubation time. Spectra were collected by reacting with equivalent volumes of 2 N HCl to denature ferrochelatase enzyme. Recovered solution from ferrochelatase reaction was added to solution with apo KatG to encourage heme intake.

site (Fig. 3.14). A larger-scale anaerobic synthesis of heme by *wt* ferrochelatase was performed in hopes of accumulating enough heme product to recover from the reaction and use for reconstitution of KatG. Figure 3.15 shows the resulting product from the reconstitution of apo KatG using the heme product synthesized by *wt* ferrochelatase. The heme was recovered by subjecting the ferrochelatase reaction to anaerobic separation by size exclusion chromatography, but the spectra after reconstitution of apo KatG indicates that perhaps not all the ferrochelatase was successfully removed from the reaction and therefore the resulting spectra in Figure 3.15 could simply be overlapping heme-bound *wt* ferrochelatase and apo KatG.

Purified KatG from expression with δ-ALA and enriched Fe salt

Isotopic enrichment of KatG was also attempted by encouraging biosynthesis of ^{57}Fe-enriched heme within the *E. coli* cells during expression by the addition of δ-ALA and ferrous ammonium sulfate. The protein purified from such expressions yielded protein with reasonable purity indices of 0.3924 for natural abundance Fe expression and 0.3144 for expression with ^{57}Fe-enriched salt (Fig. 3.16). This method has yielded KatG with the highest purity index of all methods attempted thus far, and the resulting protein exhibits activity closest to KatG expressed in the presence of commercial heme and purified in its mature form. Interestingly, however, the yield of the mature protein recovered from expression with δ-ALA and Fe^{II} salt are very low, and even lower when the isotopically labeled Fe is added to the culture (28 nmols/expression L with ^{57}Fe as opposed to 89 nmols/expression L with the naturally abundant Fe salt).

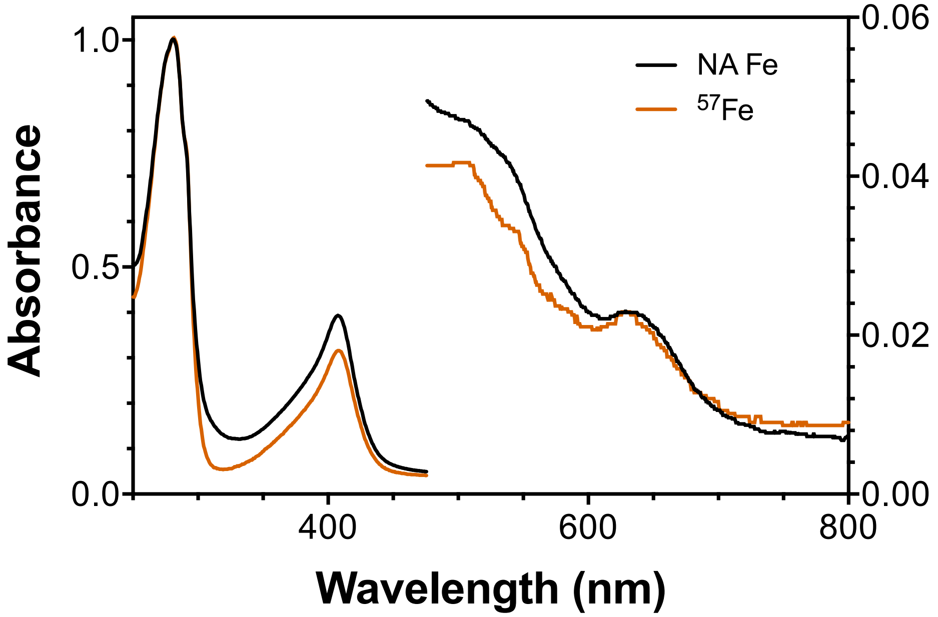

Figure 3.16. KatG purified from expression with δ-ALA and Fe salt additives. The KatG purified from expression with addition of δ-ALA and either natural abundance (black) or ^{57}Fe-enriched (orange) ferrous ammonium sulfate produces KatG at similar yields and purity indexes.

3.4. Conclusions

The enrichment protocols that yielded ^{57}Fe-enriched enzyme with the highest activity and proper heme coordination were reconstitution with heme synthesized by the Erdman procedure and *in vivo* synthesis of ^{57}Fe-enriched heme (i.e., inducing the cultures with δ-ALA and ^{57}Fe salt). Though both protocols yield active enzyme, the data suggest that the best method for enriching KatG with ^{57}Fe for Mössbauer spectroscopy is the Erdman synthetic protocol. Not only does reconstitution with the Erdman synthetic product yield more active enzyme, but also has a potential for higher heme incorporation. The purity index value (i.e., RZ value) for the Erdman reconstitution in Fig. 3.12 is lower than that presented in Fig. 3.16, but this is most likely because the heme concentration of the Erdman synthetic product was overestimated due to presence of unreacted porphyrin. Upon further optimization of the synthetic protocol and separation of the chelated heme from unreacted protoporphyrin IX, the heme concentration can be calculated more accurately, resulting in higher heme incorporation. Furthermore, utilization of the Erdman method for heme synthesis should result in less loss of ^{57}Fe-enriched product to non-target proteins (i.e., proteins other than KatG). The ^{57}Fe-enriched salt added to the bacterial cultures cannot be ensured to only be used for the synthesis of ^{57}Fe-enriched heme. The high demand for Fe by growing bacterial cultures, especially in an Fe-deficient media, almost assures the uptake and usage of ^{57}Fe for purposes other than heme synthesis. By adding ^{57}Fe-enriched heme (e.g., Erdman synthetic product) to the bacterial cultures instead of ^{57}Fe salt, the destination of the precious, isotopically enriched product can be narrowed heme-requiring enzymes, of which KatG should be the most abundant. Though this protocol would not entirely eliminate the loss of isotopically enriched product to non-KatG proteins, it would result in less loss of ^{57}Fe. Lastly, the use of ^{57}Fe-enriched heme prepared by the Erdman synthesis enables KatG to be reconstituted with heme either during overexpression or after purification. This flexibility in enzyme preparation enables more than just the catalatic mechanism of KatG to be explored by Mösbauer spectroscopy. As will be explained in the next chapter, incorporation of the heme cofactor after purification of KatG can allow for the mechanistic determination of the autocatalytic biosynthesis of KatG's unique protein-derived cofactor.

Overall, utilizing the Erdman protocol for preparation of ^{57}Fe-enriched heme is the ideal method for preparing KatG enzyme for Mössbauer spectroscopy. This method bypasses the need for expression in an Fe-deficient medium which will substantially decrease preparation time for expressions, supports more focused ^{57}Fe enrichment within the cultures, and enables flexibility in KatG sample preparations which would allow for multiple mechanisms to be explored by Mössbauer spectroscopy.

Chapter Four

Toward Mechanistic Determination of the Autocatalytic Biosynthesis of the MYW Cofactor in *Mycobacterium tuberculosis* KatG

4.1. Introduction

Catalase-peroxidase (KatG) is a bifunctional enzyme of the peroxidase-catalase superfamily of heme peroxidases. KatG's robust catalase activity is imparted by a unique post-translational modification between three residues near the active-site heme. These residues include an active-site Trp (W107), a Tyr (Y229) on a KatG-conserved loop structure, and a near-by Met (M255) residue undergo covalent linkage after reaction with peroxides in the presence of heme (*M. tuberculosis* numbering) (Fig. 4.1). The presence of this Met-Tyr-Trp structure, confirmed by x-ray crystallography (72, 119) and mass spectrophotometric analyses (86, 120, 121) to be conserved across all species of KatG, is imperative to the catalase activity of KatG, and therefore is considered a protein-derived cofactor, specifically the MYW cofactor. According to descriptions of KatG's catalase cycle, a ferryl-oxo porphyrin cation radical intermediate (Fe^{IV}=O[por]$^{\bullet+}$) is formed by an initial reaction of ferric KatG with H_2O_2. The MYW cofactor then enters the mechanism by reducing the porphyrin to generate the Fe^{IV}=O[MYW]$^{\bullet+}$ state. Presumably, the rate of intramolecular electron transfer is very rapid. The features of a Fe^{IV}=O[por]$^{\bullet+}$ state has not been observed by either UV-vis or EPR-based rapid reaction techniques.

An Arg residue (R418) resides near the MYW adduct, and its guanidinium side chain, interacts with the phenolic oxygen of Y229, at pH values particularly higher than

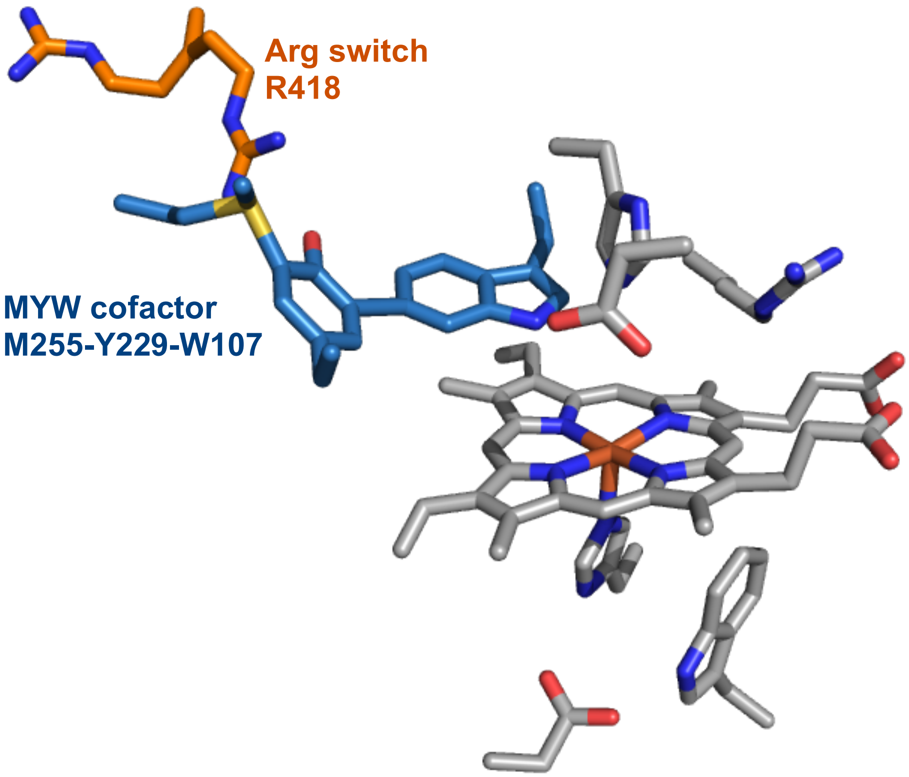
Arg switch
R418
MYW cofactor
M255-Y229-W107

Figures 4.1. Interaction between MYW cofactor and Arg switch within KatG active site. The MYW cofactor (blue) is positioned between KatG's heme cofactor and the electronic control of the enzyme, the Arg switch (orange). This placement allows for facile oxidation of the protein-derived cofactor during catalase turnover.

the Tyr's adjusted pK_a of 6.5 and is directed away from the MYW cofactor (Fig. 4.1) (122). At pH values below the apparent pK_a, the Arg side chain is pH-dependent alternation between the two conformations which gives the residue its nickname, the Arg switch. The Arg switch is considered a modulator of the active-site electronics responsible for directing electron flow within the KatG. Just as for catalase activity, the autocatalytic biosynthesis of the MYW cofactor involves oxidation of residues near the heme center. As such, it is not implausible to suppose the Arg switch would play a role in the formation in the MYW adduct as it does for catalase activity. The R418N variant of KatG was investigated to elucidate any role the Arg switch may play in the formation of the MYW cofactor.

The mechanistic details of the MYW cofactor autocatalytic biosynthesis remain undetermined despite its essential contribution to the activity of KatG. A proposed mechanism for its formation is presented in Figure 4.2. It has been proposed that the MYW cofactor is formed by two reactions with a peroxide (e.g., hydrogen peroxide or peracetic acid) involving several transient, protein-based radicals and two stable, covalent intermediates, the YW adduct and the quinoid form of the YW adduct (86, 120, 123). Despite general agreement of this mechanism within the KatG field, there is an experimentally reproducible discrepancy between the number of oxidizing equivalents proposed and actually required for MYW cofactor formation, specifically that the formation of the MYW cofactor is ~33% efficient (86, 120). The use of peracetic acid (PAA) as a two-electron oxidant for the formation of the MYW cofactor requires the use of 6 molar equivalents (86, 120). Despite a number of preliminary studies on the formation of KatG's MYW cofactor, the heme- and protein-based intermediates have yet to be experimentally determined.

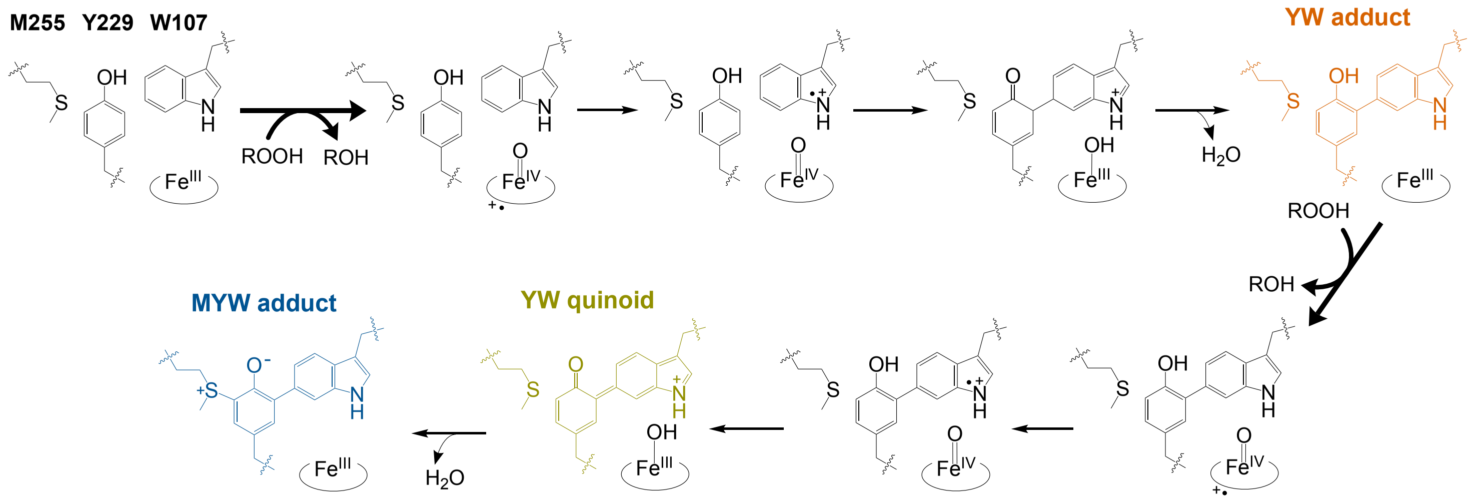
M255
Y229
W107
OH
N
H
Fe^{III}
ROOH
ROH
O
Fe^{IV}
+•
H$_2$O
OH
YW adduct
YW quinoid
MYW adduct
O$^-$
+S
S

Figure 4.2. Proposed mechanism for autocatalytic MYW cofactor formation. The covalent linkage of M255, Y229, and W107 has been proposed to progress by two peroxide-dependent steps (bolded arrows) catalyzed by high-valent heme species. Three stable protein-based intermediates are predicted to have distinct optical features: the YW adduct (orange), the quinoid rearrangement of the YW adduct (yellow), and the full MYW adduct (blue).

The heme-dependent nature of the MYW cofactor biosynthesis, requires special preparation of KatG for analysis. Typical KatG preparation involves addition of heme to the expression cultures for heme insertion during expression, yielding mature KatG (mKatG) upon purification. Therefore, to monitor the formation of the MYW cofactor, an enzyme preparation which does not allow heme to be present within the enzyme until after purification. This can be accomplished by expression of apo KatG (aKatG) followed by purification and completed by heme reconstitution of aKatG. Such a reconstitution procedure is not simple but generates reconstituted KatG (rKatG) where heme is in place, but due to the exclusion of peroxides, the MYW cofactor is not yet formed (Fig. 4.3). As KatG is a fairly large protein of 80 kDa, it does not respond well to attempts of denaturation or unfolding, though given the small size of its active-site channel unfolding will be necessary to some degree for KatG reconstitution. Given this difficulty and others not fully understood, previous expression protocols for apo protein and reconstitution protocols for KatG have not resulted in high yields required for mechanistic investigation.

Here, we utilize a highly efficient reconstitution procedure that allows for successful heme incorporation into purified aKatG. This reconstitution protocol, indeed, results in KatG with heme bound, but lacking the MYW cofactor (rKatG), in contrast to KatG protein where heme has been incorporated during expression resulting in formation of the MYW cofactor in the purified enzyme (mKatG). Additionally, we present estimates for UV absorption and fluorescence emission maxima for the three adduct intermediates for targeted spectrophotometric detection of the adduct intermediates. Obstruction from the strong heme absorption features limit the feasibility for experimental identification of the spectral features of the MYW adduct intermediates. Our methods have been confirmed by

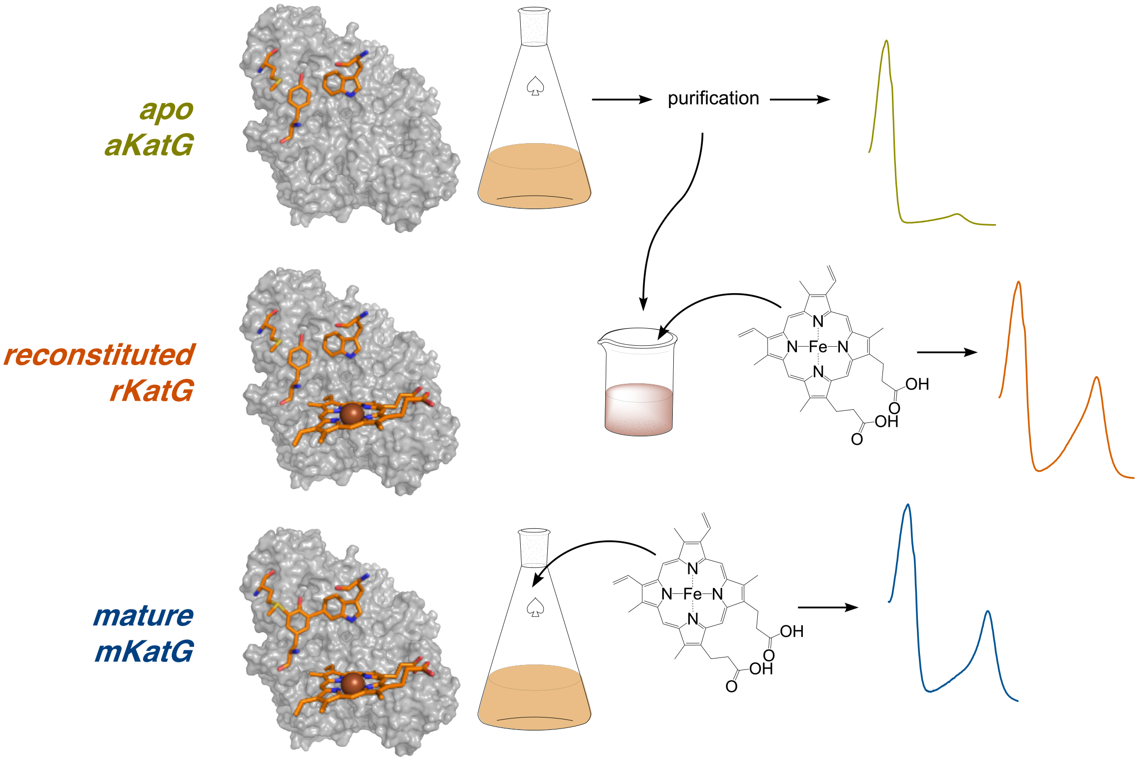
apo
aKatG
purification
reconstituted
rKatG
N
N
Fe
N
N
OH
O
OH
O
mature
mKatG
N
N
Fe
N
N
OH
O
OH
O

Figure 4.3 Schematic representation of KatG preparation. KatG expressed in the absence of heme (apo or aKatG) lacks both heme and MYW cofactor (yellow). Reconsituted or rKatG, prepared by reconstituting aKatG with heme after purification, still lacks the MYW cofactor, but has its heme cofactor in place as evidenced by protein-bound heme spectra (orange). KatG expressed in the presence of heme (mature or mKatG) results in heme incorporation during expression and subsequent formation of the MYW cofactor, presumably due to the presence of endogenous peroxides generated by host cells (blue).

LC-MS/MS and agree with previously published work. Lastly, we present promising, preliminary stopped-flow data that suggest the MYW cofactor formation process may be able to be monitored spectrally despite the presence of overwhelming heme spectral features. These stopped-flow studies also suggest that R418 may play an accessory, but not essential role in the formation of the MYW cofactor.

4.2. Materials and Methods

Site-directed mutagenesis for R418N KatG variant

Site-directed mutagenesis to prepare a plasmid for expressing R418N was performed by the "Round-the-Horn" method (83). The template for mutagenesis was pMRLB11, a pET23b-derived plasmid bearing the *M. tuberculosis katG* gene and was obtained from the TB vaccine Testing and Research Materials Contract at Colorado State University. The forward primer designed for the R418N substitution (5'-CAC**AAC**GATATGGGTCCCGTTGCGA-3') a codon replacement (i.e., R for N) (bold) as well as a mutation designed to introduce a diagnostic restriction site for PshAI (underlined). The reverse primer (5'-GATCAGCTTGTACCAGGCCTTGGCGAA-3') required no substitutions. Both primers were modified to include 5'-phosphoryl groups, allowing for blunt-end ligation following PCR. All PCR reactions were carried out using Phusion High-Fidelity polymerase in GC buffer-containing Master-Mix and 3% DMSO. All PCR products were initially treated with *DpnI* (New England Biolabs, Ispwich, MA) to degrade the starting template and then ligated using T4 DNA ligase. Ligation products were used to transform *E. coli* XL-I Blue cells by a standard heat shock protocol. Transformants were selected based on ampicillin resistance. Success of transformation was confirmed by PshAI digestion. Candidates that passed this screening were sent for full DNA sequence analysis (Laragen Sequencing, Culver City, CA).

Expression of apo KatG

Apo KatG was overexpressed in BL21 (DE3) *pLysS* cells transformed with a pET23b-derived plasmid bearing the *M. tuberculosis katG* gene and was obtained from the TB Vaccine Testing and Research Materials Contract at Colorado State University. Cultures were incubated at 37 °C in Miller LB broth in the presence of ampicillin and chloramphenicol with constant agitation to an OD_{600} between 0.45 and 0.47. Expression was then induced with 1 mM IPTG and the incubation temperature was lowered to 20 °C. Samples were withdrawn from cultures periodically throughout expression for later analysis. Following induction, cultures were incubated for 12 hours before harvesting by centrifugation at 4052 rcf for 20 mins. The resulting pellet was stored at -80 °C until purification. Successful overexpression of KatG was verified by expression analysis assay. Briefly, an aliquot of cells, collected from cultures throughout incubation times, were combined with equal volumes of cold 10% TCA to precipitate proteins. After centrifugation and drying precipitated protein pellets, samples were analyzed by SDS-PAGE.

Purification of apo KatG

The frozen cell pellet was resuspended in 50 mM phosphate, 200 mM NaCl, pH 7. The volume of resuspension buffer was 5 mL for every liter of expression culture. Phenylmethylsulfonyl fluoride (PMSF) (50 mM) was added (200 μL/expression L) as a serine protease inhibitor to the cell resuspension before homogenization using a glass tissue grinder. After homogenization, cells were lysed by sonication by 8 cycles (42 seconds on, and 42 seconds off) at 30% duty. Benzonase nuclease (2 μL/expression L) was then added to the cell lysate and incubated at 4 °C with constant stirring for four hours. The lysate was then centrifuged at 9922 rcf for 45 – 60 minutes at 4 °C to pellet cellular debris. The supernatant was retained and added to Ni-NTA resin previously equilibrated with 50 mM Tris, pH 8. The protein-resin mixture was incubated at 4 °C with gentle agitation for 12 hours. Solutions of 20, 40, 60, 75, 100, 200, and 500 mM imidazole in 50 mM phosphate, 200 mM NaCl, pH 7 were prepared as elution buffers. The KatG was observed to elute during column washes containing 40, 60, and 75 mM imidazole. These fractions were combined and concentrated using 30 kDa cutoff centrifugal filters to a volume of ~3 mL before the protein solution was passed through an Econo-Pac 10G desalting column (BioRad, #7322010) equilibrated with 5 mM phosphate, pH 7. The protein was then frozen for at least 12 hours before reconstitution.

Reconstitution of apo KatG or preparation of rKatG

Apo KatG was diluted to 100 μM in 5 mM phosphate, pH 7. A hemin stock solution was prepared in 0.1 mM NaOH solution. This heme stock solution was diluted with ddH_2O to a total volume that was half the volume of the 100 μM protein solution. The KatG to heme molar ratio desired in this mixture was 1:0.875. The heme solution was added slowly to the diluted KatG with constant, gentle mixing. The mixture was then incubated on ice for 30 minutes. 0.1 mM KP_i, pH 6.2 was then added to the protein-heme mixture to a volume twice that of the original 100 μM KatG solution. The protein was then incubated for 4-6 hours at 4 °C. KatG was then concentrated by centrifugal filtration using 30 kDa cutoff filters. The concentrated protein was then added to an Econo-Pac 10G desalting column to remove unincorporated heme and aggregated heme from the protein solution.

Purification of reconstituted KatG

After reconstitution, the protein is concentrated to ~ 1 – 2 mL in preparation for anion exchange chromatography. The reconstituted KatG was then loaded onto a Macro-Prep High Q support anion exchange column, and protein was eluted using a linear gradient of increasing NaCl for elution. Fractions from anion exchange chromatography with least contamination confirmed by SDS-PAGE analysis and the highest purity value (Abs_{406}/Abs_{281}) were combined and concentrated once more before storing the purified enzyme. The final spectrum and activity of purified enzyme were tested to ensure vitality before storing at -80 °C.

Tryptic digestion and LC-MS detection

KatG *wt* and variants were digested using Promega Sequencing-grade modified trypsin (#V5111) at 200:1 KatG to protease ratio in 50 mM ammonium bicarbonate, pH 8 for 3 hours at 37 °C. The digest was quenched with 20 μL glacial acetic acid and then stored at 4 °C prior to analysis. When pre-treated with peroxide, KatG was reacted with peroxide (5 equivalents PAA, 5 equivalents H_2O_2, or 50 equivalents H_2O_2) for 10 – 30 minutes before addition of trypsin. Analysis was performed at the Auburn University Mass Spectrometry Center housed in the Department of Chemistry and Biochemistry on an ultra-performance LC system (ACQUITY, Waters Corp., USA) coupled with a quadrupole time-of-flight mass spectrometer (Q-Tof Premier, Waters) with electrospray ionization (ESI) in positive mode using Masslynx software (V4.1). 10 μL injections of the solutions were made onto a C18 column (Waters UPLC BEH C18 2.1x50 mm, 1.7 μm) with a 300 μL/minute flow rate of mobile phase solution A (water with 0.1% formic acid) and solution B (95% acetonitrile, 5% water and 0.1% formic acid) beginning at 3% B, held for 2 minutes, then linear ramp to 50% B in 58 minutes, with a linear ramp to 100%B at 62 minutes, with hold for 5 minutes and return to 3% B in 3 minutes with 10 minutes of re-equilibration. The capillary voltage was set at 3.1 kV, the sample cone voltage was 30 V, and the extraction cone was 4.3 V. The source and desolvation temperature were maintained at 125 and 300 °C, respectively, with the desolvation gas flow at 600 L/hour. The MS scan was 1.0 second long from 100 to 4000 m/z with a 0.02 second inter-scan delay using the centroid data format. MS/MS scans were 0.5 to 1.0 second long with a 0.02 second inter-scan delay with a collision energy ramp from 20 V to 40 V. The lock mass was used to correct instrument accuracy with a 2 ng/μL solution of Leucine Enkephalin (Bachem part number 4000332).

Predictions of absorption and fluorescence emissions

Density functional theory (DFT) calculations were performed using Gaussian 16 to predict absorption features of the protonated and unprotonated states of the MYW and YW adducts as well as the quinoid YW adduct intermediate. Likewise, time-dependent density functional theory (TD-DFT) calculations were performed using Gaussian 16 to predict the fluorescent emission values for the same adducts (124). DFT and TD-DFT calculations were carried out using the B3LYP hybrid functional with a G-31+G (d,p) basis set (125, 126). All calculations were verified to have no imaginary frequencies.

Stopped-flow spectroscopy on rKatG proteins

Heme spectral transitions and other spectral feature changes of rKatG were monitored by a PC-upgraded SX18.MV rapid reaction analyzer from Applied Photophysics (Surrey, UK). In all experiments, 3 μM enzyme concentration was utilized. The reactivity of rKatG proteins (i.e., *wt* and R418N) were compared to their mKatG counterparts when reacted against a range of H_2O_2 concentrations (e.g., 4 to 667 molar equivalents). Additionally, rKatG was pre-treated with low molar equivalents of PAA (3 – 5 equivalents) and then reacted with H_2O_2 to observe changes in heme intermediate transitions that may take place as compared to mKatG or rKatG reacted with H_2O_2 alone. Pre-treatments were carried out in 50 mM phosphate at pH 7, even if the reaction with H_2O_2 was carried out in 50 mM acetate at pH 5. This was to ensure stability of the protein during exposure to PAA. The oxidation of ABTS was also monitored by stopped-flow over a range of H_2O_2 concentrations and 0.1 mM ABTS.

4.3. Results and Discussion

Reconstitution of aKatG

The incorporation of heme into purified aKatG was shown to be successful by direct comparison the heme Soret peak at 406 nm of rKatG and mKatG (Fig. 4.4). A 10-fold increase in purity ratio (Abs_{406}/Abs_{281}) from aKatG to rKatG was observed as a result of the reconstitution process (Table 4.1). Accordingly, our reconstitution process resulted in

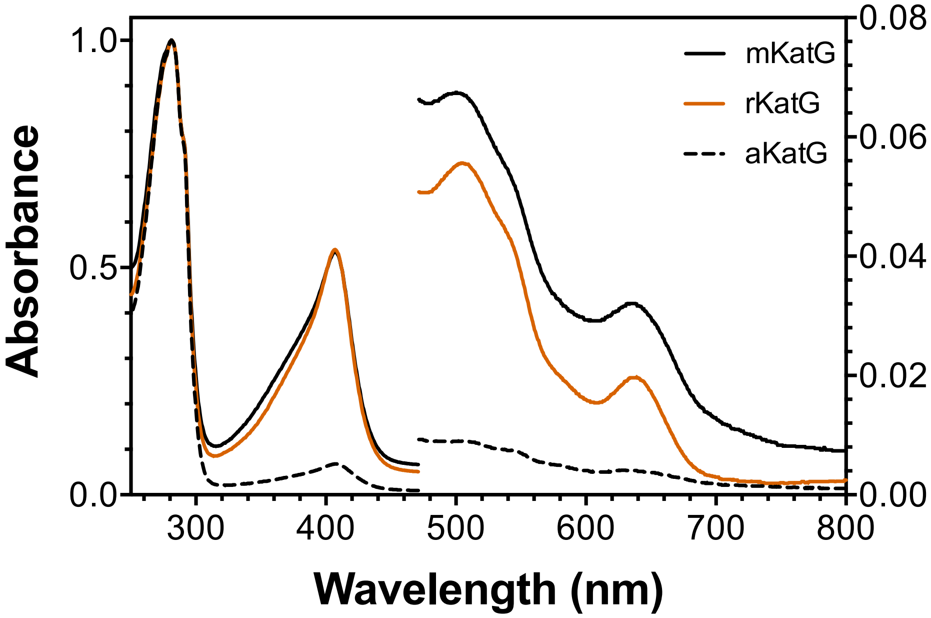

Figure 4.4. Comparison of heme incorporation methods. The normalized spectra of aKatG (dashed), rkatG (orange), and mKatG (black). Proper α, β, and γ (Soret) band of the heme spectrum at 645, 505, and 406 nm, respectively, confirm successful incorporation of heme in rKatG.

Table 4.1. Comparison of KatG proteins

	Purity ratio[a]	Spectral features	Yield of protein[b]
aKatG	0.0679	407 nm	500
rKatG	0.5098	407, 506, 639 nm	200
mKatG	0.5554	407, 502, 636 nm	40

[a] Purity ratio determined by dividing Abs at 407 nm by Abs at 281 nm. Ideal purity ratio = 0.5-0.6.

[b] Yield of purified protein provided as nmols KatG protein per L of expression culture.

protein capable of robust catalase activity comparable to mKatG, ensuring that the heme incorporation was successful (Table 4.1). Though the purified rKatG protein showed substantial heme incorporation and proper catalase activity, there are small spectral differences in the heme Soret peak between the ferric forms of the rKatG and mKatG preparations that indicate differences in heme coordination (Fig. 4.4). As purified, rKatG shows features more consistent with a high-spin (HS) 6-coordinate heme as evidenced by a narrower Soret band with a λ_{max} near 406 nm and a lesser contribution from a hypsochromic shoulder on the Soret peak, which is typical of 5-coordinate heme. This was supported by EPR spectra which show a great contribution from an axial state relative to a rhombic state (Fig. 4.5).

Reaction of rKatG with H_2O_2 results in changes in UV-visible spectral features (Fig. 4.6). Changes in the visible region of the H_2O_2-reacted rKatG spectrum do not look significantly different in character, however, the changes near the Soret peak are intriguing (Fig. 4.6 B and C). The distinct hyperchromic shift and narrowing of the Soret band of H_2O_2-reacted rKatG relative to mKatG indicates as mentioned above a greater population of HS, 6-coordinate heme in the rKatG. Additionally of interest is the increase in absorbance ~ 310 – 320 nm. This increase in absorbance is consistently observed when rKatG proteins are reacted with H_2O_2 or other peroxides and consistently, and furthermore there is no observed loss of absorbance in this region. Given the inherent absorptivity of residues like Trp and Tyr, we anticipate these spectral changes may be due to the formation of the MYW cofactor in the rKatG proteins.

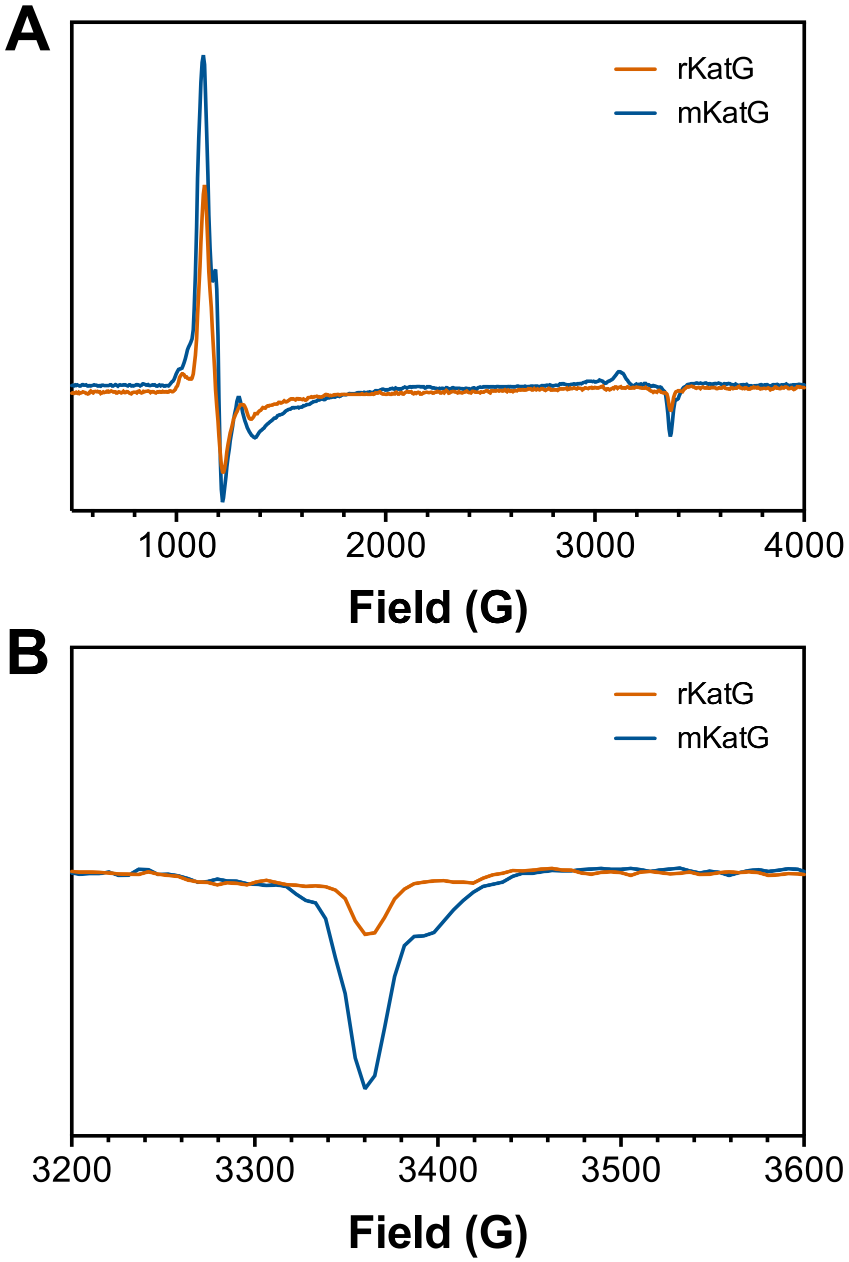

Figure 4.5. EPR comparison of heme incorporation methods. The typical mKatG (blue) heme EPR spectrum which demonstrates a mixture of rhombic and axial signal whereas the rKatG (orange) heme spectrum is more axial in character. These distinctions are most clear in the g ~2 region (B) where rKatG exhibits little contribution from a g=1.95 feature.

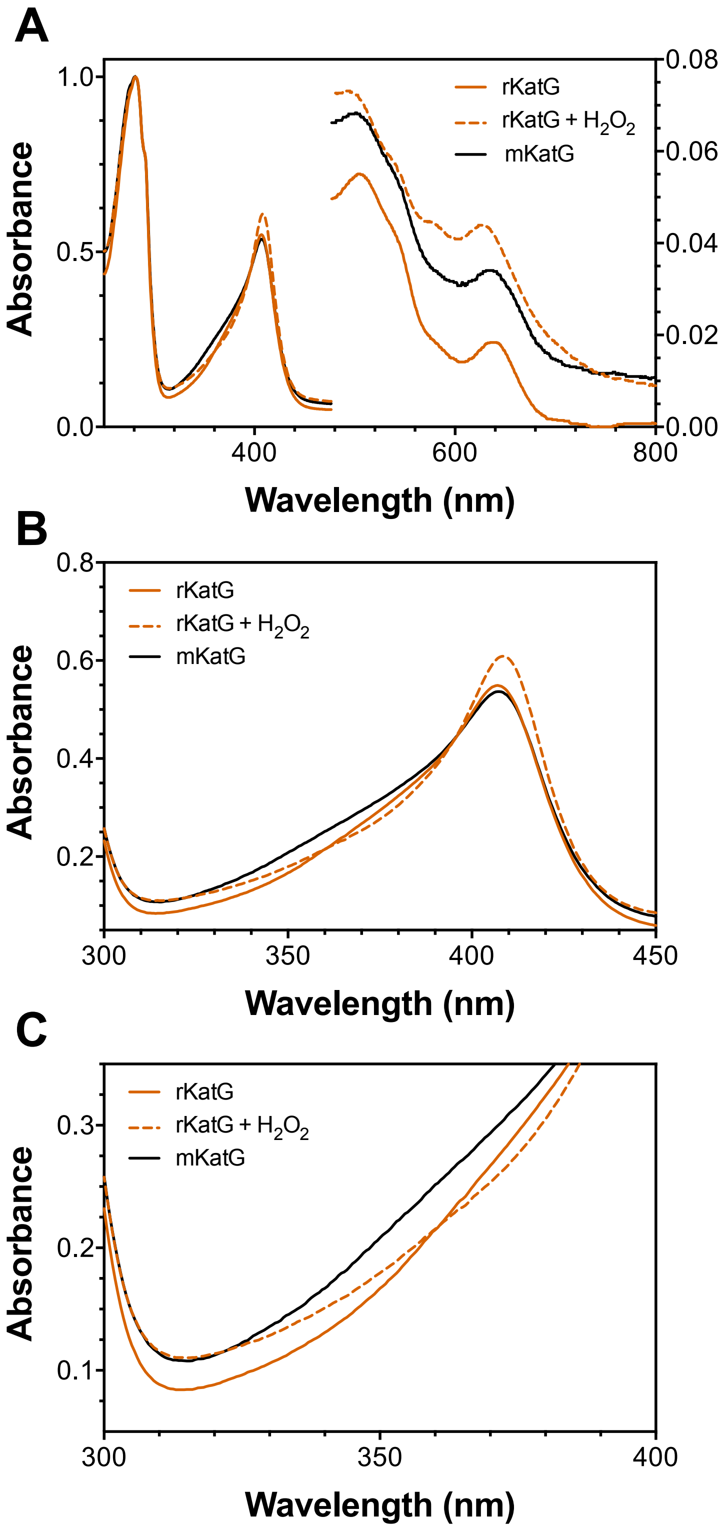

Figure 4.6. Changes in heme spectral features of rKatG upon reaction with H_2O_2. Comparison of mKatG (black), rKatG (orange), and rKatG reacted with 100 eq. H_2O_2 (dashed orange) demonstrate the minor distinctions of heme spectra across enzyme preparations.

Prediction of optical features of YW and MYW adducts

In order to inform detection of the MYW adduct within the rKatG and mKatG proteins, the UV-vis absorption and fluorescent emission characteristics of the MYW and YW adducts were calculated using computational methods. Figure 4.7 provides each adduct structures investigated and Table 4.2 provides the corresponding calculated λ_{max} for absorption and fluorescence emission of each adduct. Though these calculated values were derived from the adduct structures within a simple simulated solvent force-field, they are expected to be accurate within a range of ± 20 nm. The predicted λ_{max} for UV-vis detection of the protonated YW adduct is about 318 nm, and the protonated MYW adduct is about 390 nm. These predicted values are in agreement with previously reported LC data (86, 87). Additionally, these predicted values suggest that the reproducible increase in absorbance observed around 300 – 340 nm when rKatG proteins are reacted with peroxides may be an indication of MYW cofactor formation. Considering the heme Soret peak will greatly obscure any other absorption features ranging from 340 – 460 nm, the small changes in absorption observed from 300 – 320 nm may be the limit to visualizing the formation of the MYW cofactor within KatG by optical spectroscopy. However, the absorption of the MYW adduct should be unencumbered in the absence of heme and therefore during LC separations of KatG peptides, the MYW peptide should be distinctly visible. The predictions presented here proved useful when determining 330 nm as the best wavelength for detection of MYW adduct formation during LC-MS studies. In future studies, these predicted values can also be of use for the detection of various MYW adduct intermediates upon HPLC separation with a fluorescence detector.

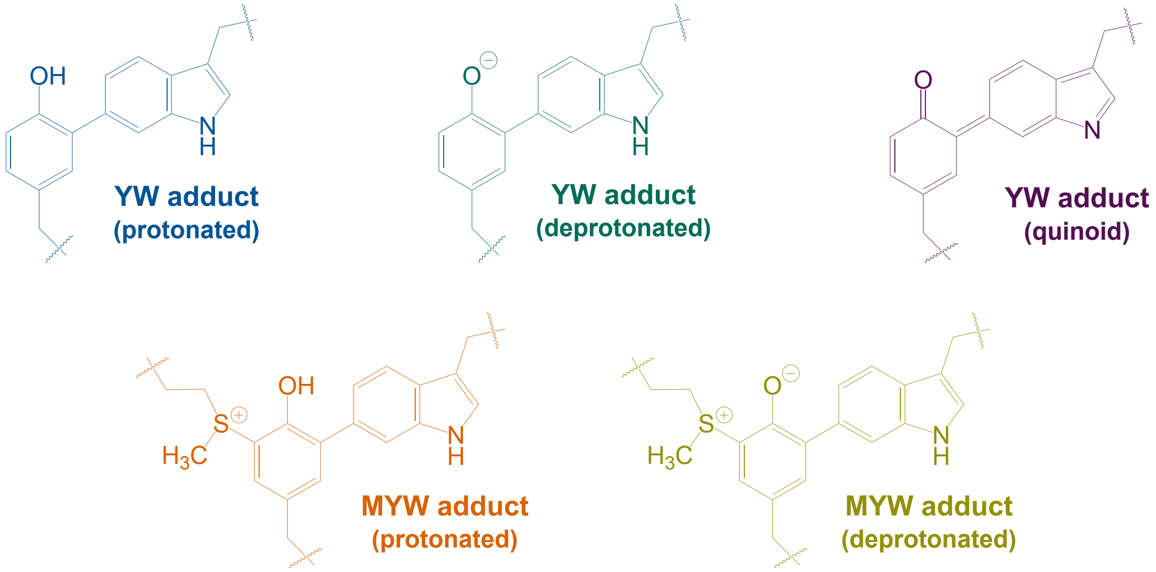
OH
N
H
YW adduct
(protonated)
O
N
H
YW adduct
(deprotonated)
O
N
YW adduct
(quinoid)
S
H3C
OH
N
H
MYW adduct
(protonated)
S
H3C
O
N
H
MYW adduct
(deprotonated)

Figure 4.7. Structures of YW and MYW adducts investigated for prediction of spectral features.

Table 4.2. Predicted YW and MYW absorption and emission values

Adduct	Visible absorption		Fluorescence emission	
	In H_2O[†]	No solvent[‡]	In H_2O[†]	No solvent[‡]
Protonated YW	318 nm	311 nm	371 nm	493 nm
Deprotonated YW	458 nm	460 nm	1081 nm	488 nm
Quinoid YW	804 nm	579 nm	800 nm	744 nm
Protonated MYW	390 nm	406 nm	747 nm	747 nm
Deprotonated MYW	354 nm	338 nm	747 nm	448 nm

[†] Computational jobs were carried out using a solvent forcefield to estimate solvation by water.
[‡] Computational jobs were carried out without using a solvent forcefield.

Mass spectrometric detection of MYW cofactor

Before determining the exact steps and the kinetics of this biosynthetic mechanism, it must first be confirmed that the rKatG protein is indeed lacking the MYW adduct and that mKatG indeed contains the formed MYW adduct upon purification. Comparison of LC chromatograms of trypsin-cleaved mKatG, rKatG, and aKatG monitored at 310 – 330 nm are consistent with this hypothesis (Fig. 4.8). Not only did the LC chromatograms confirm comparable heme incorporation for rKatG from our reconstitution procedure, but also indicated that rKatG and aKatG possessed a much lower absorbance than observed for mKatG. Detected MS ions corresponding to peptides eluting at 32 min indeed agree with the assignment of this peak as derived from the MYW cofactor (86, 120, 121). Figure 4.9 and Table 4.3 list the specific MS ions detected and their corresponding peptide structure. The full MYW cofactor, including the tryptic peptides of each MYW adduct member, was detected in a number of charged states (5+, 6+, 7+, and 8+) with a parent ion of 6880 m/z. Consistent with literature, fragmentation of the MYW adduct between the γ-carbon and the sulfur atom of the Met residue was also detected (86). This in-source fragmentation resulted in the detection of a 4861 m/z parent ion – the YW adduct with a thiomethyl group attached (including the tryptic peptides of both the Tyr and Trp adduct members) and the corresponding 2103 m/z parent ion – the M255-bearing tryptic peptide without the thiomethyl group. In particular, tandem MS analysis of 1147.6 (6+) m/z ion supports the assignment of the 672.3 (3+) m/z ion and the 1216.3 (4+) m/z ion as in-source fragments of the full MYW adduct cleaved at the sulfur atom, which agrees well with previous studies (Fig. 4.10) (86, 120, 121).

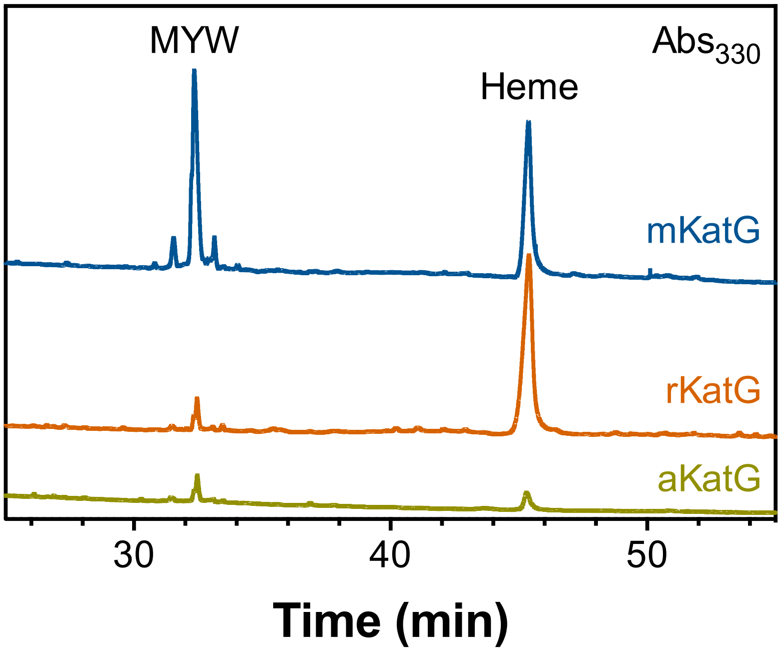

Figure 4.8. LC chromatogram of KatG MYW and heme cofactors at 330 nm. Absorbance from the MYW adduct was monitored during separation by LC-MS. Though present in apo (yellow), reconstituted (orange), and mature KatG (blue), the absorbance for the PTM is greatest for mKatG. Additionally, the absorbance for both the MYW adduct (32 min) and heme (45 min) were able to be detected at 330 nm and found to be consistent with previously collected UV-vis data.

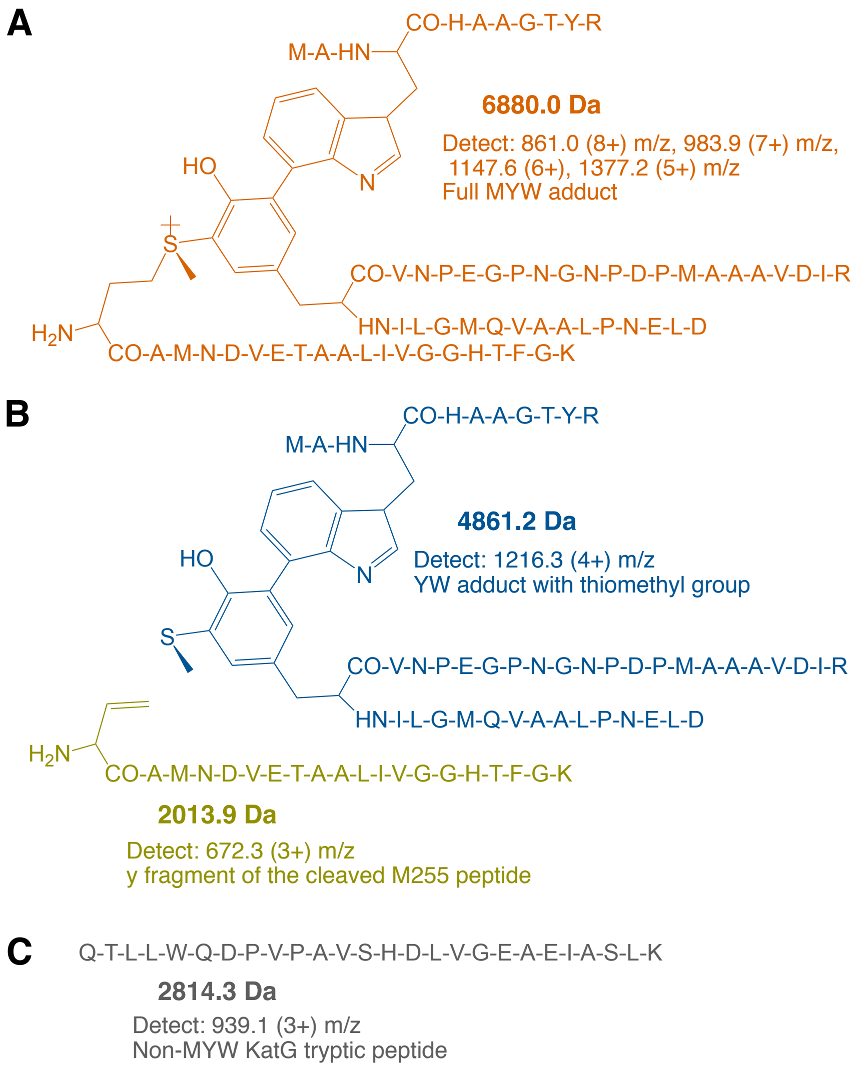
A
CO-H-A-A-G-T-Y-R
M-A-HN
6880.0 Da
Detect: 861.0 (8+) m/z, 983.9 (7+) m/z,
1147.6 (6+), 1377.2 (5+) m/z
Full MYW adduct
HO
N
S
+
CO-V-N-P-E-G-P-N-G-N-P-D-P-M-A-A-A-V-D-I-R
HN-I-L-G-M-Q-V-A-A-L-P-N-E-L-D
H$_2$N
CO-A-M-N-D-V-E-T-A-A-L-I-V-G-G-H-T-F-G-K
B
CO-H-A-A-G-T-Y-R
M-A-HN
4861.2 Da
Detect: 1216.3 (4+) m/z
YW adduct with thiomethyl group
HO
N
S
CO-V-N-P-E-G-P-N-G-N-P-D-P-M-A-A-A-V-D-I-R
HN-I-L-G-M-Q-V-A-A-L-P-N-E-L-D
H$_2$N
CO-A-M-N-D-V-E-T-A-A-L-I-V-G-G-H-T-F-G-K
2013.9 Da
Detect: 672.3 (3+) m/z
y fragment of the cleaved M255 peptide
C
Q-T-L-L-W-Q-D-P-V-P-A-V-S-H-D-L-V-G-E-A-E-I-A-S-L-K
2814.3 Da
Detect: 939.1 (3+) m/z
Non-MYW KatG tryptic peptide

Figure 4.9. Tryptic peptides detected by LC-MS and LC-MS/MS. The structures of the peptides detected are presented above along with the weight of the parent ion and the m/z values for ions detected.

Table 4.3. Tryptic peptides detected by mass spectrometry

Ion detected	Parent ion	Identity of detected ion
672.3 (3+)	2013.9	M255 peptide - SCH3 group
861.01 (8+)	6880.08	Full MYW adduct with respective peptides
939.1 (3+)	2814.3	Non-MYW peptide (Q434 - K459)
983.9 (7+)	6878.9	Full MYW adduct with respective peptides
1147.67 (6+)	6880.02	Full MYW adduct with respective peptides
1216.3 (4+)	4861.2	YW adduct + SCH3 group
1377.6 (5+)	6881.0	Full MYW adduct with respective peptides

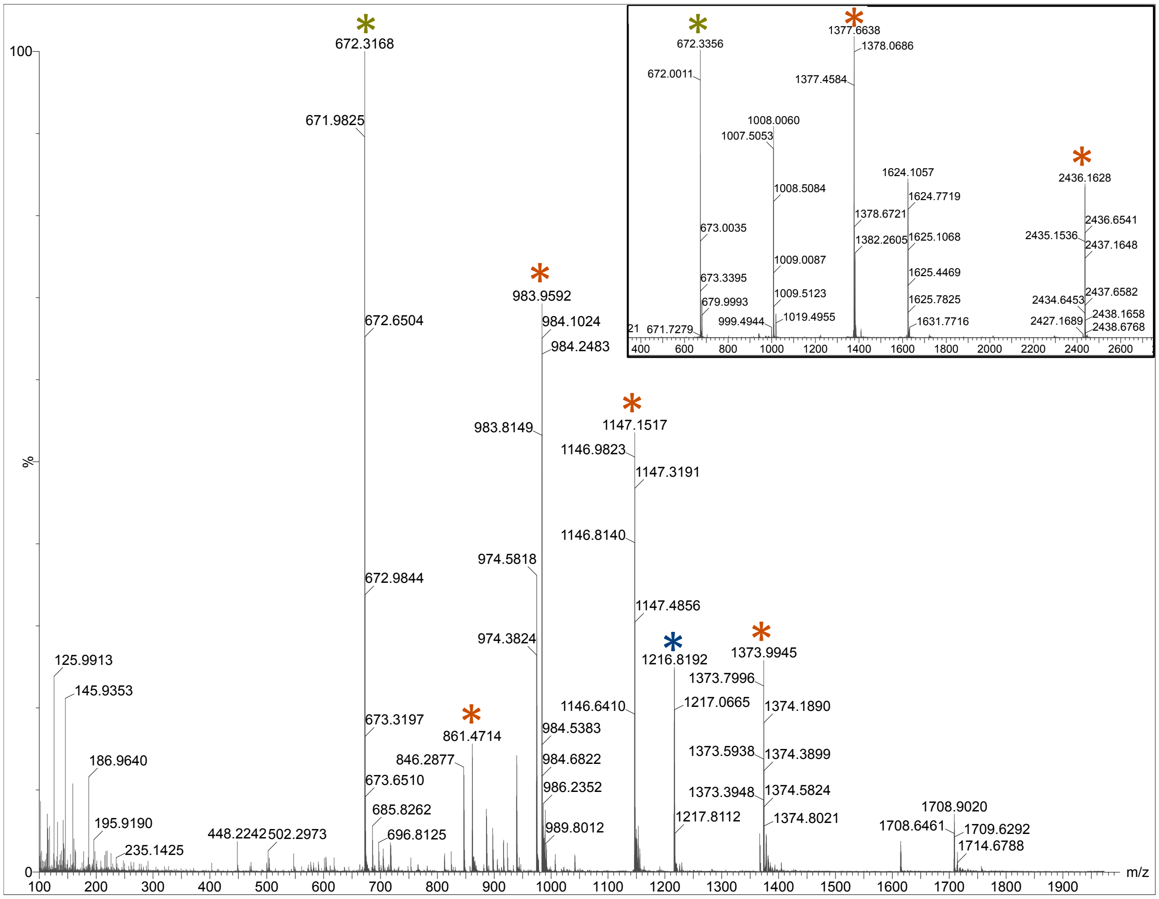

Figure 4.10. Confirmation of MYW adduct in mKatG by LC-MS and tandem MS. Presence of the formed, covalently linked MYW cofactor in mKatG was detected by LC-MS. The insert shows tandem MS of the 1377.6 m/z ion, which further confirms the formation of MYW cofactor by the identification of the M255 tryptic peptide without the thiomethyl group of M255 at 672.3 m/z.

Comparison of MS ions across aKatG, rKatG, and mKatG indicate MYW-related ions are present in each preparation of KatG, though to a much lesser extent in the rKatG and mKatG samples (Fig. 4.11). A non-MYW adduct tryptic peptide Q434 – K459, with an observed 939 (3+) m/z, co-eluted with the MYW cofactor peptide during chromatographic separation. The identity of this non-MYW peptide was confirmed by comparison with a previous peptide mapping and analysis of KatG tryptic peptides (data not shown). Though unexpected, the co-eluting peptide served as an unintentional internal standard for comparing the relative abundance of MYW-derived ions in aKatG, rKatG, and mKatG samples (Fig. 4.11). From this comparison, it is evident that mKatG contains a greater population of formed MYW cofactor than either aKatG or rKatG relative to the Q434 – K459 peptide ion. It is not unexpected that the rKatG sample(s) contain MYW-associated ions because despite expression and purification of aKatG in absence of exogenous heme, a small population of this purified KatG had received endogenous heme from the *E. coli* cells during expression (reference Fig. 4.4). The intensity of MYW-ions detected in the aKatG and rKatG samples, however, were substantially lower than for mKatG, and it is unexpected that the lower intensity of these ions to be due to difficulties in ionization between different protein preparations.

rKatG was treated with 5 molar equivalents of peracetic acid (PAA) in order to evaluate the hypothesis that treatment with a peroxide will result in the formation of the MYW cofactor. As mentioned in previous chapters, PAA is not a catalase-supporting substrate, but does support generation of higher oxidation states of the KatG heme and therefore can facilitate formation of the MYW adduct. Because of this, PAA is presumed to serve as a useful tool in encouraging the formation of the MYW cofactor by enabling

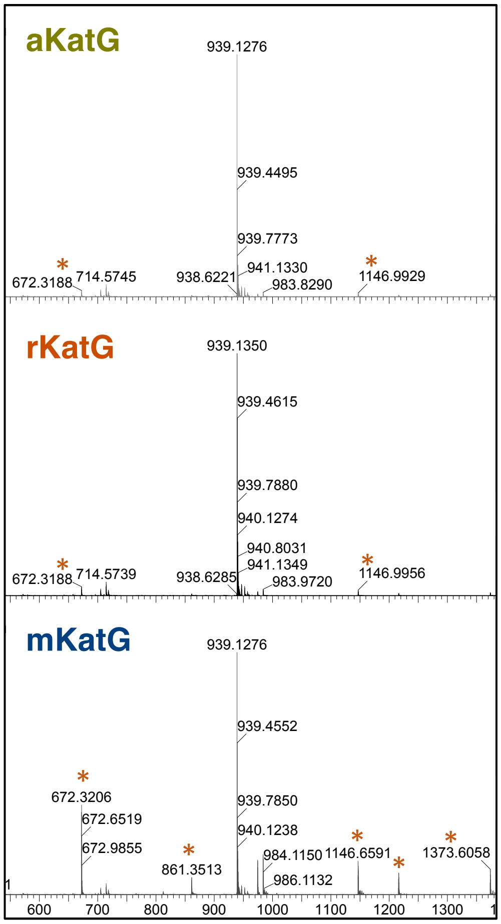

Figure 4.11. Comparison of MS spectra across KatG preparation. Though ions corresponding to the post-translational formation of the MYW adduct are present in aKatG and rKatG samples, the relative abundance of these ions is substantially less that observed in mKatG relative to a non-MYW KatG tryptic peptide that co-eluted with the MYW fragments at 939.1 m/z.

the heme cofactor to form intermediates necessary to form MYW covalent adduct without allowing the KatG population with newly formed MYW cofactor to participate in catalase turnover. Comparison of treated and untreated rKatG by tryptic LC-MS/MS shows distinct loss of any MYW-derived MS ions. Even the treatment of mKatG with PAA as a control significantly diminishes the presence of MYW-related ions as detected in the mKatG sample (Fig. 4.12). The absence of any detectible MYW cofactor ions after the treatment with PAA is most likely due to oxidative damage caused by the reaction with PAA, and such results have been reported by others (120). Though treatment with a non-catalytic peroxide like PAA is ideal for such an experiment, the loss of signal seen with PAA necessitated the use of H_2O_2 to treat KatG to initiate MYW cofactor formation. Importantly, higher amount of H_2O_2 was utilized as it is the enzyme's natural substrate and can be used for catalytic turnover once any MYW adduct is formed. MYW adduct formation was tested by treating rKatG samples were with 5 equivalents and 50 equivalents of H_2O_2. When rKatG is treated with 50 molar equivalents of H_2O_2, an increase of signal for ions associated with the MYW cofactor formation is observed compared to that of mKatG (Fig. 4.13).

In order to evaluate the role of the Arg switch in the formation of the MYW cofactor, the same evaluation was performed on R418N KatG. Similar results were observed for the mR418N and rR418N proteins. Specifically, a peak in the chromatogram with a retention time of 32 min was confirmed to correspond to peptides consistent with MYW-derived MS ions, as observed for *wt* KatG (Fig. 4.14). These MYW-derived MS ions were more prominent in the mR418N samples and upon treatment of rR418N with 50 equivalents of H_2O_2, as was observed for *wt* KatG (Fig. 4.14). Interestingly, in the R418N

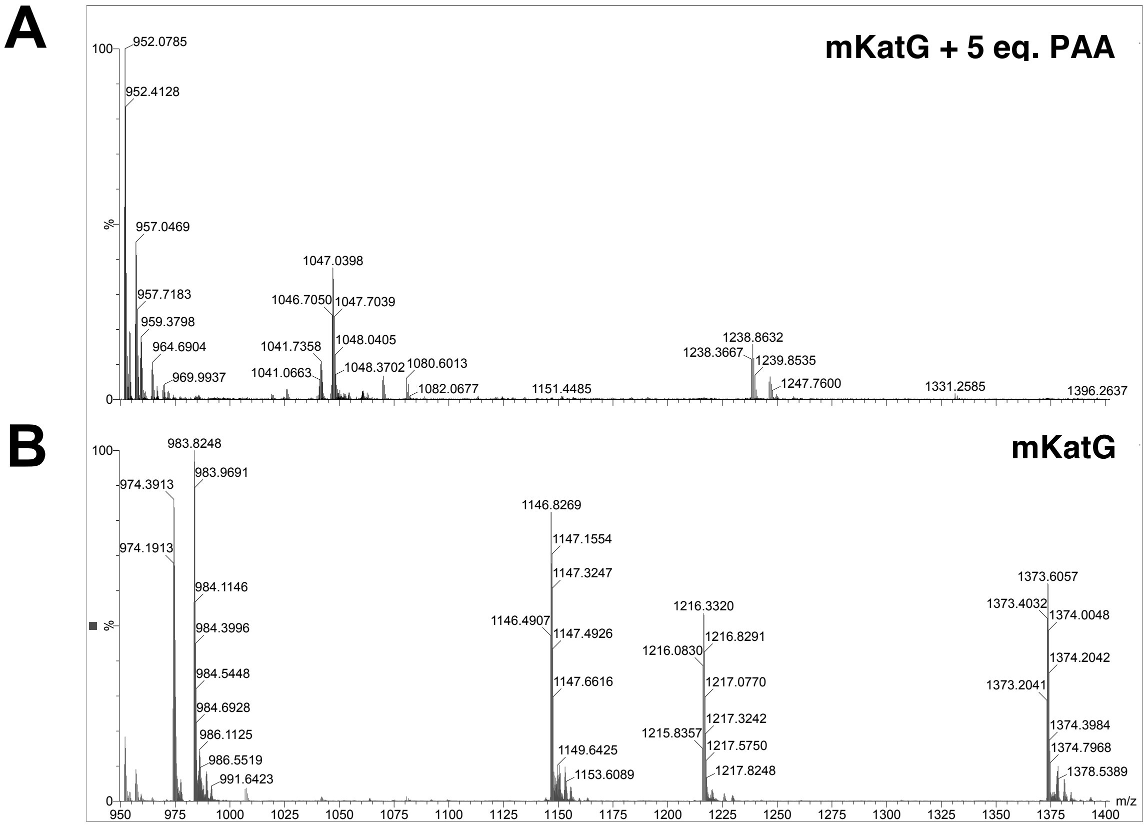

Figure 4.12. Treating mKatG *wt* with PAA results in loss of MYW-related MS ions. LC-MS spectra of the PAA-treated mKatG (A) reveals the loss of the MYW-related peptides identified in mKatG (B) data due to treatment with 5 molar equivalents of PAA.

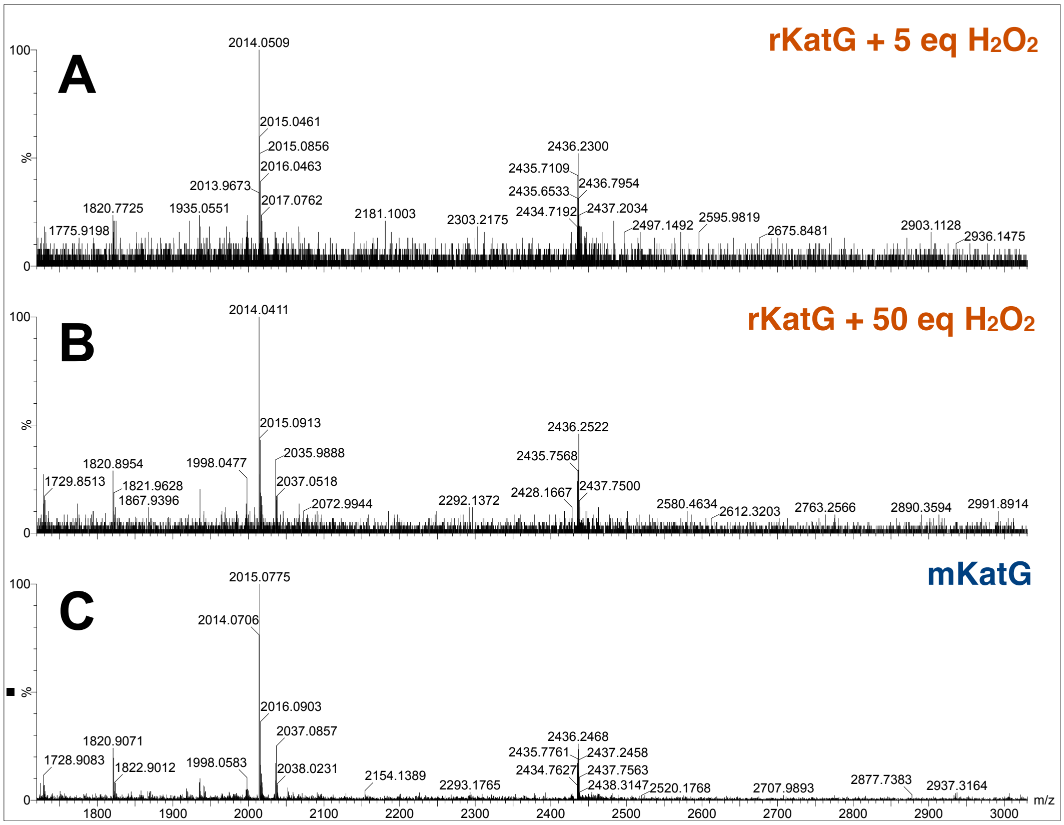

Figure 4.13. Treatment with H_2O_2 increases prominence of MYW-associated MS ions. H_2O_2 was added to rKatG to form the MYW cofactor before digestion by trypsin. An increase in H_2O_2 concentration leads to increased signal of the 2436 m/z and 2014 m/z peaks that are assigned to the YW adduct with thiomethyl group and the remaining M255 peptide, respectively.

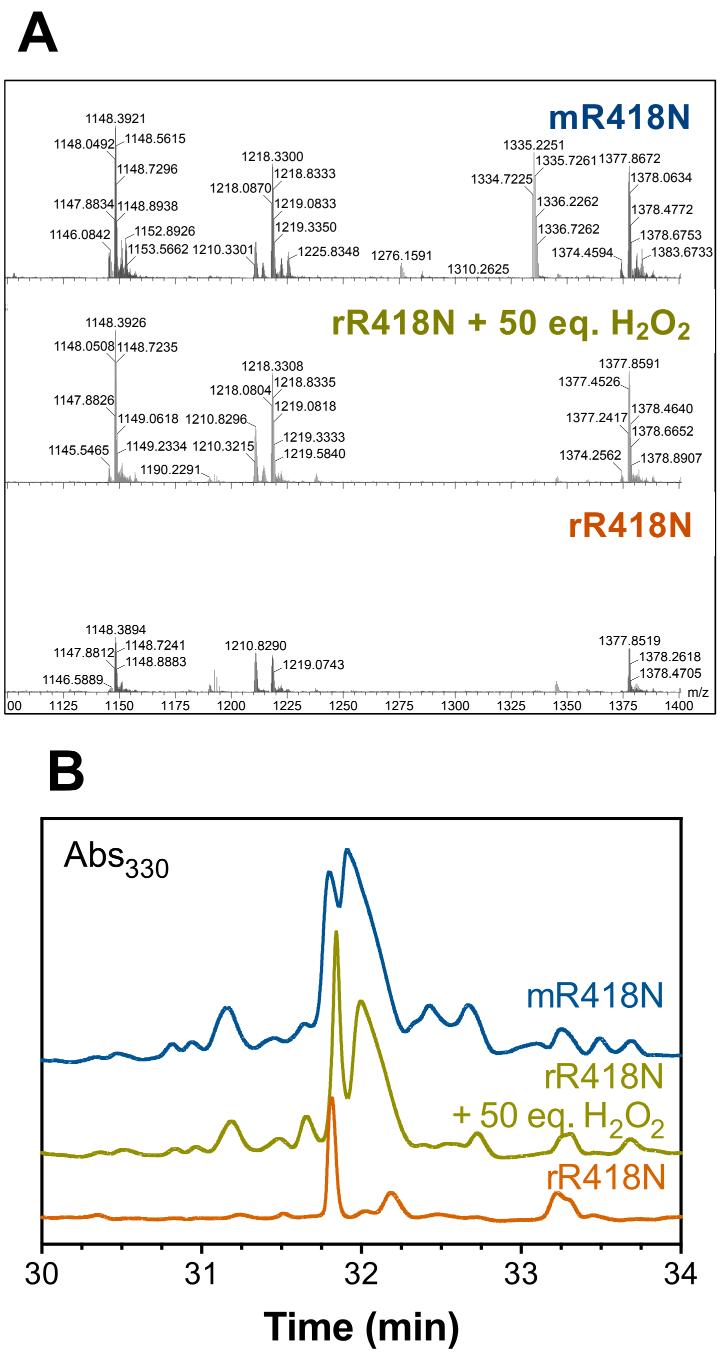

Figure 4.14. LC-MS analysis of R418N KatG variant. The ions detected by MS for the R418N protein are comparable to *wt* KatG (A), and the UV chromatogram from LC separation shows increase in peak associated with MYW adduct peptides (~32 min) when rR418N is treated with H_2O_2 (B).

KatG samples, the coeluting tryptic peptide, Q434 – K459, is visible in the LC chromatogram and has a more distinct elution time than was observed for *wt* KatG.

Heme states of rKatG involved in the formation of MYW cofactor

Changes in heme spectral transitions across mature and reconstituted forms of *wt* and R418N KatG throughout reaction with H_2O_2 were investigated to provide insight to the mechanism of MYW cofactor formation and any role of the Arg switch may play in this process. Additional transitions in heme spectra are observed for both rKatG *wt* and rR418N during reaction with low equivalents of H_2O_2 at 429 nm (Fig. 4.15). Reaction of *wt* mKatG with such a low concentration of H_2O_2 results in little, if any, observable spectral change in the heme group. Due to the presence of the fully formed MYW cofactor and the catalase activity that accompanies its presence, H_2O_2 is rapidly consumed and the relatively low concentration in the reaction is insufficient to force the rate of ferric enzyme oxidation to exceed the rate of return of oxidized heme states back to the resting, ferric state; consequently, the ferric state remains dominant throughout. In practice, ~ 42 equivalents of H_2O_2 are necessary to observe Fe^{III}-$O_2^{\bullet-}$-like features (416, 545, and 578 nm) in the steady state as opposed to the ferric form. In contrast, mR418N does exhibit heme transitions even at this concentration of H_2O_2 because R418N reaction with H_2O_2 to produce ferryl-oxo heme states occurs with a rate constant equal to or better than *wt*, but the reactivity of the ferryl-oxo heme states formed, and consequently rate of O_2 production, is substantially slower for the variant. Similar to *wt* mKatG, the spectral features observed in the steady state for mR418N are that of a ferric-superoxo-like heme state.

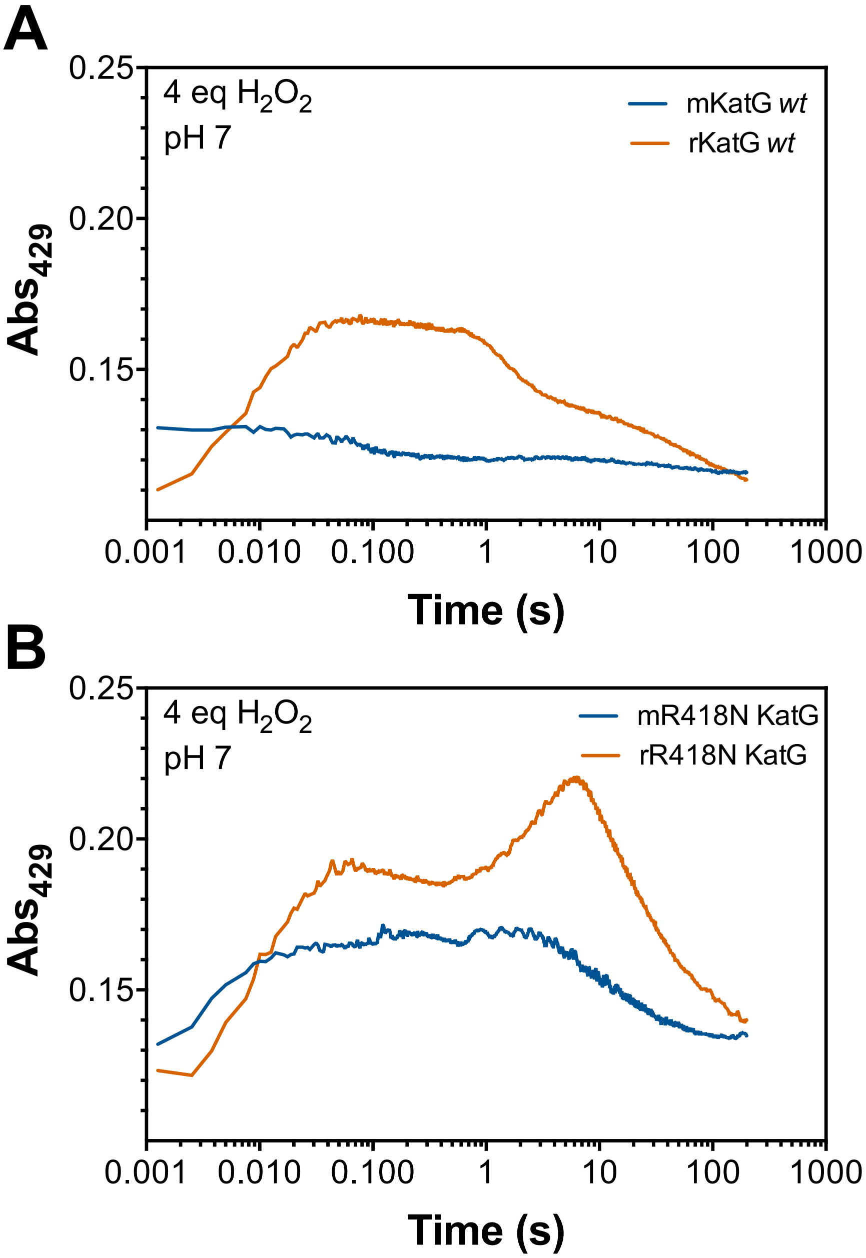

Figure 4.15. Comparison at 429 nm of R418N and *wt* KatG across mature and reconstituted proteins. Reaction of mature (blue) and reconstituted (orange) *wt* (A) and R418N (B) KatG with 4 equivalents of H_2O_2 demonstrates significant differences in accumulation of oxidized heme states.

Both *wt* rKatG and rR418N exhibit a greater number of heme transitions than their mKatG counterparts, as evidenced by the absorbance of 429 nm throughout the reaction (Fig. 4.15). The greater number of transitions demonstrated by the reconstituted proteins at low concentrations of H_2O_2 suggest, in collaboration with confirmation by MS that the reconstituted proteins lack the formed MYW adduct, that the heme intermediates responsible for MYW cofactor formation. Furthermore, the spectral features of the heme intermediates observed upon reaction of *wt* rKatG and rR418N with 4 equivalents of H_2O_2 are in striking contrast to what is observed for any mKatG protein. When *wt* rKatG is reacted with 4 equivalents of H_2O_2, the ferric, resting enzyme, with features at 406, 505, and 630 nm, transitions to ferryl-oxo type spectral features at 413, 530, and 556 nm (Fig. 4.16A). This intermediate persists from 52 ms to 558 ms and then transitions to spectral features 408, 516, and 635 nm that are similar to the ferric, resting state, but not the same as the starting enzyme (Fig. 4.16B). The enzyme then makes a slow transition from 7 s to 200 s to spectral features that match those of the resting enzyme at the beginning of the reaction (407, 504, and 638 nm) (Fig. 4.16C). These heme transitions stand apart from previously observed KatG reactions because 1) the appearance of ferryl-oxo type spectral features arise before any indication of the catalatically competent ferric superoxo-like intermediate, 2) there is no sighting of the aforementioned ferric superoxo-like intermediate, and 3) there seems to be two distinct heme states that resemble the ferric enzyme but different from one another. Each of these can be explained in light of the proposed mechanisms for MYW biosynthesis. Since rKatG is unable to carry out catalase turnover immediately because the MYW adduct is not yet formed, there is no anticipation for the catalase-active ferric superoxo-like intermediate to be present. Therefore, the

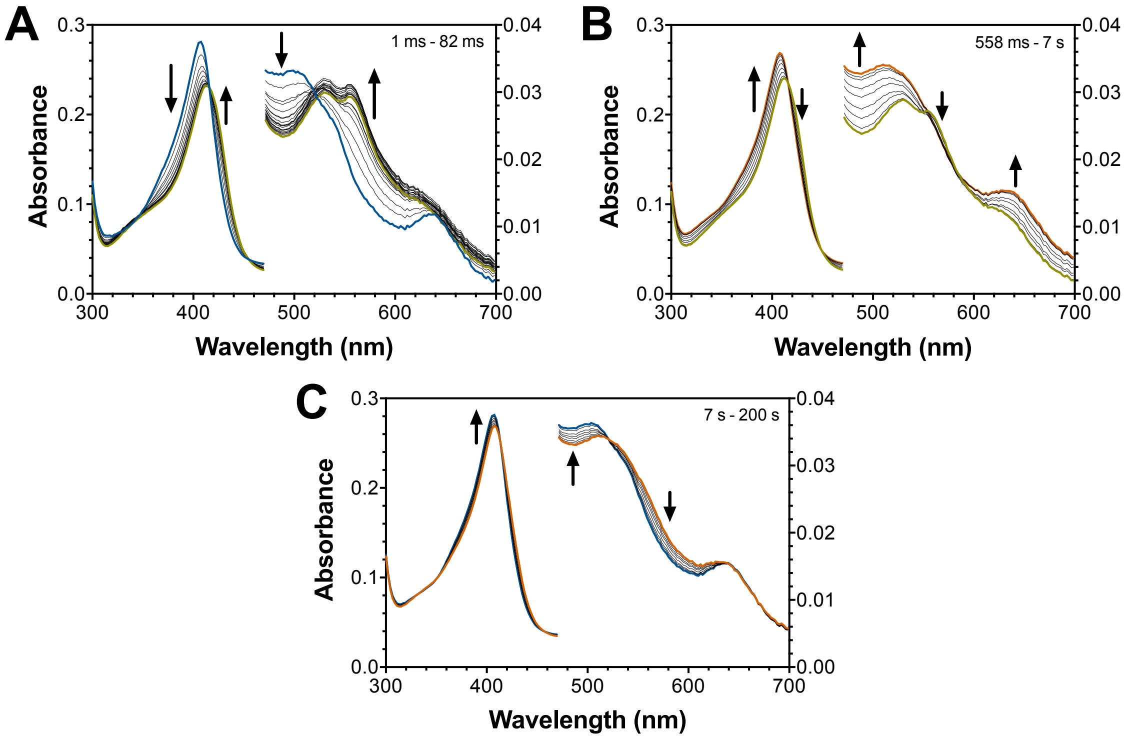

Figure 4.16. Heme transitions of rKatG *wt* reacted with 4 eq. H_2O_2 at pH 7. The earliest heme transition is from a ferric spectrum to a ferryl-oxo-like state (A). From 52 ms to 558 ms, rKatG maintains heme spectra consistent with a ferryl-oxo state, then transitions to a ferric-like state (B). Lastly, there is a slow transition to heme features more consistent with the archetype ferric state (C).

appearance of heme features commensurate of a ferryl-oxo state as the first non-ferric heme intermediate suggest these features to correspond to heme states that facilitate MYW cofactor biosynthesis. The proposed mechanism for MYW formation (Fig. 4.2) involves a number of ferryl-oxo heme states. It is not unlikely that reaction with H_2O_2 results in the 2-electron oxidation of Fe^{III} rKatG to Fe^{IV}=O[por]$^{\bullet+}$ and this heme state can then be reduced by a nearby active-site residue (specifically, W107, initiating protein-derived cofactor formation). As Fe^{IV}=O[por]$^{\bullet+}$ is so reactive, it is not long-lived enough to be observed. The Fe^{IV}=O [protein]$^{\bullet+}$ intermediate, however, is more stable and is a likely candidate to match the 416, 530, and 558 nm spectral features. Lastly, the distinct Fe^{III}-like intermediates align with the proposed mechanism which predicts both Fe^{III}-OH_2 and Fe^{III} heme states.

Similarly, when rR418N KatG is reacted with 4 equivalents of H_2O_2, four distinct heme transitions are observed. First, the ferric, resting enzyme, with spectral features at 408, 505, and 630 nm, transitions to ferryl-type features similar to those observed for *wt* rKatG with features at 414, 531, and 557 nm (Fig. 4.17A). This second intermediate persists as the dominant species from 34 ms until 430 ms when the second transition in heme spectra takes place. At this time, another intermediate with ferryl-type spectral features is observed with spectral features at 418, 536, and 559 nm (Fig. 4.17B). This intermediate was not observed in the reaction of *wt* rKatG with 4 equivalents H_2O_2. Much like the *wt* rKatG reaction, rR418N demonstrates two distinct ferric-type intermediates near the end of the reaction. Around 6 s, rR418N transitions to the first Fe^{III}-like heme state with distinct features at 410, 537, and 628 nm which then transitions to the features at 408, 504, and 630 nm for the initial resting state (Fig. 4.17C and D). As discussed for the *wt* rKatG spectra above, it is anticipated that these heme transitions are related to the formation of

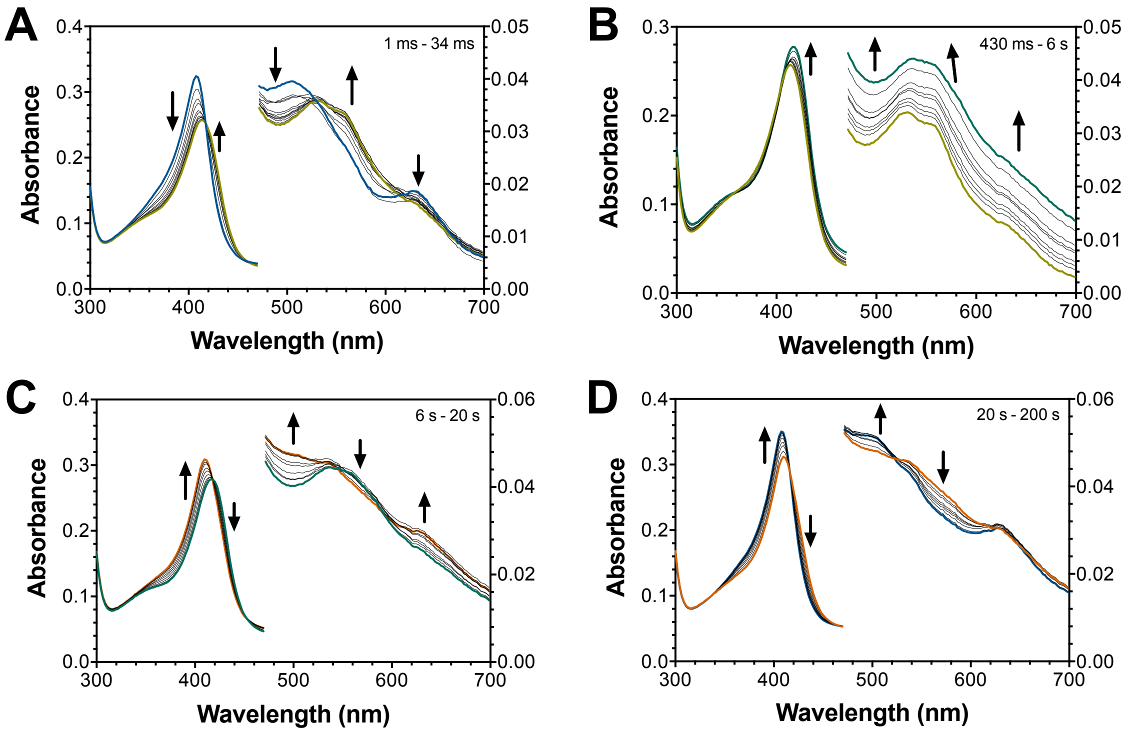

Figure 4.17. Heme transitions of rR418N KatG reacted with 4 eq. H_2O_2 at pH 7. The earliest heme transition is from a ferric spectrum to a ferryl-oxo-like state (A). Next, a transition between two ferryl-oxo-type states can be observed from features at 414, 531, and 557 nm to 418, 536, and 559 nm (B). Then from 6 to 20 s, rR418N transitions from the second ferryl-oxo state to a ferric-like state with features at 410, 537 and 628 nm (C). Lastly, there is a slow transition to heme features more consistent with the archetype ferric state at 408, 504 and 630 nm from 20 to 200 s (D).

the MYW cofactor. The intermediate observed only in the reaction with rR418N (418, 536, and 559 nm) could possibly be a ferryl-type heme with a distinct protein-based radical that is impacting the electronic structure of the heme. This would not be unlikely considering the proximity of the MYW adduct and the heme center. As seen for *wt* rKatG, the two distinct Fe^{III}-like intermediates observed from 6 s to 200 s during the rR418N reaction could easily be assigned to ferric states of the MYW formation mechanism.

This additional heme state transition, which is present in rR418N, from ~ 0.5 s – 6 s, is absent for *wt* rKatG is also observable when comparing the 429 nm traces of both reconstituted KatG proteins (Fig. 4.18A). The lifetime of this intermediate seems to correlate to the increase in absorbance at ~308 nm. As discussed earlier, it is expected that the MYW cofactor will contribute to absorption around 310 – 320 nm; 308 nm is used here due to the clarity of the spectral traces in the presented data sets, though the same trend is observed at slightly longer wavelengths, to estimate the MYW-related changes. Simulated spectra derived from global kinetic fitting of the experimental data exhibit a distinct heme intermediate with a strong absorption peak around ~ 310 nm and distinct spectral features of 420, 537, and 559 nm from the rR418N data (Fig. 4.19). The absorption characteristics of this simulated spectrum strongly agrees with the experimental rR418N data. Additionally, calculated concentration profiles strongly agree with the timing observed for the lifetime of this intermediate (Figs. 4.18 and 4.19).

The apparent rate constants (k_{obs}) for the resting enzyme's initial reaction with H_2O_2 (k_1) and k_2 were estimated across H_2O_2 concentration using global fitting software (Fig. 4.20). The results indicate that the reaction between ferric rR418N and *wt* rKatG with H_2O_2 are nearly identical with rate constants of 9.1×10^6 $M^{-1}s^{-1}$ and 8.4×10^6 $M^{-1}s^{-1}$, respectively.

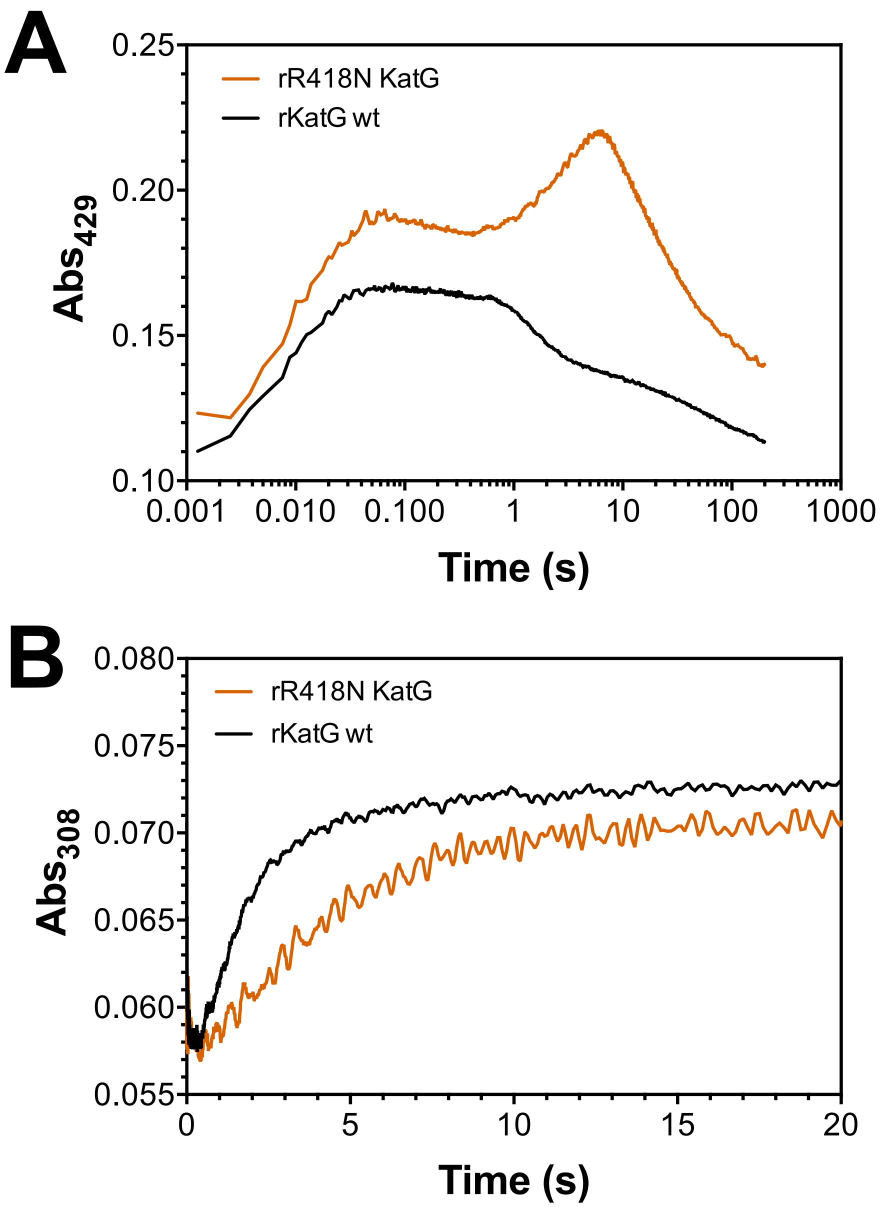

Figure 4.18. Contrast between activity of heme transitions and MYW formation for rR418N and *wt* rKatG. Heme absorbance observed at 429 nm (A) indicate distinct heme progressions between rR418N and *wt* KatG while the absorbance at 308 nm (B), which could indicate MYW formation, shows 3-fold difference in rate of formation between KatG proteins.

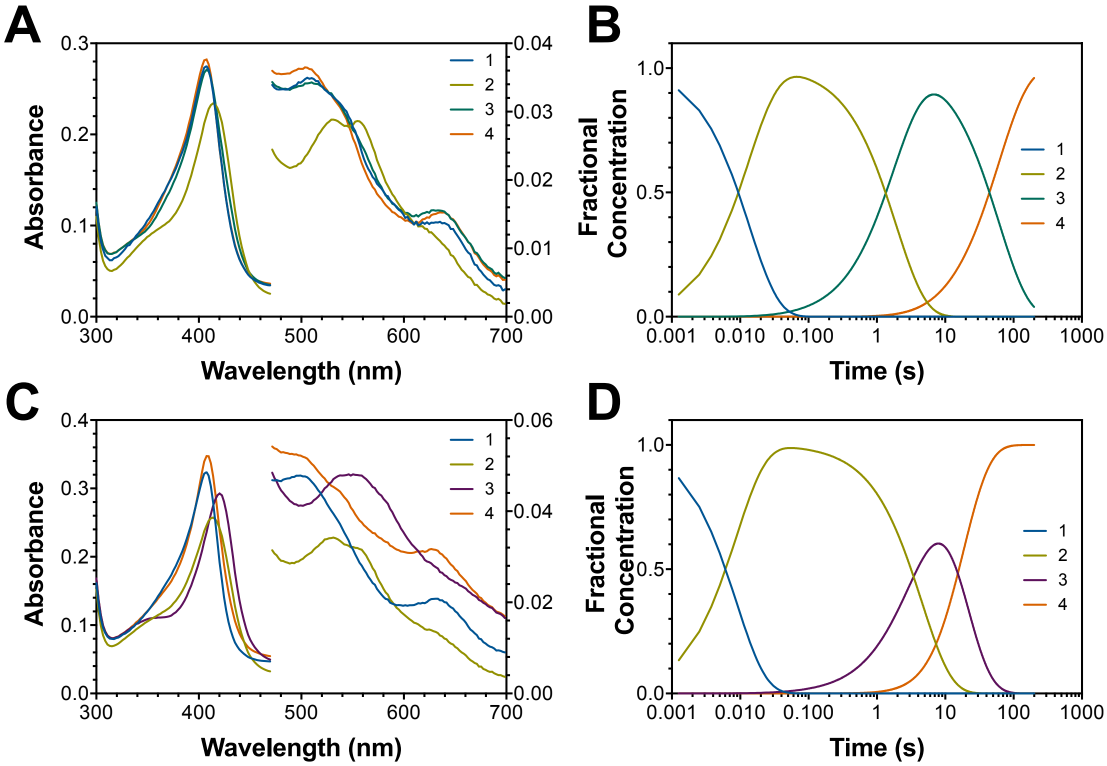

Figure 4.19. Simulated spectra and concentration profiles from global fitting of *wt* rKatG and rR418N. The simulated spectra and concentration profiles for *wt* rKatG (A and B, respectively) and rR418N (C and D, respectively) reiterate differences in observed heme states between these KatG proteins. A unique heme state exhibited by rR418N with prominent features at 420, 537, and 559 nm strongly agrees with the values observed form experimental data. Both data sets were analyzed by global kinetic fitting using the template mechanism: a → b → c→ d.

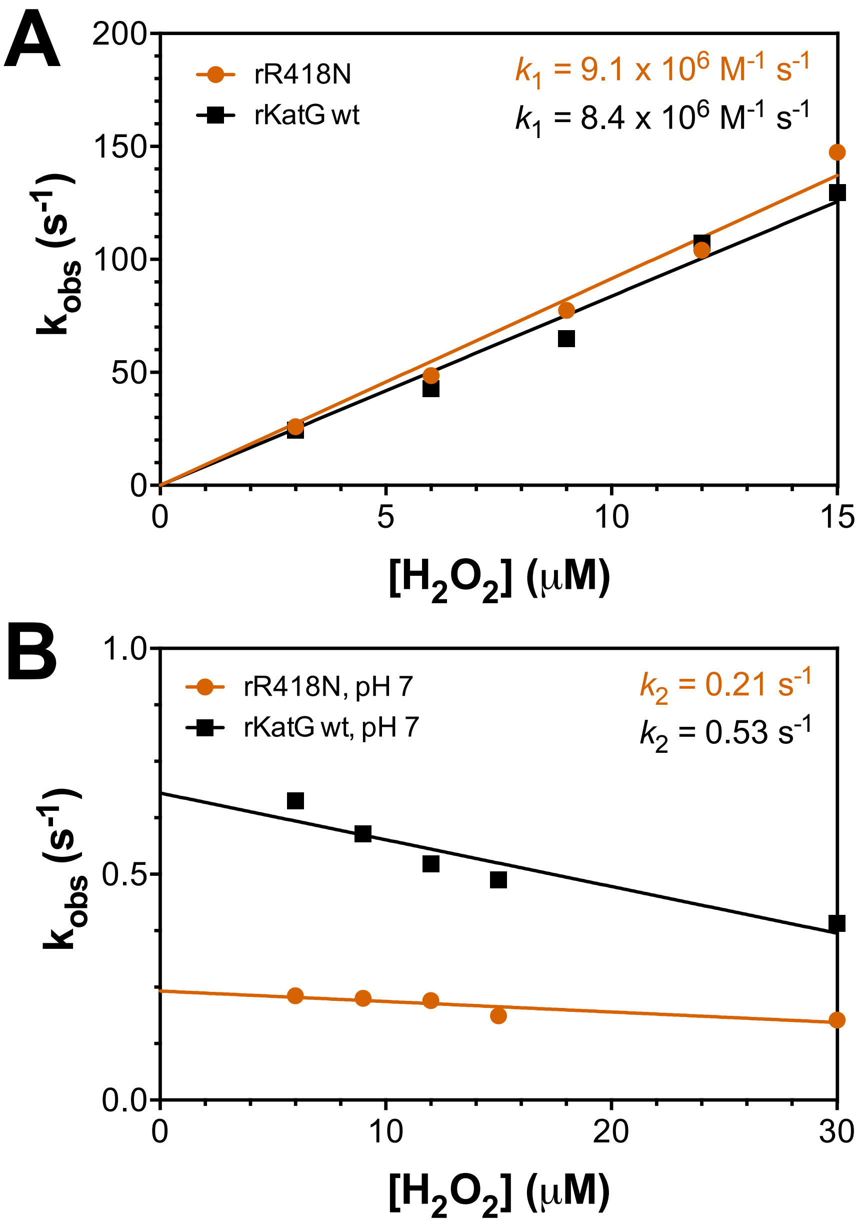

Figure 4.20. Estimated rate constants of reconstituted proteins. According to global kinetic fitting, the reactivity of rKatG *wt* and rR418N ferric enzymes with H_2O_2 is nearly indentical (A). The rate at which these proteins form the MYW adduct (increase in absorbance at ~308 nm), however, is nearly 3-fold lower for the rR418N KatG enzyme (B).

However, k_2 differs by about 3-fold with rate constants of 0.24 s^{-1} and 0.68 s^{-1}, respectively. It is suspected that this step relates to the formation of the MYW adduct. Though the data of observed heme intermediates, predicted lifetimes of the unique ferryl-like intermediate, and the increase in absorbance at 308 nm agree for the rR418N KatG variant, the *wt* rKatG protein does not show the same accumulation of the ferryl-type intermediate unique to rKatG proteins. This may indicate a decoupling of the progression of heme states and the formation of the MYW cofactor.

Reactivity of rKatG variants at high concentrations of H_2O_2

When reacted with higher concentrations of H_2O_2, rR418N and *wt* rKatG present distinct progressions of heme spectra (Fig. 4.21). *wt* rKatG demonstrates the early appearance of a $Fe^{IV}=O$ heme state that persists for ~ 2 s of reaction time (Fig. 4.21A). This species converts to the Fe^{III} enzyme over a period of minutes (Fig. 4.21B). The R418N KatG variant, on the other hand, exhibits similar $Fe^{IV}=O$-like features from 1.2 ms to 27 ms, but then a clear transition to Fe^{III}-$O_2^{\bullet-}$-like intermediate takes place (Fig. 4.21C) before the return to the Fe^{III} enzyme (Fig 4.21D). rR418N KatG clearly demonstrates that after rapid MYW cofactor formation, the enzyme then begins to carry out catalase activity, as evidenced by the appearance of the Fe^{III}-$O_2^{\bullet-}$-like intermediate (416, 545, and 578 nm peaks). Furthermore, when either *wt* rKatG or rR418N is pre-treated with low molar equivalents of PAA and then reacted with H_2O_2, the ferric superoxo-like intermediate is observed at the earliest time point, as seen for all mature proteins (data not shown here).

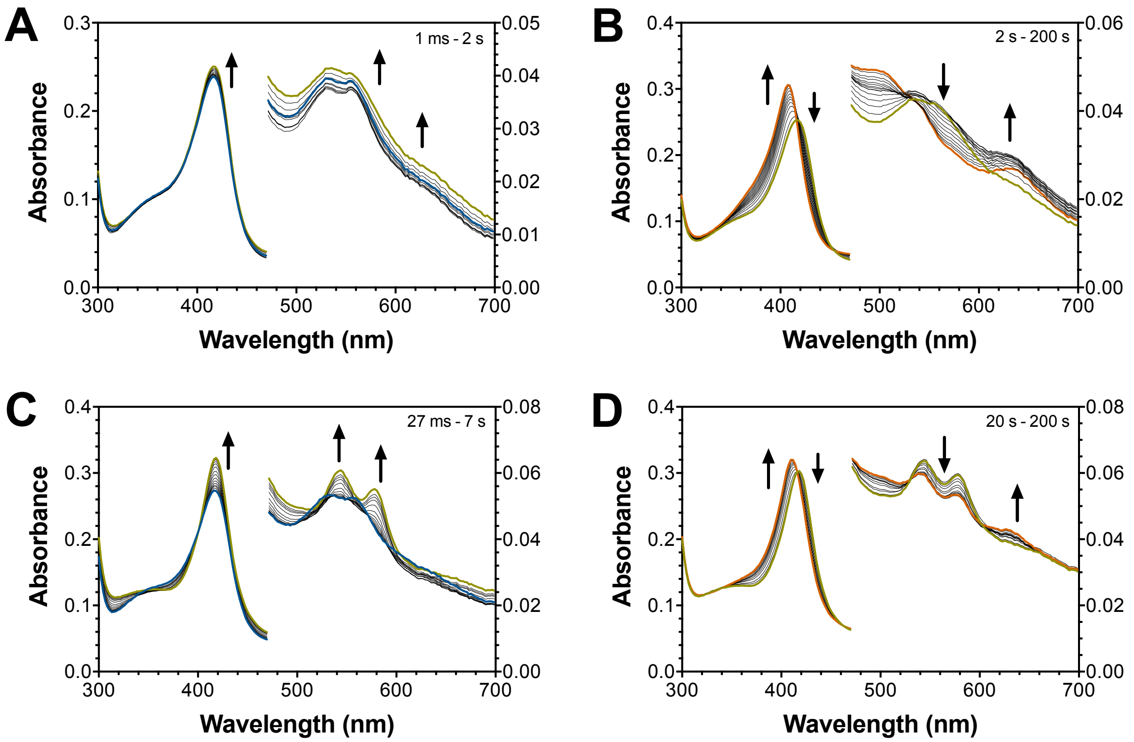

Figure 4.21. Reaction of reconstituted KatGs with 2 mM H_2O_2 (667 eq.) at pH 7. *wt* rKatG (A and B) transition from $Fe^{IV}=O$ type features to the resting enzyme whereas rR418N (C and D) progress from $Fe^{IV}=O$ type features to Fe^{III}-$O_2^{\bullet-}$-like features before returning to the ferric state.

Oxidation of ABTS by reconstituted proteins

As previously reported by our lab, oxidation of peroxidatic electron donors (PxEDs) stimulate KatG's catalase activity (78). As catalase activity requires the fully formed MYW cofactor, the oxidation of ABTS by reconstituted proteins, especially at lower concentrations of H_2O_2, may provide insight to the flow of electrons through the active site before the covalent adduct is formed. Reconstituted versions of *wt* and R418N KatG both generated considerably more $ABTS^{\bullet+}$ than their mature counterparts (Fig. 4.22A). The mR418N and rR418N demonstrate similar ratios of ABTS oxidation per H_2O_2 consumed at H_2O_2 concentrations above 100 μM, whereas the mature and reconstituted *wt* KatG demonstrate substantial differences in terms of ABTS oxidation per H_2O_2 at concentrations lower than 50 μM (Fig. 4.22B). As H_2O_2 concentrations decrease to 7.5 μM, the reconstituted proteins seem capable of generating ~2 $ABTS^{\bullet+}$ per H_2O_2 consumed. It is clear that ABTS is being oxidized more by rKatG *wt* and rR418N than their respective mature forms. This can not only be an indication that the oxidation of the MYW cofactor (pre-fully formed MYW) is not 100% efficient and off-MYW-forming oxidation may be happening, resulting in a greater propensity for hole-hopping through KatG (i.e., peroxidase activity) until the MYW cofactor is fully formed. From these results, however, it is difficult to discern whether the presence of ABTS is encouraging peroxidatic turnover by KatG and therefore distracting from formation of the protein-derived cofactor or if it is facilitating more rapid recovery of protein-based radicals within the enzyme which allows for more rapid formation of the MYW adduct. Determining which effect ABTS has on the reconstituted proteins will require stopped-flow analysis of the proteins with ABTS and also ascorbate for the suppression of $ABTS^{\bullet+}$. The R418N KatG variant will serve as a

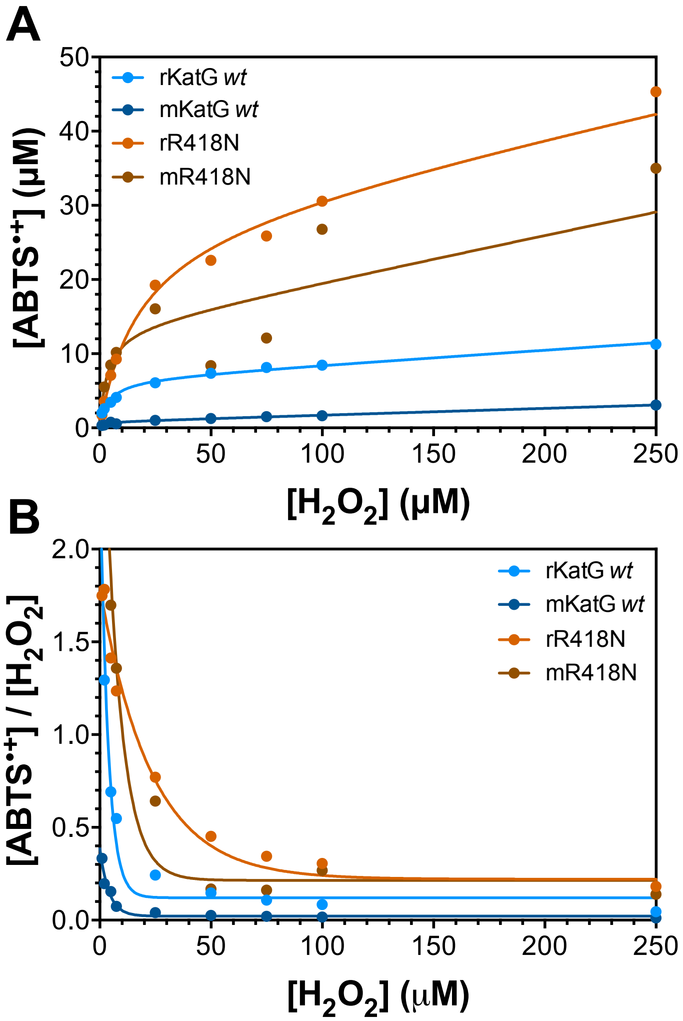

Figure 4.22. Oxidation of ABTS by KatG *wt* and R418N proteins at pH 5. The accumulation of ABTS radical (A) and the corresponding $[ABTS^{\bullet+}]/[H_2O_2]$ (B) across the same concentrations of H_2O_2 are provided for rKatG *wt* (bright blue), mKatG *wt* (dark blue), rR418N (bright orange), and mR418N (dark orange). All reactions were carried out in 50 mM acetate, pH with 3 µM protein and 0.1 mM ABTS.

useful tool in this analysis not only because R418 is the electronic switch of the enzyme, but also because the slower kinetic responses of this variant allow for unique detection of heme states of the reconstituted protein as shown above.

4.4. Conclusions

Using a highly efficient method for acquiring aKatG protein equipped with heme cofactor yet lacking the protein-derived cofactor developed in our lab, we present here preliminary data on the character and reactivity of the *wt* rKatG and rR418N proteins. LC-MS/MS analysis confirms the presence of the fully formed MYW cofactor in mKatG proteins and a substantial lack of the MYW cofactor in rKatG proteins. Absorption maxima were predicted and utilized to assist in facile detection of the MYW adduct for both MS and stopped-flow analyses. In our investigations, we have identified two ferryl-type intermediates and two ferric-like intermediates that seem distinct from each other and seem plausible as distinct intermediates of the biosynthetic mechanism. The rates for initial reaction with H_2O_2 are not affected by the R418N mutation, but the observed rate possibly associated with MYW formation has been decreased almost 3-fold. Therefore, we conclude that these preliminary data indicate the Arg switch may plan an ancillary role, but not a crucial role, in the formation of the MYW adduct. Altogether, the results presented in this chapter confirm our lab is poised for more in-depth studies of the MYW cofactor formation. Future studies will be needed to confirm the electronic structure of heme intermediates involved in MYW cofactor formation and the kinetics of each step in the mechanism. This can be accomplished with a combination of optical stopped-flow, RFQ-EPR, and Mössbauer spectroscopies along with LC-MS and LC-MS/MS analyses.

Chapter Five

Isoniazid Activation by Catalase-peroxidase (KatG)

5.1. Relationship between KatG and tuberculosis

MDR-TB and mutations of the katG *gene*

Isoniazid (INH), rifampin (RIF), ethambutol (EMB), and pyrazinamide (PZA) are the primary, front-line drugs for treatment of the lung disease tuberculosis (TB). The procedure for curing TB requires 6 to 9 months of uninterrupted treatment with multiple antitubercular medicines and can involve uncomfortable side effects (127). Under such regimens, TB patients can be cured of their infections, however, multidrug-resistant strains of *Mycobacterium tuberculosis*, the causative agent of TB, have developed. In particular, resistance to the most commonly administered drugs, INH and RIF, has arisen due to inappropriate administration or lack of compliance with a proper drug regimen to completion (128). Multidrug-resistant TB (MDR-TB) is more difficult to treat and has a higher death rate than TB, and therefore is a major health concern. As a result, it is a subject of research interest world-wide. A number of studies investigating the cause of drug resistance have concluded that 50-70% of INH-resistant strains have mutations to the *katG* gene (88, 129). Of this high percentage of INH-resistant strains of *M. tuberculosis*, the most common KatG variant identified was S315T KatG (88, 129–131). The S315T KatG variant has a minimum concentration that inhibits 50% bacterial growth (MIC_{50}) over 100-fold greater than that of *wt* KatG. Interestingly, despite its near complete loss of capacity to activate INH, S315T loses little, if any, of its catalase *or* peroxidase activities (88, 129–

131). The negligible loss in catalase activity is consistent with the prominent selection of this mutation in *M. tuberculosis* under pressure of INH treatment. In essence, a strain with this mutation can still effectively remediate oxidative stress while simultaneously abrogating INH activation. Structurally, the most notable alteration caused by the S315T substitution in KatG is a narrowing of its active-site access channel (Fig. 5.1A and B). This dramatically affects the distribution of water molecules within the active site (Fig. 5.1C and D). Despite many research endeavors, the direct correlation between these structural changes and the activation (or lack thereof) of INH is not fully understood.

Isoniazid activation by KatG and mechanism of action

INH is a pro-drug and requires activation by KatG once within the host's system (132, 133). It has been proposed that INH activation results in the conversion of INH to the corresponding isonicotinoyl radical ($IN^{\bullet}$) by KatG (65). The $IN^{\bullet}$ then reacts with NAD^{+}, creating an isonicotinoyl-NAD (IN-NAD) adduct (Fig. 5.2). Once formed, IN-NAD binds and inhibits the enoyl acyl-carrier protein reductase (InhA). This is an activity integral for mycolic acid biosynthesis, a process fundamental to the structural integrity of mycobacteria (134). However, neither the exact mechanism by which KatG initiates INH activation nor the steps leading to the formation of the IN-NAD adduct are well understood. Studies evaluating the binding of IN-NAD by InhA support the hypothesis that IN-NAD adduct formation precedes interaction with the final target, InhA(134). This indicates that binding to InhA does not facilitate IN-NAD formation and that the IN-NAD adduct is fully formed before inhibiting InhA. Understanding how KatG catalyzes the formation of $IN^{\bullet}$ and how

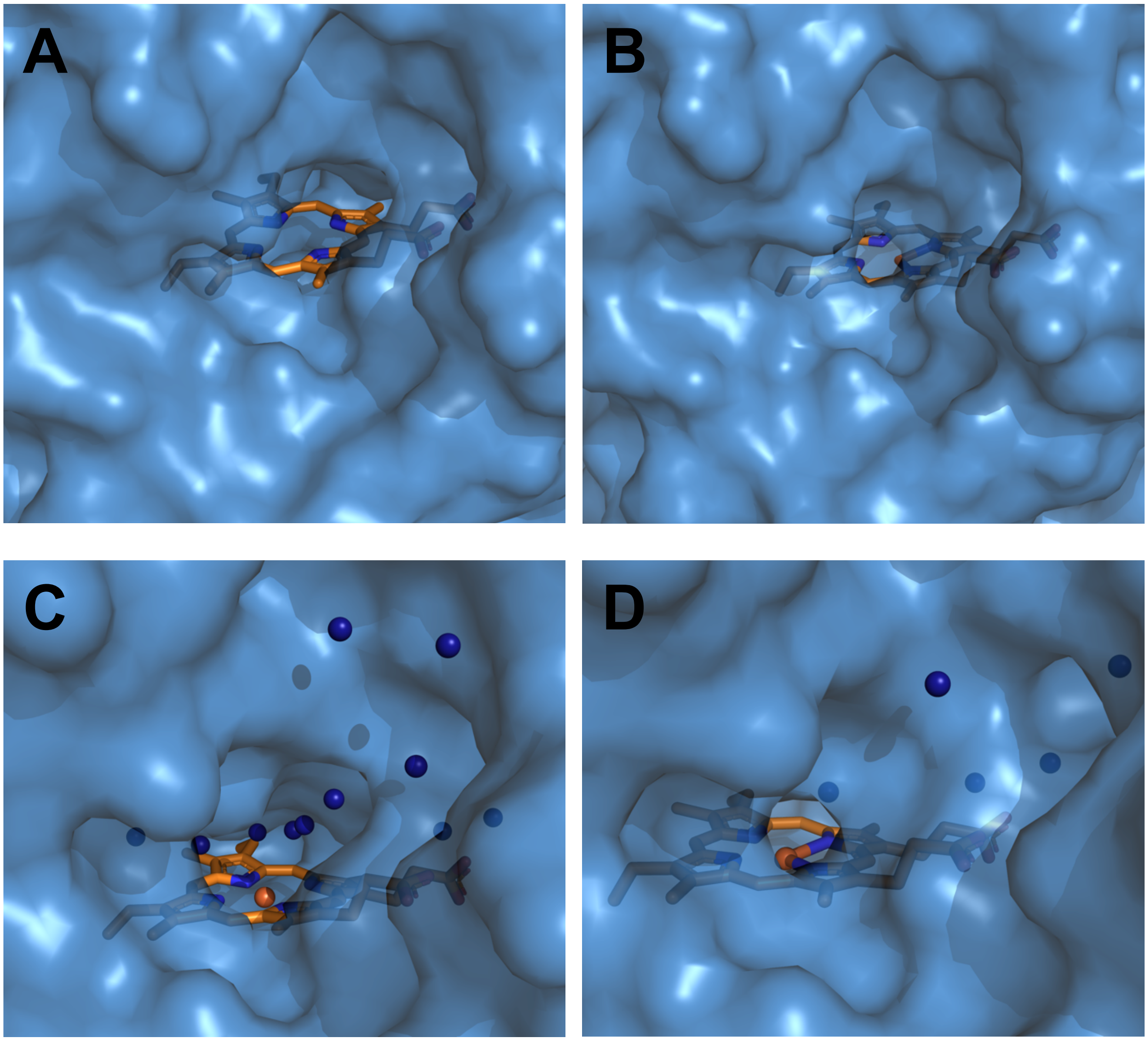

Figure 5.1. Effect of S315T mutation to the active-site channel of KatG. The active-site channel of *wt* KatG is very narrow (A) and is even narrower for the S315T KatG variant (B). The narrowing of the active-site access channel dramatically affects the water (dark blue spheres) distribution within the active site of the S315T variant (D) relative to *wt* KatG (C). PDB accession numbers: 2CCA and 2CCD.

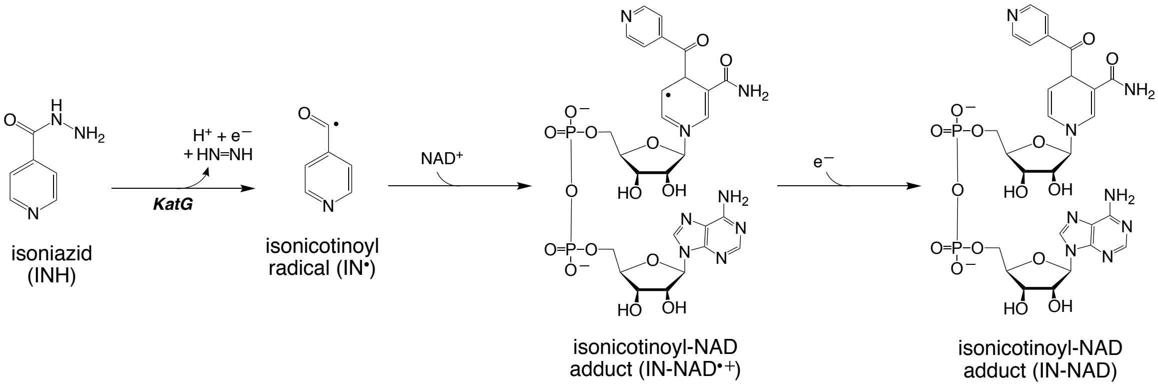
isoniazid
(INH)
H+ + e−
+ HN=NH
KatG
isonicotinoyl
radical (IN•)
NAD+
isonicotinoyl-NAD
adduct (IN-NAD•+)
e−
isonicotinoyl-NAD
adduct (IN-NAD)

Figure 5.2. Formation of IN-NAD adduct from INH and NAD$^+$. Shown is a schematic representation of the activation of INH by KatG and the subsequent adduct formation with NAD$^+$.

this leads to the formation of the IN-NAD adduct is needed for effective antitubercular drug development.

Drug development efforts and INH derivatization

A major effort being undertaken worldwide is to identify and develop new pharmaceutical leads that can be developed to serve as more effective antitubercular drugs. Most especially, candidates are sought that can be utilized for the treatment of drug-resistant strains of *M. tuberculosis.* Recently, Filomena Martins, Miguel Machuqueiro, and colleagues have developed derivatives containing longer acyl chains that are hypothesized to improve passage of the INH warhead through the cell wall of mycobacteria that serve as promising candidates for MDR-TB treatments (135). Preliminary work on an N'-acylated INH derivative, INH-C_{10}, indicates that the acylation not only stabilizes the compound leading to a lower level of spontaneous $IN^{\bullet}$ generation, but also facilitates cross-membrane transport and therefore accumulation of higher intracellular concentrations of the pro-drug compound (136). These promising results led to the generation of a panel of INH derivatives (Fig. 5.3) for kinetic evaluation and MIC_{50} determination. The compounds shown in Figure 5.4 are derivatives of INH and have been evaluated as INH analogs of INH for their ability to be converted to $IN^{\bullet}$ and ultimately, IN-NAD formation. Generation of $IN^{\bullet}$ formation was evaluated by the rate of conversion of nitro blue tetrazolium (NBT) to its formazan derivative (Fig. 5.5). Further, IN-NAD formation was detected as previously described, by monitoring absorption at 326 nm, the λ_{max} for the IN-NAD adduct (136).

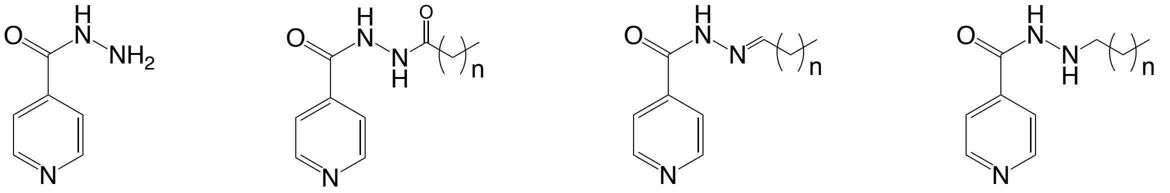

isoniazid (INH)

acyl derivative ($INH\text{-}C_n$)

imine derivative ($INH\text{-}iC_n$)

alkyl derivative ($INH\text{-}aC_n$)

Figure 5.3 Conceptual representation of INH derivatives to be evaluated. Acyl, imine, and alkyl INH derivatives will be explored in this study.

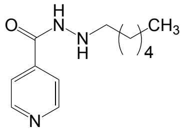

isonicotinoylhydrazide C6
INH-aC_6

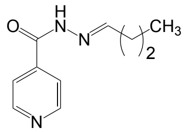

isonicotinoylhydrazone C4
INH-iC_4

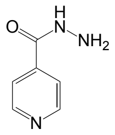

Isoniazid
INH

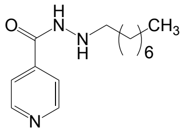

isonicotinoylhydrazide C8
INH-aC_8

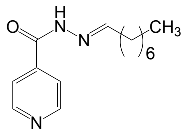

isonicotinoylhydrazone C8
INH-iC_8

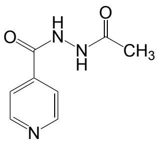

N’-acetylisonicotinohydrazide
INH-C_2

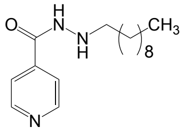

isonicotinoylhydrazide C10
INH-aC_{10}

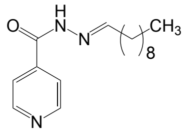

isonicotinoylhydrazone C10
INH-iC_{10}

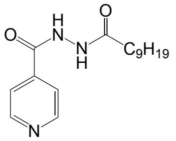

N’-decanoylisonicotinohydrazide
INH-C_{10}

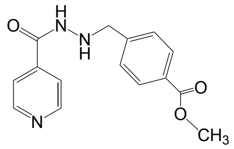

N’-isonicotinoylhydrazide
methyl 4-benzoate
N33red

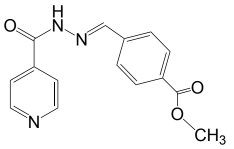

N’-isonicotinoylhydrazone
methyl 4-benzoate
N33

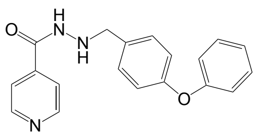

N’-isonicotinoylhydrazide
4-phenoxybenzene
N34red

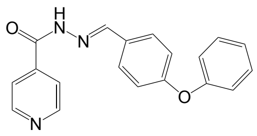

N’-isonicotinoylhydrazone
4-phenoxybenzene
N34

Figure 5.4. Structures of INH derivatives for this study.

5.2. Methods for determining activation by KatG

Nitro blue tetrazolium (NBT) assays

The tendency toward radical formation facilitated by reaction of INH derivatives with KatG was evaluated by the rate of conversion of nitroblue tetrazolium (NBT) to its corresponding formazan at 560 nm ($\varepsilon_{560} = 18{,}500\ M^{-1}\ cm^{-1}$). Reactions were carried out for 600 s (i.e., 10 min) in a solution containing 1.25 µM KatG, 0.2 mM NBT, 0.2 µM $MnCl_2$, and 1.0 mM INH or INH derivative. All assays were carried out in 50% DMSO and 50 mM Tris-HCl, pH 8.0 at room temperature. Absorption was monitored using a Shimadzu UV 160 spectrophotometer. All experiments were carried out in duplicate with three replicates for each condition, including data collected for a $MnCl_2$-negative control as well as a KatG-negative control. So-called initial rates of NBT conversion to formazan were obtained by fitting the raw traces by linear regression for the time points extending from 35 or 40 s to 100 s of the reaction. It is important to note that the first 35-40 s of the raw traces contain features consistent with mixing artifacts. These are, therefore, not included in the fitting and are represented by thin dotted lines.

Spectrophotometric evaluation of IN-NAD formation

Ultimately, KatG-dependent activation of INH results in the formation of the IN-NAD adduct. This was evaluated by monitoring the formation of the isonicotinyl-NAD (IN-NAD) adduct in the presence of INH or its acyl, imine, or alkyl derivatives. Rates of IN-NAD adduct formation were directly monitored by collecting spectra from 330-400 nm ($\varepsilon_{326} = 6{,}900\ M^{-1}cm^{-1}$) over an 840 s time window. Reactions contained 0.625 µM KatG,

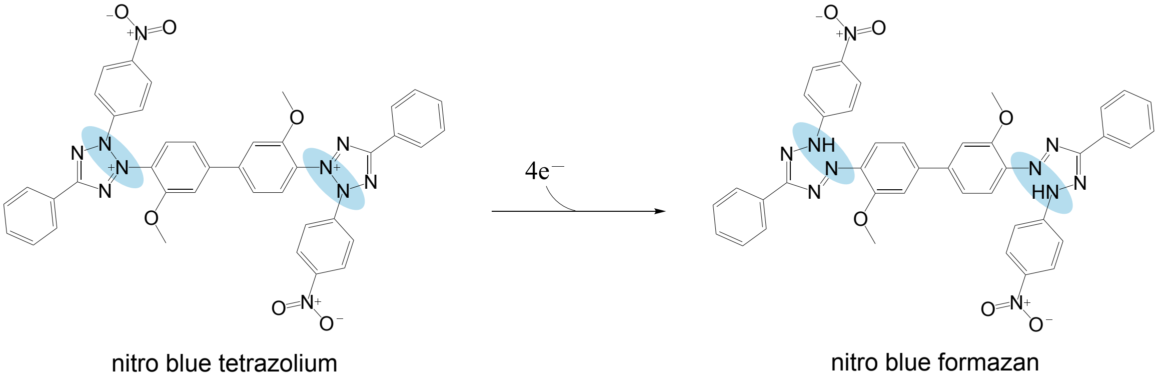
4e⁻
nitro blue tetrazolium
nitro blue formazan

Figure 5.5. Schematic representation of detection by NBT assays. Reaction with radical species in solution leads to the detection of formazan derivative at 560 nm.

0.4 mM NAD^+, 2 μM $MnCl_2$, and 1.0 mM INH or INH derivative. All assays were carried out in 50% DMSO and 50 mM Tris-HCl, pH 8.0 at room temperature. Results presented below include two experiments each, carried out with three replicates. Reactions evaluated included a $MnCl_2$-negative control and a KatG-negative control. IN-NAD formation was determined by plotting the absorbance from the λ_{max} of the difference spectra subtracted by the absorbance from the λ_{base} of the difference spectra, resulting in the effective ΔAbsorbance = Abs_{max} - Abs_{base}. Rates of IN-NAD adduct formation were determined by fitting the data to a single exponential function

Detection of IN-NAD formation by mass spectrometry

Reactions were carried out under the same conditions as described above for IN-NAD formation, except that volumes were doubled for a final reaction volume of 2 mL. Reactions were carried out at room temperature in an appropriate container for 10 mins to mirror the time analyzed in the spectrophotometer. After 10 mins, the reaction mixture was added to centrifugal filters with a 30 kDa cutoff and the reaction was filtered by centrifugation at 5,000 x *g* for 20 minutes. The filtrant, now free of KatG, was then separated by HPLC. HPLC separation was performed on an Agilent Technologies 1260 Infinity equipped with an Agilent 1100 series variable wavelength detector set to 326 nm. Filtered reaction products (24 uL) were separated on an Agilent Zorbax SB-C18 column (5 μm, 4.6 × 150 mm) heated to 50 °C with a flow rate of 0.2 mL/minute and an elution profile of 100% A (H_2O, 0.1% TFA) at t = 0 minute to 20% B (acetonitrile, 0.1% TFA) by 26 minutes. Any significant peaks from the chromatogram were collected for later MS analyses.

Mass spectrometric analyses was performed at the Auburn University Mass Spectrometry Center (Department of Chemistry and Biochemistry). An ultra-performance LC system (ACQUITY, Waters Corp., USA) coupled with a quadrupole time-of-flight mass spectrometer (Q-Tof Premier, Waters) with electrospray ionization (ESI) in positive mode using Masslynx software (V4.1). Sample (1 – 10 µL) was loaded on a C18 column (Waters UPLC BEH C18 2.1x50 mm, 1.7 µm) with a 300 µL/minute flow rate of mobile phase solution A. The capillary voltage was set at 3.1 kV, the sample cone voltage was 30 V, and the extraction cone was 4.3 V. The source and desolvation temperature were maintained at 125 and 300 °C, respectively, with the desolvation gas flow at 600 L/hour. The MS scan was 1.0 second long from 100 to 4000 m/z with a 0.02 second inter-scan delay using the centroid data format.

Synthesis of INH derivatives

Isoniazid derivatives were synthesized by collaborators at Universidad de Lisboa and confirmed by exact mass GC-MS and NMR.

5.3. Results

NBT assays

The rates of nitroblue formazan generation for INH and 12 of its INH derivatives are expected to be proportional to the $IN^\bullet$ formed in solution (Table 5.1). The parent compound, INH exhibited $IN^\bullet$ generation rates that were optimized with the inclusion of KatG and a source of Mn^{2+} ion (Fig 5.6). When KatG was excluded from the reaction, there is around a 4-fold decrease in rate of $IN^\bullet$ generation. Comparatively, there was only a ~1.5-

Table 5.1. Rate of Nitro Blue Formazan Formation by INH derivatives.

	All components	No Mn control	No KatG control
INH	$(6.76 \pm 0.76) \times 10^{-3}$	$(4.51 \pm 0.59) \times 10^{-3}$	$(1.61 \pm 0.51) \times 10^{-3}$
INH-C_2	$(2.76 \pm 2.0) \times 10^{-3}$	$(4.42 \pm 2.7) \times 10^{-3}$	$(7.79 \pm 12) \times 10^{-4}$
INH-C_{10}	$(4.48 \pm 2.18) \times 10^{-4}$	$(5.15 \pm 1.01) \times 10^{-4}$	$(6.02 \pm 6.54) \times 10^{-4}$
INH-aC_6	$(2.23 \pm 0.56) \times 10^{-2}$	$(2.09 \pm 0.40) \times 10^{-2}$	$(2.12 \pm 1.8) \times 10^{-2}$
INH-aC_8	$(1.52 \pm 0.45) \times 10^{-2}$	$(1.91 \pm 0.47) \times 10^{-2}$	$(1.30 \pm 0.92) \times 10^{-2}$
INH-aC_{10}	$(2.06 \pm 0.24) \times 10^{-2}$	$(2.20 \pm 0.67) \times 10^{-2}$	$(2.60 \pm 1.7) \times 10^{-2}$
N33Red	$(3.24 \pm 1.73) \times 10^{-3}$	$(3.08 \pm 1.58) \times 10^{-3}$	$(4.03 \pm 3.17) \times 10^{-3}$
N34Red	$(7.14 \pm 0.45) \times 10^{-3}$	$(7.65 \pm 0.09) \times 10^{-3}$	$(6.88 \pm 0.97) \times 10^{-3}$
INH-iC_4	$(2.06 \pm 0.24) \times 10^{-3}$	$(2.70 \pm 0.09) \times 10^{-3}$	$(4.69 \pm 2.1) \times 10^{-4}$
INH-iC_8	$(2.45 \pm 0.98) \times 10^{-3}$	$(3.03 \pm 0.42) \times 10^{-3}$	$(6.39 \pm 7.8) \times 10^{-4}$
INH-iC_{10}	$(2.17 \pm 0.38) \times 10^{-3}$	$(2.97 \pm 0.01) \times 10^{-3}$	$(5.45 \pm 17) \times 10^{-4}$
N33	$(7.88 \pm 5.15) \times 10^{-4}$	$(9.66 \pm 0.15) \times 10^{-4}$	$(4.60 \pm 7.77) \times 10^{-4}$
N34	$(6.09 \pm 3.59) \times 10^{-4}$	$(5.32 \pm 4.20) \times 10^{-4}$	$(6.79 \pm 5.32) \times 10^{-4}$

Values are the average rates (μM/s) of the two experiments with the range of the data representing the error.

fold decrease in rates of NBT formazan generation upon the exclusion of Mn. These data suggest that formation of $IN^{\bullet}$ from INH relies more on the presence of KatG than Mn^{2+} ion. Interestingly, the acyl derivatives of INH showed substantial rates of NBT formazan production even in the absence of KatG or added Mn^{2+}.

Indeed, activation of these compounds as judged by NBT formazan formation appeared to be inhibited by either Mn or KatG (Fig. 5.6). The alkyl derivatives aC_6, aC_8, aC_{10}, and N34Red show nearly the same rate of radical generation under all three reaction conditions (even without Mn or KatG present) (Fig 5.7). These data suggest that these compounds are participating in Mn- and KatG-independent radical generation. The imine derivative compounds exhibited a slight increase in rate in the absence of Mn^{2+}, and a significant increase in rate upon withholding KatG (Fig. 5.8). The response of the imine derivatives suggests that these compounds are not dependent on KatG to form a radical species. In contrast to other INH derivatives, N33 (imine) and N34Red (alkyl), these compounds show the most INH-like (i.e., KatG dependent) radical generation (Fig. 5.9). The increase in radical production by N33 is nearly halved when KatG is excluded from the reaction. Interestingly, N33 also exhibits an increase in rate when Mn^{2+} is absent and only KatG is present as a catalyst at 9.66×10^{-4} μM/s. The derivative N34Red shows considerably lower levels of KatG-dependent stimulation in radical production than N33; the KatG-dependent stimulation is a mere 2-fold increase in rate. Across all 12 derivatives by NBT conversion to NBT formazan, the imine derivatives of INH, especially N33, seem to be the most promising in that they are able to produce radical generation rates comparable to INH, and these rates are heavily dependent on the contribution of KatG.

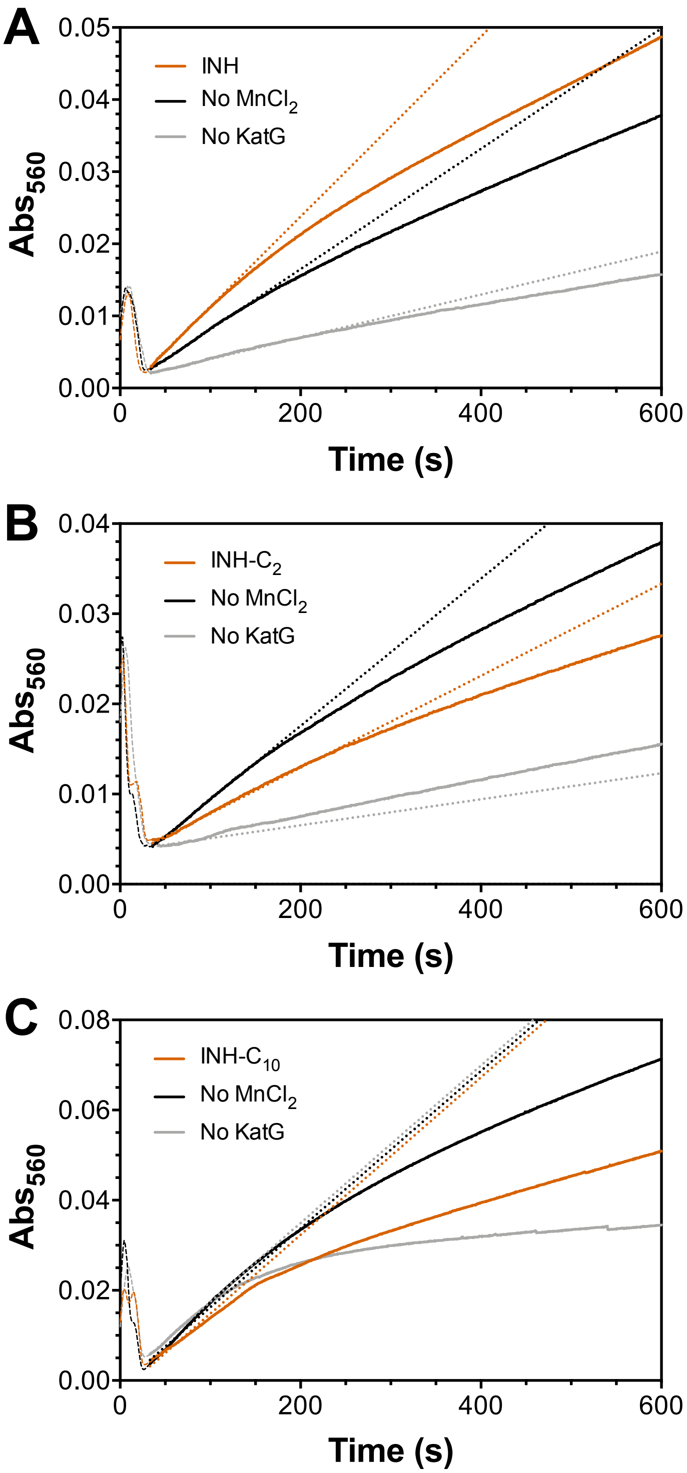

Figure 5.6. NBT assay results of INH and acyl INH derivatives. Contrast between response of radical formation by INH (A) and acyl derivatives INH-C_2 (B) and INH-C_{10} (C).

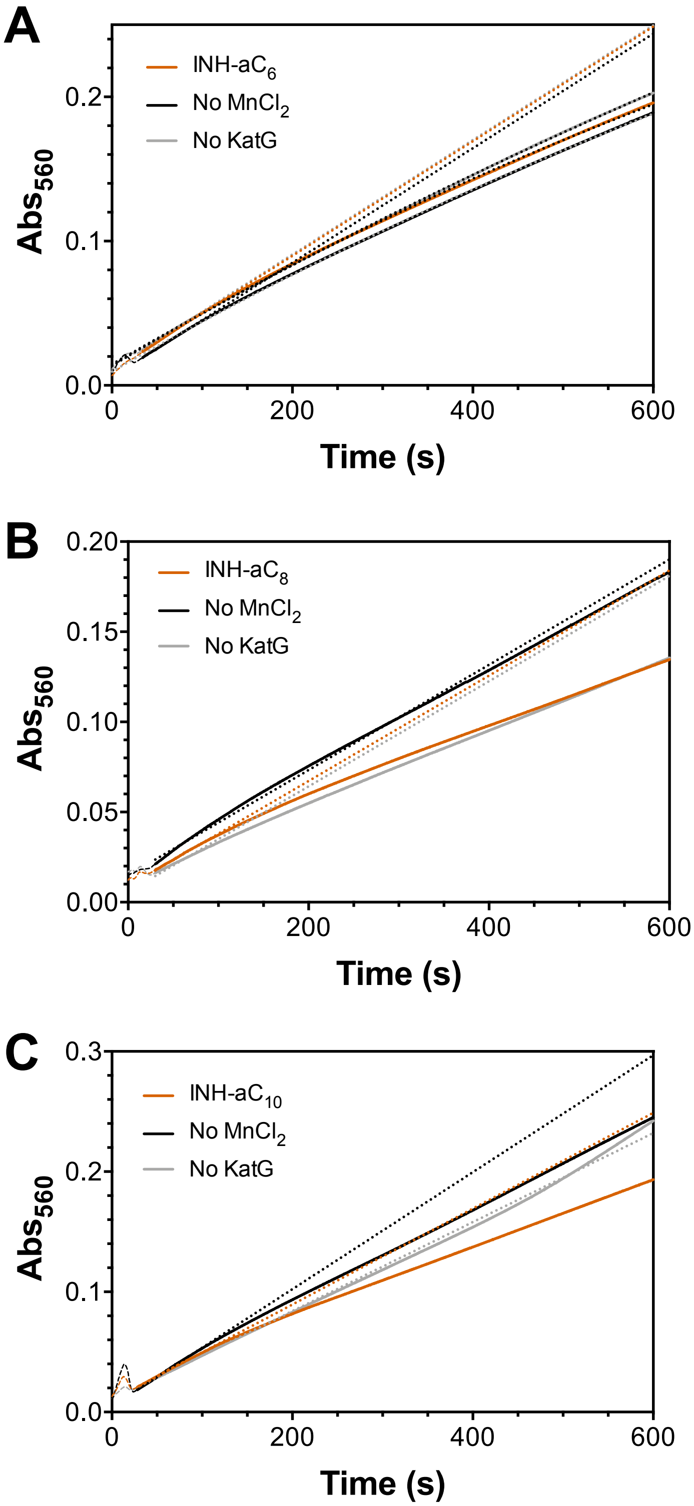

Figure 5.7. NBT assay results of alkyl INH derivatives.

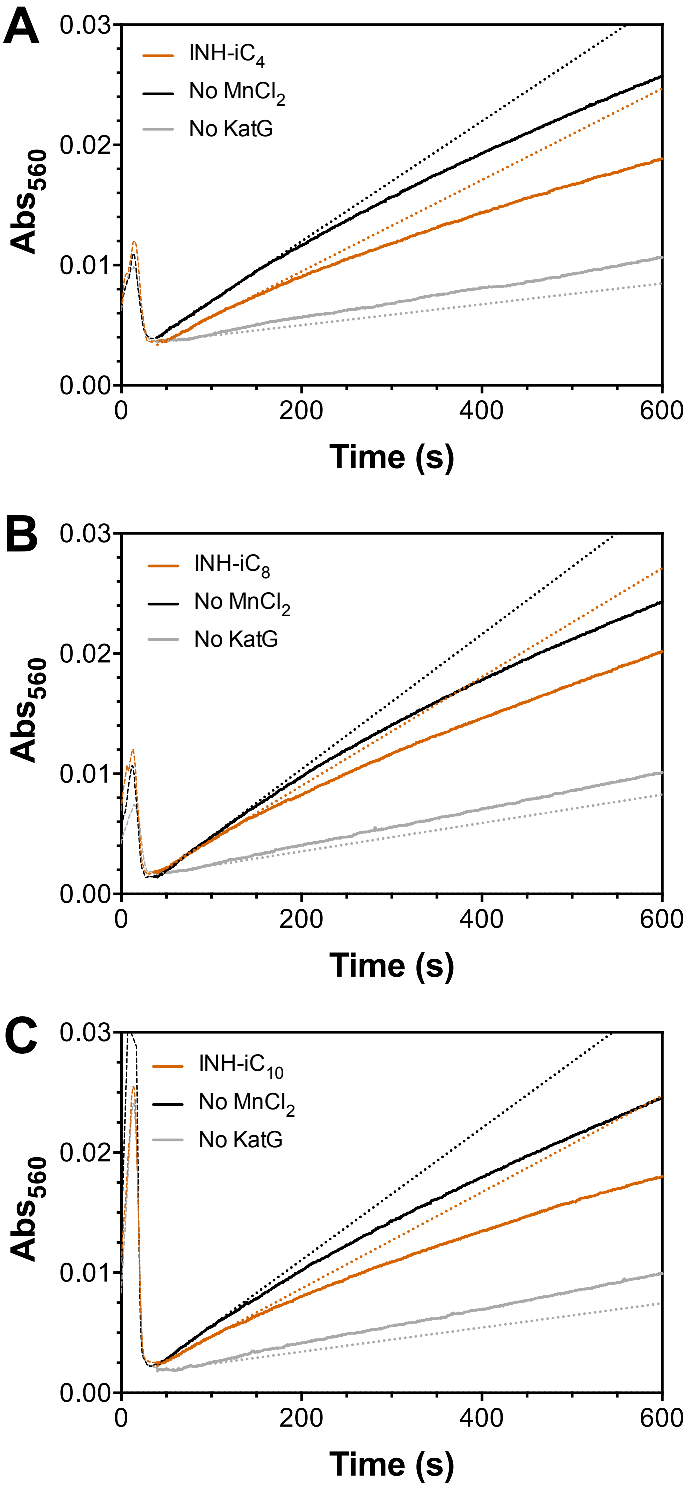

Figure 5.8. NBT assay results for imine INH derivatives.

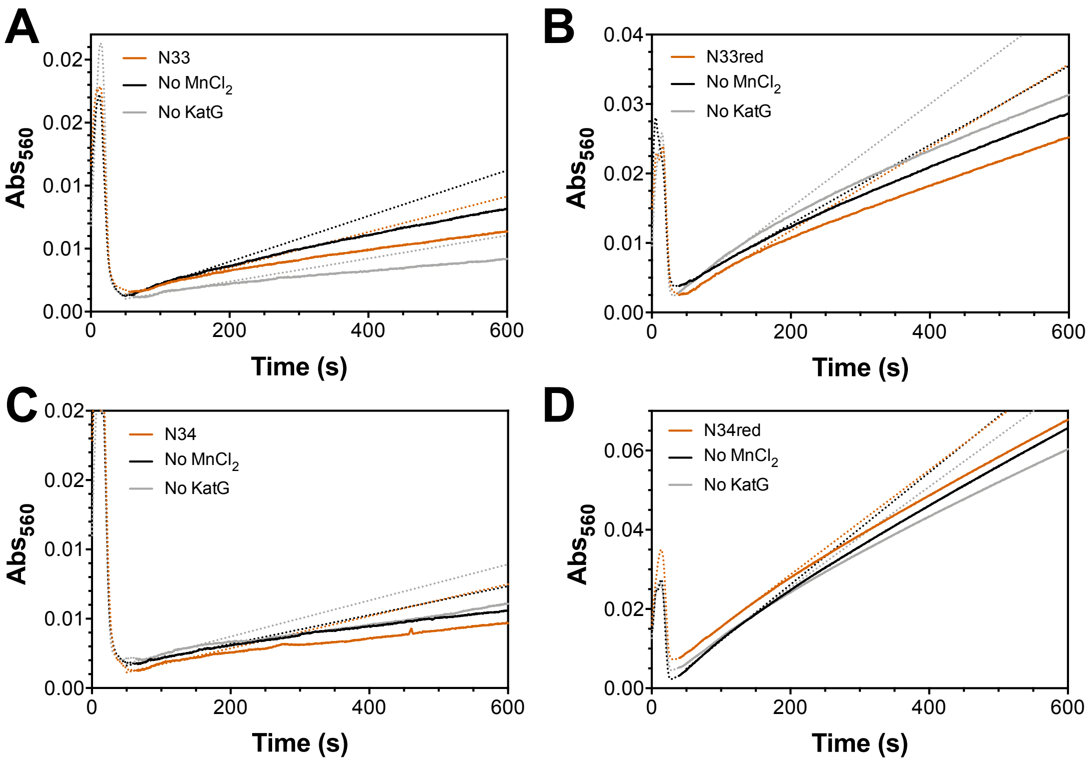

Figure 5.9. NBT assay results for N33 and N34 compounds.

Spectrophotometric evaluation of IN-NAD formation

Formation of the IN-NAD adduct from the activation of INH and eight of its derivatives was monitored by UV visible absorption. Due to the low concentration of IN-NAD actually being formed, the data were collected as difference spectra. Here the initial spectrum corresponding to the starting reaction condition served as the baseline for subsequent spectra throughout the rest of the reaction. An example is shown using difference spectra collected for INH (including the Mn- and KatG-negative controls). For INH, the amount of IN-NAD generated was dramatically affected by the presence of KatG, but not Mn^{2+} (Fig. 5.10). Across the imine derivatives, a substantial decrease in absorbance near 300 nm was observed, but a very slight increase in absorbance, presumably caused by formation of the IN-NAD, was detected at 326 nm (Fig. 5.11). This suggests that the parent imine derivative has an absorbance ≤ 300 nm and the decrease in absorbance in this region reports the conversion of this parent compound to some other species, not necessarily the IN-NAD adduct. Similarly, the alkyl derivatives seem to have little or no decrease in absorbance in the spectral region near 300 nm, and there is little or no increase in absorbance at 326 nm (Fig. 5.12). These data suggest that these compounds are also not leading to the formation of the IN-NAD adduct. Interestingly, in the difference spectra for all alkyl derivative reactions containing KatG, changes are observed in the spectrum around 400-420 nm where the KatG heme absorbs. This may indicate that there are changes occurring within KatG in these reactions. It is possible that either the absorption features of the imine derivatives are strong enough to overpower these changes in heme absorption or that the imine derivatives do not affect KatG in the same way that alkyl derivatives do.

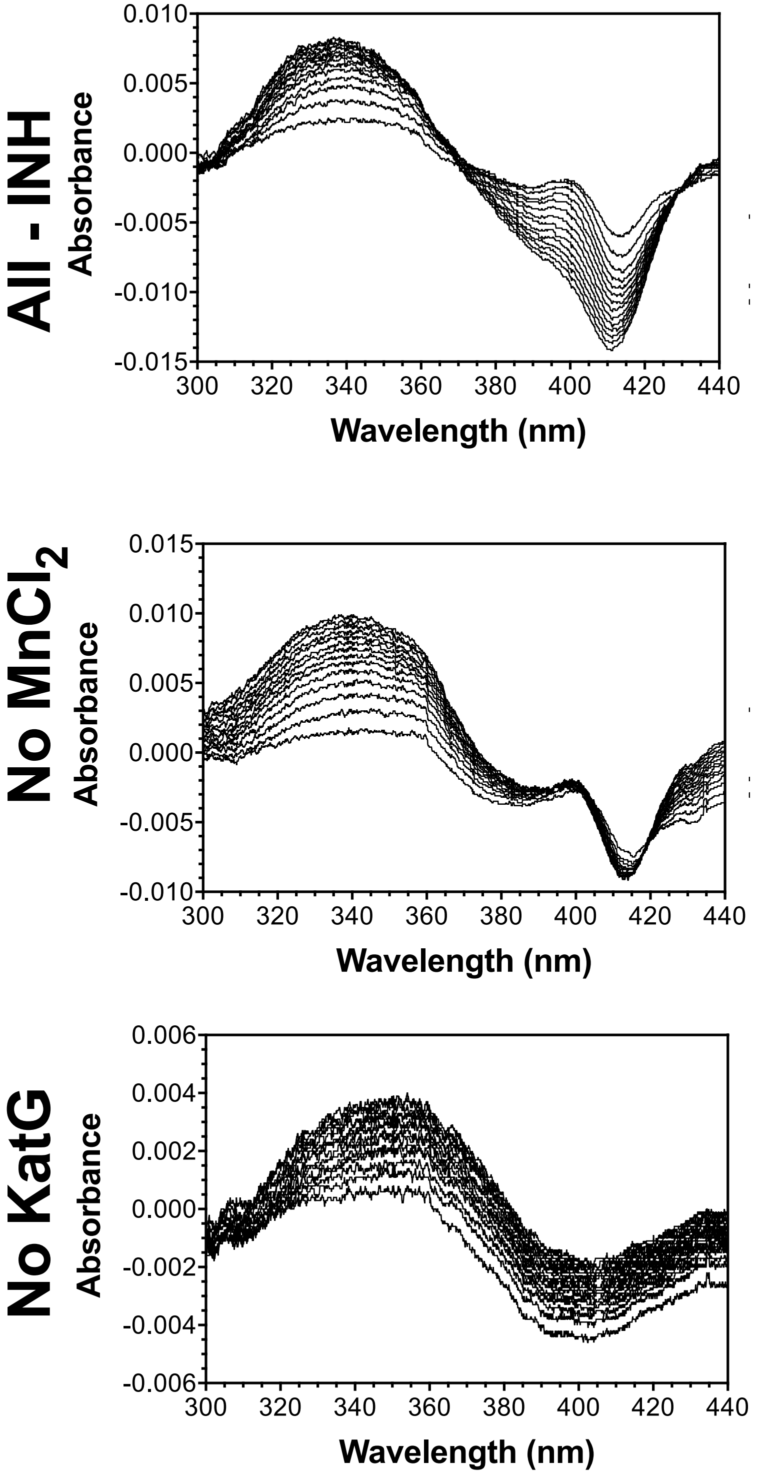

Figure 5.10. IN-NAD formation by INH and KatG. The formation of IN-NAD by KatG and INH is clarified by this series of difference spectra collected over 10 min.

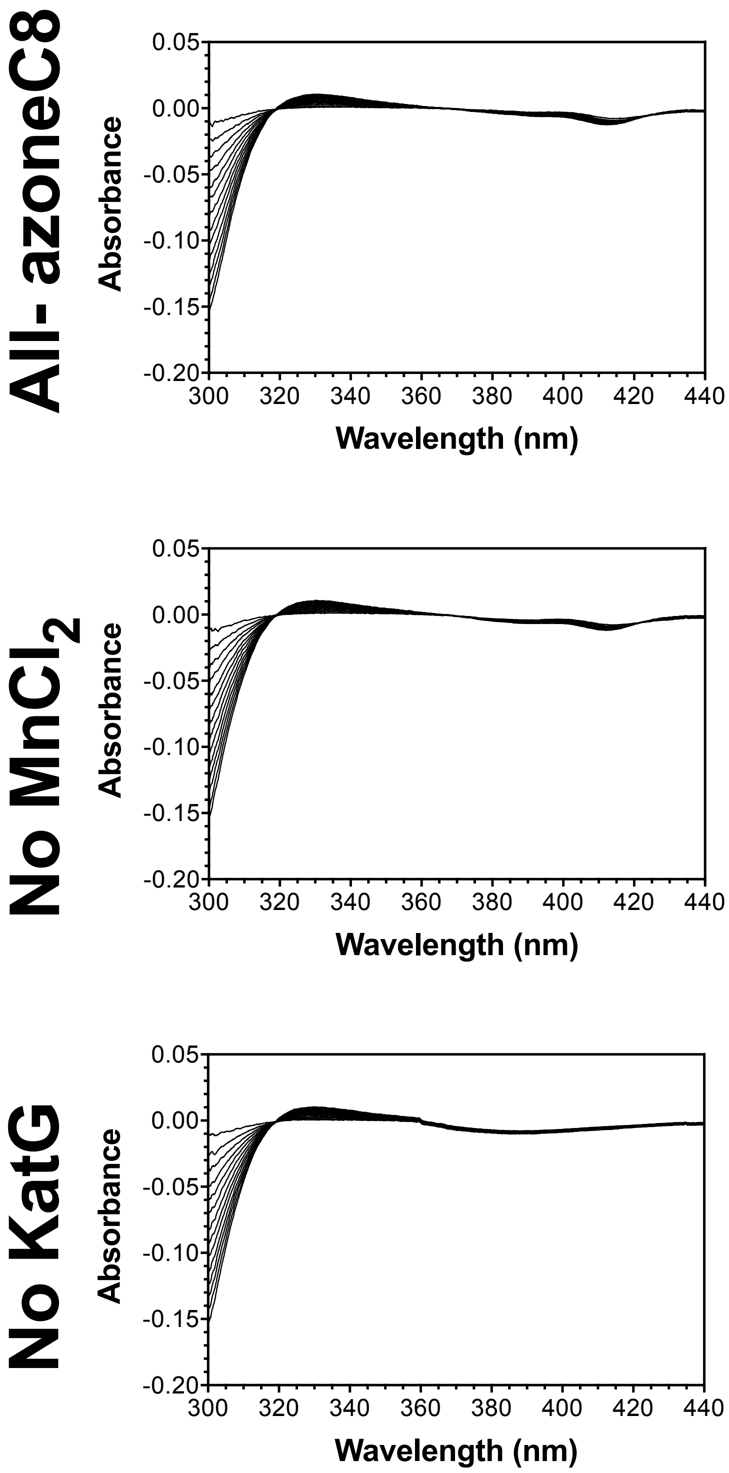

Figure 5.11. IN-NAD formation by imine derivatives.

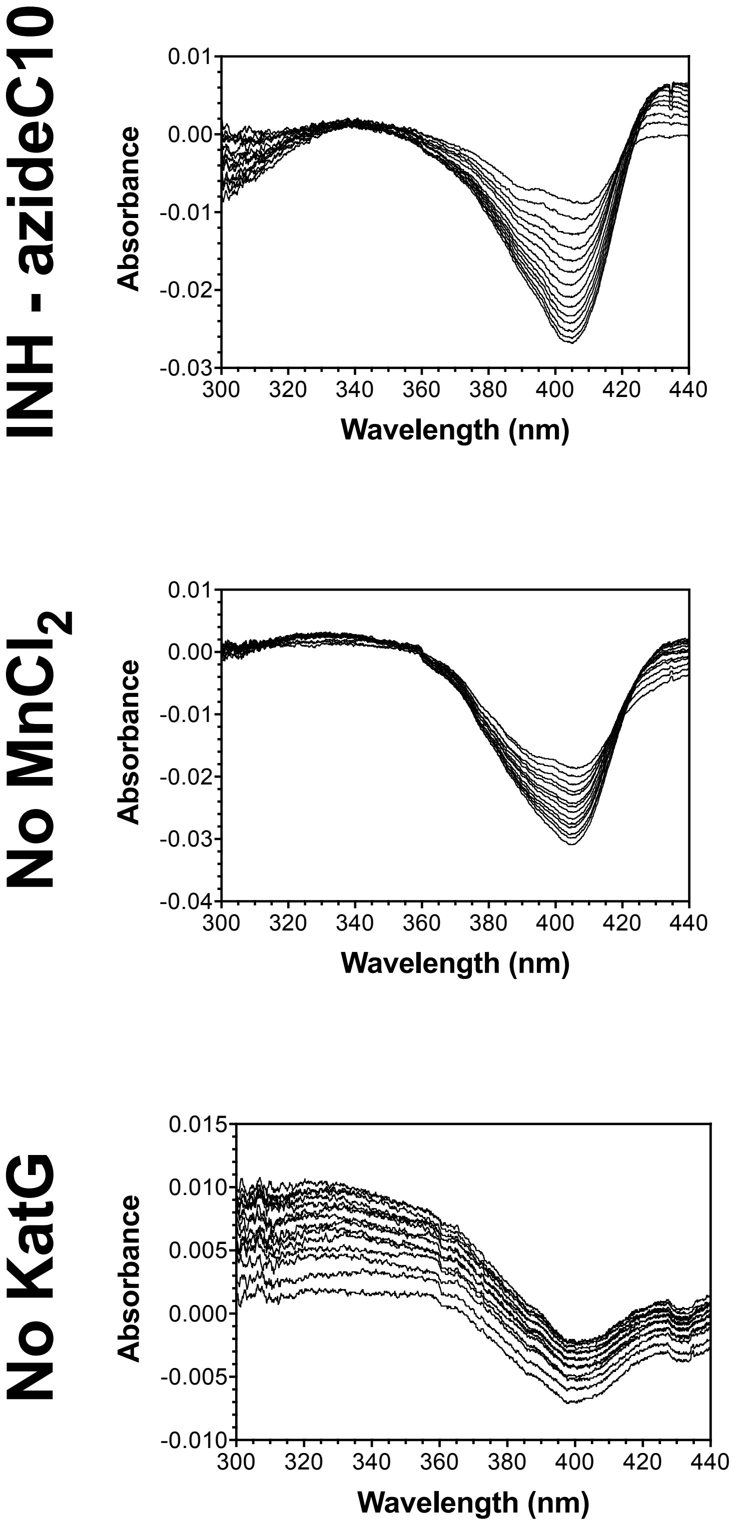

Figure 6.12. IN-NAD formation by alkyl derivatives.

To understand what these compounds are forming other than the IN-NAD adduct, products from reactions with KatG will be evaluated by mass spectrometry.

Attempts to detect IN-NAD formation by LC/MS

The HPLC/LC-MS separation protocol was tested using reaction between INH and KatG as a control. From these test reactions, INH and NAD were identified and confirmed by MS (Fig. 5.13). The amount of IN-NAD formed in the INH reactions were too small for detection by MS after HPLC separation. Future attempts will use imine derivatives as the test compound due to the much larger change in absorption observed for the imine compounds.

5.4. Conclusions

Interestingly, most of the INH derivatives synthesized for this study do not exhibit KatG-dependent radical generation, but instead undergo a spontaneous and non-enzymatic radical generation process. Additionally, these INH derivatives did not facilitate IN-NAD adduct formation. Despite this, the hydrazide INH derivatives have lower MIC_{50} (data not presented here), indicating they may be better candidates for alternative therapeutic development. Further investigation of the hydrazide INH derivatives is needed to conclude their efficacy as a therapeutic treatment. Additionally, future investigations should explore the efficacy of the INH derivatives synthesized for this study against the S315T KatG variant.

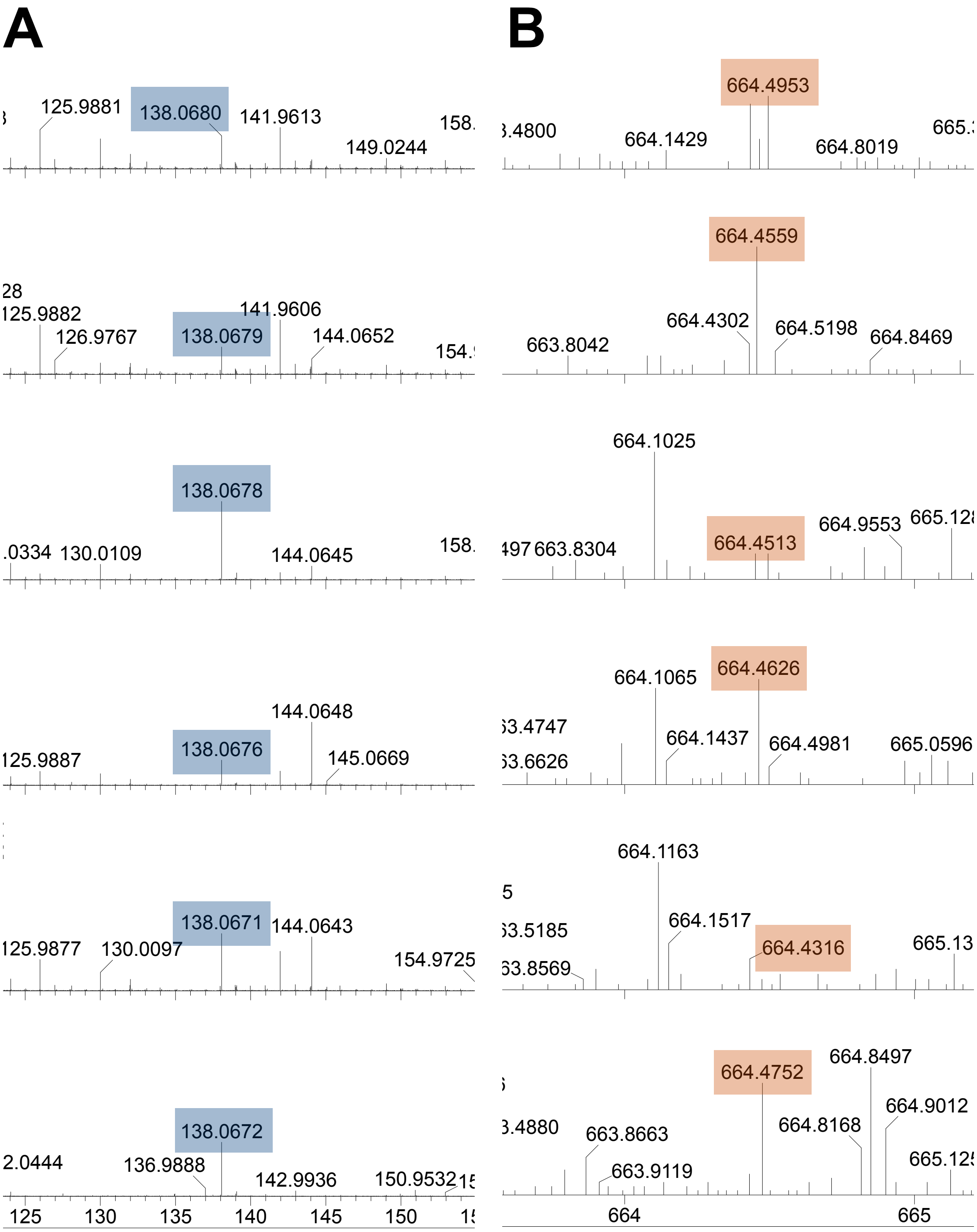

Figure 5.13. INH and NAD MS ions detected from reactions of KatG with INH separated by HPLC. Six peaks with similar retention times detected at 326 nm from three separate injections are shown above. INH can be detected in the lower m/z region (A) in addition to NAD that is detected in the higher m/z region (B) for all samples. Lacking from these samples, however is any m/z value corresponding to a 768.53 gmol^{-1} IN-NAD adduct.

Chapter Six

KatG Within the Context of the Peroxidase-Catalase Superfamily

In most contexts, protein oxidation events are recognized as detrimental to enzyme function. However, oxidative protein modification can be harnessed to the benefit of enzyme mechanism, and ultimately, cellular function. In recent years, the dramatic increase in available protein structural data has revealed a growing list of enzymes whose structures include covalent links between amino acid side chains, hydroxylations and other oxidative transformations. KatG, in particular, has evolved to not only to withstand protein oxidation, but capitalize on these events to form covalent adducts within the active site and protect enzyme function by self-sacrificial residue oxidation.

6.1. The peroxidase-catalase superfamily of heme peroxidases

The peroxidase-catalase superfamily is the largest superfamily of the heme peroxidases. Other heme peroxidase superfamilies include peroxidase-cyclooxygenase, peroxidase-chlorite dismutase, etc., however, this chapter will focus on the peroxidase-catalase superfamily. Heme peroxidases utilize H_2O_2 for the oxidation of larger biomolecules ranging from other proteins (cytochrome *c*) to phenolic compounds such as veratryl alcohol (Reference Fig. 1.6). Traditionally, members of this superfamily have been subcategorized into three classes of proteins (i.e., Class I, Class II, and Class III), however, more recent phylogenic studies have emphasized that such denotation is misleading and suggest the use of Family I, Family II, and Family III (137). A direct comparison of representatives across the three families of the peroxidase-catalase (PC) superfamily demonstrates that the majority of these enzymes are single-domain proteins. Active-site access channels tend to be broad, enabling peroxidatic electron donors (PxEDs) approach the enzyme's heme edge for oxidation by direct electron transfer (Fig. 6.1). Heme peroxidases from the peroxidase-catalase superfamily are found across a broad range of prokaryotes and eukaryotes, and both intracellular and extracellular members are known. As discussed in Chapter 1, the distal and proximal triads that are conserved across this superfamily. These are Trp/Phe, Arg, and His and Trp/Phe, Asp, and His, respectively.

Family I

The three main types of enzymes in Family I are Ascorbate peroxidases (APxs), cytochrome *c* peroxidases (C*c*Ps) and catalase-peroxidases (KatGs). Interestingly, this family bears the most structural diversity of the three families of the peroxidase-catalase heme peroxidase superfamily. All Family I enzymes have Trp residues as the third members of both distal and proximal triads. This proximal Trp residue has been identified to be oxidized in both KatGs and C*c*Ps. Oxidation of the proximal Trp in APx, however, is prevented by a K^+ ion that is bound nearby. As their names suggest, the biological electron donors of APx and C*c*P are ascorbate and cytochrome *c*, respectively. Ascorbate oxidation by APxs within the cell provide a method for acquiring a soluble antioxidant, and signal molecule for processes like cellular growth (137, 138). C*c*Ps which are assumed to be located within the intermembrane space of mitochondria, are thought to play a role in

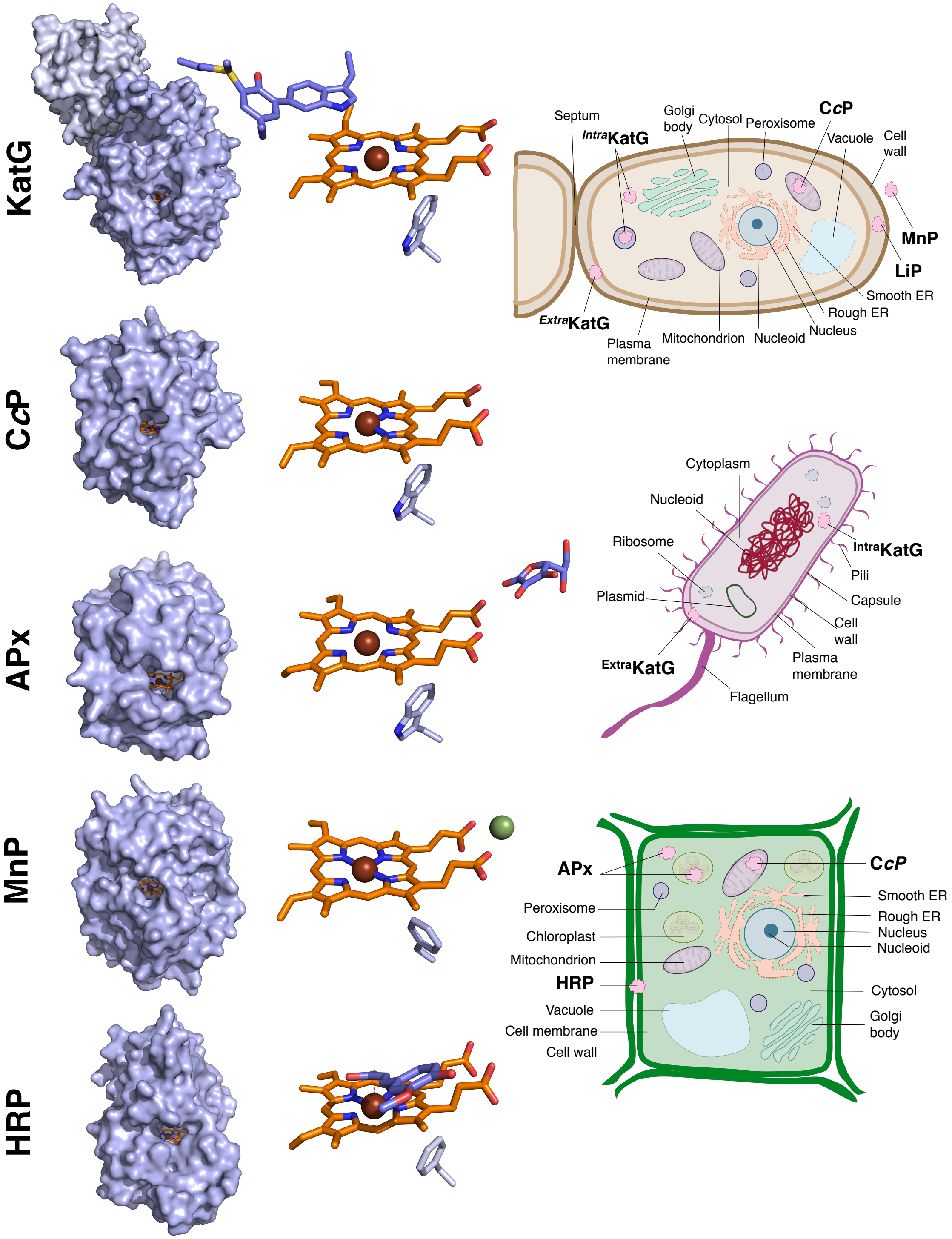
KatG
CcP
APx
MnP
HRP
Septum
IntraKatG
Golgi body
Cytosol
Peroxisome
CcP
Vacuole
Cell wall
MnP
LiP
Smooth ER
Rough ER
Nucleus
Nucleoid
Mitochondrion
Plasma membrane
ExtraKatG
Cytoplasm
Nucleoid
Ribosome
IntraKatG
Pili
Capsule
Plasmid
Cell wall
Plasma membrane
ExtraKatG
Flagellum
APx
CcP
Peroxisome
Smooth ER
Rough ER
Nucleus
Nucleoid
Chloroplast
Mitochondrion
HRP
Cytosol
Vacuole
Golgi body
Cell membrane
Cell wall

Figure 6.1. Active-site channel and *in vivo* expression comparison of PC superfamily.

oxidative stress response as a result of aerobic metabolism. C*c*P has been proposed to not only degrade H_2O_2 but also by act as a redox sensor (138, 139). An interesting result of the oxidative stress sensing capabilities of C*c*P is the preservation of its heme for transfer to a peroxisomal-mitochondrial catalase (Cta1), a more robust H_2O_2-degrading enzyme, under oxidatively stressful conditions (139). Of these enzymes, only KatGs are comprised of 2 domains (with the exception of a handful of Hybrid A2 heme peroxidases) (140). The C-terminal domain of KatG, caused by a gene duplication event, is a heme peroxidase scaffold, but it does not have the ability to bind heme (141, 142). The C-terminal domain of KatG, however, is crucial for proper folding and binding of the heme to the N-terminal domain where catalysis takes place (141, 142). Perturbation of the C-terminal domain results in a hexacoordinate heme center. Additionally, only KatG is capable of robust catalase activity in addition to the presumed peroxidase activity of this superfamily. Its robust catalase activity is facilitated by a unique post-translational modification to the distal Trp residue which involves the crosslinking of nearby Tyr and Met residues.

Family II

Family II is comprised of fungal secretory heme peroxidases including manganese peroxidase (MnP), lignin peroxidase (LiP), and versatile peroxidase (VP). These peroxidases play an important role in nature as they are responsible for the degradation of lignin by utilizing H_2O_2 to oxidize the large, irregular, polyphenolic structure. All Family II enzymes have Phe residues in both distal and proximal heme pockets. Lignin degradation by MnP is facilitated by a manganese (Mn^{II}) ion bound near the propionate chains of the heme *b* cofactor (143). The Mn^{II} ion is proposed to be oxidized to Mn^{III} by electron transfer through sigma bonds of the heme propionate near the metal ion (76). LiP oxidizes phenolic substates through long-range electron transfer via a redox cycling surface Trp (143, 144). VP is unique in that it has both the surface Trp residue analogous to LiP and the binding site for a Mn^{II} ion as seen in MnP, and therefore is capable of both mechanisms of substrate oxidation (143). Though LiP and MnP exhibit slight preferential substrate oxidation to veratryl alcohol and oxalate, respectively, generally these enzymes can oxidize a diverse panel of irregular compounds. In part, this is facilitated by relocation of the oxidizing component to the surface of the enzyme where it can interact with the substrate on the surface of the enzyme, enabling for the oxidation of a range of substrates and allowing for oxidation of substrates that by nature have highly irregular structure (i.e., lignin).

Family III

Family III, the largest group of the peroxidase-catalase superfamily, includes secretory plant peroxidases such as horseradish peroxidase (HRP), soybean peroxidase (SbPx), and peanut peroxidase (PNP). These peroxidases are responsible for the oxidation of phenolic compounds utilized in the formation of complex biomolecules such as lignin and secondary metabolites by the reduction of H_2O_2 to water (137). As such, their roles within organisms are related to cellular defense against pathogens, healing wounds, cell wall metabolism, and auxin catabolism and elongation (137, 145). The large, open active-site access channel of these peroxidases enable oxidation of the phenolic substrate compounds at the heme edge. Family III enzymes, like those of Family II, have Phe residues in place to complete the triad of conserved peroxidase residues.

Hybrid A peroxidases (APx-CcP hybrids)

Hybrid A peroxidases or APx-C*c*P hybrids are members of Family I and considered the first descendants of bacterial KatGs and the predecessors of monofunctional APxs and C*c*Ps (138). Two groups of Hybrid A enzymes have been identified. Hybrid A1 enzymes have been assigned as those from the Trypanosomatids subfamily and the Hybrid A2 enzymes have been assigned as those from eithr Excavates or Rhizaria subfamilies (138). Structurally, Hybrid A2 enzymes are the most similar to KatGs with both distal and proximal Trp residues, and a handful of APx-C*c*Ps are also two-domain proteins where the domains are highly similar to each other; in the case of the Hybrid A2 enzymes, however, both domains bind heme (138, 146). Hybrid A1 enzymes have both distal and proximal Trp residues and are single domain enzymes. Functionally, APx-C*c*Ps demonstrate both the ability to oxidize ascorbate and cytochrome *c* (138, 146, 147). Additionally, down-regulation or loss of APx-C*c*P expression results in a significant increase in intracellular H_2O_2 concentration, suggesting the major role of these enzymes to be redox mediation (146, 147).

Hybrid B peroxidases

Hybrid B peroxidases, thus far only identified in fungi, are all two-domain enzymes with an active peroxidase domain and a carbohydrate-binding C-terminal domain (140). The categorization of Hybrid B peroxidases has been difficult, and it remains to be resolved. Early studies suggested that these were most closely related to Family III enzymes, but more recent phylogenic studies suggest a common ancestor for Family II, III, and Hybrid B enzymes (138, 140, 148). Hybrid B peroxidases are not capable of ascorbate binding or cytochrome *c* oxidation but do contain the residues necessary for Mn^{II} binding near the heme propionate groups (138). The catalytically necessary distal Arg and His residues as well as the proximal Asp and His residues are conserved across all Hybrid B peroxidases (140). There is some variation, however, on the third member of both the distal and proximal triads; the majority of Hybrid B enzymes have a Phe in the distal and proximal heme pockets, though there are cases where a Tyr can be found in the distal heme pocket or where a Trp residue is situated on the proximal side of the heme (140). There are even rare cases where the distal triad consists of Lys, Tyr, and His. The reason and functionality for this unprecedented switch of Arg to Lys is not yet understood. In all, the Hybrid B peroxidases are an interesting, newly identified group from the peroxidase-catalase superfamily and their enzymatic capabilities and role within fungal cells has not been determined.

6.2. Roles of redox activity of residues within oxidoreductases

Like any other oxidoreductases, heme peroxidases encounter high levels of oxidative stress as they directly react with ROS. Cofactors, especially metallocofactors facilitate chemistry between triplet O_2 and enzymes. This frequently leads to the generation of high-valent metallo species (e.g., ferryl-oxo) and or reactive oxygen species (e.g., $O_2^{\bullet-}$) Redox-active metal centers also react with ROS themselves (e.g., H_2O_2) to generate the same kinds of high-valent metal centers. The consequences, however, of generating species with high redox potentials can be costly and likely results in protein oxidation. Protein oxidation can involve the generation of residue-based radical species, leading to residue crosslinking or interprotein aggregation, or even incorporation of oxygen into the peptide structure by residue modification. The residues with the sidechains most-likely to be oxidized in such events are Met, Cys, His, Tyr, and Trp. Among these residues, Met, Cys, Tyr, and Trp can be referred to as redox-active residues, as they participate in reversible oxidation. There are a number of ways that each redox-active residue can undergo oxidation. Figure 6.2 provides a few common examples of how these residues are structurally altered after oxidation and/or oxygenation, such as the formation of 5-hydroxytryptophan, cysteine sulfonic acid, and methionine sulfone. Other structures formed by protein oxidation that are not provided in Figure 6.2 includes simple protein-based radicals such as tryptophanyl radical. Though protein oxidation is often detrimental to function, some enzymes utilize these types of modifications for catalytic benefit. There are a number of methods by which the oxidation of the residues can play key roles in redox sensing, aiding catalysis within enzymes, or even protection of the enzyme.

Redox sensing

The reversible oxidation of Met and Cys residues often serve as a mechanism to act as a redox sensor for regulation of gene expression. A well-documented example is the activation of transcription factor OxyR from *E. coli*. When Cys199 of OxyR is oxidized to its sulfenic acid state, this initiates disulfide bond formation with Cys208. The formation of Cys199-Cys208 disulfide bond induces cooperative binding to RNA polymerase to activate transcription of genes such as *katG* and *oxyS* (149, 150). Subsequent reduction of this disulfide bond then halts transcription. Similarly, in yeast, oxidant receptor peroxidase 1 or Orp1 has been shown to be a sensor of H_2O_2 capable of signal transduction to Yap1, a transcription factor responsible for H_2O_2 homeostasis. When overwhelmed by H_2O_2,

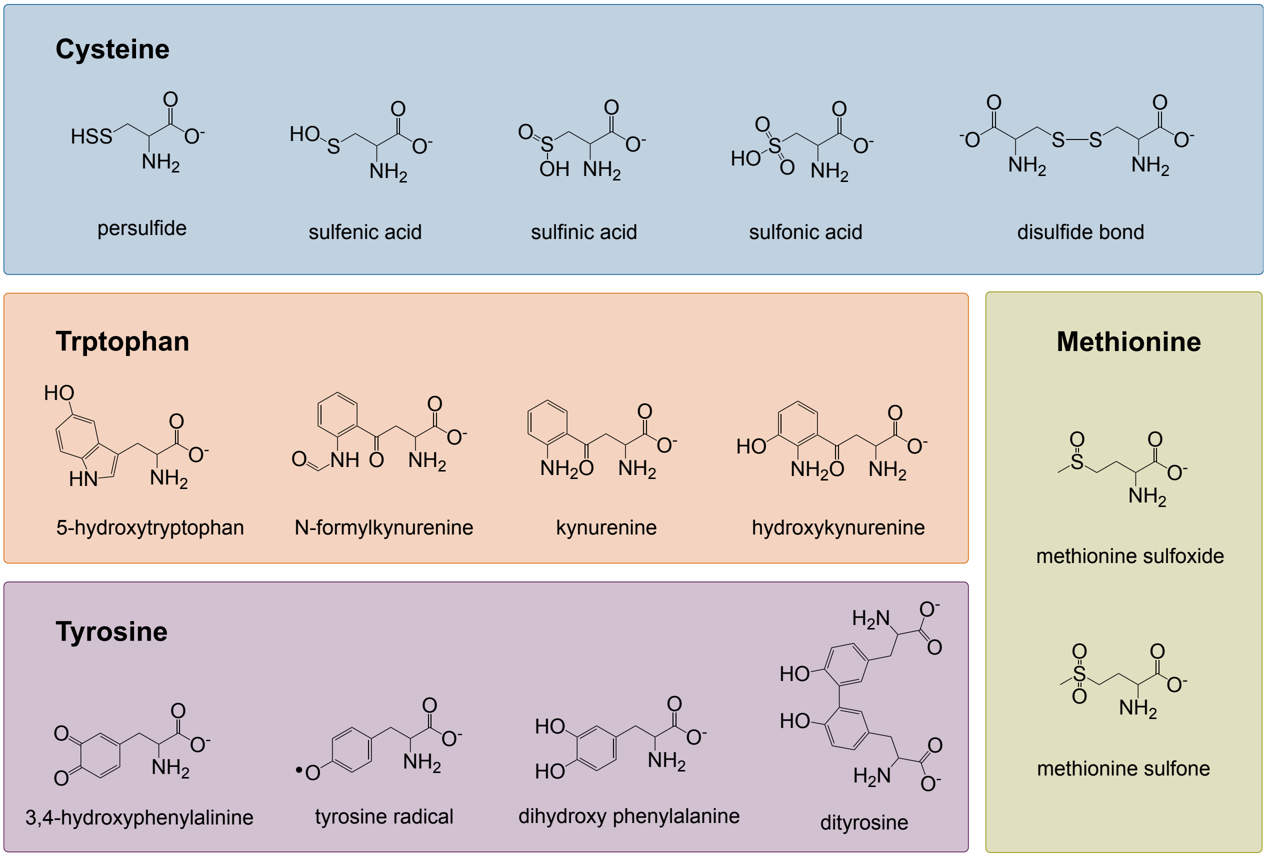
Cysteine
persulfide
sulfenic acid
sulfinic acid
sulfonic acid
disulfide bond
Trptophan
5-hydroxytryptophan
N-formylkynurenine
kynurenine
hydroxykynurenine
Methionine
methionine sulfoxide
methionine sulfone
Tyrosine
3,4-hydroxyphenylalinine
tyrosine radical
dihydroxy phenylalanine
dityrosine

Figure 6.2. Common oxidation and oxygenation products of redox-active residues.

Orp1 Cys36 is oxidized to sulfenic acid. This sulfenic acid form of Cys36 then reacts with Yap1 Cys598, generating a disulfide bond between proteins. This interprotein disulfide bond is then rearranged to yield an intramolecular disulfide bond between Yap1 Cys303 and Cys598, and the reduced form of Orp1 (151). Lastly, an example of reversible Met oxidation to methionine sulfoxide serving as redox sensor and activation mechanism for a transcription factor is HypT (or hypochlorite-responsive transcription factor) from *E. coli*. HypT is the first transcription factor to be exclusively activated by HOCl and therefore protecting the cells specifically from HOCl damage (152). Activation of HypT is dependent on the oxidation of Met123, Met206, and Met230 to methionine sulfoxides. The oxidation results in a change in oligomeric conformation form a dodecomer ring to tetramers, stimulating interaction with DNA causing the up-regulation of genes involved in Cys and Met biosynthesis and down-regulation of genes involved in Fe homeostasis (152–154). As expected, inactivation of HypT is accomplished by methionine sulfoxide reduction to Met by methionine sulfoxide reductases (154).

Enzyme preservation

A critical role of Met, Tyr, and Trp residues that has been proposed, especially within oxidoreductases, is the sacrificial self-oxidation for the preservation of active site integrity and enzymatic function. Met, Trp, and Tyr (along with Cys) all undergo facile oxidation around 1 V (vs. NHE), which is within range of most redox-active cofactors in biology (74, 81, 155, 156). These residues can undergo oxidation in lieu of oxidization of residues or the cofactors within the active site in order to avoid compromising enzymatic function. Specifically, methionine sulfoxide formation has been reported in a number of enzymes without the loss of activity (157). Furthermore, it has been observed that under acidic conditions, which would be biologically relevant for oxidative stress conditions, ROS such as H_2O_2 and HOCl oxidize Met residues preferentially (155). Drs. Gray and Winkler have executed extensive studies on the incorporation and roles of Trp and Tyr residues within enzymes. Among the oxidoreductases *that react with oxygen*, 66% and 81% were found to have an above-average Tyr and Trp content, respectively. More specifically, 68% of cytochromes P450 have Trp residue content that is above average (158). Furthermore, they have investigated the incorporation of these residues in organized chains that facilitate long-distance electron transfer (10 – 20 Å) by accomplishing numerous smaller electron transfers (5 – 8 Å) between residues (79). A general study of the Protein Data Bank revealed that oxidoreductases and hydrolases contained the greatest occurrences of chains consisting of three or more residues (81). 88% of oxidoreductases that react with O_2 contain chains of Trp and Tyr residues, and 50% have linear chains that are three or more residues long (81). These chains of Tyr and Trp residues can not only play a role in the main mechanism of an enzyme by facilitating hole-hopping to accomplish long-distance electron transfer, but also can play a protective role by redirecting damaging electron holes away from the catalytically active core of the enzyme.

Catalytic mechanism intermediate

In addition to playing accessory roles within enzymes, amino acid side chains can also directly participate in catalysis. The facile oxidation of Tyr, Trp, and Cys residues to form their respective radical forms constitutes the vast majority of protein-based catalytic intermediates that participate in catalytic mechanisms. The unique placements of these catalytically necessary residues can sometimes enable unique and selective chemistry that would not be easily mimicked by bulky cofactors. For example, prostaglandin H synthase (PGHS) is a bifunctional enzyme capable of cyclooxygenase and peroxidase activity. The formation of the Tyr385 radical is necessary for the abstraction of the 13-pro(S) hydrogen of the arachidonate by prostaglandin H synthase (159–162). The highly oxidized heme cofactor is reduced by the nearby Tyr385, positioned perfectly for H-abstraction from arachidonate. Similarly, linoleate diol synthase (LDS) another enzyme that performs deoxygenation of polyunsaturated fatty acids facilitates 13-pro(S) hydrogen abstraction through a homologous Tyr radical on Tyr376 (163–165). A Tyr radical on Tyr145 of coproheme decarboxylase (HemQ) catalyzes the decarboxylation of the heme propionate group (166, 167). Ribonucleotide reductases (RNRs) use a wide range of cofactors to catalyze the conversion of ribonucleotides to deoxyribonucleotides. In Class Ia RNRs, the di-iron center oxidizes a Tyr in the β subunit and radical transfer proceeds through a number of Tyrs and Trps 35 Å away to the α subunit where Cys349 is the oxidized for catalysis (168).

Intraprotein covalent structure

Covalent structures between residues within enzymes have been identified in a wide and continually growing range of enzymes. Some of these structures have been shown to aid in catalysis but aren't essential to the catalytic mechanism. An example is the Tyr-Cys crosslink in cysteine dioxygenase (CDO) whose structure is proposed to facilitate more catalytically efficient geometry of the CDO active site (169, 170). Similarly, a Tyr-Cys crosslink is formed in galactose oxidase (GO) stimulates catalysis by encouraging an active-site geometry that is most efficient for catalysis and also mediates the redox potential of the ligating Cu atom (171–175). A very similar effect of a His-Tyr adduct is seen in cytochrome *c* oxidase (C*c*O) between the proximal ligand His240 and Tyr244 (176).

A special class of covalent adducts are those that not only stimulate catalysis but are *necessary* for driving catalysis as a protein-derived cofactor (PDC). The majority of PDCs are redox-active amino acid residues that have been modified to form quinone-like structures. There are other PDCs that are formed by post-translational, covalent linkages between amino acid sidechains (Fig. 6.3). Amine dehydrogenases such as methylamine dehydrogenase (MADH), aromatic amine dehydrogenase (AADH), and quinohemoprotien amine dehydrogenase (QHNDH) are known to utilize quinone-type PDCs such as tryptophan tryptophylquinone (TTQ) or cysteine tyrptophylquinone (CTQ). The biosynthesis of these cofactors progresses by mechanisms that involve protein-based radical intermediates. Once formed, these structures drive the conversion from amine substrates to aldehyde products through covalent intermediates with the quinone cofactor (177, 178). The biosynthesis of TTQ in MADH is known to be catalyzed by the protein methylamine utilization protein, MauG. MauG employs two *c*-type heme cofactors (one 5- and one 6-coordinate) and multiple Trp residues to form TTQ cofactor from Trp108 and Trp57 of pre-MADH β-subunit. Electron flow from one heme to the other is facilitated by a Trp positioned in between the heme cofactors in MauG. MauG employs a unique, bis-ferryl heme state to oxidize βTrp108 through electron transfer through MauG Trp199 (179, 180). MauG and MADH are intriguing subjects because a number of applications of redox-active residues are employed sequentially to facilitate chemistry. Though the vast majority of enzymes that utilize TTQ or CTQ cofactors are dehydrogenases, recently, a new class

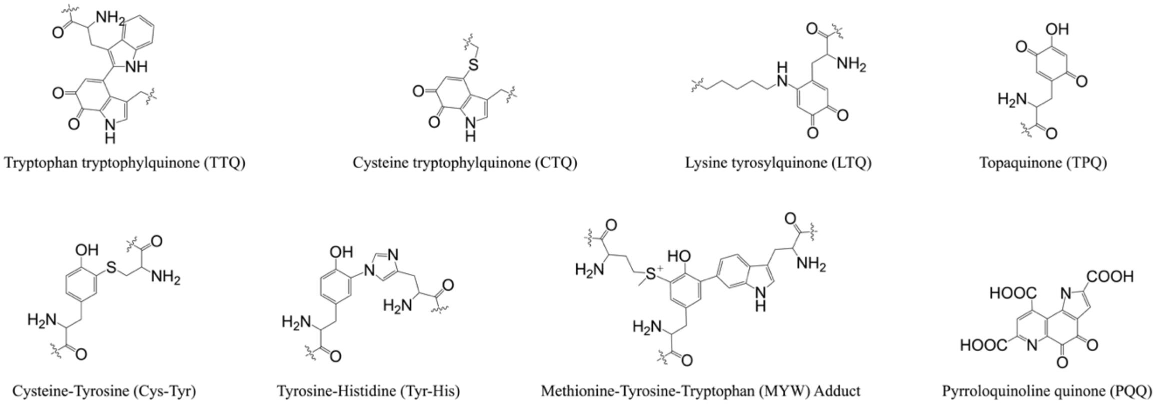

Tryptophan tryptophylquinone (TTQ)

Cysteine tryptophylquinone (CTQ)

Lysine tyrosylquinone (LTQ)

Topaquinone (TPQ)

Cysteine-Tyrosine (Cys-Tyr)

Tyrosine-Histidine (Tyr-His)

Methionine-Tyrosine-Tryptophan (MYW) Adduct

Pyrroloquinoline quinone (PQQ)

Figure 6.3. Structures of covalent adducts common among oxidoreductases.

of enzymes that act as amino acid oxidases (GoxA and B enzymes) have been confirmed to employ quinone-type PDCs. This is particularly interesting not only because it is one of the first examples of quinone PDCs as cofactors in enzymes other than dehydrogenases, but also because all other characterized amino acid oxidases employ a flavin cofactor (181).

6.4. Roles of redox activity of residues within PC superfamily

As we have established, a wide variety of enzymes employ Cys, Met, Tyr, and Trp residues for oxidative stress sensing, self-preservation, utilization of protein-based radical catalytic intermediates, or catalytically relevant covalent structures. The PC superfamily, especially Family I, serves as an exemplary group of enzymes that engage the whole range of residue utilization mentioned above. We hypothesize that the conservation of Met, Tyr, and Trp residues within the PC superfamily is influenced by enzymatic function. In this chapter, we will discuss the overall abundance of redox-active residues, the roles of amino acid redox activity in each family of the PC superfamily, and their correlation.

LiP from Family II has been confirmed to utilize a Trp-based radical for the oxidation of the large, irregular substrate lignin. The Family I enzymes demonstrate the greatest variation the PC superfamily as to how redox-active residues are utilized. C*c*P utilizes Tyr and Trp residues in a protein-based radical catalytic intermediate, hole-hopping pathway as a method of self-preservation, and also has recently been identified as a redox sensor. Due to the electronic configuration of the C*c*P active site, a of Fe^{IV}=O[porphyrin]$^{\bullet+}$ is never detected. Instead, a Fe^{IV}=O[Trp191]$^{\bullet+}$ intermediate is formed. C*c*P has displayed ability to utilize Trp and Tyr residues for hole-hopping as similarly observed within P450 enzymes (182). In particular, utilization of the hole-hopping pathways throughout C*c*P has been proposed as a method of self-preservation to protect the heme cofactor for the relocation to catalase Cta1 during oxidative stress, serving as a redox sensor (182, 183). Similarly, KatG shares many of the same aromatic redox-active residue sites with C*c*P, suggesting that the same type of hole-hopping phenomenon could be possible in KatG. The utilization of these hole-hopping pathways and their roles within KatG will be discussed later in Chapter 3. Furthermore, KatG utilizes a post-translationally modified Met-Tyr-Trp adduct within the active site as a PDC and there is evidence for the required participation of radical species of this MYW cofactor and other Tyr and Trp residues in the catalysis of KatG. The MYW cofactor, unique to KatGs imparts robust catalase activity to what would otherwise be a structure only capable of peroxidase activity (87, 92, 123, 184–186).

Redox-active residue content across PC superfamily

When comparing the composition of redox-active residues across the PC superfamily, there is a vast difference in redox-active residue incorporation across Families I, II, and III (Table 6.1). KatGs rank first for the highest number of Met, Tyr, and Trp residues, especially when considering just the catalytic, N-terminal domain. The oxidizable residue content of the N-terminal domain is over 10% of the protein structure depending on species, and this only diminishes to 8% when both KatG domains are taken into consideration. Though much lower in redox-active residue content, the C-terminal domains of KatGs rank with typical APxs above all Family II and III enzymes. The percent compositions of these redox-active residues were compared to those of a typical protein at 1.08% Trp, 2.92%, Met 2.42%, oxidizable aromatic residues 4.0%, and total oxidizable residues 6.42% to provide relative abundance of these residues across the PC superfamily

Table 6.1. Abundance of redox-active residues across the PC superfamily

Protein	Family	Total number of residues	Total Trp residues	Total Tyr residues	Total Met residues	Total aromatic oxidizable residues	Total oxidizable residues	% aromatic oxidizable residues	% oxidizable resdiues
MtKatG-N term	1	440	19	16	14	35	49	7.95	11.14
HmKatG-N term	1	430	16	11	18	27	45	6.28	10.47
MpKatG-N term	1	461	17	12	13	29	42	6.29	9.11
BpKatG-N term	1	431	18	11	10	29	39	6.73	9.05
CcP	1	294	7	14	5	21	26	7.14	8.84
MtKatG-Whole	1	740	24	21	18	45	63	6.08	8.51
HmKatG-Whole	1	731	21	18	21	39	60	5.34	8.21
LmPx	1	271	5	10	7	15	22	5.54	8.12
MpKatG2-Whole	1	764	21	18	18	39	57	5.10	7.46
BpKatG-Whole	1	728	23	14	14	37	51	5.08	7.01
HmKatG-C term	1	301	5	7	3	12	15	3.99	4.98
MpKatG-C term	1	303	4	6	5	10	15	3.30	4.95
KatG-C term	1	309	6	5	4	11	15	3.56	4.85
SbAPx	1	251	2	7	2	9	11	3.59	4.38
BpKatG- C term	1	288	5	3	4	8	12	2.78	4.17
Apx	1	249	2	7	1	9	10	3.61	4.02
CciPx	2	343	2	3	7	5	12	1.46	3.50
ArP	2	344	2	3	7	5	12	1.45	3.49
PNP	3	294	1	6	3	7	10	2.38	3.40
HRP	3	306	1	5	4	6	10	1.96	3.27
LiP	2	351	3	0	8	3	11	0.85	3.13
SbPx	3	304	1	5	3	6	9	1.97	2.96
BrPx	3	309	1	4	2	5	7	1.62	2.27
MnP	2	357	1	0	7	1	8	0.28	2.24
VPx	2	331	2	0	4	2	6	0.60	1.81

Table 6.2. Relative abundance of redox-active residues across the PC superfamily

Protein	Family	Relative Trp composition	Relative Tyr composition	Relative Met composition	Relative aromatic redox-active residues	Relative redox-active residues
MtKatG-N term	1	4.00	1.25	1.31	1.99	1.73
HmKatG-N term	1	3.45	0.88	1.73	1.57	1.63
MpKatG-N term	1	3.41	0.89	1.17	1.57	1.42
BpKatG-N term	1	3.87	0.87	0.96	1.68	1.41
CcP	1	2.20	1.63	0.70	1.79	1.38
MtKatG-Whole	1	3.00	0.97	1.01	1.52	1.33
HmKatG-Whole	1	2.66	0.84	1.19	1.33	1.28
LmPx	1	1.71	1.26	1.07	1.38	1.26
MpKatG2-Whole	1	2.55	0.81	0.97	1.28	1.16
BpKatG-Whole	1	2.93	0.66	0.79	1.27	1.09
HmKatG-C term	1	1.54	0.80	0.41	1.00	0.78
MpKatG-C term	1	1.22	0.68	0.68	0.83	0.77
KatG-C term	1	1.80	0.55	0.53	0.89	0.76
SbAPx	1	0.74	0.96	0.33	0.90	0.68
BpKatG- C term	1	1.61	0.36	0.57	0.69	0.65
Apx	1	0.74	0.96	0.17	0.90	0.63
CciPx	2	0.54	0.30	0.84	0.36	0.54
ArP	2	0.54	0.30	0.84	0.36	0.54
PNP	3	0.31	0.70	0.42	0.60	0.53
HRP	3	0.30	0.56	0.54	0.49	0.51
LiP	2	0.79	0.00	0.94	0.21	0.49
SbPx	3	0.30	0.56	0.41	0.49	0.46
BrPx	3	0.30	0.44	0.27	0.40	0.35
MnP	2	0.26	0.00	0.81	0.07	0.35
VPx	2	0.56	0.00	0.50	0.15	0.28

(Table 6.2). It is striking that the KatG N-terminal portion possesses an excess of nearly 1.75-fold oxidizable residues than the average protein. Even when comparing against family members, KatG stands again in the highest percentage of oxidizable residues, especially when considering just the N-terminal of the proteins where all activity takes place. It is also clear that Trp residues make up the majority of the redox-active residues present in KatGs, especially the N-terminal domain at four times the average for Trp content. In contrast, Family II and III enzymes exhibit a lower-than average incorporation of redox-active residues. Specifically, the Family III enzymes represented here have one third the Trp content of the average protein with a total redox-active residue count of about half that of a typical polypeptide. MnP and VP, in particular, have a very low percentage of Trp and Tyr residues. This seems to make sense when considering the function of these enzymes. For example, MnP contains only 1 Trp, perhaps to prevent from distraction of Mn^{2+} oxidation as additional Trp or even Tyr residues would be disadvantageous to this mechanism for peroxidase activity. Interestingly, it seems that what is lost in Trp and Tyr content is made up in the number of Met residues found in MnP.

Conservation of redox-active residues within peroxidase scaffold

This inventory of Trp, Tyr, and Met residues within PC heme peroxidases begs the question of which oxidizable residues correspond to those in KatG and are their placements conserved? To investigate this, the sequences of various heme peroxidases across the PC superfamily aligned to *M. tuberculosis* KatG to evaluate the conservation of Met, Tyr, and Trp residues. Sequence data was curated from RedOxiBase (188) from confirmed, non-fragment, and unique sequence entries. The collection for Family I PC members included

483 KatG, 453 C*c*P, 9 APx, 233 APx-C*c*P sequences (1178 in total). The collection of Family II was comprised of 72 LiP, 132 MnP, 33 VP, 181 CIIA, and 156 CIIB sequences (573 in total), and the Family III collection totaled to be 995 sequences. As a reference for baseline redox-active residue conservation, *Mt*KatG was aligned against all other KatG sequences (Fig. 6.4). This alignment indicates only ~15 residues that are considered redox-active in *Mt*KatG are not in the majority (i.e., 60 – 70%) of other KatGs.

Interestingly, comparison between *Mt*KatG and Family I enzymes indicates there are only a few locations on the KatG sequence which are highly conserved across the Family I enzymes (Fig. 6.5). With few exceptions, the identity of the redox-active residue within *Mt*KatG was maintained by the other members of Family I. These data suggest that the Family I enzymes other than KatG, though not maintaining the majority of the redox-active residue sites present in *Mt*KatG do seem to maintain the variety of redox-active residue identities exemplified by *Mt*KatG. Family II enzymes demonstrated few instances of redox-activity function conservation relative to *Mt*KatG (Fig. 6.6). The two positions with highest conservation across Family II enzymes are W396 and W412. Similar to Family II, the Family III enzymes show little conservation of the location of *Mt*KatG redox-active residues with Y197, W396, and W412 being the sited with the highest conservation (Fig. 6.7). The identity of the redox-active residues, however, are not strongly conserved. Overall, KatGs stand apart in yet another way from all other members of the PC superfamily by the abundant incorporation of Met, Tyr, and Trp residues (Fig. 6.8).

Both Family II and III enzymes contain Met, Tyr, or Trp residues at positions which are not redox-active residues within the *Mt*KatG sequence (Fig. 6.9 and 6.10). Though there are more redox-active sites unique to Family II than Family III, the overall conserv-

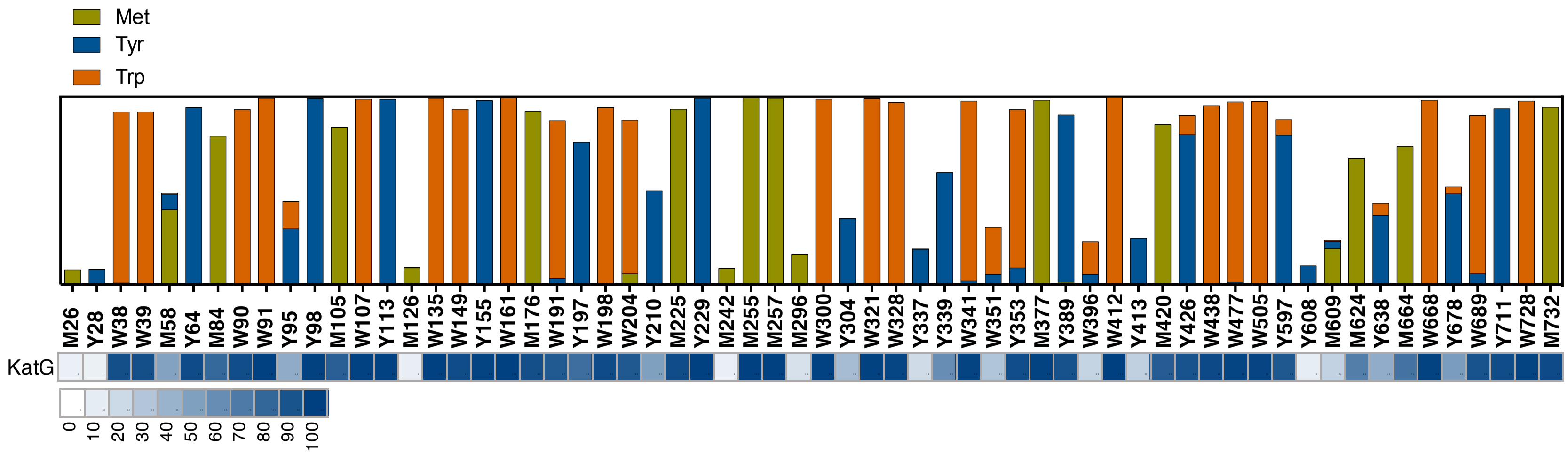

Figure 6.4. Conservation of position and identity of redox-active residues across PC superfamily. Sequences of PC superfamily enzymes were aligned to *Mt*KatG (residue positions provided across middle of the figure). The total percent of KatG sequences with redox-active residues at the corresponding position are represented by color scale (bottom of the figure). Furthermore, the identity of the redox-active residue identified at that position is represented within the bar graph at the top of the figure.

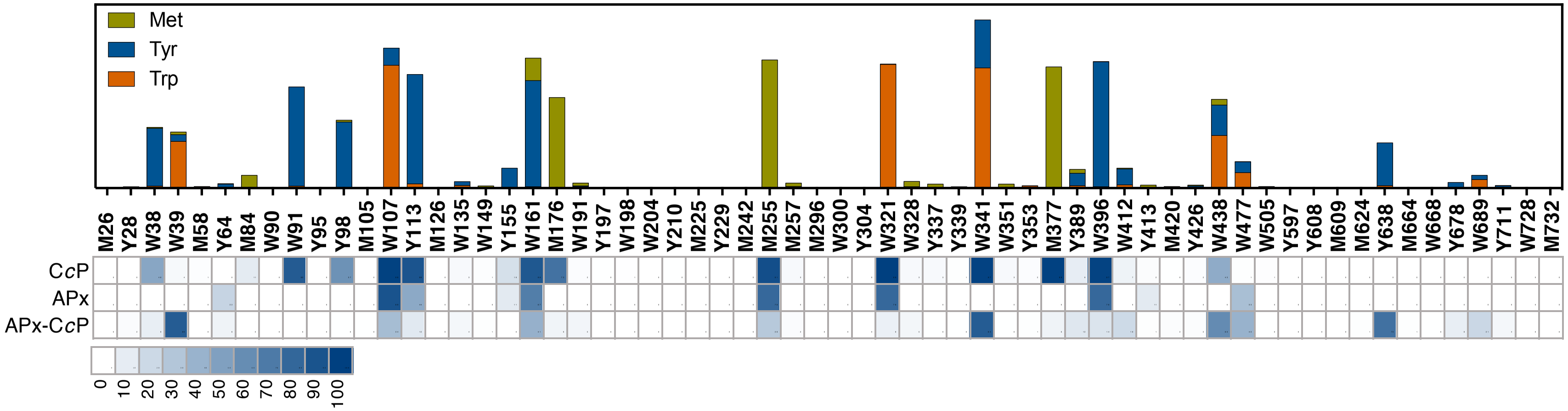

Figure 6.5. Conservation of position and identity of redox-active residues across Family I enzymes. Sequences of various Family I enzymes were aligned to *Mt*KatG (residue positions provided across middle of the figure). The total percent of KatG sequences with redox-active residues at the corresponding position are represented by color scale (bottom of the figure). Furthermore, the identity of the redox-active residue identified at that position is represented within the bar graph at the top of the figure.

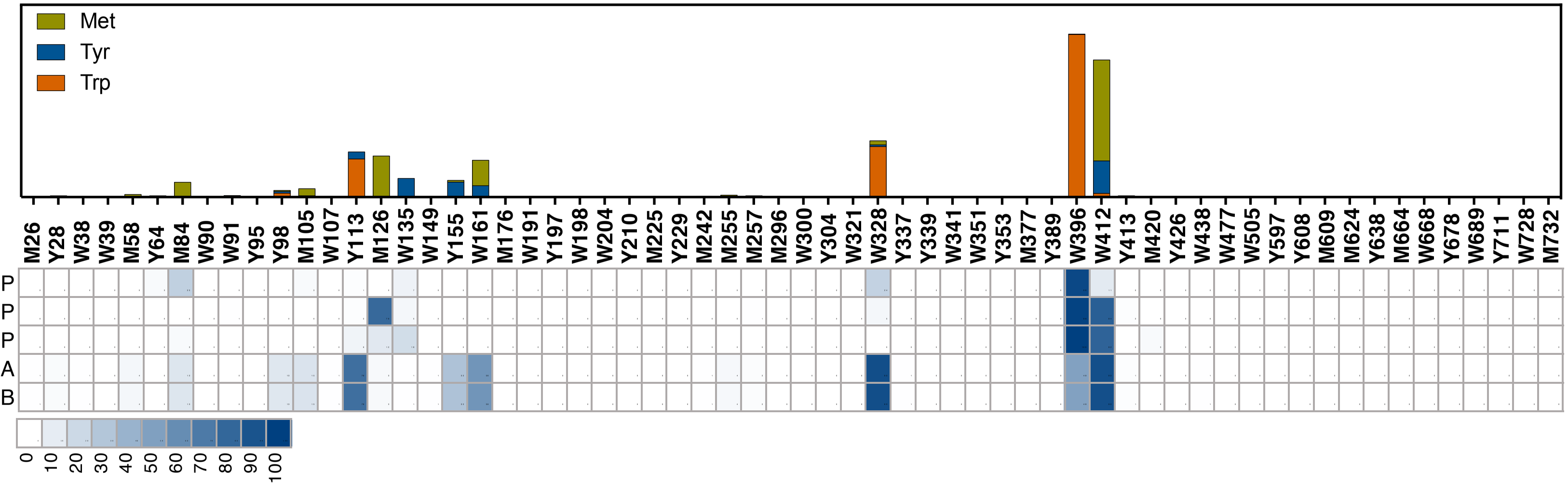

Figure 6.6. Conservation of position and identity of redox-active residues across Family II enzymes. Sequences of various Family II enzymes were aligned to *Mt*KatG (residue positions provided across middle of the figure). The total percent of KatG sequences with redox-active residues at the corresponding position are represented by color scale (bottom of the figure). Furthermore, the identity of the redox-active residue identified at that position is represented within the bar graph at the top of the figure.

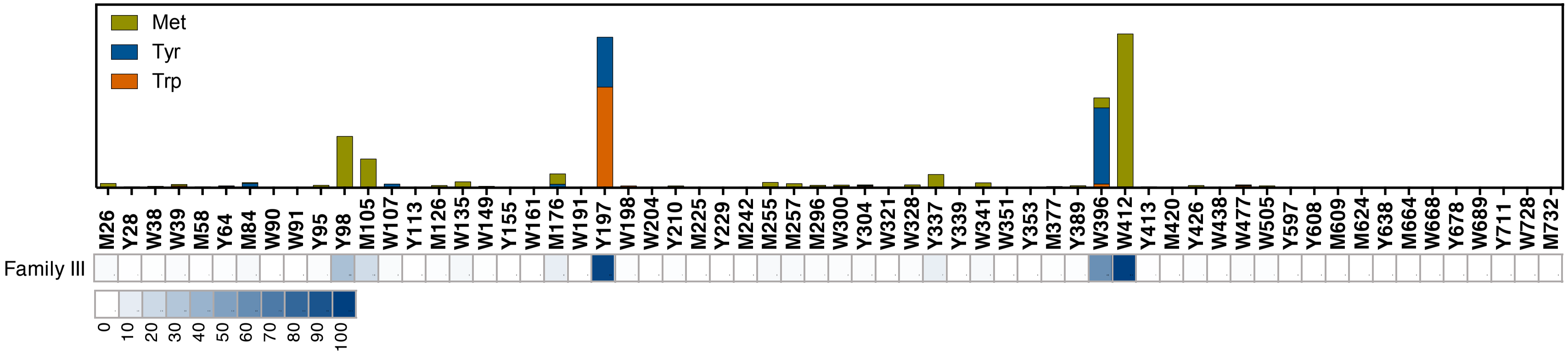

Figure 6.7. Conservation of position and identity of redox-active residues across Family III enzymes. Sequences of various Family III enzymes were aligned to *Mt*KatG (residue positions provided across middle of the figure). The total percent of KatG sequences with redox-active residues at the corresponding position are represented by color scale (bottom of the figure). Furthermore, the identity of the redox-active residue identified at that position is represented within the bar graph at the top of the figure.

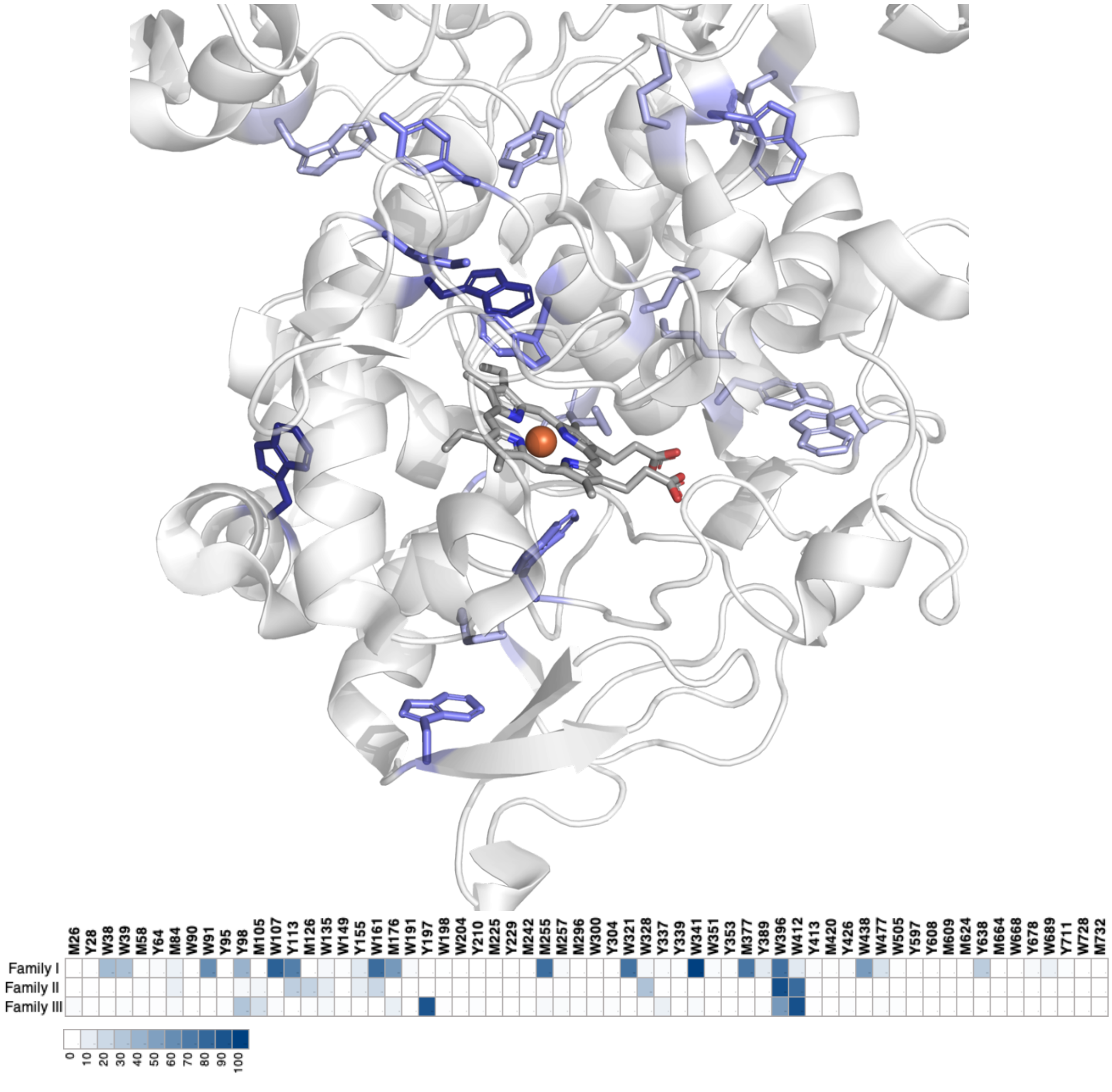
M26
Y28
W38
W39
M58
Y64
M84
W90
W91
Y95
Y98
M105
W107
Y113
M126
W135
W149
Y155
W161
M176
W191
Y197
W198
W204
Y210
M225
Y229
M242
M255
M257
M296
W300
Y304
W321
W328
Y337
Y339
W341
W351
Y353
M377
Y389
W396
W412
Y413
M420
Y426
W438
W477
W505
Y597
Y608
M609
M624
Y638
M664
W668
Y678
W689
Y711
W728
M732
Family I
Family II
Family III
0
10
20
30
40
50
60
70
80
90
100

Figure 6.8. Structural representation of conservation of redox-active residues within *Mt*KatG. The residues on the *Mt*KatG structure that are highly conserved as redox-active residues in the position (not necessarily the identity) across all three families of the PC superfamily. The residues that have > 50% conservation at this position are shown in dark blue, residues with 20 – 40% conservation at this position are shown in medium blue, and those with 5 – 15% conservation at this position are shown in light blue.

ation of these 23 sites across the Family II enzymes is low. Family III, with 15 unique redox-active residue locations, seems to have higher conservation of redox-activity at these sites than demonstrated by Family II enzymes. Perhaps even more striking is the composition of all the Met, Tyr, and Trp residues across the Family II and Family III enzymes. The various Family II and III enzymes seems exhibit preference on the identity of the redox-active residues incorporated into their sequence (Fig. 6.9B and 6.10B). MnP, VP, and CIIA enzymes contain Met as the most abundant redox-active residue, whereas LiP seems to favor incorporation of Trp residues and CIIB enzymes show nearly equal incorporation of Met, Tyr, and Trp residues.

6.5. Summary

In light of phylogenic studies of the PC superfamily that predict that KatGs are the most ancient of the PC superfamily, the fact that KatGs seem to best appropriate the redox properties of the Met, Tyr, and Trp is perhaps confusing at best given it would seem advantageous to maintain a high percentage of redox-active amino acids within a protein scaffold. If these phylogenic studies are correct, then it seems as though the PC superfamily has decreased Trp and Tyr content as a consequence of evolution and gene transfers.

The identity of redox-active residues favored for incorporation to the protein sequence seem to vary across the PC heme peroxidase Families. For example, Met residues are favored by Family II enzymes to be incorporated as redox-active residues in positions not found to have that function in KatG (Fig. 6.10B). This makes sense given the need to oxidize only select Trp residues for catalysis. Lastly, it seems Family III enzymes favor Met and Tyr incorporation over Trp (Fig. 6.8).

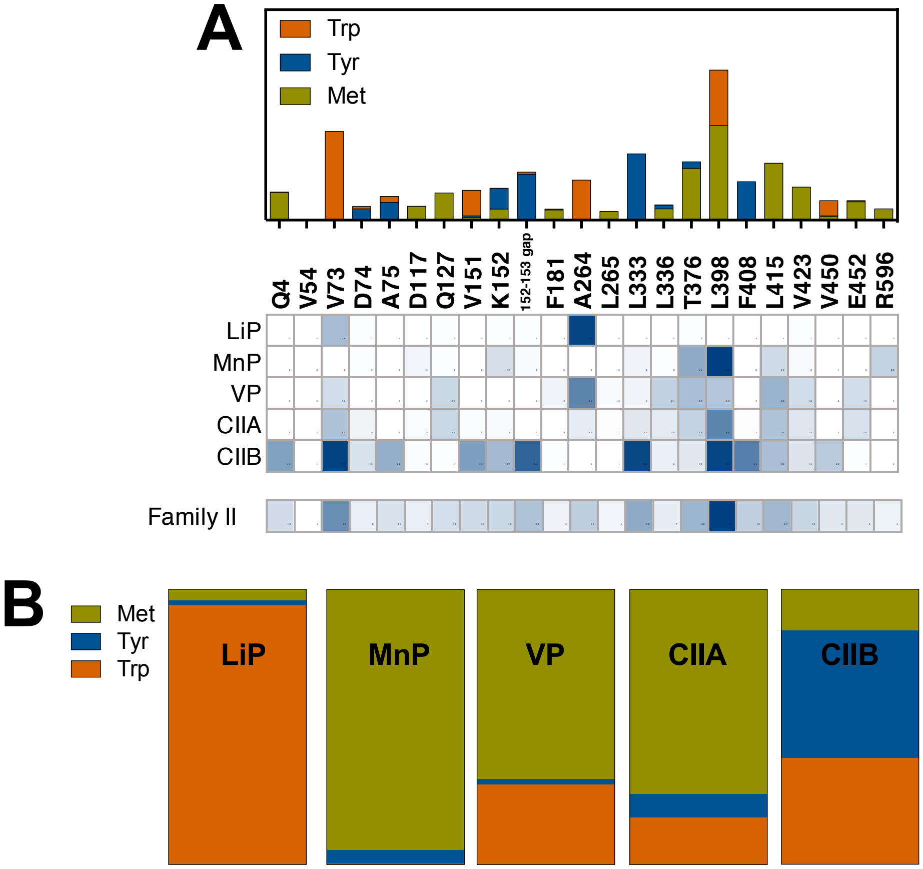

Figure 6.9. Location and preference of redox-active residues unique to Family II enzymes. The location of Met, Tyr, or Trp residues observed in Family II enzymes, but not in KatGs is given in *Mt*KatG numbering along with the identity of these residues indicated (A). The identity of redox-active residues observed for all positions, indicating any preference, is provided as parts of a whole (B).

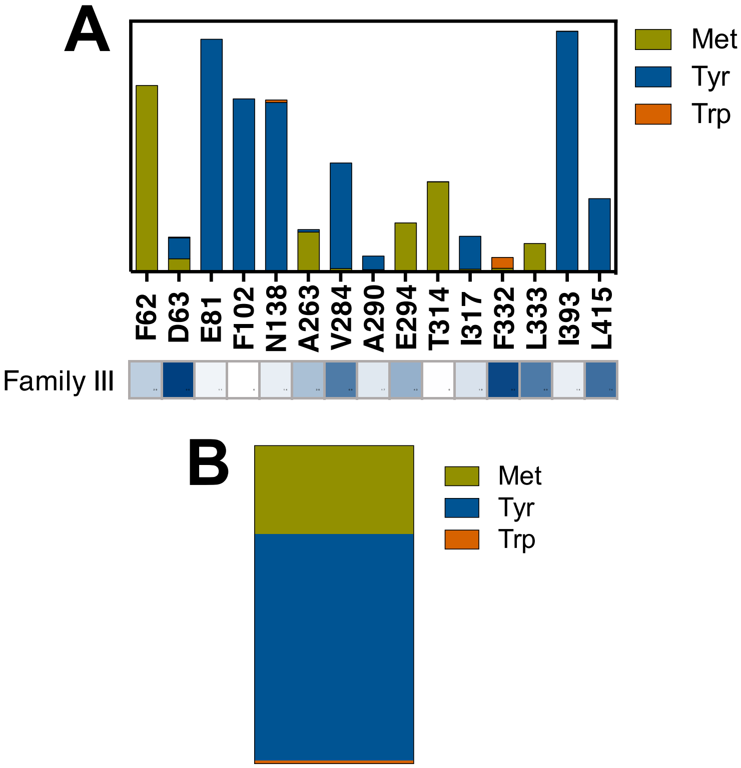

Figure 6.10. Location and preference of redox-active residues unique to Family III enzymes. The location of Met, Tyr, or Trp residues observed in Family III enzymes, but not in KatGs is given in *Mt*KatG numbering along with the identity of these residues indicated (A). The identity of redox-active residues observed for all positions, indicating any preference, is provided as parts of a whole (B).

These results could not only inform how we explore or approach assigning roles to yet uncharacterized proteins as well as possibly could inform bioengineering efforts. Incorporating more redox-active residues into enzymes that will encounter more oxidative stress can enable prolonged catalysis by providing endogenous antioxidants. The penultimate application of redox-active residues for enzyme bioengineering would be to attempt covalent adduct formation and investigate the effect of the adduct on enzyme function.

6.6. Implications of the distinctions of KatG

Structure-function relationship of oxidoreductases

KatG is a fascinating subject for scientific exploration because of its ability to employ a single active site for numerous chemical reactions. Ongoing investigations of KatG can provide fundamental understanding on structure-function relationships within enzymes, especially heme enzymes. In additional to fundamental understanding of enzymatic functions, a greater understanding of KatG can provide insight useful for combatting pathogenic enzymes. Not only do a large number of pathogenic organisms express at least one type of catalase-peroxidase enzyme, but KatG specifically activates the frontline, anti-tubercular pro-drug isoniazid. As such, KatG is an interesting subject with clinical implications and potential drug target. In addition to searching for INH derivatives that are activated even by various *Mycobacterium tuberculosis* strains that containing *katG* gene mutations, exploration of drugs that can directly target KatG function could be a promising field for future clinical research. In particular, screening for molecules that bind strongly to the C-terminal portion of KatG to disturb proper folding and heme coordination of KatG could serve as a useful first step towards KatG-targeted drug screening.

Exploring KatG as inspiration for bioengineering

The abundance of redox-active residues within KatG that give rise not only to a mechanism for catalase activity but furthermore *synergy* between catalase and peroxidase mechanisms within a peroxidase scaffolding is fascinating and reiterates that the primary structure of proteins can hold an important role in overall function. Incorporation of redox-active amino acids, even with the intention to facilitate PDC formation, within enzymes could be an incredible premise for enzyme engineering. As shown not only by KatG but other oxidoreductases (e.g., C*c*P and even P450 enzymes), the incorporation of Met, Tyr, and Trp residues can be a beneficial method for self-preservation in oxidative stress. This could be a helpful tool in bioengineering an oxidatively robust enzyme, given the residue substitutions wouldn't prevent proper function or intended function. Additionally, if the structure of the enzyme is known, adapting the active site to incorporate a protein-derived cofactor (PDC) would be an incredible feat of bioengineering.

The goal of bioengineering to incorporate a PDC would be to enhance or change the function of the enzyme. Hard-fought success of such a feat of bioengineering, however, would be conservation of native folding and catalysis. A possibility for such a bioengineering endeavor would be to generate a YW cofactor within C*c*P. As a fellow member of Family I of the PC superfamily, C*c*P is highly similar to KatG structurally, even considering the level of redox-active amino acid incorporation (see Chapter 2 for more detail). Due to the conservation of the distal active-site Trp in C*c*P only the incorporation of a Tyr residue would be needed for the formation of a YW adduct. The loop between the E and F helices of C*c*P is near to the distal Trp (Trp51 according to *Saccharomyces cerevisiae* numbering) and could serve as a promising candidate for Tyr residue incorporation.

In addition to the close proximity of the loop to the distal Trp, the flexibility of the loop structure should be amenable to a more dramatic mutation such as Pro145Tyr (Fig. 6.11). Figure 6.11B shows a PyMol prediction of the Pro145Tyr variant of C*c*P. Though the inserted Tyr is pointing away from Trp51, the distance between the Tyr *β*-carbon to C_6 of Trp indole ring is 5.6 Å. It is possible for this Tyr to rotate around the β-carbon, bringing the ortho carbons of the Tyr about 1.8 Å from the C_6 of Trp indole ring, which is well within possible distance carbon-carbon bond formation with minimal movement of the loop structure. If this strategy did not work, an alternative strategy might be to increase the length of the loop structure my one to two residues in addition to insertion of a Tyr residue.

Efforts to generate a YW adduct in C*c*P have already been attempted by a different strategy (187). In this study, Poulos and coworkers created the H52Y variant of C*c*P where the conserved, distal His52 residue was converted to a Tyr. Though this C*c*P variant successfully formed a YW adduct near the heme active site that was formed autocatalytically in a peroxide- and heme-dependent manner, the covalent linkage occurs between the indole N of the Trp and the $C_{\varepsilon 1}$ of the Tyr. The activity of this C*c*P variant was not discussed. As the distal His, which is required as an active site base during reaction with H_2O_2, was lost in the creation of this variant, it would be no surprise if the H52Y variant was incapable of peroxidase or catalase activity. The proposed strategy presented in the paragraphs above should allow for the distal His to be used for catalysis and encour-

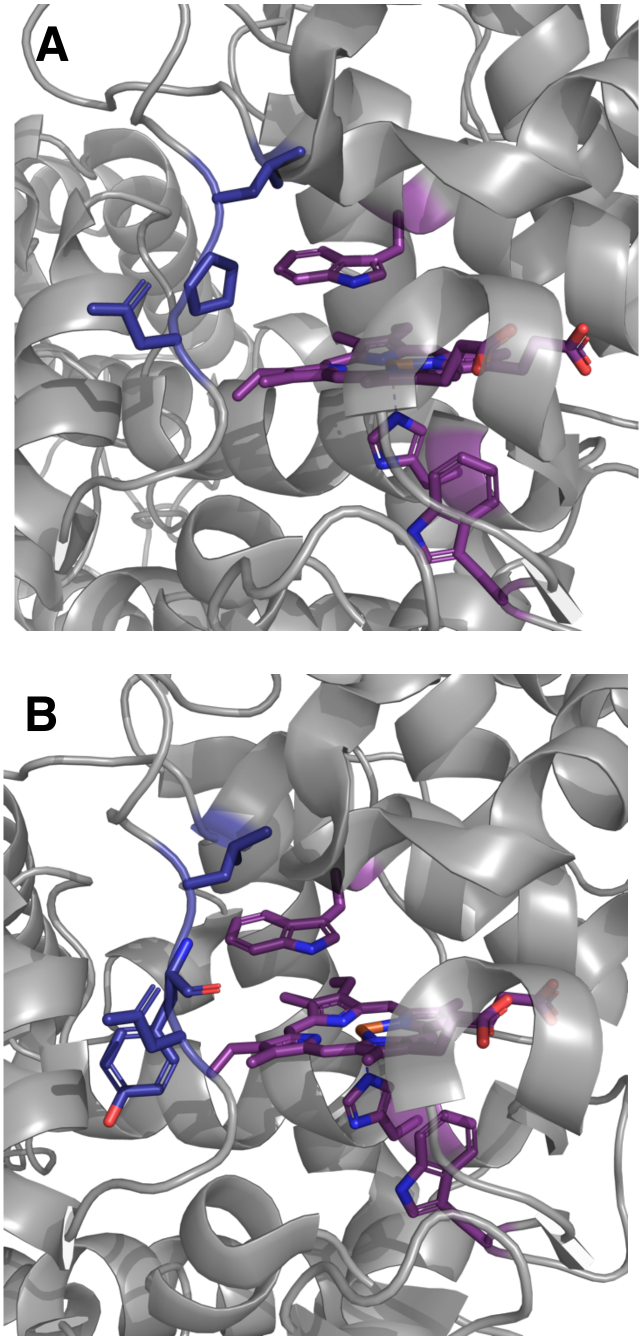

Figure 6.11. Proposed mutation for YW formation within C*c*P. Heme cofactor and C*c*P residues are presented in bright purple and residues near to Trp51 are represented in royal blue for native enzyme (A) and proposed P145Y variant (B). PDB: 4XVA

age the formation of a YW adduct in the C*c*P active site. It should be noted that KatG variants that form only the YW adduct are not capable of catalase activity, but that may not be the case for C*c*P with a YW adduct.

The incorporation of redox-active residues can extend past the purpose of PDC formation but could be to equip a protein for robust response to oxidative stress by the incorporation of these residues throughout the protein structure. The best candidate for such an experiment would be a heme protein that has a high number of Phe residues that could be altered to Tyr or Trp residues by site-directed mutagenesis. The mutations might need to be accomplished consecutively to ensure proper protein expression and folding are maintained. If this strategy proves to be successful, it would be interesting to perform the same experiment on non-heme proteins, especially Cu or non-heme Fe proteins. The extent of cofactor-dependence of this mechanism of hole-hopping through Met, Tyr, and Trp residues is not yet been defined. In addition to engineering new proteins with high Met, Tyr, and Trp counts, the intense study of pre-existing non-heme enzymes that contain a high number of redox-active residues could also provide beneficial information on the impact of various cofactors to the mechanism of intraprotein electron transfer.

6.9. Methodology

Amino acid alignments

A curated collection of amino acid sequences from the peroxidase-catalase superfamily was compiled from UniProt Database where only full, reviewed, and non-redundant sequencese were selected for alignment. Additionally, complete sequences from RedOxiBase (188) were added to the curated collection to increase the number of sequences aligned, specifically for Family II and the recently discovered hybrid enzymes. The reason for compiling a curate collection is to limit repetition of sequences and inclusion of incomplete or unknown sequences in this study. In all, this study includes 734 KatG, 128 APx, 592 C*c*P, 616 Family II (including MnP, LiP, VP, and Asco Family II enzymes), 4,446 Family III, and 234 APx-C*c*P hybrid sequences. Sequence alignments were made using Clustal Omega (189, 190). First all sequences of the same protein were aligned across species, then these alignments were aligned with alignments of other members of the Family I, II, III distinctions. Finally, members across families could then be directly compared. Alignments were visualized and annotated with Jalview 2.11.1.3. Jalview was also used to do a general investigation on the conservation of residues within alignments.

Visualization of structural similarities

Conservation of identity and function of redox-active residues across the PC family were carried out by aligning the protein structures of representative enzymes in PyMol. Color coding was carried out according to the degree of conservation exhibited by the proteins being align against *M. tuberculosis* KatG and is described in each figure legend where relevant. Each redox-active residue of KatG was identified and then the corresponding residues from other proteins were identified, and as a result that group of residues were assigned a color based on the conservation of the identity or function of the redox-active residue. When published x-ray crystal structure coordinates were not available (i.e., Hybrid A and Hybrid B enzymes), structure predictions were carried out using the Phyre 2.0 server, and then compared to KatG in PyMol as previously described.

References

1. Wood, P. M. (1988) The potential diagram for oxygen at pH 7. *Biochemical Journal*. **253**, 287–289

2. Massey, V. (1994) Activation of molecular oxygen by flavins and flavoproteins. *Journal of Biological Chemistry*. **269**, 22459–22462

3. Zangar, R. C., Davydov, D. R., and Verma, S. (2004) Mechanisms that regulate production of reactive oxygen species by cytochrome P450. *Toxicology and Applied Pharmacology*. **199**, 316–331

4. Nam, T. G. (2011) Lipid peroxidation and its toxicological implications. *Toxicological Research*. **27**, 1–6

5. Lynch, T., and Price, A. (2007) *The Effect of Cytochrome P450 Metabolism on Drug Response, Interactions, and Adverse Effects*, [online] www.aafp.org/afp. (Accessed June 8, 2021)

6. Romero, E., Gómez Castellanos, J. R., Gadda, G., Fraaije, M. W., and Mattevi, A. (2018) Same Substrate, Many Reactions: Oxygen Activation in Flavoenzymes. *Chemical Reviews*. **118**, 1742–1769

7. Escutia, M. R., Bowater, L., Edwards, A., Bottrill, A. R., Burrell, M. R., Polanco, R., Vicuña, R., and Bornemann, S. (2005) Cloning and sequencing of two Ceriporiopsis subvermispora bicupin oxalate oxidase allelic isoforms: Implications for the reaction specificity of oxalate oxidases and decarboxylases. *Applied and Environmental Microbiology*. **71**, 3608–3616

8. Varotsis, C., Zhang, Y., Appelman, E. H., and Babcock, G. T. (1993) Resolution of the reaction sequence during the reduction of O2 by cytochrome oxidase. *Proceedings of the National Academy of Sciences of the United States of America*. **90**, 237–241

9. Turrens, J. F. (2003) Mitochondrial formation of reactive oxygen species. *Journal of Physiology*. **552**, 335–344

10. Chen, Q., Vazquez, E. J., Moghaddas, S., Hoppel, C. L., and Lesnefsky, E. J. (2003) Production of reactive oxygen species by mitochondria: Central role of complex III. *Journal of Biological Chemistry*. **278**, 36027–36031

11. Goncalves, R. L. S., Bunik, V. I., and Brand, M. D. (2016) Production of superoxide/hydrogen peroxide by the mitochondrial 2-oxoadipate dehydrogenase complex. *Free Radical Biology and Medicine*. **91**, 247–255

12. Quinlan, C. L., Perevoshchikova, I. v., Hey-Mogensen, M., Orr, A. L., and Brand, M. D. (2013) Sites of reactive oxygen species generation by mitochondria oxidizing different substrates. *Redox Biology*. **1**, 304–312

13. Bielski, B. H. J., Cabelli, D. E., Arudi, R. L., and Ross, A. B. (1985) Reactivity of HO2/O−2 Radicals in Aqueous Solution. *Journal of Physical and Chemical Reference Data*. **14**, 1041–1100

14. Lu, H. F., Chen, H. F., Kao, C. L., Chao, I., and Chen, H. Y. (2018) A computational study of the Fenton reaction in different pH ranges. *Physical Chemistry Chemical Physics*. **20**, 22890–22901

15. Chen, H. Y. (2019) Why the Reactive Oxygen Species of the Fenton Reaction Switches from Oxoiron(IV) Species to Hydroxyl Radical in Phosphate Buffer Solutions? A Computational Rationale. *ACS Omega*. **4**, 14105–14113

16. Keyer, K., and Imlay, J. A. (1996) Superoxide accelerates DNA damage by elevating free-iron levels. *Proceedings of the National Academy of Sciences of the United States of America*. **93**, 13635–13640

17. Liochev, S. I. (1996) The role of iron-sulfur clusters in in vivo hydroxyl radical production. *Free Radical Research*. **25**, 369–384

18. Jang, S., and Imlay, J. A. (2007) Micromolar intracellular hydrogen peroxide disrupts metabolism by damaging iron-sulfur enzymes. *Journal of Biological Chemistry*. **282**, 929–937

19. Taurog, A., Dorris, M. L., and Doerge, D. R. (1996) Mechanism of simultaneous iodination and coupling catalyzed by thyroid peroxidase. *Archives of Biochemistry and Biophysics*. **330**, 24–32

20. Furtmüller, P. G., Jantschko, W., Regelsberger, G., Jakopitsch, C., Arnhold, J., and Obinger, C. (2002) Reaction of lactoperoxidase compound I with halides and thiocyanate. *Biochemistry*. **41**, 11895–11900

21. Furtmüller, P. G., Burner, U., Regelsberger, G., and Obinger, C. (2000) Spectral and kinetic studies on the formation of eosinophil peroxidase compound I and its reaction with halides and thiocyanate. *Biochemistry*. **39**, 15578–15584

22. Furtmuller, P. G., Burner, U., and Obinger, C. (1998) Reaction of myeloperoxidase compound I with chloride, bromide, iodide, and thiocyanate. *Biochemistry*. **37**, 17923–17930

23. Zederbauer, M., Furtmüller, P. G., Brogioni, S., Jakopitsch, C., Smulevich, G., and Obinger, C. (2007) Heme to protein linkages in mammalian peroxidases: Impact on spectroscopic, redox and catalytic properties. *Natural Product Reports*. **24**, 571–584

24. Conner, G. E., Salathe, M., and Forteza, R. (2002) Lactoperoxidase and hydrogen peroxide metabolism in the airway. in *American Journal of Respiratory and Critical Care Medicine*, American Lung Association, 10.1164/rccm.2206018

25. Fragoso, M. A., Fernandez, V., Forteza, R., Randell, S. H., Salathe, M., and Conner, G. E. (2004) Transcellular thiocyanate transport by human airway epithelia. *Journal of Physiology*. **561**, 183–194

26. Harper, R. W., Xu, C., Eiserich, J. P., Chen, Y., Kao, C. Y., Thai, P., Setiadi, H., and Wu, R. (2005) Differential regulation of dual NADPH oxidases/peroxidases, Duox1 and Duox2, by Th1 and Th2 cytokines in respiratory tract epithelium. *FEBS Letters*. **579**, 4911–4917

27. Bafort, F., Parisi, O., Perraudin, J. P., and Jijakli, M. H. (2014) Mode of Action of Lactoperoxidase as Related to Its Antimicrobial Activity: A Review. *Enzyme Research*. 10.1155/2014/517164

28. Nguyen, G. T., Green, E. R., and Mecsas, J. (2017) Neutrophils to the ROScue: Mechanisms of NADPH oxidase activation and bacterial resistance. *Frontiers in Cellular and Infection Microbiology*. **7**, 373

29. El-Benna, J., Hurtado-Nedelec, M., Marzaioli, V., Marie, J. C., Gougerot-Pocidalo, M. A., and Dang, P. M. C. (2016) Priming of the neutrophil respiratory burst: role in host defense and inflammation. *Immunological Reviews*. **273**, 180–193

30. Vignais, P. v. (2002) The superoxide-generating NADPH oxidase: Structural aspects and activation mechanism. *Cellular and Molecular Life Sciences*. **59**, 1428–1459

31. Magnani, F., Nenci, S., Fananas, E. M., Ceccon, M., Romero, E., Fraaije, M. W., and Mattevi, A. (2017) Crystal structures and atomic model of NADPH oxidase. *Proceedings of the National Academy of Sciences of the United States of America*. **114**, 6764–6769

32. Förstermann, U., and Sessa, W. C. (2012) Nitric oxide synthases: Regulation and function. *European Heart Journal*. **33**, 829

33. Ferrer-Sueta, G., Campolo, N., Trujillo, M., Bartesaghi, S., Carballal, S., Romero, N., Alvarez, B., and Radi, R. (2018) Biochemistry of Peroxynitrite and Protein Tyrosine Nitration. *Chemical Reviews*. **118**, 1338–1408

34. Castro, L., Rodriguez, M., and Radi, R. (1994) Aconitase is readily inactivated by peroxynitrite, but not by its precursor, nitric oxide. *Journal of Biological Chemistry*. **269**, 29409–29415

35. Hausladen, A., and Fridovich, I. (1994) Superoxide and peroxynitrite inactivate aconitases, but nitric oxide does not. *Journal of Biological Chemistry*. **269**, 29405–29408

36. Whittaker, J. W. (2012) Non-heme manganese catalase - The “other” catalase. *Archives of Biochemistry and Biophysics*. **525**, 111–120

37. Barynin, V. v., Whittaker, M. M., Antonyuk, S. v., Lamzin, V. S., Harrison, P. M., Artymiuk, P. J., and Whittaker, J. W. (2001) Crystal structure of manganese catalase from Lactobacillus plantarum. *Structure*. **9**, 725–738

38. Ma, Z., Strickland, K. T., Cherne, M. D., Sehanobish, E., Rohde, K. H., Self, W. T., and Davidson, V. L. (2018) The Rv2633c protein of Mycobacterium tuberculosis is a non-heme di-iron catalase with a possible role in defenses against oxidative stress. *Journal of Biological Chemistry*. **293**, 1590–1595

39. Ma, Z., Abendroth, J., Buchko, G. W., Rohde, K. H., and Davidson, V. L. (2020) Crystal structure of a hemerythrin-like protein from Mycobacterium kansasii and homology model of the orthologous Rv2633c protein of M. Tuberculosis. *Biochemical Journal*. **477**, 567–581

40. Wengenack, N. L., Jensen, M. P., Rusnak, F., and Stern, M. K. (1999) Mycobacterium tuberculosis KatG is a peroxynitritase. *Biochemical and Biophysical Research Communications*. **256**, 485–487

41. Carpena, X., Wiseman, B., Deemagarn, T., Herguedas, B., Ivancich, A., Singh, R., Loewen, P. C., and Fita, I. (2006) Roles for Arg426 and Trp111 in the modulation of NADH oxidase activity of the catalase-peroxidase KatG from Burkholderia pseudomallei inferred from pH-induced structural changes. *Biochemistry*. **45**, 5171–5179

42. Singh, R., Wiseman, B., Deemagarn, T., Donald, L. J., Duckworth, H. W., Carpena, X., Fita, I., and Loewen, P. C. (2004) Catalase-peroxidases (KatG) exhibit NADH oxidase activity. *Journal of Biological Chemistry*. **279**, 43098–43106

43. Eum, S. Y., Kong, J. H., Hong, M. S., Lee, Y. J., Kim, J. H., Hwang, S. H., Cho, S. N., Via, L. E., and Barry, C. E. (2010) Neutrophils are the predominant infected phagocytic cells in the airways of patients with active pulmonary TB. *Chest*. **137**, 122–128

44. Corleis, B., Korbel, D., Wilson, R., Bylund, J., Chee, R., and Schaible, U. E. (2012) Escape of Mycobacterium tuberculosis from oxidative killing by neutrophils. *Cellular Microbiology*. **14**, 1109–1121

45. Ng, V. H., Cox, J. S., Sousa, A. O., MacMicking, J. D., and McKinney, J. D. (2004) Role of KatG catalase-peroxidase in mycobacterial pathogenisis: Countering the phagocyte oxidative burst. *Molecular Microbiology*. **52**, 1291–1302

46. Li, Z., Kelley, C., Collins, F., Rouse, D., and Morris, S. (1998) Expression of katG in Mycobacterium tuberculosis is associated with its growth and persistence in mice and guinea pigs. *Journal of Infectious Diseases*. **177**, 1030–1035

47. Wilson, T. M., de Lisle, G. W., and Collins, D. M. (1995) Effect of inhA and katG on isoniazid resistance and virulence of Mycobacterium bovis. *Molecular Microbiology*. **15**, 1009–1015

48. Oyston, P. C. F., Sjostedt, A., and Titball, R. W. (2004) Tularaemia: Bioterrorism defence renews interest in Francisella tularensis. *Nature Reviews Microbiology*. **2**, 967–978

49. Honn, M., Lindgren, H., Bharath, G. K., and Sjöstedt, A. (2017) Lack of OxyR and KatG results in extreme susceptibility of Francisella tularensis LVS to oxidative stress and marked attenuation in vivo. *Frontiers in Cellular and Infection Microbiology*. **7**, 14

50. Garcia, E., Nedialkov, Y. A., Elliott, J., Motin, V. L., and Brubaker, R. R. (1999) Molecular characterization of katy (antigen 5), a thermoregulated chromosomally encoded catalase-peroxidase of yersinia pestis. *Journal of Bacteriology*. **181**, 3114–3122

51. Fukuto, H. S., Svetlanov, A., Palmer, L. E., Karzai, A. W., and Bliska, J. B. (2010) Global gene expression profiling of Yersinia pestis replicating inside macrophages reveals the roles of a putative stress-induced operon in regulating type III secretion and intracellular cell division. *Infection and Immunity*. **78**, 3700–3715

52. Han, Y., Geng, J., Qiu, Y., Guo, Z., Zhou, D., Bi, Y., Du, Z., Song, Y., Wang, X., Tan, Y., Zhu, Z., Zhai, J., and Yang, R. (2008) Physiological and regulatory characterization of KatA and KatY in Yersinia pestis. *DNA and Cell Biology*. **27**, 453–462

53. Uhlich, G. A. (2009) KatP contributes to OxyR-regulated hydrogen peroxide resistance in Escherichia coli serotype O157:H7. *Microbiology*. **155**, 3589–3598

54. Zhang, M., Yan, Q., Mao, L., Wang, S., Huang, L., Xu, X., and Qin, Y. (2018) KatG plays an important role in Aeromonas hydrophila survival in fish macrophages and escape for further infection. *Gene*. **672**, 156–164

55. Jittawuttipoka, T., Buranajitpakorn, S., Vattanaviboon, P., and Mongkolsuk, S. (2009) The catalase-peroxidase KatG is required for virulence of Xanthomonas campestris pv. campestris in a host plant by providing protection against low levels of H2O2. *Journal of Bacteriology*. **191**, 7372–7377

56. Zámocký, M., Droghetti, E., Bellei, M., Gasselhuber, B., Pabst, M., Furtmüller, P. G., Battistuzzi, G., Smulevich, G., and Obinger, C. (2012) Eukaryotic extracellular catalase-peroxidase from Magnaporthe grisea - Biophysical/chemical characterization of the first representative from a novel phytopathogenic KatG group. *Biochimie*. **94**, 673–683

57. Guo, Y., Yao, S., Yuan, T., Wang, Y., Zhang, D., and Tang, W. (2019) The spatiotemporal control of KatG2 catalase-peroxidase contributes to the invasiveness of Fusarium graminearum in host plants. *Molecular Plant Pathology*. **20**, 685–700

58. Gao, S., Gold, S. E., and Glenn, A. E. (2018) Characterization of two catalase-peroxidase-encoding genes in Fusarium verticillioides reveals differential responses to in vitro versus in planta oxidative challenges. *Molecular Plant Pathology*. **19**, 1127–1139

59. Tanabe, S., Ishii-Minami, N., Saitoh, K. I., Otake, Y., Kaku, H., Shibuya, N., Nishizawa, Y., and Minami, E. (2011) The role of catalase-peroxidase secreted by Magnaporthe oryzae during early infection of rice cells. *Molecular Plant-Microbe Interactions*. **24**, 163–171

60. Tanabe, S., Nishizawa, Y., and Minami, E. (2009) Effects of catalase on the accumulation of H2O2 in rice cells inoculated with rice blast fungus, Magnaporthe oryzae. *Physiologia Plantarum*. **137**, 148–154

61. Barry, C. E., Lee, R. E., Mdluli, K., Sampson, A. E., Schroeder, B. G., Slayden, R. A., and Yuan, Y. (1998) Mycolic acids: Structure, biosynthesis and physiological functions. *Progress in Lipid Research*. **37**, 143–179

62. Barkan, D., Liu, Z., Sacchettini, J. C., and Glickman, M. S. (2009) Mycolic Acid Cyclopropanation is Essential for Viability, Drug Resistance, and Cell Wall Integrity of Mycobacterium tuberculosis. *Chemistry and Biology*. **16**, 499–509

63. Rozwarski, D. A., Grant, G. A., Barton, D. H. R., Jacobs, W. R., and Sacchettini, J. C. (1998) Modification of the NADH of the isoniazid target (InhA) from Mycobacterium tuberculosis. *Science*. **279**, 98–102

64. Vilchèze, C., Morbidoni, H. R., Weisbrod, T. R., Iwamoto, H., Kuo, M., Sacchettini, J. C., and Jacobs, W. R. (2000) Inactivation of the inhA-encoded fatty acid synthase II (FASII) enoyl- acyl carrier protein reductase induces accumulation of the FASI end products and cell lysis of Mycobacterium smegmatis. *Journal of Bacteriology*. **182**, 4059–4067

65. Lei, B., Wei, C. J., and Tu, S. C. (2000) Action mechanism of antitubercular isoniazid: Activation by Mycobacterium tuberculosis KatG, isolation, and characterization of InhA inhibitor. *Journal of Biological Chemistry*. **275**, 2520–2526

66. L. Wengenack, N., M. Hoard, H., and Rusnak, F. (1999) Isoniazid Oxidation by Mycobacterium tuberculosis KatG: A Role for Superoxide Which Correlates with Isoniazid Susceptibility. *Journal of the American Chemical Society*. **121**, 9748–9749

67. Chouchane, S., Lippai, I., and Magliozzo, R. S. (2000) Catalase-peroxidase (Mycobacterium tuberculosis KatG) catalysis and isoniazid activation. *Biochemistry*. **39**, 9975–9983

68. Chouchane, S., Lippai, I., and Magliozzo, R. S. (2000) Catalase-Peroxidase (Mycobacterium tuberculosis KatG) Catalysis and Isoniazid Activation. *Biochemistry*. **39**, 9975–9983

69. Scior, T., Meneses Morales, I., Garcés Eisele, S. J., Domeyer, D., and Laufer, S. (2002) Antitubercular isoniazid and drug resistance of Mycobacterium tuberculosis - A review. *Archiv der Pharmazie*. **335**, 511–525

70. Wiseman, B., Carpena, X., Feliz, M., Donald, L. J., Pons, M., Fita, I., and Loewen, P. C. (2010) Isonicotinic acid hydrazide conversion to isonicotinyl-NAD by catalase-peroxidases. *Journal of Biological Chemistry*. **285**, 26662–26673

71. Cade, C. E., Dlouhy, A. C., Medzihradszky, K. F., Salas-Castillo, S. P., and Ghiladi, R. A. (2010) Isoniazid-resistance conferring mutations in Mycobacterium tuberculosis KatG: Catalase, peroxidase, and INH-NADH adduct formation activities. *Protein Science*. **19**, 458–474

72. Zhao, X., Yu, H., Yu, S., Wang, F., Sacchettini, J. C., and Magliozzo, R. S. (2006) Hydrogen peroxide-mediated isoniazid activation catalyzed by Mycobacterium tuberculosis catalase-peroxidase (KatG) and its S315T mutant. *Biochemistry*. **45**, 4131–4140

73. Gray, H. B. (1983) *Iron Porphyrins, Part I* (Lever, A. B. P. ed), Addison-Wesley Publishing Company, Reading, Massachusetts

74. Gray, H. B., and Winkler, J. R. (2018) Living with Oxygen. *Accounts of Chemical Research*. **51**, 1850–1857

75. Gill, S. C., and von Hippel, P. H. (1989) Calculation of protein extinction coefficients from amino acid sequence data. *Analytical Biochemistry*. **182**, 319–326

76. Dunford, H. B. (1999) *Heme Peroxidases*, Wiley-VCH, New York

77. Lever, A. B. P., and Gray, H. B. (eds.) (1989) *Iron Porphyrins Part III*, VCH Publishers, Inc., New York, New York

78. Ndontsa, E. N., Moore, R. L., and Goodwin, D. C. (2012) Stimulation of KatG catalase activity by peroxidatic electron donors. *Archives of Biochemistry and Biophysics*. **525**, 215–222

79. Winkler, J. R., and Gray, H. B. (2014) Electron flow through metalloproteins. *Chemical Reviews*. **114**, 3369–3380

80. Winkler, J. R., and Gray, H. B. (2015) Could tyrosine and tryptophan serve multiple roles in biological redox processes? *Philosophical Transactions of the Royal Society A: Mathematical, Physical and Engineering Sciences*. 10.1098/rsta.2014.0178

81. Gray, H. B., and Winkler, J. R. (2015) Hole hopping through tyrosine/tryptophan chains protects proteins from oxidative damage. *Proceedings of the National Academy of Sciences*. **112**, 10920–10925

82. Gray, H., and Winkler, J. Protein Redox Chain Database

83. Moore, S. 'Round-the-horn site-directed mutagenesis

84. Njuma, O. J., Davis, I., Ndontsa, E. N., Krewall, J. R., Liu, A., and Goodwin, D. C. (2017) Mutual synergy between catalase and peroxidase activities of the bifunctional enzyme KatG is facilitated by electron-hole hopping within the enzyme. *Journal of Biological Chemistry*. 10.1074/jbc.M117.791202

85. Loewen, P. C., Malaka, P., Silva, D., Donald, L. J., Switala, J., Villanueva, J., Fita, I., and Kumar, A. (2018) KatG-Mediated Oxidation Leading to Reduced Susceptibility of Bacteria to Kanamycin. 10.1021/acsomega.8b00356

86. Ghiladi, R. A., Knudsen, G. M., Medzihradszky, K. F., and Ortiz de Montellano, P. R. (2005) The Met-Tyr-Trp cross-link in Mycobacterium tuberculosis catalase-peroxidase (KatG): autocatalytic formation and effect on enzyme catalysis and spectroscopic properties. *J Biol Chem*. **280**, 22651–22663

87. Ghiladi, R. A., Medzihradszky, K. F., and Ortiz de Montellano, P. R. (2005) Role of the Met-Tyr-Trp cross-link in Mycobacterium tuberculosis catalase-peroxidase (KatG) as revealed by KatG(M255I). *Biochemistry*. **44**, 15093–15105

88. Cade, C. E., Dlouhy, A. C., Medzihradszky, K. F., Salas-Castillo, S. P., and Ghiladi, R. A. (2010) Isoniazid-resistance conferring mutations in Mycobacterium tuberculosis KatG: catalase, peroxidase, and INH-NADH adduct formation activities. *Protein Sci*. **19**, 458–474

89. Zhao, X., Suarez, J., Khajo, A., Yu, S., Metlitsky, L., and Magliozzo, R. S. (2010) A Radical on the Met-Tyr-Trp Modification Required for Catalase Activity in Catalase-Peroxidase Is Established by Isotopic Labeling and Site-Directed Mutagenesis. *Journal of the American Chemical Society*. **132**, 8268–8269

90. Machuqueiro, M., Victor, B., Switala, J., Villanueva, J., Rovira, C., Fita, I., and Loewen, P. C. (2017) The Catalase Activity of Catalase-Peroxidases Is Modulated by Changes in the p K a of the Distal Histidine. *Biochemistry*. **56**, 2271–2281

91. Wang, B., Fita, I., and Rovira, C. (2018) Theory Uncovers the Role of the Methionine-Tyrosine-Tryptophan Radical Adduct in the Catalase Reaction of KatGs: O 2 Release Mediated by Proton-Coupled Electron Transfer. *Chemistry - A European Journal*. **24**, 5388–5395

92. Zhao, X., Khajo, A., Jarrett, S., Suarez, J., Levitsky, Y., Burger, R. M., Jarzecki, A. A., and Magliozzo, R. S. (2012) Specific function of the Met-Tyr-Trp adduct radical

and residues Arg-418 and Asp-137 in the atypical catalase reaction of catalase-peroxidase KatG. *J Biol Chem*. **287**, 37057–37065

93. Christa Jakopitsch, ‡, Jutta Vlasits, ‡, ben Wiseman, §, Peter C. Loewen, § and, and Christian Obinger*, ‡ (2007) Redox Intermediates in the Catalase Cycle of Catalase-Peroxidases from Synechocystis PCC 6803, Burkholderia pseudomallei, and Mycobacterium tuberculosis†. 10.1021/BI062266+

94. Kruft, B. I., Magliozzo, R. S., and Jarzęcki, A. A. (2015) Density Functional Theory Insights into the Role of the Methionine–Tyrosine–Tryptophan Adduct Radical in the KatG Catalase Reaction: O2 Release from the Oxyheme Intermediate. *The Journal of Physical Chemistry A*. **119**, 6850–6866

95. Schulz, C. E., Rutter, R., Sage, J. T., Debrunner, P. G., and Hager, L. P. (1984) Moessbauer and electron paramagnetic resonance studies of horseradish peroxidase and its catalytic intermediates. *Biochemistry*. **23**, 4743–4754

96. Lang, G., Spartalian, K., and Yonetani, T. (1976) Mössbauer spectroscopic study of compound es of cytochrome c peroxidase. *Biochimica et Biophysica Acta (BBA) - General Subjects*. **451**, 250–258

97. Harami, T., Maeda, Y., Morita, Y., Trautwein, A., and Gonser, U. (1977) Mössbauer spectroscopic determination of the electronic structure of highly oxidized iron in hemoproteins. *The Journal of Chemical Physics*. **67**, 1164–1169

98. Garcia-Serres, R., Davydov, R. M., Matsui, T., Ikeda-Saito, M., Hoffman, B. M., and Huynh, B. H. (2007) Distinct Reaction Pathways Followed upon Reduction of Oxy-Heme Oxygenase and Oxy-Myoglobin as Characterized by Mössbauer Spectroscopy. *Journal of the American Chemical Society*. **129**, 1402–1412

99. Lang, G., and Marshali, W. (1966) Mössbauer effect in some haemoglobin compounds. *Proceedings of the Physical Society*. **87**, 3–34

100. Sharrock, M., Münck, E., Debrunner, P. G., Marshall, V., Lipscomb, J. D., and Gunsalus, I. C. (1973) Mössbauer Studies of Cytochrome P-450cam. *Biochemistry*. **12**, 258–265

101. Spartalian, K., Lang, G., Collman, J. P., Gagne, R. R., and Reed, C. A. (1975) Mössbauer spectroscopy of hemoglobin model compounds: evidence for conformational excitation. *The Journal of Chemical Physics*. **63**, 5375–5382

102. Simaan, A. J., Banse, F., Girerd, J. J., Wieghardt, K., and Bill, E. (2001) The electronic structure of non-heme iron(III)-hydroperoxo and iron(III)-peroxo model complexes studied by Mössbauer and electron paramagnetic resonance spectroscopies. *Inorganic Chemistry*. **40**, 6538–6540

103. Hayashi, T., Dejima, H., Matsuo, T., Sato, H., Murata, D., and Hisaeda, Y. (2002) Blue Myoglobin Reconstituted with an Iron Porphycene Shows Extremely High Oxygen Affinity. *Journal of the American Chemical Society*. **124**, 11226–11227

104. Maeda, Y., and Morita, Y. (1967) Mössbauer effect in peroxidase-hydrogen peroxide compounds. *Biochemical and Biophysical Research Communications*. **29**, 680–685

105. Yonetani, T. (1967) Studies on cytochrome c peroxidase. X. Crystalline apo-and reconstituted holoenzymes. *J Biol Chem*. **242**, 5008–5013

106. Caughey, W. S., Fujimoto, W. Y., Bearden, A. J., and Moss, T. H. (1966) Mossbauer Spectroscopic Evidence for Low-Spin Iron in Dehydrated Metmyoglobin. *Biochemistry*. 10.1021/bi00868a019

107. Adler, A. D., Longo, F. R., Kampas, F., and Kim, J. (1970) On the preparation of metalloporphyrins. *Journal of Inorganic and Nuclear Chemistry*. **32**, 2443–2445

108. Gordon Erdman, J., and Corwin, A. H. (1947) The Nature of the Non-Porphyrin Bonding in Derivatives of Ferriheme. *Journal of the American Chemical Society*. **69**, 750–755

109. Dreselt, E. I. B., and Falk, J. E. *Studies on the Biosynthesis of Blood Pigments 2. HAEM AND PORPHYRIN FORMATION IN INTACT CHICKEN ERYTHROCYTES**

110. Vogel, W., Richert, D. A., Pixley, B. Q., and Schulman, M. P. (1960) Heme Synthesis in Iron-deficient Duck Blood. *Journal of Biological Chemistry*. **235**, 1769–1775

111. Sellers, V. M., Wu, C. K., Dailey, T. A., and Dailey, H. A. (2001) Human ferrochelatase: Characterization of substrate - Iron binding and proton-abstracting residues. *Biochemistry*. **40**, 9821–9827

112. Burden, A. E., Wu, C. K., Dailey, T. A., Busch, J. L. H., Dhawan, I. K., Rose, J. P., Wang, B. C., and Dailey, H. A. (1999) Human ferrochelatase: Crystallization, characterization of the [2Fe-2S] cluster and determination that the enzyme is a homodimer. *Biochimica et Biophysica Acta - Protein Structure and Molecular Enzymology*. **1435**, 191–197

113. Najahi-Missaoui, W., and Dailey, H. A. (2005) Production and characterization of erythropoietic protoporphyric heterodimeric ferrochelatases. *Blood*. **106**, 1098–1104

114. Porra, R. J., Vitols, K. S., Labbe, R. F., and Newton, N. A. (1967) Studies on ferrochelatase. The effects of thiols and other factors on the determination of activity. *The Biochemical journal*. **104**, 321–327

115. Silver, J., and Lukas, B. (1983) Mössbauer studies on protoporphyrin IX iron(III) solutions. *Inorganica Chimica Acta*. **78**, 219–224

116. Jung, C., Lendzian, F., Schünemann, V., Richter, M., Böttger, L. H., Trautwein, A. X., Contzen, J., Galander, M., Ghosh, D. K., and Barra, A.-L. (2005) Multi-frequency EPR and Mössbauer spectroscopic studies on freeze-quenched reaction intermediates of nitric oxide synthase. *Magnetic Resonance in Chemistry*. **43**, S84–S95

117. Meilleur, F., Contzen, J., Myles, D. A. A., and Jung, C. (2004) Structural stability and dynamics of hydrogenated and perdeuterated cytochrome P450cam (CYP101). *Biochemistry*. **43**, 8744–8753

118. Charkin, O. P., Klimenko, N. M., Nguyen, P. T., Charkin, D. O., Mebel, A. M., Lin, S. H., Wang, Y.-S., Wei, S.-C., and Chang, H.-C. (2005) Fragmentation of heme and hemin+ with sequential loss of carboxymethyl groups: A DFT and mass-spectrometry study. *Chemical Physics Letters*. **415**, 362–369

119. Bertrand, T., Eady, N. A. J., Jones, J. N., Nagy, J. M., Jamart-Grégoire, B., Raven, E. L., and Brown, K. A. (2004) Crystal structure of Mycobacterium tuberculosis catalase-peroxidase. *Journal of Biological Chemistry*. **279**, 38991–38999

120. Ghiladi, R. A., Medzihradszky, K. F., and Ortiz de Montellano, P. R. (2005) Role of the Met-Tyr-Trp cross-link in Mycobacterium tuberculosis catalase-peroxidase (KatG) as revealed by KatG(M255I). *Biochemistry*. **44**, 15093–15105

121. Donald, L. J., Krokhin, O. v., Duckworth, H. W., Wiseman, B., Deemagarn, T., Singh, R., Switala, J., Carpena, X., Fita, I., and Loewen, P. C. (2003) Characterization of the catalase-peroxidase KatG from Burkholderia pseudomallei by mass spectrometry. *Journal of Biological Chemistry*. **278**, 35687–35692

122. Carpena, X., Wiseman, B., Deemagarn, T., Singh, R., Switala, J., Ivancich, A., Fita, I., and Loewen, P. C. (2005) A molecular switch and electronic circuit modulate catalase activity in catalase-peroxidases. *EMBO Reports*. **6**, 1156–1162

123. Njuma, O. J., Ndontsa, E. N., and Goodwin, D. C. (2014) Catalase in peroxidase clothing: Interdependent cooperation of two cofactors in the catalytic versatility of KatG. *Archives of Biochemistry and Biophysics*. **544**, 27–39

124. Jacquemin, D., Planchat, A., Adamo, C., and Mennucci, B. (2012) TD-DFT Assessment of Functionals for Optical 0−0 Transitions in Solvated Dyes. 10.1021/ct300326f

125. Ditchfield, R., Hehre, W. J., and Pople, J. A. (1971) Self-Consistent Molecular-Orbital Methods. IX. An Extended Gaussian-Type Basis for Molecular-Orbital Studies of Organic Molecules. *The Journal of Chemical Physics*. **54**, 724–728

126. Rassolov, V. A., Pople, J. A., Ratner, M. A., and Windus, T. L. (1998) 6-31G* basis set for atoms K through Zn. *Journal of Chemical Physics*. **109**, 1223–1229

127. Treatment for TB Disease | Treatment | TB | CDC [online] https://www.cdc.gov/tb/topic/treatment/tbdisease.htm (Accessed May 5, 2021)

128. Tuberculosis: Multidrug-resistant tuberculosis (MDR-TB) [online] https://www.who.int/news-room/q-a-detail/tuberculosis-multidrug-resistant-tuberculosis-(mdr-tb) (Accessed May 5, 2021)

129. Rouse, D. A., DeVito, J. A., Li, Z., Byer, H., and Morris, S. L. (1996) Site-directed mutagenesis of the katC gene of Mycobacterium tuberculosis: Effects on catalase-peroxidase activities and isoniazid resistance. *Molecular Microbiology*. **22**, 583–592

130. Scior, T., Meneses Morales, I., Garcés Eisele, S. J., Domeyer, D., and Laufer, S. (2002) Antitubercular isoniazid and drug resistance of Mycobacterium tuberculosis - A review. *Archiv der Pharmazie*. **335**, 511–525

131. Marttila, H. J., Soini, H., Huovinen, P., and Viljanen, M. K. (1996) katG mutations in isoniazid-resistant Mycobacterium tuberculosis isolates recovered from Finnish patients. *Antimicrobial Agents and Chemotherapy*. **40**, 2187–2189

132. Middlebrook, G., and Cohn, M. L. (1953) Some observations on the pathogenicity of isoniazid-resistant variants of tubercle bacilli. *Science*. **118**, 297–299

133. Zhang, Y., Heym, B., Allen, B., Young, D., and Cole, S. (1992) The catalase - Peroxidase gene and isoniazid resistance of Mycobacterium tuberculosis. *Nature*. **358**, 591–593

134. Rawat, R., Whitty, A., and Tonge, P. J. (2003) The isoniazid-NAD adduct is a slow, tight-binding inhibitor of InhA, the Mycobacterium tuberculosis enoyl reductase: Adduct affinity and drug resistance. *Proceedings of the National Academy of Sciences of the United States of America*. **100**, 13881–13886

135. Martins, F., Santos, S., Ventura, C., Elvas-Leitão, R., Santos, L., Vitorino, S., Reis, M., Miranda, V., Correia, H. F., Aires-De-Sousa, J., Kovalishyn, V., Latino, D. A. R. S., Ramos, J., and Viveiros, M. (2014) Design, synthesis and biological evaluation of novel isoniazid derivatives with potent antitubercular activity. *European Journal of Medicinal Chemistry*. **81**, 119–138

136. Vila-Viçosa, D., Victor, B. L., Ramos, J., Machado, D., Viveiros, M., Switala, J., Loewen, P. C., Leitao, R., Martins, F., and Machuqueiro, M. (2017) Insights on the Mechanism of Action of INH-C10 as an Antitubercular Prodrug. *Molecular Pharmaceutics*. **14**, 4597–4605

137. Zámocký, M., Hofbauer, S., Schaffner, I., Gasselhuber, B., Nicolussi, A., Soudi, M., Pirker, K. F., Furtmüller, P. G., and Obinger, C. (2015) Independent evolution of

four heme peroxidase superfamilies. *Archives of Biochemistry and Biophysics*. **574**, 108–119

138. Zamocky, M., Gasselhuber, B., Furtmuller, P. G., and Obinger, C. (2014) Turning points in the evolution of peroxidase-catalase superfamily: molecular phylogeny of hybrid heme peroxidases. *Cell Mol Life Sci*. **71**, 4681–4696

139. Kathiresan, M., and English, A. M. (2017) LC-MS/MS suggests that hole hopping in cytochrome c peroxidase protects its heme from oxidative modification by excess H2O2. *Chem Sci*. **8**, 1152–1162

140. Zámocký, M., Janeček, Š., and Obinger, C. Fungal Hybrid B heme peroxidases-unique fusions of a heme peroxidase domain with a carbohydrate-binding domain. 10.1038/s41598-017-09581-8

141. Baker, R. D., Cook, C. O., and Goodwin, D. C. (2004) Properties of catalase–peroxidase lacking its C-terminal domain. *Biochemical and Biophysical Research Communications*. **320**, 833–839

142. Baker, R. D., Cook, C. O., and Goodwin, D. C. (2006) Catalase-peroxidase active site restructuring by a distant and “inactive” domain. *Biochemistry*. **45**, 7113–7121

143. Floudas, D., Binder, M., Riley, R., Barry, K., Blanchette, R. A., Henrissat, B., Martínez, A. T., Otillar, R., Spatafora, J. W., Yadav, J. S., Aerts, A., Benoit, I., Boyd, A., Carlson, A., Copeland, A., Coutinho, P. M., de Vries, R. P., Ferreira, P., Findley, K., Foster, B., Gaskell, J., Glotzer, D., Górecki, P., Heitman, J., Hesse, C., Hori, C., Igarashi, K., Jurgens, J. A., Kallen, N., Kersten, P., Kohler, A., Kües, U., Kumar, T. K. A., Kuo, A., LaButti, K., Larrondo, L. F., Lindquist, E., Ling, A., Lombard, V., Lucas, S., Lundell, T., Martin, R., McLaughlin, D. J., Morgenstern, I., Morin, E., Murat, C., Nagy, L. G., Nolan, M., Ohm, R. A., Patyshakuliyeva, A., Rokas, A., Ruiz-Dueñas, F. J., Sabat, G., Salamov, A., Samejima, M., Schmutz, J., Slot, J. C., John, F. S., Stenlid, J., Sun, H., Sun, S., Syed, K., Tsang, A., Wiebenga, A., Young, D., Pisabarro, A., Eastwood, D. C., Martin, F., Cullen, D., Grigoriev, I. v., and Hibbett, D. S. (2012) The paleozoic origin of enzymatic lignin decomposition reconstructed from 31 fungal genomes. *Science*. **336**, 1715–1719

144. Falade, A. O., Nwodo, U. U., Iweriebor, B. C., Green, E., Mabinya, L. v., and Okoh, A. I. (2017) Lignin peroxidase functionalities and prospective applications. *MicrobiologyOpen*. **6**, 394

145. Hiraga, S., Sasaki, K., Ito, H., Ohashi, Y., and Matsui, H. (2001) A large family of class III plant peroxidases. *Plant and Cell Physiology*. **42**, 462–468

146. Ishikawa, T., Tajima, N., Nishikawa, H., Gao, Y., Rapolu, M., Shibata, H., Sawa, Y., and Shigeoka, S. (2010) Euglena gracilis ascorbate peroxidase forms an intramolecular dimeric structure: Its unique molecular characterization. *Biochemical Journal*. **426**, 125–134

147. Adak, S., and Datta, A. K. (2005) Leishmania major encodes an unusual peroxidase that is a close homologue of plant ascorbate peroxidase: A novel role of the transmembrane domain. *Biochemical Journal*. **390**, 465–474

148. Lazzarotto, F., Turchetto-Zolet, A. C., and Margis-Pinheiro, M. (2015) Revisiting the Non-Animal Peroxidase Superfamily. *Trends in Plant Science*. **20**, 807–813

149. González-Flecha, B., and Demple, B. (1999) Role for the oxyS gene in regulation of intracellular hydrogen peroxide in Escherichia coli. *Journal of Bacteriology*. **181**, 3833–3836

150. Choi, H. J., Kim, S. J., Mukhopadhyay, P., Cho, S., Woo, J. R., Storz, G., and Ryu, S. E. (2001) Structural basis of the redox switch in the OxyR transcription factor. *Cell*. **105**, 103–113

151. Delaunay, A., Pflieger, D., Barrault, M. B., Vinh, J., and Toledano, M. B. (2002) A thiol peroxidase is an H2O2 receptor and redox-transducer in gene activation. *Cell*. **111**, 471–481

152. Gebendorfer, K. M., Drazic, A., Le, Y., Gundlach, J., Bepperling, A., Kastenmüller, A., Ganzinger, K. A., Braun, N., Franzmann, T. M., and Winter, J. (2012) Identification of a hypochlorite-specific transcription factor from Escherichia coli. *Journal of Biological Chemistry*. **287**, 6892–6903

153. Drazic, A., and Winter, J. (2014) The physiological role of reversible methionine oxidation. *Biochimica et Biophysica Acta - Proteins and Proteomics*. **1844**, 1367–1382

154. Drazic, A., Miura, H., Peschek, J., Le, Y., Bach, N. C., Kriehuber, T., and Winter, J. (2013) Methionine oxidation activates a transcription factor in response to oxidative stress. *Proceedings of the National Academy of Sciences of the United States of America*. **110**, 9493–9498

155. Vogt, W. (1995) Oxidation of methionyl residues in proteins: Tools, targets, and reversal. *Free Radical Biology and Medicine*. **18**, 93–105

156. Ener, M. E., Gray, H. B., and Winkler, J. R. (2017) Hole Hopping through Tryptophan in Cytochrome P450. *Biochemistry*. **56**, 3531–3538

157. Levine, R. L., Berlett, B. S., Moskovitz, J., Mosoni, L., and Stadtman, E. R. (1999) Methionine residues may protect proteins from critical oxidative damage. *Mechanisms of Ageing and Development*. **107**, 323–332

158. Jay, R. W., and Gray, H. B. (2015) Could tyrosine and tryptophan serve multiple roles in biological redox processes? *Philosophical Transactions of the Royal Society A: Mathematical, Physical and Engineering Sciences*. 10.1098/rsta.2014.0178

159. Egan, R. W., Paxton, J., and Kuehl Jr., F. A. (1976) Mechanism for irreversible self-deactivation of prostaglandin synthetase. *J Biol Chem*. **251**, 7329–7335

160. Smith, W. L., Eling, T. E., Kulmacz, R. J., Marnett, L. J., and Tsai, A. L. (1992) Tyrosyl radicals and their role in hydroperoxide-dependent activation and inactivation of prostaglandin endoperoxide synthase. *Biochemistry*. **31**, 3–7

161. Marnett, L. J. (2000) Cyclooxygenase mechanisms. *Curr Opin Chem Biol*. **4**, 545–552

162. Blobaum, A. L., and Marnett, L. J. (2007) Structural and Functional Basis of Cyclooxygenase Inhibition. *Journal of Medicinal Chemistry*. **50**, 1425–1441

163. Garscha, U., and Oliw, E. (2008) Pichia expression and mutagenesis of 7,8-linoleate diol synthase change the dioxygenase and hydroperoxide isomerase. *Biochemical and Biophysical Research Communications*. **373**, 579–583

164. Garscha, U., and Oliw, E. H. (2008) Critical amino acids for the 8(R)-dioxygenase activity of linoleate diol synthase. A comparison with cyclooxygenases. *FEBS Letters*. **582**, 3547–3551

165. Jernerén, F., Garscha, U., Hoffmann, I., Hamberg, M., and Oliw, E. H. (2010) Reaction mechanism of 5,8-linoleate diol synthase, 10R-dioxygenase, and 8,11-hydroperoxide isomerase of Aspergillus clavatus. *Biochimica et Biophysica Acta - Molecular and Cell Biology of Lipids*. **1801**, 503–507

166. Streit, B. R., Celis, A. I., Shisler, K., Rodgers, K. R., Lukat-Rodgers, G. S., and DuBois, J. L. (2017) Reactions of Ferrous Coproheme Decarboxylase (HemQ) with O2 and H2O2 Yield Ferric Heme b. *Biochemistry*. **56**, 189–201

167. Celis, A. I., Gauss, G. H., Streit, B. R., Shisler, K., Moraski, G. C., Rodgers, K. R., Lukat-Rodgers, G. S., Peters, J. W., and DuBois, J. L. (2017) Structure-Based Mechanism for Oxidative Decarboxylation Reactions Mediated by Amino Acids and Heme Propionates in Coproheme Decarboxylase (HemQ). *Journal of the American Chemical Society*. **139**, 1900–1911

168. Torrents, E. (2014) Ribonucleotide reductases: essential enzymes for bacterial life. *Frontiers in cellular and infection microbiology*. **4**, 52

169. Njeri, C. W., and Ellis, H. R. (2014) Shifting redox states of the iron center partitions CDO between crosslink formation or cysteine oxidation. *Arch Biochem Biophys*. **558**, 61–69

170. Dominy Jr., J. E., Hwang, J., Guo, S., Hirschberger, L. L., Zhang, S., and Stipanuk, M. H. (2008) Synthesis of amino acid cofactor in cysteine dioxygenase is regulated by substrate and represents a novel post-translational regulation of activity. *J Biol Chem*. **283**, 12188–12201

171. Ito, N., Phillips, S. E. v, Stevens, C., Ogel, Z. B., McPherson, M. J., Keen, J. N., Yadav, K. D. S., and Knowles, P. F. (1991) Novel thioether bond revealed by a 1.7 Å crystal structure of galactose oxidase. *Nature*. **350**, 87–90

172. Paukner, R., Staudigl, P., Choosri, W., Haltrich, D., and Leitner, C. (2015) Expression, purification, and characterization of galactose oxidase of Fusarium sambucinum in E. coli. *Protein Expression and Purification*. **108**, 73–79

173. Whittaker, M. M., and Whittaker, J. W. (2003) Cu(I)-dependent biogenesis of the galactose oxidase redox cofactor. *J Biol Chem*. **278**, 22090–22101

174. Whittaker, M. M., Kersten, P. J., Nakamura, N., Sanders-Loehr, J., Schweizer, E. S., and Whittaker, J. W. (1996) Glyoxal oxidase from Phanerochaete chrysosporium is a new radical-copper oxidase. *J Biol Chem*. **271**, 681–687

175. Ravikiran, B., and Mahalakshmi, R. (2014) Unusual post-translational protein modifications: The benefits of sophistication. *RSC Advances*. **4**, 33958–33974

176. Proshlyakov, D. A., Pressler, M. A., DeMaso, C., Leykam, J. F., DeWitt, D. L., and Babcock, G. T. (2000) Oxygen activation and reduction in respiration: involvement of redox-active tyrosine 244. *Science (New York, N.Y.)*. **290**, 1588–91

177. Davidson, V. L., Graichen, M. E., and Jones, L. H. (1995) Mechanism of reaction of allylamine with the quinoprotein methylamine dehydrogenase. *Biochemical Journal*. **308**, 487–492

178. Roujeinikova, A., Hothi, P., Masgrau, L., Sutcliffe, M. J., Scrutton, N. S., and Leys, D. (2007) New insights into the reductive half-reaction mechanism of aromatic amine dehydrogenase revealed by reaction with carbinolamine substrates. *Journal of Biological Chemistry*. **282**, 23766–23777

179. Choi, M., Shin, S., and Davidson, V. L. (2012) Characterization of Electron Tunneling and Hole Hopping Reactions between Different Forms of MauG and Methylamine Dehydrogenase within a Natural Protein Complex. **51**, 22

180. Shin, S., Choi, M., Williamson, H. R., and Davidson, V. L. (2014) A simple method to engineer a protein-derived redox cofactor for catalysis. *Biochimica et Biophysica Acta - Bioenergetics*. **1837**, 1595–1601

181. Campillo-Brocal, J. C., Chacón-Verdú, M. D., Lucas-Elío, P., and Sánchez-Amat, A. (2015) Distribution in microbial genomes of genes similar to lodA and goxA which encode a novel family of quinoproteins with amino acid oxidase activity. *BMC Genomics*. **16**, 231

182. Kathiresan, M., and English, A. M. (2017) LC-MS/MS suggests that hole hopping in cytochrome c peroxidase protects its heme from oxidative modification by excess H2O2. *Chemical Science*. **8**, 1152–1162

183. Martins, D., Kathiresan, M., and English, A. M. (2013) Cytochrome c peroxidase is a mitochondrial heme-based H2O2 sensor that modulates antioxidant defense. *Free Radical Biology and Medicine*. **65**, 541–551

184. Smulevich, G., Jakopitsch, C., Droghetti, E., and Obinger, C. (2006) Probing the structure and bifunctionality of catalase-peroxidase (KatG). *Journal of Inorganic Biochemistry*. **100**, 568–585

185. Yu, S., Girotto, S., Zhao, X., and Magliozzo, R. S. (2003) Rapid Formation of Compound II and a Tyrosyl Radical in the Y229F Mutant of Mycobacterium tuberculosis Catalase-peroxidase Disrupts Catalase but Not Peroxidase Function*. 10.1074/jbc.M304757200

186. Zhao, X., Yu, S., Ranguelova, K., Suarez, J., Metlitsky, L., Schelvis, J. P. M., and Magliozzo, R. S. (2009) Role of the oxyferrous heme intermediate and distal side adduct radical in the catalase activity of Mycobacterium tuberculosis KatG revealed by the W107F mutant. *Journal of Biological Chemistry*. **284**, 7030–7037

187. Bhaskar, B., Immoos, C. E., Shimizu, H., Sulc, F., Farmer, P. J., and Poulos, T. L. (2003) A novel heme and peroxide-dependent tryptophan-tyrosine cross-link in a mutant of cytochrome c peroxidase. *Journal of Molecular Biology*. **328**, 157–166

188. Savelli, B., Li, Q., Webber, M., Jemmat, A. M., Robitaille, A., Zamocky, M., Mathé, C., and Dunand, C. (2019) RedoxiBase: A database for ROS homeostasis regulated proteins. *Redox Biology*. **26**, 101247

189. Sievers, F., and Higgins, D. G. (2014) Clustal omega, accurate alignment of very large numbers of sequences. *Methods in Molecular Biology*. **1079**, 105–116

190. Sievers, F., Wilm, A., Dineen, D., Gibson, T. J., Karplus, K., Li, W., Lopez, R., McWilliam, H., Remmert, M., Söding, J., Thompson, J. D., and Higgins, D. G. (2011) Fast, scalable generation of high-quality protein multiple sequence alignments using Clustal Omega. *Molecular Systems Biology*. **7**, 539

191. Shannon, P., Markiel, A., Ozier, O., Baliga, N. S., Wang, J. T., Ramage, D., Amin, N., Schwikowski, B., and Ideker, T. (2003) Cytoscape: A software Environment for integrated models of biomolecular interaction networks. *Genome Research*. **13**, 2498–2504